INFORMATION TO USERS

This manuscript has been reproduced from the microfilm master. UMI films the text directly from the original or copy submitted. Thus, some thesis and dissertation copies are in typewriter face, while others may be from any type of computer printer.

The quality of this reproduction is dependent upon the quality of the copy submitted. Broken or indistinct print, colored or poor quality illustrations and photographs, print bleedthrough, substandard margins, and improper alignment can adversely affect reproduction.

In the unlikely event that the author did not send UMI a complete manuscript and there are missing pages, these will be noted. Also, if unauthorized copyright material had to be removed, a note will indicate the deletion.

Oversize materials (e.g., maps, drawings, charts) are reproduced by sectioning the original, beginning at the upper left-hand corner and continuing from left to right in equal sections with small overlaps.

Photographs included in the original manuscript have been reproduced xerographically in this copy. Higher quality 6" x 9" black and white photographic prints are available for any photographs or illustrations appearing in this copy for an additional charge. Contact UMI directly to order.

Bell & Howell Information and Learning
300 North Zeeb Road, Ann Arbor, MI 48106-1346 USA

UMI®
800-521-0600

RADAR IMAGING OF SATELLITES AT METER WAVELENGTHS

A DISSERTATION
SUBMITTED TO THE DEPARTMENT OF ELECTRICAL ENGINEERING
AND THE COMMITTEE ON GRADUATE STUDIES
OF STANFORD UNIVERSITY
IN PARTIAL FULFILLMENT OF THE REQUIREMENTS
FOR THE DEGREE OF
DOCTOR OF PHILOSOPHY

Arlen D. Schmidt
November 1999

I certify that I have read this dissertation and that in my opinion it is fully adequate, in scope and quality, as a dissertation for the degree of Doctor of Philosophy.

Prof. Howard A. Zebker
(Principal Adviser)

I certify that I have read this dissertation and that in my opinion it is fully adequate, in scope and quality, as a dissertation for the degree of Doctor of Philosophy.

Prof. G. Leonard Tyler

I certify that I have read this dissertation and that in my opinion it is fully adequate, in scope and quality, as a dissertation for the degree of Doctor of Philosophy.

Prof. Dwight G. Nishimura

Approved for the University Committee on Graduate Studies:

Abstract

Earth-based radar imaging of orbiting satellites at frequencies below about 1 GHz requires compensation of the dispersive effects of the ionosphere. Without the appropriate compensation, image resolution is limited to about 10–100 m at radar frequencies of 300 MHz, depending on ionospheric conditions. With compensation, the resolution expected in the absence of ionospheric dispersion can be achieved. For stable ionospheric conditions and frequencies above about 200 MHz, a $1/f$ phase model characterizes the propagation path to sufficient accuracy to allow mitigation of the ionospheric effects, provided that a sufficiently accurate estimate of total electron content (TEC) is available. The information required to estimate TEC is inherent in the radar observations. An initial estimate, accurate to about $\pm 2 \times 10^{16}$ e^-/m^2, is obtained from group-delay difference measurements across frequency subbands. That initial estimate is refined to the requisite accuracy by using radar image contrast as a measure of performance. A phase correction, calculated from the TEC estimate, provides compensated data from which full-resolution images are produced, provided the radar echo is not scintillating and the SNR is above about 10 dB. The accuracy of the TEC estimates obtained through imaging depends on center frequency, bandwidth, and angular aperture.

Radar imaging through the ionosphere is demonstrated with full-resolution ultra-wide bandwidth images of the Mir Space Station produced from data collected between January, 1998, and June, 1998, using SRI-International dish antennas at Stanford University and on Ascension Island. The two sites provided observations through both the benign mid-latitude ionosphere (Stanford), and the thicker, more-turbulent equatorial ionosphere (Ascension). Range and cross-range resolutions of 0.7 m and 0.5 m, respectively, are achieved in 200 to 400 MHz radar images of Mir as well as other satellites, confirming that, for these examples, the ionospheric effects are mitigated. The corresponding TEC estimates are self-consistent across 30-degree subaperture images to better than about 10^{15} e^-/m^2, in agreement with

the accuracy predicted by analysis. Thus, the experimental results are consistent with the predicted performance, both in terms of resolution and TEC estimation accuracy.

Acknowledgments

It has truly been a privilege to work with a professional and highly-skilled team of engineers at SRI on the project that led to this thesis. I was fortunate in being granted the responsibility for analyzing the radar data and developing techniques for producing VHF satellite images. That role was particularly rewarding in that I was able to see, and benefit from, the team's efforts to collect high-quality data—the fundamental ingredient for high-resolution radar images and unambiguous validation of the ionospheric compensation techniques. The research described in this thesis would have been impossible without the efforts of each member of the team; I gratefully acknowledge their many contributions. In particular, Mr. Philip Bentley designed most of the RF hardware and was responsible for system installation and subsystem testing. Dr. David Bubenik provided software for producing ephemeris and tracking control files from the two-line element sets, as well as guidance and tutelage in the area of orbital mechanics. Mr. George Carpenter, my supervisor at SRI, completed most of the initial system design. Dr. Michael Cousins designed and supervised the construction of the Ascension Island radar site, and managed the Stanford and Ascension Island radar sites. Dr. Kenneth Dreyer sold and managed the project, and nurtured the idea of forming VHF satellite images. Mr. Terje Oseberg wrote most of the software for the data acquisition system. I have enjoyed immensely working with the members of this team, whom I now count as good friends.

Foremost, I gratefully acknowledge the many contributions of my friend and mentor, Mr. Gary Price, an integral part of the SRI team. Several ideas presented herein originated with Gary. He made countless direct contributions to this research, at both macroscopic and microscopic levels, especially in the areas of ionospheric physics and signal processing.

I thank my reading committee, Dr. Howard Zebker, Dr. G. Leonard Tyler, and Dr. Dwight Nishimura. Without their efforts, this document would be much more difficult to read and understand.

Finally, I could not have completed this thesis without the unending love and support of my wife, Joyce, and our children, Jacob, Adam, and Nicola. They made as many sacrifices and put as much effort into seeing this research through to completion as I. Thank you, Joyce. Thank you, Jacob. Thank you, Adam. Thank you, Nicola.

Contents

List of Tables

List of Figures

List of Symbols

$A_{i,j}$ . . . . . amplitude of pixel (i,j) in the image.
$\mathbf{B}$ . . . . . geomagnetic flux density vector (Wb/m^2).
B . . . . . signal bandwidth (Hz); magnitude of geomagnetic field (Wb/m^2).
B_0 . . . . . nominal geomagnetic field, $= 0.5 \times 10^{-5}$ Wb/m^2 $= 0.5$ gauss.
B_c . . . . . coherence bandwidth (Hz).
B_{cr} . . . . . cross-range coherence bandwidth (Hz).
B_F . . . . . fractional bandwidth, $= B/f_c$.
b . . . . . propagation coefficient, $= 1.591 \times 10^3$ m^3/s^2.
C . . . . . cost function.
CP . . . . . circular polarization.
CT . . . . . computed tomography.
c . . . . . free-space velocity of light, $= 2.997925 \times 10^8$ m/s.
dBsm . . . . decibels relative to one square meter (RCS units).
$\mathbf{E}$ . . . . . electric field intensity vector (V/m).
EIRP . . . . . effective isotropic radiated power (W).
EM . . . . . electromagnetic.
e . . . . . charge on an electron, $= 1.6022 \times 10^{-19}$ C.
$\mathbf{F}$ . . . . . force on a free electron (N).
F_g . . . . . system Green's function.
FAIM . . . . Fully Analytic Ionospheric Model.
FM . . . . . frequency modulation.
FT . . . . . Fourier transform.
f . . . . . frequency (Hz).
f_oF_2 . . . . . plasma frequency at the peak of the F region (Hz).
f_l . . . . . center frequency of lower subband in TDOA processing (Hz).

f_2 . . . . . center frequency of higher subband in TDOA processing (Hz).
f_c . . . . . center frequency or local oscillator frequency (Hz).
f_D . . . . . Doppler frequency shift (Hz).
f_{max} . . . . . maximum frequency in signal band (Hz).
f_N . . . . . cyclical plasma frequency (Hz), $= \omega_N/2\pi$.
f_x . . . . . spatial frequency in the image range direction (cycles/m).
f_y . . . . . spatial frequency in the image cross-range direction (cycles/m).
GPS . . . . . Global Positioning System.
$\mathbf{H}$ . . . . . geomagnetic field intensity vector (A/m).
H . . . . . scale height parameter for the Chapman profile (m).
h_a . . . . . impulse response of the matched filter.
I . . . . . in-phase component of the baseband signal.
IRI . . . . . International Reference Ionosphere.
ISAR . . . . . inverse synthetic aperture radar.
K_p . . . . . geomagnetic index.
k . . . . . free-space wavenumber (m^{-1}), $= 2\pi/\lambda$.
k_c . . . . . free-space wavenumber at the center frequency (m^{-1}), $= 2\pi/\lambda_c$.
LCP . . . . . left-hand circular polarization.
LEO . . . . . low Earth orbit.
LO . . . . . local oscillator.
LOS . . . . . line-of-sight.
l_g . . . . . group path length (m).
l_p . . . . . phase path length (m).
m . . . . . mass of an electron, $= 9.1095 \times 10^{-31}$ kg.
N . . . . . number density of free electrons (e^-/m^3).
N_m . . . . . peak electron number density in the Chapman profile (e^-/m^3).
N_{max} . . . . . maximum electron number density along the ray (e^-/m^3).
N_T . . . . . total electron content (e^-/m^2).
N_{T2} . . . . . quadratic component of residual TEC at edge of aperture (e^-/m^2).
N_{Tc} . . . . . best constant fit to the residual TEC (e^-/m^2).
N_{Tl} . . . . . best linear fit to the residual TEC (e^-/m^2).
N_{Tnl} . . . . . nonlinear component of the residual TEC (e^-/m^2).
NASA . . . . . National Aeronautics and Space Administration.

n . . . . . complex refractive index (unitless).

n_{O} . . . . . complex refractive index for the ordinary wave(unitless).

n_{X} . . . . . complex refractive index for the extraordinary wave(unitless).

O . . . . . the ordinary wave.

$\mathbf{P}$ . . . . . electric polarization vector ($\mathrm{C/m^2}$).

PCA . . . . . point of closest approach.

PRF . . . . . pulse repetition frequency (Hz).

PRI . . . . . pulse repetition interval (s), $= 1/\mathrm{PRF}$.

PSF . . . . . point spread function.

Q . . . . . quadrature component of the baseband signal.

QL . . . . . quasi-longitudinal.

QT . . . . . quasi-transverse.

q . . . . . charge on a particle (C).

R . . . . . range to a point on the target (m).

R_0 . . . . . target range at $t = 0$ (m).

R_1 . . . . . total constant-velocity drift of the target over the imaging period (m); distance from the ground to an ionospheric irregularity (m).

R_2 . . . . . distance from the source to an ionospheric irregularity (m).

R_{A} . . . . . apparent range to target (m).

R_{f} . . . . . radius of first Fresnel zone (m).

R_{t} . . . . . range to origin of target coordinate frame (m).

RCP . . . . . right-hand circular polarization.

RCS . . . . . radar cross section ($\mathrm{m^2}$).

rms . . . . . root-mean-square.

S . . . . . time duration of pass (s).

$S_{2\mathrm{nl}}$ . . . . . nonlinear component of S_2.

S_2 . . . . . factor in φ_{i2} term, $= \int NB\cos\Theta dl$.

SAR . . . . . synthetic aperture radar.

SNR . . . . . signal to noise ratio (dB).

SRI . . . . . Stanford Research Institute.

s . . . . . slow-time or time in the pass (s).

TDOA . . . . . time difference of arrival (s).

TEC . . . . . integrated columnar, or total, electron content ($\mathrm{e^-/m^2}$).

TECU . . . . TEC units, 1 TECU = 10^{16} e^-/m^2.

t . . . . . time (s).

U . . . . . $1 - iZ$ for electrons (unitless).

UHF . . . . . ultra high frequency (300–3000 MHz).

UV . . . . . ultraviolet.

UWB . . . . ultra-wide bandwidth ($B_F \geq 25\%$).

VHF . . . . . very high frequency (30–300 MHz).

$\mathbf{v}$ . . . . . electron velocity (m/s).

v . . . . . target velocity (m/s).

v_a . . . . . complex received signal.

v_g . . . . . group velocity (m/s).

v_p . . . . . phase velocity (m/s).

vTEC . . . . vertical TEC (e^-/m^2).

W_{cr} . . . . . cross-range extent of target (m).

W_{rg} . . . . . range extent of target (m).

X . . . . . the extraordinary wave.

X . . . . . ω_N^2/ω^2 (unitless).

x_c . . . . . cross-range coordinate of a point on the target (m).

x_{off} . . . . . cross-range offset of the origin of the image (m).

x_r . . . . . range coordinate of a point on the target (m).

Y . . . . . ω_H/ω (unitless).

Z . . . . . ν/ω for electrons (unitless).

z . . . . . altitude (m).

z_m . . . . . altitude of the Chapman peak (m).

α . . . . . polar angle-coordinate of a point on the target (rad).

ϵ_o . . . . . permittivity of free space, $= 8.854 \times 10^{-12}$ F/m.

Δl_g . . . . . additional group path length due to the ionosphere (m).

Δl_p . . . . . additional phase path length due to ionosphere (m).

$\Delta l_{p,O}$ . . . . . additional phase path length of the ordinary wave (m).

$\Delta l_{p,X}$ . . . . . additional phase path length of the extraordinary wave (m).

ΔR . . . . . range shift used in motion compensation (m).

Δt . . . . . time shift used in motion compensation (s).

$\Delta\tau$ . . . . . additional group delay due to the ionosphere (s).

$\Delta\tau_1$ . . . . . additional group delay of the lower subband in TDOA processing (s).

$\Delta\tau_2$ . . . . . additional group delay of the higher subband in TDOA processing (s).

$\Delta\phi$ . . . . . phase difference (rad).

$\Delta\phi_e$ . . . . . phase difference at the edge of the aperture (rad).

δf . . . . . spacing between temporal frequency domain samples (Hz).

δx_c . . . . . cross-range resolution (m).

δx_r . . . . . range resolution (m).

$\delta\theta_{max}$ . . . . . maximum aspect angle change between pulses (rad).

ζ . . . . . normalized altitude for the Chapman profile (unitless).

Θ . . . . . aperture angle (rad); angle between ray and geomagnetic field (rad).

Θ_c . . . . . QL to QT transition angle (rad); coherent aperture (rad).

θ . . . . . aspect angle (rad).

λ . . . . . free-space wavelength (m).

λ_c . . . . . free-space wavelength at the center frequency (m).

λ_{min} . . . . . minimum wavelength in the transmitted waveform (m).

μ_o . . . . . permeability of free space, $= 4\pi \times 10^{-7}$ H/m.

ν . . . . . effective electron collision frequency (rad/s).

ξ . . . . . out-of-plane angle (rad).

ρ . . . . . polar range-coordinate of a point on the target (m).

τ . . . . . group delay (s).

ϕ . . . . . polar angle (rad).

ϕ_{lin} . . . . . linear phase component (rad).

ϕ_{MC} . . . . . phase correction used in motion compensation (rad).

ϕ_r . . . . . phase of the received signal (rad).

ϕ_{sin} . . . . . sinusoidal phase component (rad).

φ_c . . . . . incoherent phase threshold (rad).

φ_e . . . . . ionospheric phase contribution at the upper band edge (rad).

φ_{e2} . . . . . quadratic component of ϕ_e (rad).

φ_{e3} . . . . . cubic component of ϕ_e (rad).

φ_i . . . . . additional signal phase due to the ionosphere (rad).

φ_{i1} . . . . . linear component of φ_i (rad).

φ_{i2} . . . . . quadradic component of φ_i (rad).

φ_{i2e} . . . . . φ_{i2} at the upper band edge (rad).

φ_{i3a} . . . . . first term of cubic component of φ_i (rad).

φ_{i3b} . . . . . second term of cubic component of φ_i (rad).

Ω . . . . . Faraday rotation angle (rad).

Ω_{QT} . . . . . polarization ellipse rotation angle for QT propagation (rad).

ω . . . . . angular frequency (rad/s).

ω_c . . . . . center frequency or local oscillator frequency (rad/s).

ω_H . . . . . electron gyro-frequency (rad/s), $= eB/m$.

ω_{H0} . . . . . ω_H when $B = B_0$ (rad/s), $= 8.794 \times 10^5$ rad/s $= 1.400$ MHz.

ω_{HL} . . . . . longitudinal component of ω_H (rad/s).

ω_{HT} . . . . . transverse component of ω_H (rad/s).

ω_N . . . . . plasma frequency (rad/s), $= \sqrt{Ne^2/\epsilon_o m}$.

ω_t . . . . . target rotation rate (rad/s).

Chapter 1

Introduction

Radar has been used to observe and track satellites since the early 1960s, beginning shortly after the first artificial Earth satellites were launched. The primary purpose of these satellite-tracking radar systems has been to acquire and maintain tracking information for precise orbit control. For the most part, these systems have operated in the 1–10 GHz frequency range, although some systems have used frequencies as low as 100 MHz and others as high as 100 GHz. The choice of frequency has been a tradeoff between system complexity and propagation issues. At frequencies below about 1 GHz, signal delay caused by the ionosphere degrades the accuracy of the range measurements and, as a result, the accuracy of the orbit estimate. At frequencies above about 10 GHz, hardware performance along with higher atmospheric absorption have limited the maximum range of detection, especially in the early systems. Further discussion of satellite-tracking radar is given in, for example, *Barton* (1965), *Millman* (1965), *Hoffman et al.* (1969), *Lerch* (1970), and *Coster et al.* (1993).

Radar imaging of satellites, which also started in the 1960s, has been used to identify satellites and to determine their orientation (e.g., *Bromaghim and Perry*, 1978; *Ausherman et al.*, 1984). The frequency range for imaging radar systems, however, has been kept above about 2 GHz in order to achieve high resolution with a relatively short satellite illumination time and to avoid the delay and distortion introduced on electromagnetic signals—including radar pulses—by the ionosphere. These delay and distortion effects become worse, very rapidly, as lower frequencies are used, significantly degrading image quality for frequencies below about 1 GHz. Previously, the very high frequency (VHF) range was not a viable

option, as ionospheric effects would degrade the radar image to the point of being unrecognizable. This research develops methods for estimating and removing those ionospheric effects from the radar data with the result of full recovery of image resolution, at least for moderate ionospheric conditions.

This thesis provides an analysis of the effects of the ionosphere on radar images, along with techniques for estimating and removing those effects by compensation of the radar data. The techniques are applied to the specific problem of imaging satellites from ground-based radar systems. They extend the ability to image satellites into the central VHF range—100 to 150 MHz—with the lower frequency limit determined by ionospheric conditions. The techniques also produce high-precision estimates of the total electron content of the ionosphere integrated over the radar-to-target ray path.

The results of this research, including both the analysis of ionospheric effects and the development of techniques for estimating and removing those effects, are also applicable, in many respects, to the complementary problem of using very high frequencies for imaging Earth from a satellite.

1.1 Motivation

In the past decade, there has been increasing interest in the use of longer wavelengths for radar imaging of Earth, motivated primarily by the ability to penetrate foliage and ground to greater depths as the wavelength is increased beyond about a half meter.[1] This rapidly developing ability to 'see' through media that are opaque to microwave radar is opening a wide variety of new applications for VHF radar—including, for example, terrain mapping through foliage (*Fleischman et al.*, 1996; *McCorkle*, 1993; *Sheen et al.*, 1992), forest biomass estimation (*Rignot et al.*, 1995; *LeToan et al.*, 1992), and buried object detection (*Grosch*, 1994; *Sargis et al.*, 1994). To date, these 'penetrating radar systems' have largely operated in the VHF (30 to 300 MHz) and UHF (300 to 3000 MHz) ranges. They have been vehicle-mounted (*Happ et al.*, 1996; *Blejer et al.*, 1994) or airborne (*Sheen et al.*, 1994; *Gustavsson et al.*, 1993; *Vickers et al.*, 1992; *Held et al.*, 1988), and have survey rates that are suitable only for mapping relatively small areas, typically measured in acres per hour for the vehicular systems, or tens to hundreds of square kilometers per hour for the airborne

[1] The degree of penetration depends on the type and density of the foliage or the constitutive parameters of the soil, as well as the angle of incidence, which is determined by the imaging geometry.

systems. To achieve global coverage at reasonable cost, it may be possible to eventually fly enhanced versions of some of these penetrating radar systems on satellites. However, those systems would be subject to the dispersive effects of the ionosphere.

Recent studies have shown that the ionosphere would severely degrade the performance of a satellite-borne VHF or UHF radar (e.g., *Ishimaru et al.*, 1999; *Kim and van Zyl*, 1998; *Fitzgerald*, 1997; *Quegan and Lamont*, 1986).[2] Those studies, however, have not considered the possibility of estimating and removing the ionospheric effects from the radar data.[3] That possibility has been the primary motivation behind the research described in this thesis, which includes both analysis of the effects and proposal and development of estimation and compensation techniques.

Once estimation and compensation techniques have been proposed, the natural question is how to validate their performance prior to making the large investment in designing and launching a VHF radar satellite. One approach to validation, admittedly limited in value, is to use a computer simulation to generate synthetic radar data that are distorted by the *expected* ionospheric effects. Such a simulation would need to incorporate a man-made model of the continually varying ionosphere. The synthetic data produced by simulation could be used in preliminary testing of the ionospheric estimation and compensation techniques.

This research considers another approach to validation: the complementary problem of imaging a satellite through the ionosphere from an Earth-based VHF radar. Specifically, by producing satellite images from an Earth-based radar, this research confirms that the techniques are able to estimate and compensate all significant aspects of the *actual* ionospheric effects.

Some aspects of the complementary problems—satellite imaging and Earth imaging—are indeed different. Most notably, the size of the image area is several orders of magnitude larger for the Earth-imaging problem. Also, the satellite is immersed in the ionosphere and potentially much closer to any ionospheric irregularities. For a satellite-borne radar, this leads to the possibility of amplitude scintillation in radar echoes from targets on the ground, due to differential bending of the ray, followed by propagation over large distances. For an Earth-based radar, under the same ionospheric conditions, a satellite echo might

[2]Further analysis of ionospheric effects on VHF satellite radar systems can be found in *Brown and Cable* (1993), *Knepp and Mokole* (1992), *Knowles* (1987), *Rino and Owen* (1984), and *Bush* (1978).

[3]One study, *Kim and van Zyl* (1998), does mention that it would be important to compensate for the ionospheric effects, and suggests using a dual-frequency measurement technique similar to that used for ionospheric compensation of Global Positioning System signals.

not exhibit amplitude scintillation, since the bending occurs closer to the target. Although there are differences, the fundamental challenge for both imaging problems is estimating and compensating the ionospheric effects. This thesis deals with the satellite-imaging problem; the extensions needed to solve the Earth-imaging problem are left for future research.

1.2 History

Radar imaging began in the 1950s when engineers realized that a moving radar receives echoes in which the Doppler frequency history of a scatterer depends on the location of the scatterer in the area illuminated by the radar. This led to the development of airborne radar systems for terrain mapping, an application known as synthetic aperture radar (SAR). A review of the early developments is given in *Sherwin et al.* (1962).

By the early 1960s, radar hardware had evolved to the point where echoes could be detected from Mercury, Venus, and Mars—a development that stimulated interest and significant research in the new field of planetary radar astronomy. Scientists used the range measurements obtained from the radar echo delays to refine the orbit estimates to the accuracy needed for the first spacecraft encounters with those planets. Further radar performance improvements, including higher coherent transmitter power, lower receiver system noise temperature, and larger antennas at Arecibo, Puerto Rico, and Goldstone, California, provided radar echoes that contained a wealth of new information about the near-Earth planets. Analysis of those radar echoes, for example, provided estimates of the size and spin rate of Venus, whose surface is hidden to optical observations by thick clouds. Radar data, collected at Arecibo in 1975, provided the first 'high resolution'—10 to 20 km—images of the surface of Venus. A detailed review of the fascinating history of planetary radar astronomy is given by *Pettengill et al.* (1980) and *Ostro* (1993).

The first radar images of Earth's natural satellite, the moon, were published in the early 1960s by *Leadabrand et al.* (1960) and *Pettengill* (1960). Those images had a resolution of about 100 km. By the mid-1960s, technology had evolved to the point where 20- to 50-km resolution could be readily achieved in images of the moon (*Thompson and Dyce*, 1966; *Hagfors et al.*, 1968).

The open literature contains less discussion of radar imaging of artificial Earth satellites. A 1960s vintage system called the Space Object Identification radar was built by the Aerospace Corporation and is described in *Hoffman et al.* (1969). It used a 94-GHz

carrier frequency and a 1-GHz bandwidth to obtain high resolution with a short target illumination time. A 1970s vintage system called the Long-Range Imaging Radar was built by Lincoln Laboratory and is described in *Bromaghim and Perry* (1978). It was installed at the Haystack Observatory and operated at X-band. In all cases, these systems have used microwave or millimeter wave frequencies. No record has been found of previous attempts to generate high-resolution radar images of satellites using frequencies less than about 2 GHz.

A detailed review of the history of the various imaging radar systems, including SAR, planetary imaging, and satellite imaging, is given in *Ausherman et al.* (1984).

1.3 Inverse Synthetic Aperture Radar

All of the radar imaging applications mentioned above—terrain, planets, and satellites—rely on the unique range-Doppler history of individual scatterers in the scene, and originally used a form of range-Doppler filtering to generate an image. The variations in Doppler frequency constitute information that can be used to image the target, whether Earth, other planets, or satellites. That imaging information, however, does not arise from the translational motion of the radar or target, but from the *rotation* of the target with respect to the radar. In terrain mapping, or SAR, apparent rotation is a result of the changing angle to the target as the radar flies past. In the case of satellite imaging, however, the radar is stationary and the angle change is a result of target motion. Thus, satellite imaging is an example of a class of imaging problems known as *inverse synthetic aperture radar*, or ISAR, where 'inverse' is used to emphasize that target motion produces most of the rotation.

Other ISAR applications include imaging of aircraft from ground-based radar, and imaging of ships or maneuvering ground vehicles from airborne radar. A more common application of ISAR is the test-range evaluation of the radar cross section (RCS) of aircraft. In that application, an aircraft or scale model is placed on a turntable and rotated while being observed by a stationary radar. These radar observations provide a measure of the detectability of the aircraft. They can also be combined to form images, an application called RCS imaging. Those images can be used to produce templates that are then used operationally for aircraft identification (e.g., *Mensa*, 1991).

SAR and ISAR possess fundamental similarities and, from a signal processing perspective, the distinctions are minor. Differences in image size and distance to the target, however, have led to significant differences in the implementation of the imaging algorithms.

Furthermore, ISAR applications often have targets that are isolated—that is, in an area containing no other targets and low levels of clutter.

1.4 Satellite Imaging at VHF

In order to form an ISAR image, the radar repeatedly illuminates a satellite with its transmitted pulses, and receives the corresponding echoes. Those echoes are processed to extract information about the arrangement of the target's scattering centers. For a single pulse, the information is one-dimensional and is not sufficient to form a radar image, the two- or three-dimensional mapping of the target's scattering centers. To 'fill in' the other dimensions, the radar needs to observe the target over some period of time, and some range of orientations, as it flies by. Basically, the more the target rotates during the observation time, the more information is collected and the higher the potential resolution of the final image. At VHF that information is corrupted by the dispersive effects of the ionosphere, the medium through which the signal travels. Additionally, the ionosphere varies both spatially and temporally, so the dispersive effects change from pulse to pulse. More generally, the problem can be described as attempting to form a coherent image through a dispersive medium that is inhomogeneous and time-varying. The dispersive effects of the ionosphere often distort the radar echo to the extent that coherence is lost and the image is seriously degraded or destroyed. To recover a high-resolution image, the ionospheric effects must be estimated and removed from the radar signal with a compensation technique that can handle the pulse-to-pulse variations.

Adding to this already difficult task are several further challenges in forming satellite images. For example, at VHF, fine range resolution requires a high fractional bandwidth, and fine cross-range resolution requires a wide aperture. Also, target range variations across the aperture are generally not known from available orbit information to the accuracy needed for imaging. These challenges add further complexity to the system design and to the data processing and imaging algorithms.

1.5 Estimating and Removing Ionospheric Effects

The dispersive effects of the ionosphere on a radio wave signal can largely be characterized by the integrated columnar free electron content along the propagation path, known as the

'total electron content,' or TEC. It will be shown that those effects can be removed from the radar data if a sufficiently accurate estimate of TEC is available. Once the dispersive effects of the ionosphere are removed from the radar data, the satellite can be imaged using traditional ISAR techniques. In practice, however, a sufficiently accurate estimate of TEC is usually not available, except possibly through observation of the ionosphere's effects on the radar signal itself. The success in *imaging through the ionosphere* at VHF frequencies is then determined by the answer to a simply-stated question:

> Is it possible to estimate adequately the total electron content of the ionosphere for coherent radar imaging by observing the ionosphere's effects on the radar echoes?

This research shows that the short answer to this question is: Yes, at least for moderate ionospheric conditions.

The idea of measuring the ionosphere by observing its effects on signals is not new. For example, the L-band signals used by the Global Positioning System (GPS) are subject to significant ionospheric effects (in particular, group delay is the primary effect at L-band). Full positioning accuracy is only achieved after those effects are removed from the signals. GPS receivers estimate TEC and remove ionospheric effects by measuring path length differences between two frequencies (e.g., *Lanyi and Roth*, 1988). Those TEC measurements are also used, in at least one system, to form global synoptic maps of TEC by incorporating measurements from a globally distributed network of GPS receivers(e.g., *Wilson et al.*, 1995).

In the case of GPS, the transmitted signal is known, and the ionospheric effects can be directly observed as differences between the transmitted and received signals. With radar echoes, however, the received signal contains both the dispersive effects of the ionosphere and the scattering effects of the target. To estimate TEC, the ionospheric and scattering effects need to be separated. This research demonstrates that that can be accomplished through imaging, at least in some instances. Basically, an ISAR image is formed, and the components of the radar signal that are inconsistent with the expected image structure are attributed to the ionosphere.

To achieve 1-meter resolution in a VHF radar image, this research shows that the TEC estimate must be accurate to within about $2 \times 10^{15} e^{-}/m^2$. The TEC estimate from GPS, by comparison, is only accurate to within about $2 \times 10^{16} e^{-}/m^2$ (e.g., *Klobuchar et al.*,

1993; *Sardón and Zarraoa*, 1997). For 1-meter resolution then, the required accuracy is at least an order of magnitude better than available from GPS, while at finer resolution the accuracy requirement is even more stringent. This research shows that such accuracy is indeed achievable in many situations.

The answer to the earlier question is that not only can TEC be estimated from radar echoes, but it can be estimated at least an order of magnitude more accurately than with GPS. The art in achieving this accuracy lies in the imaging procedure described in the following chapters.

1.6 Experimental Verification

The analyses and techniques described in this thesis were developed and tested with radar data collected at SRI International sites at Stanford, California, and Ascension Island, United Kingdom. The initial data, collected at Stanford, have relatively low levels of ionospheric dispersion, primarily because ionospheric conditions are usually benign at mid-latitudes. The benign ionospheric conditions allowed algorithm development and testing to proceed with actual data, but without the added complexity of turbulent ionospheric conditions and higher-order ionospheric effects that may be significant at equatorial and polar latitudes.

After initial development and demonstration of feasibility with the Stanford data, an SRI radar facility on Ascension Island was used to collect radar data during satellite passes through the thicker and more turbulent equatorial ionosphere.[4] These data are used to test the imaging and TEC estimation algorithms, and to quantify algorithm performance in the equatorial ionosphere.[5]

Nominal parameters for the Stanford and Ascension Island radar systems are listed in Table 1.1. Values from this table are used in examples in later sections to illustrate ISAR imaging concepts and the effects of the ionosphere on radio wave signals and radar images.

Given the relatively modest transmitter power of the two systems, a positive single-pulse signal-to-noise-ratio (SNR) is achieved only for low-Earth orbit (LEO) satellites that have

[4] Ascension Island is located in the mid-Atlantic Ocean at geographic coordinates of 7°55′ south, 14°25′ west and at a magnetic latitude of about 16° south, near the crest of the equatorial anomaly.

[5] Unfortunately, none of the 20 or so satellite passes collected at Ascension exhibit any significant scintillation, so the effects of that (common) situation on imaging performance remains to be demonstrated. It is expected that the large amplitude and phase fluctuations induced on the radar echo during periods of ionospheric instability would significantly degrade image quality.

Site	Stanford, CA	Ascension Island, U.K.
Location	37.4085°N, 122.1797°W	7.9585°S, 14.3259°W
Frequency band	200 to 400 MHz	same
Center frequency	300 MHz ($\lambda = 1$ m)	same
Bandwidth	200 MHz	same
Fractional bandwidth	67%	same
PRF	50 Hz	same
Peak power	9 kW	4.5 kW
Antenna diameter	45.7 m	27 m
Antenna gain @ 300 MHz	40 dB	35.5 dB
Transmit polarization	RCP	same
Receive polarization	LCP	same
Waveform	100 μs, linear FM	same
Chirp rate	2×10^{12} Hz/s	same
Bandwidth-time product	20,000	same
Sample rate	250 MHz, 8-bit I, 8-bit Q	same
Angular aperture	30° - 60°	same
SNR for Mir — single pulse, uncompressed	~ -15 dB (± 10 dB)	
SNR for Mir — single pulse, match filtered	$\sim +15$ dB (± 10 dB)	

Table 1.1: Nominal radar parameters. These parameters characterize a typical configuration of the Stanford and Ascension Island radar systems used in this research. The performance of the two systems is similar, except for transmitter power and antenna gain.

a relatively large RCS.[6] Table 1.2 lists the satellites for which radar data were collected at Stanford and Ascension along with their altitudes and RCS values as published in the NASA 'Satellite Situation Report.' Those satellites were chosen because of their relatively large RCSs and low altitudes, which combine to give positive SNR in the received signal.

Radar data, collected during one pass of the Mir space station, are analyzed in some detail in the following chapters. Those data were collected by the author at Ascension Island on March 25, 1998. The geometry and ionospheric conditions for that pass are also used in several examples and illustrations. Parameters for the pass, designated '8084a,' are included in Table 1.3 for future reference.

[6] In contrast, the ALTAIR UHF radar at Kwajalein Atoll transmits at a peak power of about 5 MW at 422 MHz, and the Millstone UHF radar at Millstone Hill, Massachusetts, transmits at a peak power of about 5 MW at 440 MHz (see *Coster*, 1991). Both have the ability to obtain positive SNR for small satellites at ranges of up to a few thousand kilometers.

Satellite	Altitude (km)	RCS (dBsm)
Mir	380	27
Hubble Space Telescope (HST)	610	18
Gamma Ray Observatory (GRO)	510	17
Cosmos 2335 (EORSAT)	410	13
Cosmos 2347 (EORSAT)	410	13
Tropical Rainfall Measuring Mission (TRMM)	345	11

Table 1.2: Candidate satellites. These satellites were the preferred targets for this research as their relatively low altitudes and large RCSs combine to provide a positive SNR for the radar parameters listed in Table 1.1. Radar data sets were collected during passes of each of these satellites. Chapter 5 and Appendix C contain images produced from Mir and Cosmos 2347 data sets.

1.7 Contributions

The research documented in this thesis includes (1) analysis of ionospheric effects on radar images, (2) development of imaging techniques, and (3) experimental testing of the accuracy of the analyses and robustness of the techniques. There are two main contributions:

i) A new, technical approach leading to the first ISAR images of satellites at frequencies below 1 GHz.

ii) A new technique for making high-precision measurements of ionospheric TEC using radar echoes.

These two items are closely linked. To form ISAR satellite images at VHF, it is necessary to remove the effects of the ionosphere. That can be accomplished through estimation of the TEC during the imaging procedure. Conversely, the TEC can be estimated from radar echoes if the dispersive effects of the ionosphere and the scattering effects of the target can be separated. That separation can be accomplished through imaging.

Several further contributions supported the goal of forming VHF radar images of satellites, including:

i) Analysis of the effects of a dispersive and changing medium on a coherent imaging process. This is applied to the problem of imaging satellites through the ionosphere, but could also be applied to the complementary problem of VHF radar imaging of Earth from a satellite.

Pass name	8084a
Target	Mir
Site	Ascension Island
Date (UT)	March 25, 1998
Start time (UT)	08:22:34.0
PRF	50 Hz
Data collection period	160.0 s
Satellite altitude	378 km
Maximum elevation	56.5°
Sunspot number	79
vTEC to target altitude	$\sim 1 \times 10^{17}\ e^-/m^2$
Radar parameters	as specified in Table 1.1
Waveform parameters	as specified in Table 1.1

Table 1.3: Pass 8084a parameters. The radar data set, named 8084a, was collected at Ascension Island during one pass of the Mir space station. That data set is used in several examples in this thesis.

ii) Development of a technique for separating media effects from scattering effects using automatic focusing of the radar image.

iii) Development of a technique for removing the dispersive effects of the ionosphere from a radar echo.

iv) Analysis of the expected performance of the imaging and dispersion-mitigation techniques.

v) Verification of the performance of the techniques by applying them to actual data and measuring the quality of the resulting images.

1.8 Overview of Chapters

This chapter provides an overview of the problem of ionospheric effects in VHF radar imaging, along with a qualitative description of the approach used to solve that problem.

Chapter 2 develops the theory of ISAR with emphasis on issues that are important for high-resolution imaging at VHF. Equations are given for image resolution and maximum sample spacing. The classical range-Doppler imaging procedure is described and related to the ISAR procedure. Motion compensation is introduced as a method for removing target range variations, and its implementation is described. An algorithm for automatically

focusing the image provides the necessary improvements in the flight track estimate. That same algorithm is used for estimating other items that affect image quality, in particular, the ionosphere. Finally, the implications of the frequency and angle dependence of the target's scattering characteristics are discussed.

Chapter 3 begins with a short introduction to the ionosphere and some of the processes that determine its morphology. The Appleton-Hartree formula is given as the equation for the ionosphere's refractive index, and then applied to quantify the ionosphere's effects on electromagnetic waves at frequencies above about 100 MHz. Coherence bandwidth is defined and an equation for its value is derived. The next topic is use of group delay differences for obtaining rough initial estimates of TEC. The effects of polarization on propagation characteristics are discussed. Faraday rotation is introduced and equations for polarization rotation are given. Finally, ionospheric irregularities are introduced and their effects on radio wave signals are described.

Chapter 4 provides an analysis of the character and magnitude of the effects of the ionosphere on a radar image. First, the effects of the ionosphere on range resolution are discussed, and equations are developed to quantify those effects. A similar analysis is performed for the effects of the ionosphere on cross-range resolution. The point spread function of the ionospheric filter is introduced, and a specific example is given. Next, a procedure that uses the radar image to estimate ionospheric TEC is described. To this point, the ionosphere's effects have been modeled as having a $1/f$ phase behavior; the limitations of that model are analyzed. Finally, the effects and significance of refraction are evaluated.

Chapter 5 presents some results of application of the theory and techniques of Chapters 2 through 4 to actual radar data. The experimental results are shown to be consistent with theoretical expectations.

Chapter 6 summarizes the results of this work and suggests areas of further research.

Appendix A gives a brief description of the radar systems used to collect experimental data for this research.

Appendix B documents the data processing and imaging algorithms developed in this research. Three stages are described: (1) preprocessing, (2) initial range and TEC estimation, and (3) imaging.

Finally, Appendix C contains examples of some of the other satellite images produced during the course of this research.

Chapter 2

Radar Imaging of Satellites

This chapter describes techniques for forming high-resolution radar images of satellites. It begins by introducing the geometry and notation of the imaging problem. Then, the radar imaging algorithm is developed from a tomographic viewpoint, and the equivalence of the tomographic imaging algorithm and the classical range-Doppler imaging algorithm is discussed. Some basic equations that describe the resolution and sampling requirements are given. The chapter also discusses some unique challenges and interesting aspects of radar imaging that are independent of the ionosphere, but occur as a result of operation at VHF—such as the need for large angular apertures and large fractional bandwidths to obtain high resolution. Also, with the combination of frequency, bandwidth, and aperture used here, the resolution cell is comparable to the radar wavelength—an uncommon situation in imaging applications.

Some of the practical issues that need to be addressed when forming radar images are also discussed in this chapter. Radar images, in the context of this work, are formed by coherently combining many observations of an object, called the target, over a range of frequencies and viewing geometries. The imaging process is coherent in that it uses the phase as well as the amplitude of the target echoes. Anything that degrades system coherence also degrades the quality of the final image. One such item is uncorrected radial target motion, which causes the radar echoes to be shifted in range. These shifts may be removed from the signal during imaging using a technique called motion compensation. A high level of precision in the measurement of the satellite flight track is needed to implement motion compensation with the required accuracy. In order to achieve the necessary precision, the radar data themselves can be used to refine the flight track estimates in an algorithmic

process called 'autofocus.' Motion compensation and autofocus are described in detail later in this chapter.

At a fundamental level, radar imaging techniques attempt to extract information about the spatial arrangement of a target's various scattering components from the radar echoes. That information is 'encoded' in differences in the echoes as a function of frequency and viewing geometry. The amount of information contained in the variations over frequency is limited by the frequency span, or bandwidth, of the transmitted waveform. Similarly, the amount of information contained in the variations over viewing geometry is limited by the span of the viewing angle. The *polar format algorithm* (PFA), described in the next two sections, is one approach to 'decoding' the echo information. This particular algorithm is commonly used to image individual targets, including satellites at frequencies above about 1 GHz, as well as aircraft and ships.

Imaging of satellites from the ground falls into a class of problems in which target motion accounts for most of the change in viewing geometry over the observation period. As mentioned in Chapter 1, such target-imaging situations are given the monicker *inverse synthetic aperture radar*, or ISAR. 'Inverse' is used to emphasize the importance of target motion, in contrast to *synthetic aperture radar*, or SAR, where platform motion accounts for most of the change in viewing geometry over the observation period.

From the 'ISAR perspective,' radar imaging reconstructs a map of the target's complex scattering amplitude from the collection of radar echoes, each of which is a projection of that function at a specific rotation angle.[1] The description of radar imaging in terms of projections, and the fundamental insight that description provides, can be traced back to the work of *Walker* (1980). The concepts developed in Walker's paper form the basis of the polar format imaging algorithm described in this chapter. An alternative description of the polar format algorithm can be found in *Carrara et al.* (1995b).

Radon (1917) originated the theory for determining a function from its projections. *Mersereau and Oppenheim* (1974) give a tutorial review of that theory. *Bracewell* (1956) was the first to use Radon's results for an actual problem. *Walker* (1980) shows that a radar 'samples' the frequency space of the target's complex scattering amplitude. That insight leads directly to the 'ISAR perspective' stated above. *Brown* (1980) extends and clarifies Walker's results. Similar results are also given in *Chen and Andrews* (1980b). A general

[1] In this work, the term 'projection' is used in a mathematical sense to describe integrals of a function over parallel lines in two dimensions or parallel planes in three dimensions.

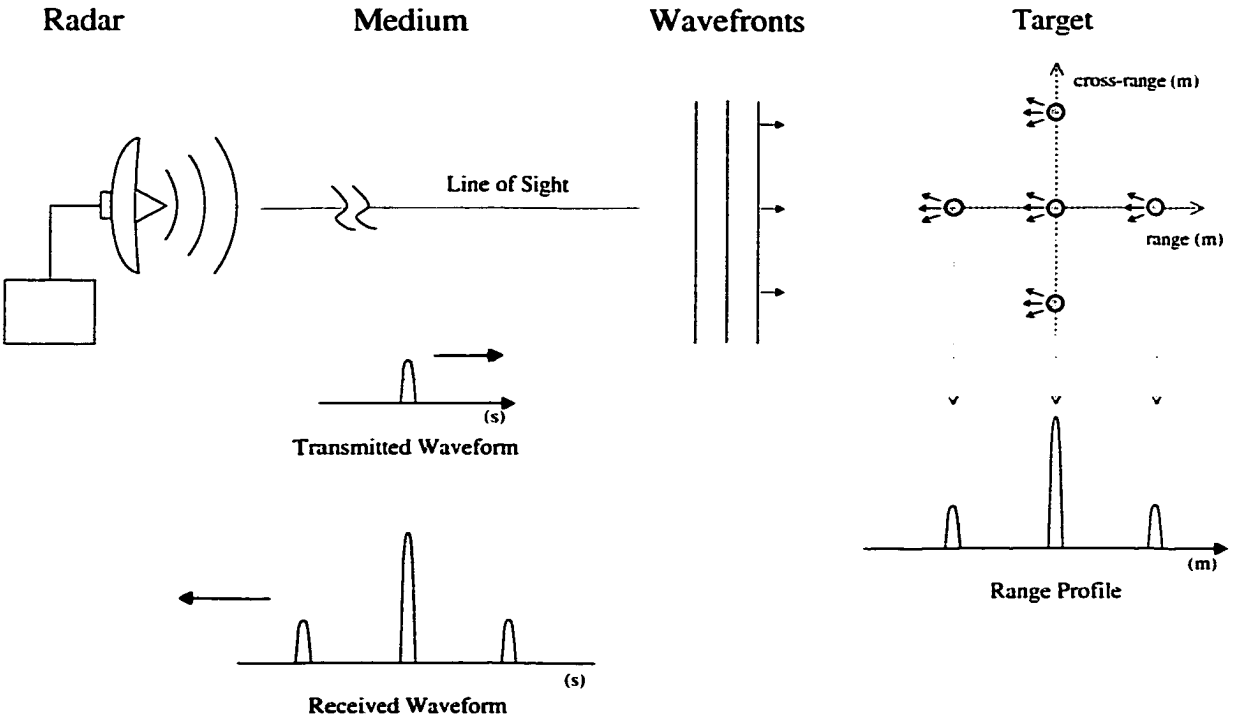

Figure 2.1: A simple ISAR system. The radar transmits a waveform, illustrated with a pulse, that propagates through the medium to the target. The pulse is scattered by the various parts of the target. The backscattered component of the total scattered energy propagates back, and is received by the radar. The received waveform is a range profile of the target—a projection of the target onto the LOS—convolved with the transmitted waveform.

development of radar imaging from the ISAR perspective is given in *Munson et al.* (1983) and *Mensa* (1991).

2.1 ISAR Basics

Consider the simplified ISAR system depicted in Figure 2.1. A two-dimensional system, existing in the plane of the paper, is used to illustrate this initial discussion. It includes a radar, a medium through which the radar signal propagates, and the object(s) of interest, called the target. For this illustration, the target in the figure comprises five point scatterers. The line connecting the radar to the target is called the radar *line-of-sight* (LOS). A vector along that line, from the radar to target, defines the *range* direction. In this two-dimensional case, the orthogonal direction is defined as the *cross-range* direction. The radar transmits an

electromagnetic pulse that propagates through the medium to the target. Upon reaching the target, it is scattered by the target's various components. It is assumed that the distance to the target, the range, is sufficiently large for the wavefronts to be considered planar. This is equivalent to assuming that the target is much smaller than a Fresnel zone radius in cross-range extent—an assumption that simplifies the imaging algorithm. For the monostatic configuration shown here, the radar observes the backscattered part of the total scattered signal. The ideal point scatterers composing the target each produce an echo that is an exact replica of the transmitted waveform. The observed signal, called a *range profile*, is the sum of the individual echoes. The range profile begins with the echo from the point on the target nearest the radar and ends with the echo from the farthest point. In Figure 2.1, the three points on the vertical line through the origin are at the same range from the radar, so their echoes add to form a single component in the range profile having three times the amplitude of that due to a single point. This illustrates the idea that range profiles are projections, or integrals of the target's complex scattering amplitude. More precisely, in two dimensions the range profile is the result of integrating the complex scattering amplitude along lines in the cross-range direction. It is a complex amplitude signal, in the sense that magnitude and phase are preserved for use in the coherent imaging process.

Note that a single pulse contains direct information about the locations of the target's components in the range direction, but no information about their locations in the cross-range direction. Also, the width of the transmitted pulse determines the accuracy with which the locations can be measured in the range direction.

Now, if the target is rotated, and another pulse is transmitted, the range profile may look something like that plotted in Figure 2.2. The difference between the range profile in Figure 2.1 and that of the rotated target in Figure 2.2 provides information about the target in the cross-range direction. If a number of range profiles are collected as the target rotates through a known set of angles, those profiles can be processed to separate target components into appropriate range and cross-range locations. The procedure used in this thesis for processing the range profiles to form an image is described in the next section.

Note that the range and cross-range directions, defined with respect to the individual radar pulses, rotate with respect to the target. Another definition of range and cross-range, in this case with respect to the image, is given below, and used in most of the following descriptions. In that definition, the range and cross-range directions are constant with

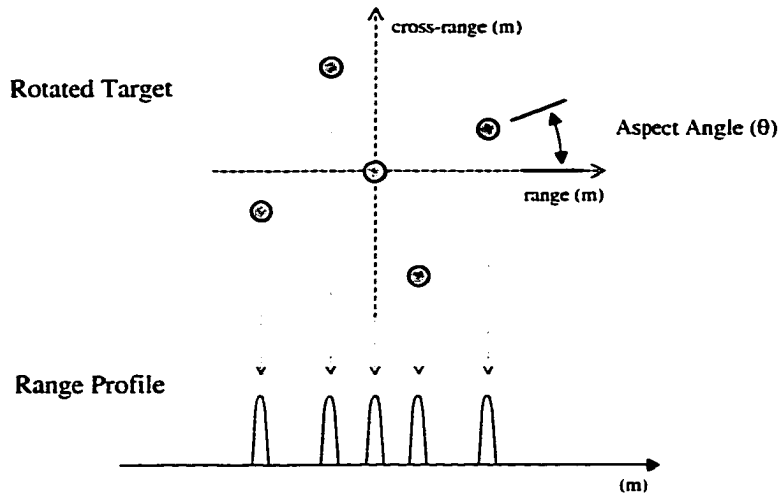

Figure 2.2: A simple ISAR system; target rotated. As the target rotates, its range profile, or projection onto the LOS, changes. The differences between the range profiles collected at various aspect angles provide information about the cross-range locations of the target's scattering centers.

respect to the image, and defined by the corresponding directions of the radar pulse that occurs at the center of the target observation period.

Returning to Figure 2.2, the angle of the target coordinate frame relative to a stationary frame is called the *aspect angle*, and the total angular span over which data are collected is called the ISAR angular aperture, or simply, the aperture. The aperture determines the cross-range resolution of the final image, and the angular spacing between adjacent range profiles determines the unambiguous cross-range extent of the image area. Resolution and unambiguous range are discussed and quantified in Section 2.3.

For simplicity, the target in Figure 2.1 was two-dimensional. Also, it was assumed that the radar LOS was in the target plane and that the axis of rotation was normal to the target plane. Actual targets, however, are three-dimensional, and the axis of rotation usually is neither perpendicular to the radar LOS nor stationary with respect to the radar. The geometry of the configuration and the variations in the aspect angle during data acquisition in an actual system are most easily visualized by considering the system geometry from the perspective of the target. To assist in the visualization, a preliminary coordinate frame is fixed to the target with an arbitrary orientation. That frame is then rotated, with respect to the target, to obtain a *target-fixed frame* appropriate for imaging. In choosing the orientation of the target-fixed frame, it is convenient first to imagine a unit sphere

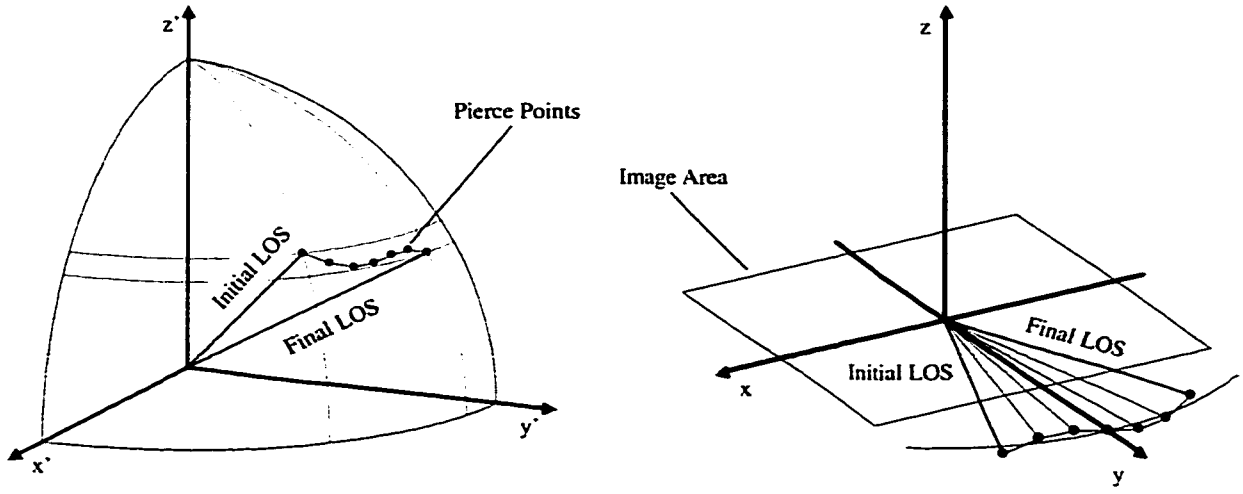

a: Preliminary Frame

b: Target-Fixed Frame

Figure 2.3: Image plane orientation. A preliminary coordinate frame is fixed to the target, and the points where the LOS vector pierces the unit sphere in that frame are calculated. The target-fixed frame is then defined such that its x-y plane is an optimal fit to the LOS vectors and its y-axis is centered on the angular span of the LOS vectors. The radar image is formed in the x-y plane of the target-fixed frame.

fixed to the target. Then consider the points at which the LOS vector pierces that sphere each time a radar pulse is transmitted. In operational ISAR systems, those pierce points generally follow some curved trajectory on the surface of the sphere, such as that illustrated in Figure 2.3a. The orientation of the target-fixed frame is then chosen such that its x-y plane provides a good fit to the pierce points, say, by minimizing the root-mean-square distance from the pierce points to the plane. The y-axis is chosen as the direction of the LOS at the center of the aperture. This orientation for the target-fixed frame is illustrated in Figure 2.3b. The locations of the pierce points can now be specified by two angles: the azimuthal or in-plane angle, θ, and the polar or out-of-plane angle, ξ. The image is formed in the x-y plane. With this orientation of the target-fixed frame, the angular span is centered on the y-axis. Also, the x-axis defines the cross-range direction in the image, and the y-axis defines the range direction.

The polar format algorithm described in the next section produces two-dimensional images. Using two dimensions to image a three-dimensional object is appropriate if the out-of-plane angle remains sufficiently small (see Section 2.2), since the radar echoes then

contain no information about the third, orthogonal dimension. If the pierce points all lie in the x-y plane ($\xi = 0$), the distance from a point on the target to the radar is independent of the z-coordinate. When that happens, the radar is unable to resolve the target in the z-dimension. In the parlance of radar, the system has no aperture in the third dimension—that is, the z-dimension. The resulting image can be thought of as the projection of the three-dimensional object onto the image plane. The image value at each pixel is then the integral of the complex scattering amplitude of the target along the line through the pixel and perpendicular to the image plane.

2.2 ISAR Imaging

To understand how range profiles observed at different aspect angles can be combined to form an image, it is important to remember that they constitute projections of the target onto a line parallel to the radar LOS. For a three-dimensional object, the points in the *ideal* range profile are integrals of the target's complex scattering amplitude over planes perpendicular to the radar LOS. The *observed* range profile is then the convolution of the ideal range profile and the transmitted waveform. For two-dimensional imaging of a three-dimensional object, the target is resolved in the range and cross-range dimensions, but not in the third dimension, that normal to the range/cross-range plane. Again, the range direction is along the radar LOS at the center of the angular aperture. For an arbitrary target-rotation vector, cross-range is normal to the plane defined by the LOS and the target-rotation vector. The unresolved dimension is normal to the LOS and in the plane defined by the LOS and the target rotation vector.

Historically, one of the first procedures for forming radar images directly from range profiles was with coherent back projection (e.g., *Munson et al.*, 1983; *Arikan and Munson*, 1989; *Desai and Jenkins*, 1992). In this method, an image area is first defined. Then, for each range profile, the sample values are added into all image pixels along a line through the sample and normal to the LOS. That is, each sample is added into the pixel locations that could have contributed to it. This can be thought of as *projecting* the range profile *back* over the image area. Since the LOS vector rotates between the individual range profiles, the back projections are made over a set of angles having a span equal to the angular aperture.[2] Although the back-projection technique is conceptually simple, it is

[2]It may seem surprising that this conceptually simple process produces an image, but, in fact, it can be shown that this image is the same as would be obtained with the complex correlation technique used in

computationally inefficient because it requires interpolating and adding each range profile at every pixel location in the image.

A more efficient procedure makes use of the *projection slice theorem* (*Radon*, 1917; also see *Bracewell*, 1995, for further discussion), which states that *the Fourier transform of a projection of an object at a given aspect angle is a slice through the spectrum of the object at that same angle.* The radar collects projections of the target over a range of aspect angles, and the projection slice theorem provides the theoretical basis for a procedure that combines them to form an image. That procedure is depicted in Figure 2.4, where a two-dimensional object and its two-dimensional Fourier transform are displayed on the left side, and the range profile and its one-dimensional Fourier transform are displayed on the right side. The steps in that imaging procedure are:

i) Calculate the Fourier transform of each range profile. Each one-dimensional transform is a 'line-slice' through the two-dimensional Fourier transform of the target's complex scattering amplitude.

ii) Construct the two-dimensional Fourier transform of the target by placing the slices along radial lines at angles equal to the aspect angles of the original range profiles. This gives the two-dimensional Fourier transform with samples along radial lines at polar (r, θ) locations.

iii) Interpolate the polar sample locations onto a rectangular grid. *Bracewell* (1995, Chapter 7) and *Carrara et al.* (1995b, Chapter 4) discuss some of the many issues in implementing this two-dimensional non-uniform resampling of the frequency-domain data.

iv) Calculate the inverse two-dimensional Fourier transform to obtain the image.

Figure 2.5 is an example of an actual two-dimensional spectrum and the resulting image of the space station Mir. This image, formed with the technique described above, is discussed in more detail in Chapter 5. During data collection, the radar samples an area of the object's frequency space, called the *frequency domain support region.* That region is the intersection of an annular area whose limits are determined by the frequency span of the radar and a sectoral area whose limits are determined by the angular aperture. The

SAR. It is also the same as the image that would be formed by synthesizing a phased antenna array from the radar positions at each transmitted pulse time.

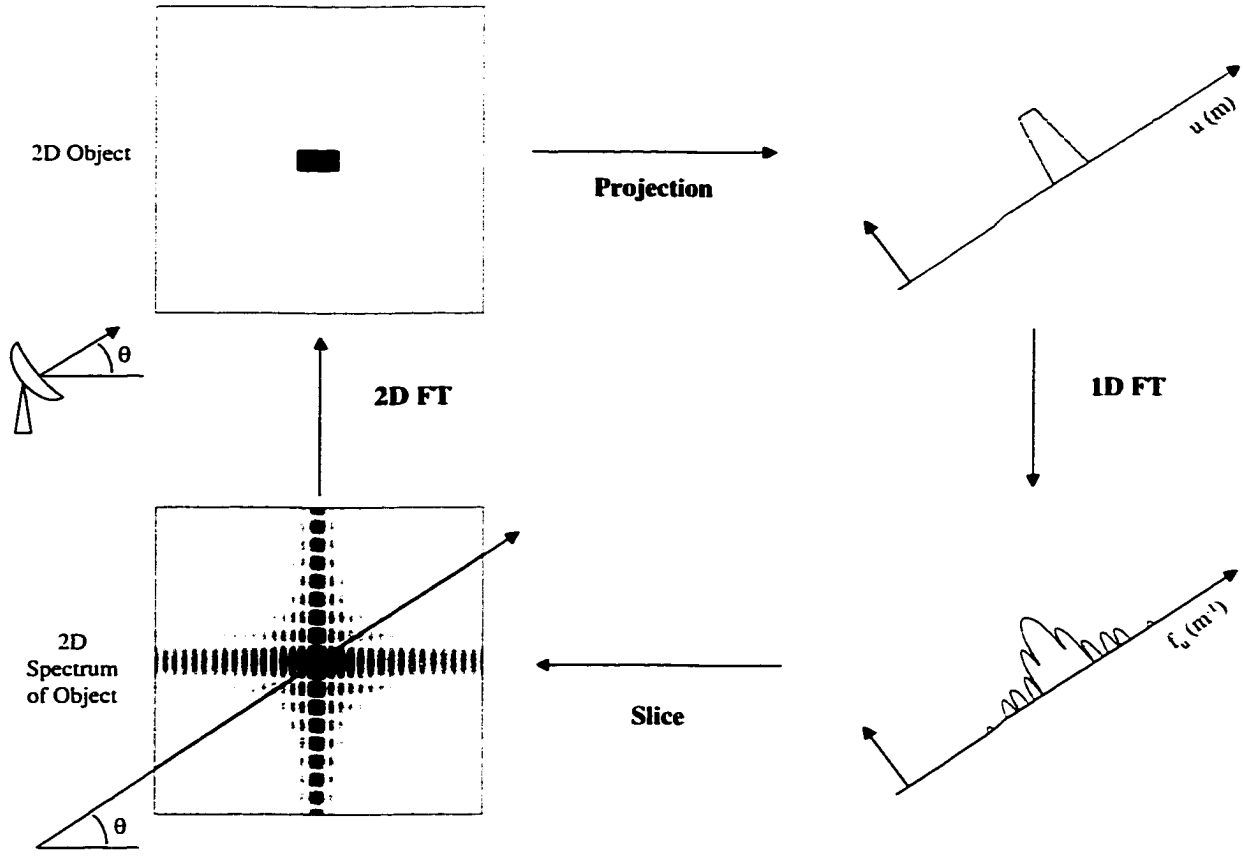

Figure 2.4: Illustration of the projection slice theorem. A two-dimensional (2D) object and its projection onto a line with polar angle θ are illustrated in the top frames. The 2D Fourier transform of the object and a slice through that transform, again at angle θ, are illustrated in the lower frames. From the projection slice theorem, the one-dimensional (1D) Fourier transform of the projection gives the slice through the spectrum of the object.

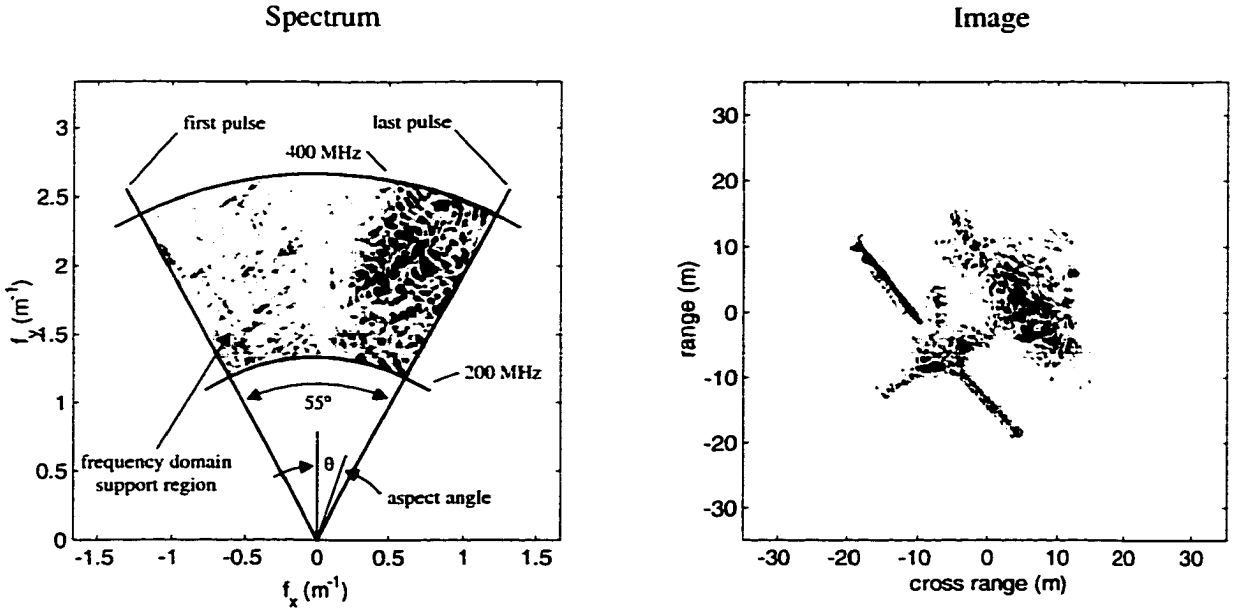

Figure 2.5: Mir image and spectrum. The left frame illustrates actual two-dimensional spectral data, collected on this project, and displayed with the appropriate aspect angles. The right frame is the corresponding image, calculated simply as the inverse two-dimensional Fourier transform of the spectral data in the left frame.

data in Figure 2.5 have a frequency domain support region that covers an angular aperture of 55 degrees and a temporal-frequency span of 200 to 400 MHz. Spectral data outside that region are not observed by the radar. In this example, the Fourier transform of the first range profile provides the values along the leftmost radial line in the two-dimensional spectrum. Likewise, the Fourier transform of the last range profile, which is collected after the LOS vector has rotated through 55 degrees, provides the values along the rightmost radial line. The samples along the arc closest to the origin are the Fourier transform values of each range profile at 200 MHz, and the samples along the arc farthest from the origin are the corresponding 400-MHz values.

The spatial frequencies used in the axes in the plot of the spectrum are related to the temporal frequency in the radar echo, f, and the aspect angle, θ, through

$$f_x = \frac{2f}{c}\sin\theta = \frac{k}{\pi}\sin\theta, \tag{2.1}$$

$$f_y = \frac{2f}{c}\cos\theta = \frac{k}{\pi}\cos\theta, \tag{2.2}$$

where c is the speed of light, and $k = 2\pi/\lambda$ is the free-space wavenumber.

The shape of the frequency domain support region is a result of the geometry of the imaging process. The support region can be expanded by collecting data over a wider range of frequencies and aspect angles. The result would be finer resolution in the final image. Since the radar and imaging algorithm are linear, their combined performance is fully described by their net response to an ideal point target, called the *point spread function* (PSF). The effect of the imaging geometry on the PSF can be understood by thinking of the frequency domain support region as the result of masking or windowing the object's full spectrum. The window function is the intersecting area of the annulus and sector described above.

The relationship between the three-dimensional object and the two-dimensional image can also be understood in terms of window functions. A three-dimensional object has a three-dimensional spectrum. The radar samples that three-dimensional spectrum along LOS lines—that is, along one-dimensional 'line-slices' through the three-dimensional spectrum. Those line slices are arranged side-by-side, then interpolated to obtain the values over a surface that slices through the three-dimensional spectrum of the object. For imaging purposes, it is important that the out-of-plane angle remains small, so that the spectral surface remains close to the image plane. When forming a two-dimensional image, the spectral values outside the image plane are assumed to be zero. The two-dimensional frequency-domain support region can then be thought of as a windowing of the three-dimensional object spectrum with a planar Dirac delta function. Thus, in the direction normal to the plane, the resolution cell size is infinite since the transform of the Dirac delta is a constant. That is, there is no resolution in the direction normal to the image plane. From the projection slice theorem, it then follows that since the only values available are from a planar slice through the three-dimensional spectrum, the values of the inverse transform (the image) are projections (integrals) along lines perpendicular to the plane.

For two-dimensional images, a non-zero out-of-plane angle causes a blurring, or defocusing, that becomes worse with increasing distance from the origin of the image plane, primarily in the range direction. The defocusing is caused by the difference between the radar/target geometry during data collection and that assumed in the imaging algorithm. The radar samples the target's three-dimensional spectrum over the curved surface illustrated in Figure 2.3b, but the imaging algorithm expects those samples to come from the image plane. The defocusing increases with out-of-plane angle, object size, and frequency.

Fortunately, for satellites having stable attitudes, the out-of-plane angle is usually less than 1 or 2 degrees over the satellite pass time for a properly chosen image plane. For tumbling objects, however, such as space debris or rocket bodies, a suitable image plane—that is, one near all the pierce points—may not exist. In this work, $\xi = 0$ is used when $|\xi|$ is bounded by small angles. Further discussion of the implications of non-zero out-of-plane angles can be found in *Ausherman et al.* (1984) and *Carrara et al.* (1995b).

The defocusing effects of non-zero out-of-plane angles can be partially compensated by resampling the radar signal with a smaller sample spacing. The appropriate dilation, or stretching of the signal provides a sample spacing in the image plane that matches what it would have been, had the radar LOS stayed in the image plane—that is, with the same aspect angle, but $\xi = 0$. If the original samples have a spacing of Δt, the resampled values should have a spacing of $\Delta t \cos \xi$, where ξ is the out-of-plane angle. This corrects the focus for parts of the target in the image plane. Parts outside the image plane (those having a non-zero z coordinate) are still defocused by non-zero out-of-plane angles. Note that the resampling procedure is similar to slant-to-ground range conversion in SAR, where the sampling is in the slant plane, but the object and image are in the ground plane.

Readers familiar with computed tomography (CT) may recognize a striking similarity between CT and ISAR. In medical CT, a narrow X-ray beam is scanned across the human body along a plane of interest and projections of the body are collected over a set of angles. (More accurately, the projections are of the body's absorption of X-rays.) The CT projections are combined to form images using techniques that are similar to the ISAR techniques described in this chapter. One fundamental difference between CT and ISAR imaging is that CT projections are non-coherent—in that, they contain no phase information—so an additional filtering step is needed to improve the image quality and obtain full resolution. For CT, projections are usually collected over a full 180-degree angular span with an angular increment of about 1 degree. For ISAR, the angular aperture is limited by the radar/target geometry during the observation period, and is usually much less than 180 degrees. Details on CT imaging techniques can be found in *Scudder* (1978), *Macovski* (1983), or *Kak and Slaney* (1988). A discussion of the relationship between CT imaging and radar imaging is given in *Munson and Jenkins* (1981).

2.3 Resolution and Sampling

As discussed above, system performance is limited by the frequency span of the transmitted waveform and the angular aperture, and can be characterized by the two-dimensional point spread function. For general discussions, however, it is convenient to summarize system performance with a few simple scalar parameters, including resolution, and peak and integrated sidelobe levels. These can be measured on the PSF, or calculated from the size and shape of the frequency domain support region. The resolution, for example, can be determined from the width of the frequency domain support region in the range and cross-range directions (e.g., *Wehner*, 1995, p. 427).

In the range direction, the resolution can be defined as

$$\delta x_r = \frac{c}{2B}, \tag{2.3}$$

where B is the radar system bandwidth and c is the speed of light. This simple inverse relationship follows from the Fourier transform pair of a rectangular spectral window and a 'sinc function' impulse response. Similarly, in the cross-range direction, the resolution is defined as

$$\delta x_c = \frac{\lambda}{4\sin(\Theta/2)}, \tag{2.4}$$

where λ is the wavelength at the radar center frequency and Θ is the angular aperture. Both definitions follow from analysis of the minimum separation needed to distinguish two point targets. Also, note that these resolution equations are the same as those given for a mapping SAR, except that Θ is usually small for SAR applications so $\delta x_c \approx \lambda/2\Theta$ (e.g., *Wehner*, 1995, p. 265).

Equations 2.3 and 2.4 are valid only when system and medium dispersion are insignificant and when perfect flight track data are used in forming the image. Also, they do not account for variations in target scattering over frequency or aspect angle. Equations 2.3 and 2.4 give the *ideal* resolution values, as distinct from the *actual* or *achieved* resolutions, which include the effects of scattering, media and system dispersion, and imaging and flight track errors.

In the range direction, Equation 2.3 is valid only when all frequency components in the target echo have phase values that match those used in the design of the pulse compression filter. System dispersion and ionospheric dispersion contribute a frequency-dependent phase

to the radar echo, and thus degrade the range resolution. The system dispersion is usually constant or very slowly drifting, and can be removed by careful calibration of the radar electronics. In contrast, ionospheric dispersion can change rapidly and is much more difficult to deal with. It is discussed in the next two chapters.

In the cross-range direction, Equation 2.4 is valid only if all echoes have the expected delay and phase when they are combined to form the image. Time-varying ionospheric dispersion and errors in the estimate of the flight track affect the delay and phase of the echoes, and thus the cross-range resolution. The cross-range effects of ionospheric dispersion are also discussed in the next two chapters. The procedures used to estimate and compensate target motion effects in the radar echoes are discussed in the following sections.

In order to avoid aliasing in the cross-range direction, range profiles must be collected at a sufficiently fine spacing across the angular aperture. The maximum tolerable change in aspect angle between radar pulses can be easily calculated by referring to the frequency domain representation of the radar data afforded by the projection slice theorem. The sample spacing in the frequency domain is inversely proportional to the unaliased, or unambiguous span in the spatial domain. This gives a maximum allowable change in aspect angle between pulses,

$$\delta\theta_{\max} = \frac{\lambda_{\min}}{2\,W_{\mathrm{cr}}}, \tag{2.5}$$

where $\lambda_{\min}$ is the wavelength of the highest frequency in the radar signal, and W_{cr} is the size of the target in the cross-range direction. As the cross-range size of the target increases, more radar pulses are needed at more finely spaced aspect angles. If the requirement of Equation 2.5 is violated, the cross-range sampling becomes ambiguous, and the radar data no longer contain sufficient information to uniquely separate the various parts of the target in the cross-range direction. The resulting aliased image will appear to be made up of multiple overlapping copies of the true image.

When combined with the angular velocity of the target, the maximum change in aspect angle, $\delta\theta_{\max}$, determines the minimum pulse repetition frequency of the radar,

$$\mathrm{PRF} \geq \frac{\omega_{\mathrm{t}}}{\delta\theta_{\max}} = \frac{2\,\omega_{\mathrm{t}} W_{\mathrm{cr}}}{\lambda_{\min}}, \tag{2.6}$$

where ω_{t} is the rotation rate of the target with respect to the radar.

In order to avoid aliasing in the range direction, the range profile must be sampled adequately. The requisite sample spacing in the frequency domain is inversely proportional

to the range extent of the target. Here, the maximum spacing between the temporal-frequency-domain samples is

$$\delta f \leq \frac{c}{2\,W_{\rm rg}}, \tag{2.7}$$

where $W_{\rm rg}$ is the size of the target in the range direction. In the time domain, this equation is equivalent to saying that the radar signal must be sampled over the entire time during which an echo is present. When stepped-frequency waveforms are used, Equation 2.7 specifies the maximum size of the frequency steps.

2.4 Motion Compensation

In the ISAR imaging formulation of Section 2.2, it is assumed that the target remains at a constant range, and that the only motion is rotation with respect to the radar. For satellite ISAR, the distance to the target may change by several hundred kilometers—$10^{5-6}\lambda$ at 300 MHz—during the data acquisition period, and the effects of that motion must be removed from the radar data prior to imaging. The procedure for estimating and removing the effects of radial target motion from the radar data is called motion compensation (e.g., *Mims and Farrell*, 1972; *Farrell et al.*, 1973; *Kirk*, 1975).

Errors in the estimate of the flight track, or target trajectory, can have a major effect on the resolution and quality of the radar image. These effects show up first in degradation of the cross-range resolution. To achieve ideal cross-range resolution, the flight track estimate must have a precision of a fraction of the shortest wavelength in the transmitted waveform. The need for such high-precision estimates of the target trajectory, for use in motion compensation, is common to all operational SAR and ISAR systems. The development of methods for achieving the requisite precision is a continuing topic of active research (*Chen et al.*, 1987; *Blacknell and Quegan*, 1991; *Carrara et al.*, 1995a; *Cantalloube et al.*, 1996; *Thomas et al.*, 1996).

Removing the effects of radial motion from the radar signal is relatively straightforward. If the radar echo is digitized directly, without down-conversion, motion compensation is accomplished by a simple time shift of the sampled waveform. In most radar systems, however, the signal is mixed to baseband or offset IF before recording in order to minimize the required bandwidth of the recording system. Motion compensation then involves a time shift plus a phase shift to account for the phase change in the local oscillator (LO). The

required phase shift, ϕ_{MC}, is constant over individual pulses and is given by

$$\phi_{MC} = 2\pi f_c \Delta t = \frac{4\pi}{c} f_c \Delta R, \tag{2.8}$$

where ΔR is the range shift, $\Delta t = 2\Delta R/c$ is the corresponding time shift, and f_c is the LO frequency for homodyne receivers or the total frequency shift for heterodyne receivers.

Removal of the bulk range variations—the variations in the distance from the phase center of the radar antenna to the origin of the target coordinate frame—does not change the imaging information content of the radar data. Since it is assumed that the wavefronts are planar, range variations do not affect the shape of the echo signal, only its strength and delay. The fact that the target is observed over a pass that is hundreds of kilometers long does not provide any direct information for imaging. Again, it is only the rotation of the target with respect to the radar that produces the differences between the individual radar echoes, and thus, the information needed for imaging.

A value for the maximum tolerable error in the satellite range estimates can be obtained by observing that the imaging procedure relies on coherent combination of the individual echoes. The pulse-to-pulse coherence starts to degrade when the error in the range to the target is some fraction of the shortest wavelength in the transmitted waveform. The value used here is $\pm\lambda/8$, corresponding to a phase error of $\pm\pi/4$ radians. With a maximum frequency of 400 MHz, the maximum tolerable error in the flight track estimate is less than about 10 cm. This precision must be maintained over the entire angular aperture. In the examples in Chapter 5, that translates into a 10-cm precision over a satellite track length of up to 1500 km.

2.5 Automatic Focusing Techniques for Range Correction

Initial estimates of the satellite trajectory can be obtained from published orbital information in the form of element sets or state vectors and/or from active tracking of the satellite. These element sets are typically accurate enough only to predict satellite tracks to within a few hundred meters. That accuracy is sufficient to keep antenna pointing errors less than a few tenths of a degree—a tolerable error, considering that antenna beamwidths are at least 1 or 2 degrees at VHF. Precision tracking with microwave radar can do better, with errors approaching the dimensions of the target. In either case, the precision is usually not sufficient to achieve the ideal resolution values of Section 2.2. In this research, the

imaging radar observations themselves provide the necessary improvement to the precision of the range estimates through a two-stage process. In the first stage, range and Doppler frequency are measured, then used to calculate an initial correction to the flight track estimate. Several factors limit the accuracy of the range and Doppler frequency measurements, but this first stage can usually reduce the errors in the flight track estimate to some fraction of the target's range extent. That fraction has been about 1/4 for the data processed to date.[3] Even after this first stage of correction, though, the residual error is still one or two orders of magnitude larger than can be tolerated if the finest resolution is to be achieved. The second stage uses the radar image, in a procedure called *autofocus*, to further refine the flight track estimate.

Autofocus algorithms automatically correct range estimation errors by searching over the space of all reasonable range error functions for one that provides an 'optimal' image. The range function corresponding to the optimized image is taken as the new range estimate, in a manner closely corresponding to the maximum likelihood method. To mechanize the search, it is necessary to define a cost function, a quantitative measure of image quality. Success of this approach depends on finding a function that has a sharp global extremum when range errors are zero. The function may involve statistical measures such as pixel value probability densities (*Blacknell et al.*, 1992; *Berizzi and Corsini*, 1996), image entropy (*Flores et al.*, 1996), spatial correlation measures, or localized heuristic measures such as edge sharpness and point-target mainlobe width (*Jakowatz et al.*, 1989; *Wahl et al.*, 1994). *Carrara et al.* (1995b) provide a description of various alternate autofocus techniques.

For the image in Figure 2.5, and those in Chapter 5, the cost function, C, is the normalized variance of the image amplitude,

$$C = \frac{\mathrm{var}(A_{i,j})}{\mathrm{mean}(A_{i,j})^2}, \tag{2.9}$$

where the $A_{i,j}$ are the pixel amplitudes. Equation 2.9 provides a statistical measure that depends only on the probability density function of the image pixel values. Note that it does not appear to be directly related to the sharpness of focus, that is, to the 3-dB width of the PSF. It works well for discrete targets, as opposed to distributed targets, because errors in range cause uncompensated time and phase shifts in the echoes and, when the echoes are

[3] *Wehner* (1995, pp. 376–380) describes several procedures for using inter-pulse range and Doppler frequency shifts to improve the flight track estimate.

added, the complex sum has lower amplitude along with lower variance. *Hildebrand* (1974) discusses this assertion in more detail.

In this research, the range error is modeled with a set of orthogonal Legendre polynomials. The polynomial coefficients are the free variables in the optimization. Note that the constant coefficient is not treated as a free variable since it only produces a range shift in the final image. The number of free variables is then the same as the order of the polynomial. The choice of order is based on the expected amount of structure in the range error. It must be large enough to provide sufficient degrees of freedom for the polynomial to fit the actual error with residual differences of less than about $\pm\lambda/8$. Since the search time increases with the number of free variables, it is also important to use the minimum order consistent with the fit requirement. For small apertures typical of microwave ISAR, a quadratic is often sufficient, but for the wide apertures used at VHF, fourth- or higher-order polynomials are often needed for the examples used in this research.

Once the cost function and range error functions are defined, the autofocus procedure becomes a multidimensional search for the set of free variable values that produce the optimal image. Here the simplex search algorithm is used to find the range error polynomial coefficients that produce a maximum contrast image. Any robust search algorithm could be used; simplex is chosen for ease of implementation. The steps in the autofocus procedure are:

i) Initialize range error estimates to zero.

ii) Generate the image using current range estimates.

iii) Calculate image contrast.

iv) Modify polynomial coefficients based on current and previous contrast values (e.g., the simplex algorithm).

v) If changes in contrast or range are greater than some user-defined convergence threshold, return to 'ii).' Otherwise, done.

The scattering characteristics of different targets vary widely. In an operational system, the performance of the autofocus algorithm can be degraded by the dependence of the cost function on the scattering characteristics. Autofocus algorithms can be expected to converge to the optimal solution defined by the cost function, but the resulting *optimal* image may

not be the *correct* image. If there is a difference, the corresponding range estimates will also contain errors. Another common problem, especially for noisy data, is that the cost function may contain many local maxima in which the search algorithm can get stuck.

The autofocus procedure described here is a method for refining the estimate of the range from the radar to the target. When the range is not known with sufficient precision, such a procedure is required in order to form a well-focused image; but other unknowns may also adversely affect image focus. In ISAR imaging of ships, for example, the variations in aspect angle are produced by the pitching and rolling of the ship in the ocean swell. The angle variations are not readily available from observations and must be inferred from the radar data in much the same way as the range. During imaging, aspect angle can be treated as another unknown and also modeled with a polynomial. For imaging of ships, the aspect angle variations may be periodic, so a sinusoidal or Fourier series expansion may also be an appropriate model.

For ISAR imaging of satellites at VHF, a principal unknown is the ionosphere. Its effects on the radar signal are sufficient to seriously degrade image quality. However, it will be shown that if the ionospheric effects can be estimated, they can be removed from the radar observations. In this research, the autofocus procedure treats the ionosphere as another unknown. Details are given in the next two chapters.

2.6 The Range-Doppler Description of Radar Imaging

This section discusses an alternate approach to radar imaging: the range-Doppler technique. The technique is first introduced in general terms. Then, to illustrate the ideas and formulation, an equation is given for the range to a point target in the image area. The Doppler frequency of the target echo is related to the time-rate-of-change of that range equation. To illustrate the use of the range-Doppler formulation, the effect of uncompensated constant-velocity radial target motion is evaluated. Using the range-Doppler formulation simplifies the analysis of the effects of this particular error source. Other error sources, however, including ionospheric defocusing effects, are more conveniently handled with the polar format, or target-projection formulation.

2.6.1 The Range-Doppler Technique

Section 2.2 describes ISAR imaging in terms of target projections. In contrast, classical range-Doppler theory describes imaging in terms of the range and Doppler-frequency history of points in the image area over the target observation period (see *Brown and Fredericks*, 1969). The idea of using the Doppler frequency shift of the target echo for imaging purposes, which originated in the early 1950s, is credited to Carl Wiley of the Goodyear Aircraft Corporation. A description of the development of his idea is given by *Sherwin et al.* (1962). The two viewpoints—target projections vs. range-Doppler—are mathematically equivalent but provide complementary perspectives on the radar imaging problem. Also, formulation of the imaging procedure from the range-Doppler viewpoint is helpful in analyzing some aspects of image quality.

In the range-Doppler imaging technique, points on the target are 'sorted' into appropriate (x, y) bins based on their observed trajectories during the imaging period. In the range direction, the sorting is based on the distance from the radar to the target scattering points. The resolution is again limited by radar bandwidth, since bandwidth determines the accuracy with which the distance can be measured. In the cross-range direction, the sorting is based on the Doppler frequency history of the points over the imaging period. More precisely, the ideal Doppler frequency histories of points in the image area are compared, often through cross-correlation, with observed histories, along appropriate trajectories, in the radar data. For a more detailed description of the technique, refer to *Cutrona et al.* (1961), *McCord* (1962), or *Kovaly* (1972).

The Doppler frequency shift of the echo from a point target is given by

$$f_{\mathrm{D}} = \frac{1}{2\pi}\frac{d\phi_{\mathrm{r}}(t)}{dt} = \frac{-2}{\lambda}v(t), \tag{2.10}$$

where $\phi_{\mathrm{r}}(t)$ is the phase of the received signal and $v(t)$ is the radial velocity of the target. Radar systems that employ continuous wave (CW) signals allow observation of the Doppler frequency shift directly. For pulsed radar systems, however, the phase of the echo from the point target is a single sample of the phase function, $\phi_{\mathrm{r}}(t)$, at the time the pulse reaches the target. The Doppler frequency is found from the time rate-of-change of the phase samples from the set of echoes collected during the imaging period. Since coherent pulsed radar systems measure phase directly, it is more convenient to describe the imaging procedure in

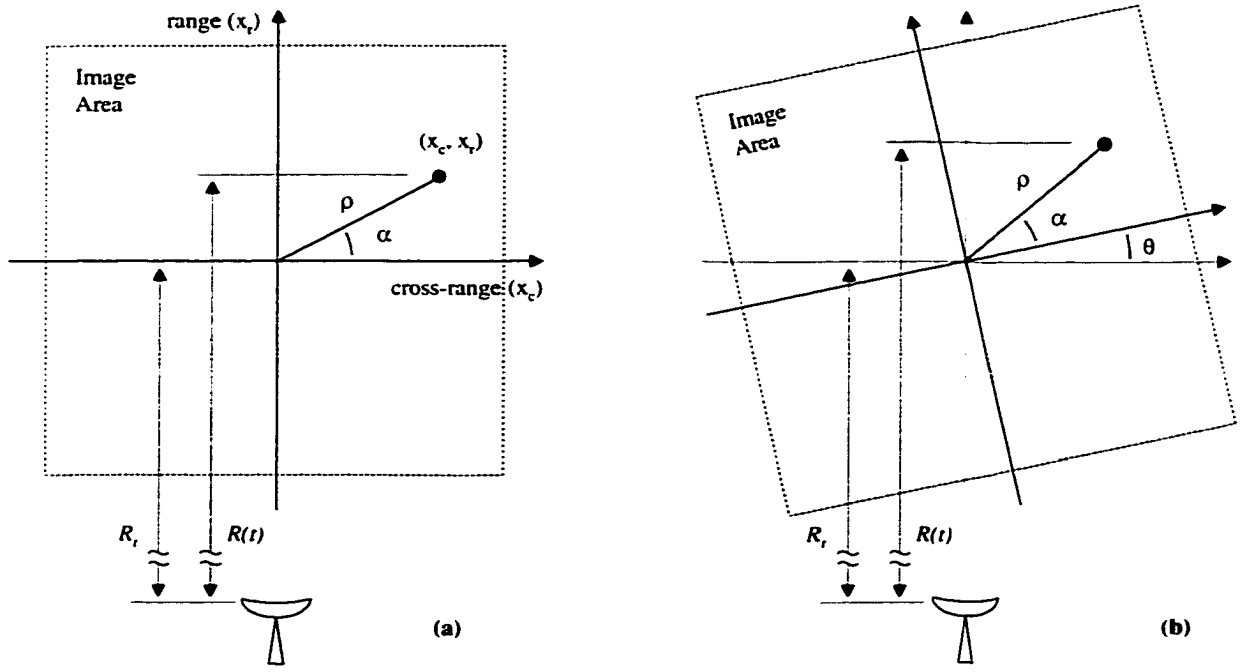

Figure 2.6: Distance to a point in the image area. As the target rotates, the distance, $R(t)$, from the radar to a point (x_c, x_r) on the target varies sinusoidally with θ. The 'amplitude' and 'phase' of that sinusoidal range variation encode the range and cross-range location of the point.

terms of phase history rather than Doppler-frequency history. The results, of course, can be written in terms of the Doppler frequency by differentiating the phase function.

The phase history of a target can be described by considering a point in the image area, as depicted in Figure 2.6a. The point is offset from the origin of a coordinate frame fixed to the target by x_r in range and x_c in cross-range. The distance from the radar to the point (x_c, x_r) is $R = R_t + \rho \sin\alpha$, where R_t is the distance from the radar to the origin of the target-fixed coordinate frame, and (ρ, α) are the polar coordinates of the point. As the target rotates through the aspect angle $\theta(t)$, the distance to the point becomes (Figure 2.6b),

$$\begin{aligned} R(t) &= R_t + \rho \sin(\theta(t) + \alpha) \\ R(t) &= R_t + x_c \sin\theta(t) + x_r \cos\theta(t), \end{aligned} \tag{2.11}$$

where $x_c = \rho\cos\alpha$, $x_r = \rho\sin\alpha$, and t is the observation time. The total target observation time is S, and $t = 0$ is taken as the time at the center of the aperture. The imaging period is

then given by $-S/2 < t < S/2$. Equation 2.11 describes a unique trajectory for each point in the image area. Again, imaging involves matching point-target trajectories observed in the data to those described by Equation 2.11. The resolution is determined by the minimum detectable difference in an observed trajectory. For coherent systems, the distance to the point target is determined from the radar signal phase, $\phi_r(t) = -2kR(t)$. As a result, the accuracy of the trajectory measurement depends on the accuracy of the phase measurement. Using standard range-Doppler imaging techniques, two trajectories can be separated, or uniquely identified, if the total change in phase over the two trajectories differs by at least 2π radians.

2.6.2 The Effect of Uncompensated Radial Target Motion

The usefulness of the range-Doppler viewpoint can be illustrated by analyzing a target's uncompensated constant-velocity radial motion. Such motion produces a cross-range shift and a small amount of blurring of the image. For the analysis, consider points along the cross-range axis, $x_r = 0$. The conclusions obtained for $x_r = 0$ can be applied to all points on the target by shifting the origin of the target-fixed frame to give $x_r = 0$ at the point of interest. With $x_r = 0$, the trajectory depends only on the cross-range coordinate and the aspect angle through $R(t) = R_t + x_c \sin\theta(t)$. This simplified form of Equation 2.11 is plotted in Figure 2.7 for $-30° < \theta(t) < +30°$ (i.e., a 60° aperture), and for $x_c = 5$, 10, and 20 m. A line having the same slope at the origin as the $x_c = 20$ curve is also plotted. The three sinusoidal curves can be approximated by straight lines for small values of θ and, from Equation 2.11, the slope of each line is equal to the cross-range coordinate of the scatterer. This illustrates a commonly observed uncompensated motion effect in radar imaging. In the imaging formulation, it is assumed that the range to the origin of the target-fixed frame, R_t, is constant. However, if R_t changes with a constant velocity, v, a constant slope is added to the observed trajectories. Then, $R_t(t) = R_0 + vt$, where R_0 is the range at $t = 0$, and v is the constant radial velocity of the target frame. The trajectories produced in a constant-radial-velocity target-fixed frame look similar to those produced in a stationary frame in which the entire target has been shifted in the cross-range direction. The result: *Uncompensated constant-velocity radial target motion causes cross-range translation of the image.* The amount of translation can be calculated by equating the slope of the constant-velocity range line to the slope of the sinusoid at the center of the aperture. The cross-range

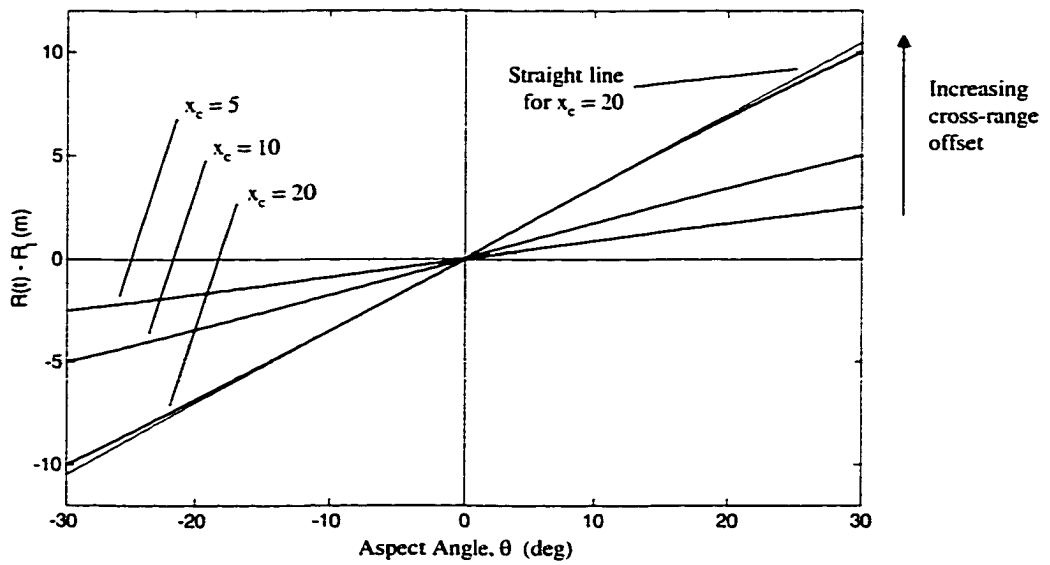

Figure 2.7: Target trajectories for cross-range offsets of 5, 10, and 20 m, and a line with the same slope at the origin as the $x_c = 20$ trajectory. For aspect angle variations less than about ± 30 degrees over the target observation period, the sinusoidal range variations can be approximated by a line. As a result, uncompensated constant-velocity target translation produces a cross-range shift of the image.

translation, or offset of the image, is then given by

$$\begin{aligned} \left.\frac{d}{dt}(vt)\right|_{t=0} &= \left.\frac{d}{dt}(x_{\text{off}} \sin \omega_t t)\right|_{t=0} \\ x_{\text{off}} &= \frac{v}{\omega_t} = \frac{vS}{\omega_t S} \\ x_{\text{off}} &= \frac{R_l}{\Theta}, \end{aligned} \tag{2.12}$$

where x_{off} is the cross-range offset of the image, v is the constant-velocity component of the target's radial motion, ω_t is the target's angular rotation rate, $R_l = vS$ is the total (constant velocity) drift of the target over the imaging period, and Θ is the angular aperture.

As the angular aperture increases, so does the difference between the trajectories produced by constant-radial-velocity and cross-range offset of the target. That difference can lead to defocusing of the image. The point at which the defocusing becomes significant can be determined from the integrated difference between the phase histories of the two

trajectories over the imaging period. The phase difference is

$$\begin{aligned}\Delta\phi(t) &= \phi_{\sin} - \phi_{\text{lin}} \\ &= -2k\left((R_0 + x_{\text{off}}\sin\theta(t)) - (R_0 + vt)\right) \\ &= \frac{4\pi}{\lambda}(vt - x_{\text{off}}\sin\theta(t)),\end{aligned} \tag{2.13}$$

where ϕ_{lin} is the phase history produced by constant radial velocity, v, and $\phi_{\sin}$ is the phase history produced by a cross-range target offset, x_{off}. Using Equation 2.12, and expanding $\sin\theta$, the phase difference at the edge of the aperture, $\Delta\phi_e$, is given by

$$\Delta\phi_e = \frac{4\pi}{\lambda}\cdot\frac{x_{\text{off}}}{6}\cdot\left(\frac{\Theta}{2}\right)^3 = \frac{\pi}{12\lambda}\cdot vS\cdot\Theta^2. \tag{2.14}$$

Provided $\Delta\phi_e < \pm\pi/4$, the defocusing effect of the $\Delta\phi_e$ phase difference is insignificant.[4] Using the $\pi/4$ threshold for the maximum phase difference, constant velocity target drift does not degrade image focus, provided the total drift over the angular aperture, R_1, is limited to

$$\begin{aligned}\frac{\pi}{12\lambda}\cdot R_1\cdot\Theta^2 &< \frac{\pi}{4} \\ R_1 &< \frac{3\lambda}{\Theta^2}.\end{aligned} \tag{2.15}$$

As an example, for a 1-m wavelength and a 30-degree aperture—which together indicate about 1-m cross-range resolution—a constant velocity radial drift does not degrade image focus as long as the total drift, R_1, is less than 12 m. For a 60-degree aperture, the requirement is $R_1 < 3$ m.

The range-Doppler and polar-format/target-projection techniques provide complementary viewpoints to the radar imaging problem. The same image is produced by both techniques, but with very different imaging algorithms. Both viewpoints are valuable when analyzing error effects and image quality. The range-Doppler technique, as illustrated above,

[4]See Chapter 4 for further discussion of the effects of phase errors on image focus.

provides a simple approach to analyzing the effects of uncompensated target motion. However, it does not lend itself to analysis of the system point-spread function: that is easier to understand and analyze from the target-projection viewpoint.

2.7 Issues at VHF

Using very-high frequencies for ISAR imaging raises a number of challenges that are not significant when using microwave frequencies for imaging. The first of these is that large fractional-bandwidth signals, referred to as ultra-wide bandwidth (UWB) signals[5], are needed to obtain high range resolution. Fractional bandwidth is defined as the ratio of bandwidth to center frequency,

$$B_F = \frac{B}{f_c} = 2 \cdot \frac{(f_{max} - f_c)}{f_c}, \tag{2.16}$$

where B is the signal bandwidth, f_c is the center frequency, and f_{max} is the maximum frequency. From Equation 2.3, a 1-m range resolution requires a bandwidth of 150 MHz. If the center frequency is 300 MHz, the system has a 150/300 = 50% fractional bandwidth. For comparison, at 9 GHz the same range resolution requires a fractional bandwidth of only about 1.7%. A large fractional bandwidth increases the difficulty of designing radar hardware that has a good impulse response—specifically, a spectral response that is flat in amplitude and linear in phase. In UWB systems, the impulse response is optimized by careful design and hardware calibration. However, even with well-designed hardware, significant differences from the ideal impulse response can be expected. Those differences need to be measured with calibration signals and removed during digital signal processing.

Another challenge is related to the large aperture needed for high-resolution imaging at VHF. In order to maintain a specified resolution, the required aperture, quantified in Equation 2.4, increases as the frequency decreases. For 1-m resolution at 9 GHz, for example, the required aperture is 1 degree, while at a VHF frequency of 300 MHz, the required aperture is 30 degrees. To obtain a larger aperture, the target must be observed over a longer period of time. This complicates the motion compensation and imaging procedures.

[5]UWB is commonly used to refer to signals having fractional bandwidths greater than about 25% (e.g., *Taylor*, 1995, p. 2), although other definitions have been used by some authors. Similarly, wideband signals have fractional bandwidths between about 1% and 25%, and narrowband signals have bandwidths less than about 1%.

The next challenge at VHF is achieving a sufficient SNR in the received signal. Our experience to date indicates that a single-pulse SNR of at least 6 dB is required, but autofocus techniques work best when the SNR is at least 15 dB. The variables in the radar equation that can be used to improve SNR, without compromising resolution, include transmit power, pulse length, and antenna directivity. The first two variables are determined by transmitter performance and the third is primarily determined by antenna size. Since the target is localized, it is desirable to have a small antenna beamwidth along with the correspondingly large directivity. For the Stanford 'Big Dish,' the beamwidth at 300 MHz is $\lambda/D \approx 1/45 \approx 1.5$ degrees, and the directivity is about 43 dBi. Even with this large directivity, the single-pulse SNR—calculated with the radar equation using the nominal radar parameters from Table 1.1 and the distances and cross sections from Table 1.2—is less than 0 dB for most satellites. For the Mir space station, which is quite large and in a low orbit, the single-pulse SNR is typically between 10 and 30 dB, depending on range and RCS. Note, also, that at least in the case of Mir, the RCS varies with aspect angle by 10 to 20 dB.

Interference adds another challenge to the use of VHF and/or UHF signals for radar imaging. Although the antenna is pointed upwards, terrestrial interference leaks in through the sidelobes and individual interference sources often have levels that are 40 to 60 dB higher than the radar echo. This interference is generated by a variety of sources, including television, personal communication systems, aircraft communications, and radar system components that contain digital electronics—especially computers, where clock rates currently fall in the middle of the VHF band. Fortunately, many of these interferers are narrowband and can be removed, for the most part, from the signal during data processing by notching the offending frequencies from the spectral data. However, this has the undesired effect of also removing the radar signal at those frequencies and leaving narrow holes in the spectrum. If the number of spectral bins that are notched is a small fraction of the total, the procedure does not have a significant effect on resolution, but it does increase sidelobe levels.[6]

[6]This assertion can be quantified, in a statistical sense, by comparing the total energy in the point-target response to the energy removed by spectral notching.

2.8 Scattering Issues

In the ISAR imaging formulation of Section 2.2, the target is described as a collection of point scatterers, each having a complex scattering amplitude that is independent of frequency and aspect angle. That target description provides an idealized model that is suitable for development of the imaging algorithm. However, actual targets consist of a collection of scattering centers whose scattering characteristics can vary with frequency and aspect angle. Those variations can have a significant effect on the radar image.

The assumption of ideal point scattering is suitable as long as the complex scattering amplitudes of the target's scattering centers remain constant over the frequencies and aspect angles used in forming the image. For microwave radar, where the fractional bandwidth and angular aperture are small, this assumption is reasonably good. For VHF radar, however, the fractional bandwidth and angular aperture are usually much larger, often leading to dramatic changes in the scattering characteristics over frequency and aspect angle. The result of those scattering variations is degradation in the quality of the final image. They reduce resolution, increase sidelobe levels, and introduce artifacts. Several of the phenomenological factors that cause these scattering variations are listed below.

i) Shadowing: As the aspect angle changes through the 30 to 60 degree spans used here, some components of the target move behind others and become shadowed over a part of the aperture.

ii) Multiple reflections: Many modern satellites are complex structures with a variety of external metallic pieces. When the radar pulse is scattered for such structures, part of the signal 'bounces' off more than one surface before returning to the radar. This results in 'false echoes,' appearing in the image at farther range than the 'single-bounce' echoes.

iii) Time-delayed response: The large fractional bandwidth provides a range resolution cell that can be smaller than a component's 'delayed response.' The component echo is then separated into several range pixels. Spherical or cylindrical objects, for example, exhibit additional echoes after their main response due to creeping waves.

iv) Electromagnetic coupling: The ideal point-target model assumes that the components in the target act in isolation; that is, their response does not change as more components are added. In reality, energy is coupled between the components, and addition of a new component produces a small change in the response of all the others.

v) Variations with frequency: Many components have significant variations in complex scattering amplitude over the frequencies in the UWB waveform. This can be thought of as the frequency domain equivalent of the time-delayed response listed above.

vi) Variations with aspect angle: Many pieces of the target can also have significant variations in complex scattering amplitude over the large span of the aspect angle. One example is scattering from a flat plate; another is scattering from a wire. This 'scattering pattern,' the variation in complex scattering amplitude with aspect angle, produces a response that spreads over some finite area in the image. Note that in many cases the size of the response in the image is an approximate match for the size of the object that produced the scattering.

The effect of variations in the target's scattering characteristics on the final image can be characterized with a two-dimensional complex-spectral-weighting function over the frequency-domain support region of the image. If the target is considered as an ensemble of point scatterers—matching the scattering model used in developing the imaging algorithm—that spectral weighting function characterizes the difference between an image of the ensemble of point scatterers and the actual image.

Further analysis of the frequency and aspect-angle dependence of the complex scattering amplitude, together with examples of the effects on radar images, can be found in *Axellson* (1995) and *Toups et al.* (1996).

Some applications attempt to use variations in the scattering characteristics of an object to separate it from its surroundings and to identify it. The particular scattering characteristics compose the 'signature' of the target. Procedures for finding target signatures in radar data are referred to as target detection, discrimination, and identification. Development of robust techniques is an active area of research (e.g., *Baum et al.*, 1991; *Baum*, 1995; *Brunzell*, 1997).

Chapter 3

Ionosphere

The ionosphere is the region of the Earth's upper atmosphere extending from altitudes of about 100 to 1000 km where free charged particles, electrons and positive ions, exist in sufficient numbers to affect radio-wave propagation. It is produced primarily by the ultraviolet (UV) and X-ray components of the solar radiation. Electromagnetic waves interact with the charged particles of the ionosphere, causing the waves to be delayed, dispersed, attenuated, and refracted. These effects are more severe at lower wave frequencies, and can have a significant deleterious impact on the performance of radar systems operating at VHF. For VHF radio-wave propagation, the primary interaction is between the wave and free electrons. As a result, the effects of the ionosphere at VHF and higher frequencies are well-characterized by the free electron density N (e^-/m^3), which is a function of altitude, latitude, longitude, and time.

The existence of an ionized layer in Earth's upper atmosphere was postulated independently, in 1902, by A. E. Kennelly and Oliver Heaviside, to help explain Marconi's successful transatlantic radio-wave transmissions. In the following years, a number of theoretical attempts were made to understand both the potential ionization mechanisms and the interaction of radio waves with ionized particles (see *Ratcliffe*, 1959, for details). However, it was not until 1926 that the existence of an ionized layer was finally proven, when *Breit and Tuve* (1926) published the results of their landmark sounding experiments. What was then known as the 'Heaviside layer' is now called the ionosphere. The understanding of the ionosphere's effects on radio-wave propagation developed rapidly in the years following Breit and Tuve's experiments (e.g., *Appleton*, 1927; *Lassen*, 1927; *Hartree*, 1931; *Appleton*, 1932), and the study of the complex chemistry and physics of the ionosphere, along with

ionospheric effects on transionospheric radio-wave propagation, continues to this day. Surveys of the history of ionospheric research are given in, for example, *Booker* (1974), *Green* (1974), and *Villard* (1976).

The ionosphere is highly variable, both spatially and temporally, on spatial scales ranging from meters to hundreds of kilometers and temporal scales ranging from seconds to years. Some of the variations follow a known pattern, while others come and go on an irregular and seemingly random basis. The variations are caused by transport phenomena and changes in the ionization and recombination rates. As a result, ionization density varies with, for example, time of day, season, sunspot number, and geomagnetic K_p index. The Sun drives the ionization, causing large diurnal variations with a maximum at midday and a minimum in the early hours before sunrise. The ratio of the diurnal maximum to minimum is about 10. The ionosphere also has large latitudinal and seasonal variations that can be related to the solar zenith angle. Solar flares increase the Sun's UV radiation and thus produce large random variations in ionization density and a trend that follows the 11-year solar cycle. These are just a few of the items affecting ionization density; a more detailed discussion can be found in *Kelley* (1989).

To understand the effects of the ionosphere on radio-wave propagation, it is necessary to understand both plasma electrodynamics (i.e., how the free electrons affect the wave), and ionospheric morphology (i.e., how the free electron density varies with space and time). The former is discussed in Sections 3.2, 3.3, and 3.4, and the latter in Sections 3.1 and 3.8.

A spherically symmetric shell model in which the spatial variations of the electron density are dependent only on altitude is used in most of the following analyses of ionospheric effects. It is also used as the model that is fit to the measurements obtained from the radar data. For such a model, a vertical electron-density profile, $N(z)$, fully specifies the spatial variations. A simple electron-density profile, such as a uniform slab with appropriate peak and integrated electron densities, can provide useful order-of-magnitude estimates of ionospheric effects. More precise results require a profile produced by a physics-based model, such as the Chapman profile, or a profile produced by one of the many advanced ionosphere-modeling programs, such as the Fully Analytic Ionospheric Model (FAIM) or the current International Reference Ionosphere (IRI-95). In the following sections, either a uniform profile or a Chapman profile is used for most analyses. The IRI and FAIM models are used to compare measured and predicted profiles and to evaluate the limitations of higher-order effects.

3.1 Electron Density Profiles

The shape of the electron-density profile depends on the density of the neutral atmosphere and the intensity and spectral content of the ionizing radiation. At altitudes above about 1000 km the gases of the atmosphere are almost fully ionized, but their combined density is small, so N is small. At these high altitudes, the free electron density is sufficiently small to have only a negligible effect on VHF radio waves, except when the integrated electron density along the ray path becomes significant over large propagation distances. This can occur, for example, with radar echoes from the moon, since the integrated electron density from the surface of the Earth to 1000 km is about the same as that from 1000 km to the moon. As solar radiation penetrates to greater depths in the atmosphere, its intensity is reduced due to absorption at the higher levels. However, the gas density increases with decreasing altitude; the net result is that ionization density increases to a broad peak at an altitude of about 300 to 400 km. Below 300 km, the ionization density gradually decreases until about 100 km, where a thinner peak or enhancement occurs. At altitudes below 100 km, the ionization drops rapidly to near zero by about 60 km. In the daytime, a weaker enhancement also develops at an altitude of about 80 km.

The part of the ionosphere around the 300-km peak, called the F region, is generated primarily by UV radiation. The predominant ion species at that altitude is atomic oxygen, O^+. Note that even though the maximum of the free electron density occurs in the F region, the density of the electrons (and positive ions) is only about 10^{-5} of the density of the neutral particles. The area around the peak at 100 km, called the E region, is generated primarily by extreme ultraviolet (EUV) radiation and coronal X-rays. In the E region, the predominant ion species are molecular oxygen and molecular nitrogen, O_2^+ and N_2^+. The enhancement at 80 km, called the D region, is generated primarily by X-rays, as most lower-energy photons are absorbed at higher altitudes. Although the D region has a low ionization density, it is where most radio-wave absorption occurs during daylight hours. Several other enhancements in ionization occur as a result of the spectral content of the solar radiation and the various gas species that occupy the different levels of the atmosphere. Details can be found, for example, in *Rees* (1989) or *Hargreaves* (1992).

The values for electron density and altitude given in the discussions in this chapter are nominal. Actual values for specific situations can vary significantly, depending on ionospheric conditions. The peak of the F region, for example, can occur at an altitude of

anywhere from 200 to 400 km, and at times even higher. Also, the free electron density, N, at the peak of the F region can vary from about $10^{10}e^{-}/m^3$ in the hours after midnight to almost $10^{13}e^{-}/m^3$ during periods of high solar activity.

An analytic vertical profile of the electron density can be calculated for a planar geometry if a few simplifying assumptions are made. First, it is assumed that the atmosphere has a constant composition and temperature at all altitudes. The vertical density profile of the neutral atmosphere is then exponentially decreasing with altitude. Next, it is assumed that the absorption and recombination coefficients are constant. This implies that the ionization rate depends only on radiation intensity, and the recombination rate depends only on ionization density. Finally, plasma transport is neglected. The analysis of this simplified situation was first done by *Chapman* (1939) and the result, called a *Chapman profile*, is given by

$$N(z) = N_{\mathrm{m}} \exp\left(\frac{1}{2}(1 - \zeta - e^{-\zeta})\right), \tag{3.1}$$

$$\zeta = (z - z_{\mathrm{m}})/H, \tag{3.2}$$

where N is the electron density, z is the altitude, ζ is the scaled altitude, and H is the scale height. In the Chapman profile, H essentially specifies the width of the ionosphere, z_{m} specifies the altitude at the maximum, and N_{m} specifies the peak density. Specifically, $N(z)$ reaches a maximum of N_{m} at an altitude of z_{m}. The quantities N_{m}, z_{m}, and H each depend on the intensity of the solar radiation, the solar zenith angle, the radiation absorption coefficient of the atmosphere, the recombination coefficient, and the atmospheric density. All these values can be estimated when modeling the ionosphere, but operationally it is easy to measure the peak altitude and density with an ionosonde. These measured values can be used directly in the Chapman profile equations.

The simple Chapman profile does not provide an adequate fit to actual ionospheric profiles for many applications. Its errors are caused primarily by variations in the absorption coefficient for the different radiation frequency constituents, variations in the composition of the ionosphere with altitude, and plasma transport. However, the Chapman profile is often used because it is easy to calculate and provides an analytic tool for making initial estimates of ionospheric effects. It is used in later sections of this thesis to illustrate ionospheric effects.

Elaborate models have been developed to more accurately represent the full state of the ionosphere. These incorporate additional information such as local time, latitude, and sunspot number to obtain a better estimate of $N(z)$. They also incorporate expressions for the dynamics of the ionosphere and a database of historical observations. Even so, the best models often have factor-of-two errors due to limitations in the input data and unmodeled or unmeasured drivers such as upper atmospheric weather. One example of a limitation in the input data is that sunspot number and 10.7-cm solar flux measurements are proxies for solar radiation intensity, but they do not provide full spectral details. *Brown et al.* (1991) compares predictions from several of the most popular models to measured data.

One of the most widely used models is the International Reference Ionosphere—current version IRI-95—sponsored by the International Union of Radio Science (URSI) and the Committee on Space Research (COSPAR) (*Rawer et al.*, 1978; *Bilitza et al.*, 1993; *Rawer*, 1996; *Decker et al.*, 1997). This model has been evolving for more than two decades, with broad support from the international research community. The model is empirical in nature; it relies on a large database of observations taken from a variety of sources and globally distributed locations. In addition to free electron density, the model provides electron temperature, ionization densities for various atomic and molecular species, ion temperature, and drift velocities. The electron density is the only parameter used in this work, but the other parameters produced by the IRI model are needed in studies of ionospheric chemistry, physics, and electrodynamics.

For an example of an electron-density profile, the IRI-95 model calculations were performed with the location and time of the satellite pass described in Table 1.3. The free electron-density profile is plotted in Figure 3.1. A Chapman profile is also plotted, with N_m and z_m chosen to match the IRI profile and H chosen to give the same integrated density to the 378-km altitude of the satellite. For this example, $N_m = 6.3 \times 10^{11}$ e$^-$/m^3, $z_m = 266$ km, $H = 71$ km, and the plasma frequency at the peak of the Chapman profile is 7.1 MHz.

Another popular ionosphere model used in later sections of this work is the Fully Analytic Ionospheric Model (FAIM), developed by *Anderson et al.* (1989). A description of its predecessor, SLIM, is given in *Anderson et al.* (1987), and a successor, PIM, in *Daniell et al.* (1995). FAIM uses parameterizations of first-principle theoretical models to describe the ionosphere. One advantage of this approach is that FAIM captures ionospheric structure that can be missed, or 'smeared out,' in the empirical models. Low-latitude morphology—notably the equatorial anomaly—is one area where FAIM does better than IRI.

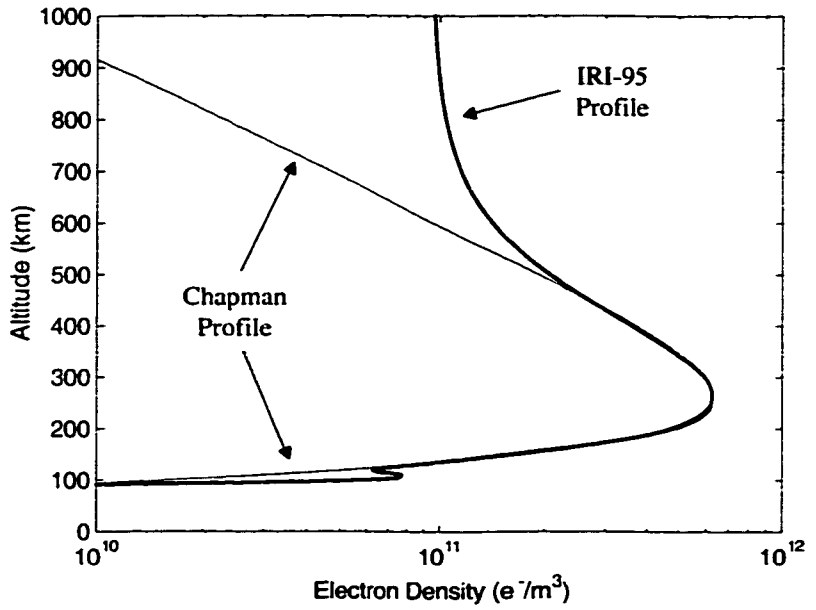

Figure 3.1: IRI and Chapman electron-density profiles. The electron-density profile was produced by the IRI-95 model for Ascension Island, March 25, 1998, 08:22 UT. The Chapman profile parameters were calculated to give an optimal fit to the IRI-95 profile.

3.2 Wave-Plasma Interactions

The ionosphere affects radio-wave propagation through interaction between the electromagnetic (EM) radio wave and the ionized particles. That interaction is quantified by the Lorentz force law, which gives the force, $\mathbf{F}$, on a charged particle as

$$\mathbf{F} = q(\mathbf{E} + \mathbf{v} \times \mathbf{B}), \tag{3.3}$$

where q is the charge on the particle, $\mathbf{v}$ is the velocity of the particle, $\mathbf{E}$ is the electric field strength, and $\mathbf{B}$ is the magnetic flux density. The main component of the interaction is the acceleration of the electrons and ions by the electric field of the EM wave. This interaction causes the particles to oscillate at the frequency of the wave, with an amplitude that depends on the mass of the particle and the frequency of the wave. Since the positive ions are at least 2000 times more massive than the electrons, their range of motion is smaller by about the same ratio. For frequencies greater than a few hundred kilohertz, the motion of the ions has a negligible effect on the radio wave. The motion of the electrons, however, has a significant effect that extends to frequencies above 2 GHz. As a result, for discussion and

analysis it is convenient to think of the plasma as an electrically neutral medium consisting of a sea of free electrons floating among an equal number of fixed ions.

The equations that characterize the effects of the ionosphere on a radio wave can be derived by considering the wave-plasma interaction with either a *microscopic* or *macroscopic* approach. The microscopic approach was used by *Hartree* (1931), while the macroscopic approach was used, for example, by *Appleton* (1932). Both approaches lead to the same expression for the complex refractive index of the ionosphere.

In the macroscopic approach, the ionosphere is treated as a medium containing a uniform distribution of free electrons. Those electrons are driven by the electric field of the radio wave, causing them to oscillate about their undisturbed locations. The ensemble average effect of that motion is a volumetric polarization, **P**, of the medium, specified in units of induced dipole moment per unit volume. The relative permittivity and the complex refractive index (Equation 3.6) of the medium can then be calculated, using Maxwell's equations, from the polarization vector (see *Ratcliffe*, 1959, p. 8).

In the microscopic approach, the complex refractive index is deduced by considering the total scattered wave that is reradiated from the accelerating electrons. The scattered wave is calculated by integrating the infinitesimal contributions from the individual electrons over the wavefront of the incident wave. The total EM wave, given by the sum of the incident and scattered waves, is found to have a phase delay relative to the incident wave. That phase delay can be related to the refractive index of the medium, producing the same expression as the macroscopic approach (see *Ratcliffe*, 1959, p. 21).

Now consider the random thermal motion of the electrons. Electrons in the F region of the ionosphere have thermal velocities on the order of 10 km/s. Although this is at least two orders of magnitude larger than the velocities imparted by radio waves at VHF, the random thermal motion can be ignored for most radio-wave-propagation problems. The insensitivity to thermal motion can be explained with statistical thermodynamics. Basically, only the 'organized' part of the total collisions has a net effect on the radio wave. Verification of the insensitivity to thermal velocity can be found in statistical thermodynamics texts such as *Clemmow and Dougherty* (1969).

Collisions between oscillating electrons and other particles can cause attenuation of radio waves in the ionosphere. To a good first approximation, the power lost by a radio wave is linearly related to the collision frequency. It is interesting to note that the collisions due to the random thermal motion of the electrons do not contribute to the attenuation of

the wave; the attenuation is only due to the incremental collisions caused by the additional velocity imparted by the wave. Again, this can be explained with statistical thermodynamic analysis.

At VHF, the attenuation due to collisions is small and usually amounts to only a fraction of a decibel for waves that propagate from Earth's surface through the top of the ionosphere. The collision rate is highest where the neutral density is highest—at the lower edge of the ionosphere—so in spite of low ionization density, the radio-wave absorption peak occurs in the D region at an altitude of about 80 km.

Equation 3.3 indicates that the motion of the ionospheric electrons would also be affected by Earth's magnetic field.[1] The presence of the magnetic field has a very small effect on the propagation characteristics at VHF, and that effect is justifiably ignored in most of the following sections. However, some issues that are related to the presence of the magnetic field do become important in certain applications. Two of these, polarization rotation and higher-order propagation effects, are discussed in later sections.

The direction of the $\mathbf{v} \times \mathbf{B}$ component of the Lorentz force depends both on the direction of the electron velocity vector, $\mathbf{v}$, and the direction of the geomagnetic field, $\mathbf{B}$. The electron motion is driven by the radio wave's electric field, $\mathbf{E}$, which is perpendicular to the *wave normal*. The effects of the geomagnetic field on the radio wave thus depend on the angle between the geomagnetic field and the wave normal, Θ. For this reason, propagation in an *electron magnetoplasma* is anisotropic, as the propagation characteristics depend on the direction of propagation of the wave.

Anisotropy leads to two characteristic modes of propagation, the ordinary (O) and extraordinary (X) waves, that have opposite senses of polarization. These two modes can be thought of as eigenfunctions of the system since their polarizations are preserved as the waves propagate through the ionosphere. Differences in their interaction with the magnetic field result in small differences in their refractive indices along with small differences in their phase and group velocities.

A wave with an arbitrary polarization can be decomposed into a linear combination of the characteristic modes. As in linear systems theory, the characteristic-mode components of the wave can be separately analyzed and then combined to determine the ionosphere's effect on the original wave.

[1] The magnetic field of the radio wave also has a small effect, but that effect is negligible in most situations.

For a wave with an arbitrary polarization, phase velocity differences in the characteristic-mode components change the polarization of the wave as it propagates through the ionosphere. For example, for most directions of propagation, a linearly polarized wave remains linear, but its polarization angle rotates. The total change in polarization angle over the ray path is called the *Faraday rotation.*

Calculation of magnetic field effects, including Faraday rotation, is complicated by variations of the magnetic flux density and Θ along the ray path. The magnetic field changes slowly with latitude and longitude, and as the cube of distance from the center of the Earth. The magnetic deviation angle (the horizontal angle relative to true north) and the dip angle (the angle relative to a horizontal plane) characterize the direction of $\mathbf{B}$.[2] Both angles vary with latitude, longitude, and altitude. *Brookner* (1977b) provides plots of typical geomagnetic flux density, deviation angle, and dip angle versus latitude and longitude, along with further discussion of Faraday rotation.

Instabilities often develop in the ionosphere and produce large spatial and temporal variations in electron density. A radio wave passing through those irregularities can suffer large variations in amplitude and phase. The effect, called scintillation, is discussed in Section 3.8.

3.3 The Refractive Index of the Ionosphere

A medium's complex permittivity characterizes the medium's effects on a radio wave. In the case of the ionosphere at VHF, the medium is linear; that is, the permittivity is independent of the wave amplitude. Unfortunately, it is also inhomogeneous and anisotropic, so the behavior of a radio wave depends on its location and direction of travel. At VHF, the ionosphere can be described as a *cold electron magnetoplasma.*[3] Derivations of its permittivity are given in *Ratcliffe* (1959) and *Budden* (1988). *Lawrence et al.* (1964) discusses many specific aspects of transionospheric propagation that are important at VHF. In this section, the permittivity equation is listed and then simplified as appropriate for the problem of radar imaging at VHF.

[2]The deviation angle is sometimes called the magnetic declination, and the dip angle is sometimes called the magnetic inclination.

[3]The temperature of the ionosphere in the F region is greater than 1000 kelvin; a *cold* plasma is defined as one in which the thermal velocity of the electrons does not have a significant effect on wave propagation.

Two derived frequencies appear in the permittivity equation, the plasma frequency and electron gyro-frequency. The ionosphere reflects EM waves with frequencies below its *plasma frequency*, or cutoff frequency, given by

$$\omega_{\mathrm{N}} = \sqrt{\frac{Ne^2}{\epsilon_o m}} = 56.42 \cdot \sqrt{N}, \tag{3.4}$$

where N is the free electron density ($\mathrm{e^-/m^3}$), e is the electronic charge, ϵ_o is the permittivity of free space, and m is the mass of an electron. The angular plasma frequency, ω_{N}, is related to the cyclical plasma frequency, f_{N}, through $\omega_{\mathrm{N}} = 2\pi f_{\mathrm{N}}$, so $f_{\mathrm{N}} = 8.98\sqrt{N}$. Since the plasma frequency depends on N, it varies with latitude, longitude, altitude, and time. Typical values in the F region range between about 3 and 8 MHz. Peak electron density is often specified in terms of plasma frequency. For example, it is more common to specify $\mathrm{f_oF_2}$, the plasma frequency at the peak of the F region, than N_{m}, the electron density at the peak. For the Chapman profile in Figure 3.1, $\mathrm{f_oF_2} = 7.1$ MHz.

Free electrons in a magnetic field follow helical paths centered on the magnetic field lines. The frequency of rotation about the field lines is called the *electron gyro-frequency*,

$$\omega_{\mathrm{H}} = \frac{eB}{m} = 0.1759 \times 10^{12} \cdot B, \tag{3.5}$$

where B is the magnitude of the magnetic field $\mathbf{B}$ ($\mathrm{Wb/m^2}$). Since the gyro-frequency depends on the geomagnetic field, it also depends on latitude, longitude, and altitude. Typical values range between about 0.5 and 1.5 MHz.

The complex permittivity is given by the Appleton-Hartree formula (*Appleton*, 1927; *Lassen*, 1927; *Hartree*, 1931; *Appleton*, 1932),

$$n^2 = 1 - \frac{X(U-X)}{U(U-X) - \frac{1}{2}Y^2\sin^2\Theta \pm \left\{\frac{1}{4}Y^4\sin^4\Theta + Y^2\cos^2\Theta(U-X)^2\right\}^{1/2}}, \tag{3.6}$$

$$U = 1 - iZ, \tag{3.7}$$

$$X = \frac{\omega_{\mathrm{N}}^2}{\omega^2}, \tag{3.8}$$

$$Y = \frac{\omega_{\mathrm{H}}}{\omega}, \tag{3.9}$$

$$Z = \frac{\nu}{\omega}, \tag{3.10}$$

where n is the refractive index, ω is the radio wave's angular frequency (radians/s), and ν is the effective collision frequency (radians/s). The + and − signs correspond to the two characteristic modes (the ordinary and extraordinary waves).

Equation 3.6 incorporates many ionospheric propagation effects that are not significant at VHF, so it can be simplified to obtain a more manageable form. The simplification steps are included here so that their validity can be checked when specific applications are evaluated.

The first simplification is to assume that the ionosphere is lossless at VHF. The effect of collisions is small at VHF, amounting to only a fraction of a decibel attenuation over the ray path. This can be verified from the plot of effective collision frequency vs. altitude in *Budden* (1988, p. 12). At VHF, the plot indicates that $Z = \nu/\omega \ll 1$, and thus $U \approx 1$. When it is assumed there are no collisions, the ionosphere becomes lossless, with $\nu = 0$, $Z = 0$, and $U = 1$. Then,

$$n^2 = 1 - \frac{X(1-X)}{(1-X) - \frac{1}{2}Y^2\sin^2\Theta \pm \left\{\frac{1}{4}Y^4\sin^4\Theta + Y^2\cos^2\Theta(1-X)^2\right\}^{1/2}}. \tag{3.11}$$

A further simplification results by noting that at VHF the plasma frequency (ω_N) and electron gyro-frequency (ω_H) are one or two orders of magnitude smaller than the radio-wave frequency, so X and Y are much smaller than unity. As a result, the second term in the square root in Equation 3.11 is much larger than the first for most directions of propagation. This effect is used to simplify further the equation by defining the propagation direction as quasi-longitudinal (QL) when the second term is dominant, or quasi-transverse (QT) when the first term is dominant. For QL propagation, the component of the wave vector, **k**, along the magnetic field lines is dominant; for QT propagation, the normal component is dominant. When the terms are about the same, the full expression is needed.

For QT propagation, the relation between the terms in the square root is

$$\frac{1}{4}Y^4\sin^4\Theta \gg Y^2\cos^2\Theta(1-X)^2.$$

Then, from Equation 3.11, for the ordinary wave,

$$n^2 = 1 - X, \tag{3.12}$$

and for the extraordinary wave,

$$n^2 = 1 - \frac{X(1-X)}{(1-X) - Y^2 \sin^2 \Theta}. \tag{3.13}$$

The characteristic polarizations for QT propagation are linear. The **E** field of the wave is parallel to the geomagnetic field for ordinary wave propagation, and perpendicular to the geomagnetic field for extraordinary propagation.

For QL propagation,

$$\frac{1}{4} Y^4 \sin^4 \Theta \ll Y^2 \cos^2 \Theta (1-X)^2.$$

Then, for the O and X waves,

$$n^2 = 1 - \frac{X}{1 \pm Y \cos \Theta}, \tag{3.14}$$

and the characteristic polarizations are circular. When Θ is acute ($\cos \Theta > 0$), the ordinary wave is left circularly polarized (LCP) and the extraordinary wave is right circularly polarized (RCP)[4]. To remember the mode definitions, note that for the extraordinary wave the electric field rotates in the same direction as the electron's gyro-rotation. In the northern hemisphere, Θ is acute for a downward propagating wave, so in that case, RCP is extraordinary.

In the transition between QL and QT propagation, the polarizations of the O and X waves are elliptical. This transition occurs when the terms in the radical in Equation 3.11 have similar magnitudes. The angle at which the terms are equal, called the transition angle, Θ_c, is determined from

$$\frac{1}{4} Y^4 \sin^4 \Theta_c = Y^2 \cos^2 \Theta_c (1-X)^2.$$

[4]The definition of Θ in this work agrees with that in *Lawrence et al.* (1964). In analysis of transionospheric propagation at lower frequencies where positive ions can affect the wave, Θ is often defined as the angle between the wave normal and **Y**, where $|\mathbf{Y}| = Y$, and where **Y** is antiparallel to **B** for electrons and parallel to **B** for positive ions (see *Budden*, 1988, pp. 46 and 372). For that definition of Θ, the polarizations of the O and X waves are opposite to those given here.

At VHF, $X \ll 1$, so that

$$\tan\Theta_c \sin\Theta_c \approx \frac{Z}{Y}.$$

Since $Y \ll 1$, Θ_c must be close to $\pi/2$. Then $\sin\Theta_c \approx 1$, and

$$\Theta_c \approx \arctan\left(2\frac{\omega}{\omega_H}\right). \tag{3.15}$$

For $B = 0.5$ gauss (a nominal value at the surface of the Earth) and $f = 300$ MHz, $\Theta_c = 89.87°$. At $f = 100$ MHz, $\Theta_c = 89.60°$. Thus, at VHF, propagation is QL for all directions except when the wave vector and **B** are within a few tenths of a degree of perpendicular.

The refractive index equations for the QL and QT propagation directions were calculated above for later use in derivation of the Faraday rotation. For calculation of the first-order effects of the ionosphere on the radio wave, return to Equation 3.11 and note that $Y \ll 1$. With this approximation, Equation 3.11 simplifies to

$$n \approx \sqrt{1 - X} = \sqrt{1 - \frac{\omega_N^2}{\omega^2}}. \tag{3.16}$$

The same result can be obtained by using $Y \ll 1$ in Equations 3.12, 3.13, and 3.14. Removal of Y from the equation is equivalent to saying that magnetic effects are sufficiently small to be ignored. For VHF radio-wave propagation, this approximation is not justified in some situations. Its validity is reviewed in more detail in Chapter 4.[5]

The radical in Equation 3.16 can be expanded as

$$n = 1 - \frac{1}{2}X - \frac{1}{8}X^2 - \frac{1}{16}X^3 + \cdots. \tag{3.17}$$

Since $X \ll 1$,

$$n \approx 1 - \frac{1}{2}X. \tag{3.18}$$

Substituting for X,

$$n = 1 - \left(b \cdot \frac{1}{\omega^2} \cdot N(z,\theta,\phi,t)\right), \tag{3.19}$$

[5]Also note that Equation 3.16 has the same form as the propagation coefficient in a waveguide operating near cutoff (*Ramo et al.*, 1994, p. 400). The dispersive characteristics of the ionosphere, with the approximations made so far, are the same as those of a waveguide when the ratio of wave frequency to cutoff frequency, ω/ω_N, is the same.

where the *propagation coefficient*, b, is a constant defined by

$$b = \frac{e^2}{2\epsilon_o m} = 1.591 \times 10^3 \ \ \mathrm{m^3/s^2}, \tag{3.20}$$

and where z, θ, ϕ, and t are included to emphasize the spatial and temporal variations of N. With this definition of the propagation coefficient, the plasma frequency is given by

$$\omega_N = \sqrt{2bN}. \tag{3.21}$$

The much-simplified refractive index of Equation 3.19 is the form used in most of the following sections. Note that it is valid to first order for QL *and* QT propagation. It consists of a free space term and a term due to the presence of the ionosphere. The effects of the ionosphere on the radio wave are given by the refractivity, $\Delta n = n - 1$. They vary linearly with the local electron density and with the inverse square of the radio-wave frequency.

3.4 VHF Propagation

3.4.1 Ionospheric Phase Contribution

The total effect of the ionosphere on a waveform is calculated by integrating the differential effects over the ray path; that is, the path the transmitted waveform follows as it propagates through the ionosphere. In this chapter, the effects of refraction are neglected, and the ray path is approximated with a straight line connecting the radar and target. The limitations of the straight-line approximation are evaluated in Chapter 4. Since losses are negligible at VHF, the ionosphere affects only the phase of the signal frequency components, producing a purely dispersive effect. One way of characterizing the total effect over the ray path is with the change in phase path length—the wavefront transit time multiplied by c, or the total number of wavelengths along the ray multiplied by the free-space wavelength—caused by the ionosphere, Δl_p, where

$$\Delta l_p = 2\int (n-1)dl = -\int X dl = -\frac{2b}{\omega^2}\int N(z,\theta,\phi)dl. \tag{3.22}$$

The integral is over the ray path connecting the radar and target, and the factor of two accounts for the two-way trip of the radar pulse. The presence of the ionosphere causes a

change in the phase of the received signal, φ_i, of

$$\varphi_i = -\frac{2\pi}{\lambda}\Delta l_p = \frac{2\pi b}{\lambda\omega^2} \cdot 2\int N dl, \tag{3.23}$$

where λ is the free-space wavelength. This equation can be written as

$$\varphi_i = \frac{2b}{c} \cdot \frac{1}{\omega} \cdot N_T, \tag{3.24}$$

$$N_T = \int N(z,\theta,\phi)dl, \tag{3.25}$$

where N_T, the *total electron content* (TEC), is the integral of the electron density along the ray,[6] and where c is the free-space velocity of light. The TEC depends on the spatial distribution of free electrons along the propagation path at the time the pulse passes through the ionosphere. Note that, since the TEC depends directly on the free electron density, N, it has the same wide variability with such things as time of day and latitude. Values typically range between 10^{16} e^-/m^2 and 10^{18} e^-/m^2. For notational simplicity, N_T is often specified in 'TEC units,' or TECU, where 1 TECU = 10^{16} e^-/m^2. Typical values of N_T then vary between 1 and 100 TECU.

Equation 3.24 is the model used to describe the effects of the ionosphere on VHF radio-wave propagation in most of the rest of this thesis. It is fundamental to this work since it relates a physical quantity, the TEC, to the effects of the ionosphere on the radio-wave signal. The equation is simple and easily inverted, so to the accuracy of the preceding approximations, it can be used to compensate the ionospheric effects on the signal. Since the effects are linear, there is no coupling between frequencies in the signal spectrum. Thus, the corrections are most conveniently made in the frequency domain. If an estimate of TEC is available, either from direct measurement or from modeling, the ionospheric effects can be removed by calculating, then correcting, the observed phase by the amount given in Equation 3.24. Conversely, if additional phase is observed in the radar signal, Equation 3.24 can be used to estimate TEC.

The ionosphere can also be viewed as a filter that disperses the free-space signal. Equation 3.24 then describes that filter as having a transfer function with a $1/f$ phase response.

[6] In the literature, TEC is often used to describe the one-way vertical equivalent of Equation 3.25. Here TEC is used for the integral along the ray path, and vTEC is used for the integral along the vertical path.

The effects of the ionosphere are removed, for this case, by applying the appropriate matched filter—that is, one that has a $-1/f$ phase response.

3.4.2 Ionospheric Group Delay

Another way of characterizing ionospheric effects is with the incremental group delay, described as the additional signal delay caused by the presence of the ionosphere.

For bandlimited signals, the *total group delay* is defined by

$$\tau = -\frac{d\phi(\omega)}{d\omega}, \tag{3.26}$$

where ω is the angular frequency, and $\phi(\omega)$ is the additional signal phase contributed by propagation through the system. Note that this equation gives the signal delay both for waves propagating through a medium and for signals 'propagating' through a circuit.

Group delay is a narrowband concept; if τ is a function of ω, and if the signal bandwidth is too large, the signal is also spread, or dispersed, in time. The bandwidth at which dispersion becomes significant is called the *coherence bandwidth.* An equation for the coherence bandwidth of the ionosphere is derived in the next section.

The *incremental group delay*, $\Delta\tau$, due to the presence of the ionosphere, is then defined as

$$\begin{aligned} \Delta\tau &= -\frac{d\varphi_{\mathrm{i}}(\omega)}{d\omega} \\ &= \frac{2b}{c}\cdot\frac{N_{\mathrm{T}}}{\omega^2} = 0.2689\times 10^{-6}\cdot\frac{N_{\mathrm{T}}}{f^2}, \end{aligned} \tag{3.27}$$

where φ_{i} is the ionospheric phase contribution from Equation 3.24. For propagation through the ionosphere, group delay is an inverse function of frequency. An example of the additional signal delay described by Equation 3.27 is illustrated in Figure 3.2 for an ionosphere having $N_{\mathrm{T}} = 10$ TECU, and for frequencies between 160 and 500 MHz.

For signals having large fractional bandwidths, the ionosphere causes significant spreading. A rough idea of the signal delay, however, can still be obtained from Equation 3.27 by using the center frequency of the signal band. For example, for a 200 to 400 MHz pulse passing through an ionosphere having $N_{\mathrm{T}} = 10$ TECU, Figure 3.2 indicates a 0.30-μs group delay at the 300-MHz center frequency.

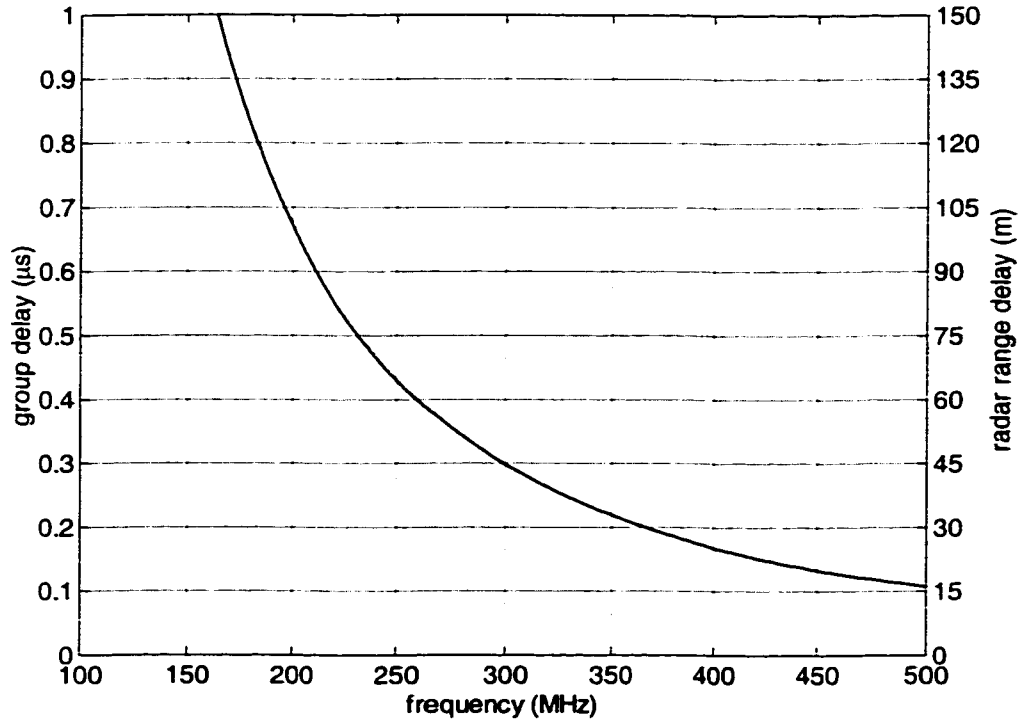

Figure 3.2: Ionospheric group delay for two-way propagation through an ionosphere having a total electron content of 10^{17} e^-/m^2. Group delay, $\Delta\tau$, in microseconds, is given by the left axis, and apparent radar range increase, $c\Delta\tau/2$, in meters, is given by the right axis.

Pulse spreading can be described qualitatively, from an alternate perspective, in terms of the variations in group delay across the pulse's frequency components. That is, the various frequency components of the pulse propagate through the ionosphere in different amounts of time, thus producing pulse spreading. For the 200 to 400 MHz pulse of the previous example, the 200- and 400-MHz frequency components are delayed by 0.67 and 0.17 μs, respectively, so the pulse is spread to a time-width of about $0.67 - 0.17 = 0.5\mu$s. Quantitative calculations of dispersion, however, use the ionospheric phase contribution of Equation 3.24.

For reference, the group velocity, v_g, and group path length, l_g, through the ionosphere, are also derived below. The group velocity is given by

$$v_g = \frac{d\omega}{dk} = \frac{c}{n + \omega \dfrac{dn}{d\omega}}. \tag{3.28}$$

Using n from Equation 3.16,

$$v_g = cn, \tag{3.29}$$

and thus,

$$v_g v_p = c^2, \tag{3.30}$$

where $v_p = c/n$ is the phase velocity. The group path length—the signal transit time multiplied by c—is then

$$\begin{aligned} l_g &= 2\int \frac{c}{v_g} dl, \\ &= 2\int \frac{1}{n} dl \approx 2\int \left(1 + \frac{1}{2}X\right) dl, \end{aligned} \tag{3.31}$$

where the factor of two again accounts for the two-way trip of the radar waveform. The increase in group path length, Δl_g, due to the presence of the ionosphere, is

$$\Delta l_g = -\Delta l_p = \frac{2b}{\omega^2} \cdot N_T, \tag{3.32}$$

where Δl_p is the additional phase path length given by Equation 3.22. Note that the group path length times $1/c$ gives the group delay of Equation 3.27.

As an example of the magnitude of the extra group path length, consider a moderate TEC of 10^{17} e^-/m^2, and a center frequency of 250 MHz. In this case the ionosphere adds 129 m to the group path. The additional path length varies as the inverse square of frequency, so up at the GPS L1 frequency, f_c = 1575.42 MHz, the additional group path is only 1.6 m (divide the result of Equation 3.32 by two for one-way propagation). This is still unacceptable for many GPS applications, and is estimated and removed with a dual-frequency technique similar to the TDOA technique described in Section 3.6.

3.4.3 An Example of Ionospheric Dispersion

An intuitive feel for the character and magnitude of the effects of the ionosphere can be obtained by examining its impulse response. For example, the upper frame of Figure 3.3 is a plot of the response to a 200 to 400 MHz Blackman-windowed 'impulse' for an ionosphere with N_T = 20 TECU. As expected, the ionosphere delays and spreads the impulse. The

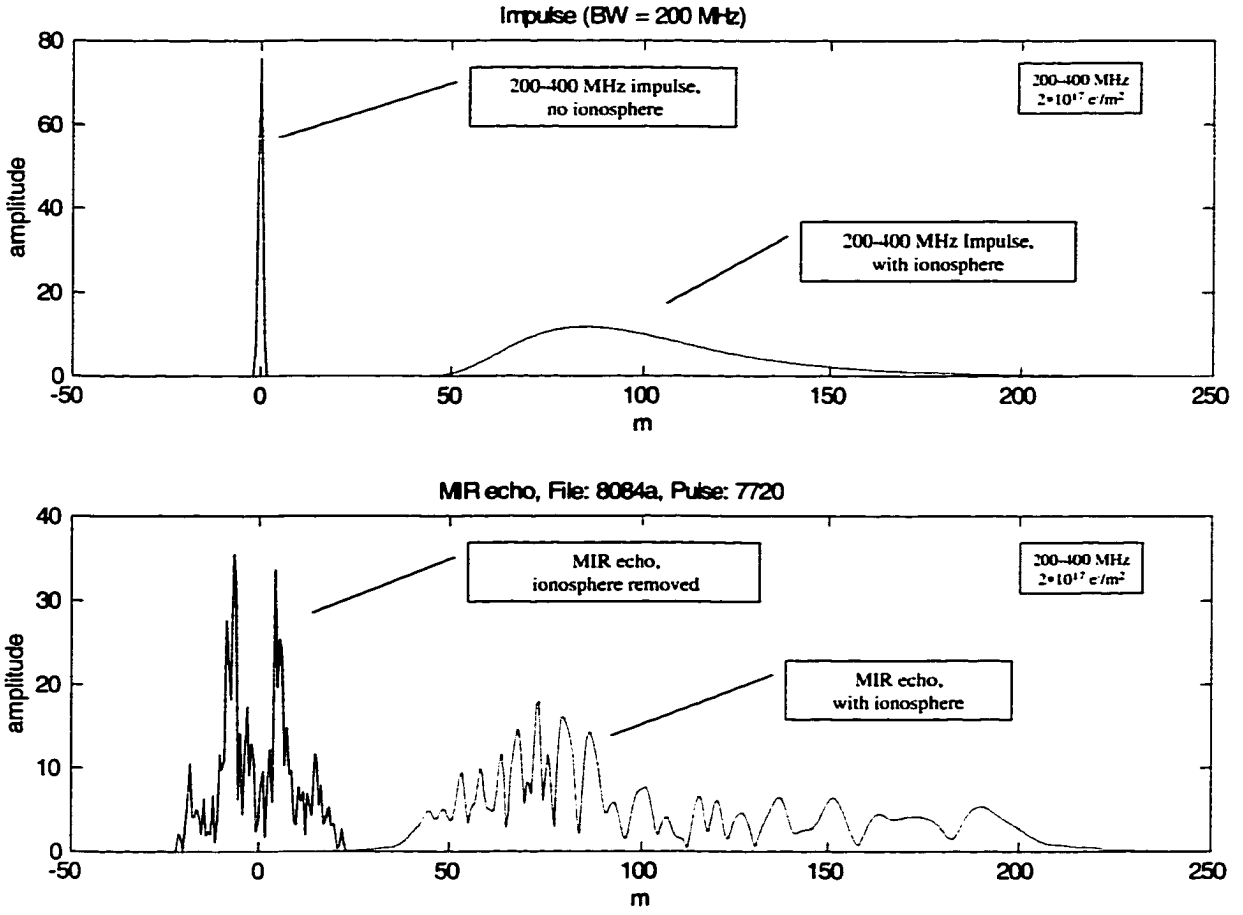

Figure 3.3: An example of ionospheric effects. Signals that propagate through the ionosphere are delayed and dispersed. The upper frame illustrates the effect of the ionosphere on a 200 to 400 MHz Blackman-windowed impulse. The lower frame illustrates the effect on an echo from Mir, pass 8084a. The envelopes of the signals are plotted in terms of radar range ($c\tau/2$). $N_T = 20$ TECU for both frames.

spreading also reduces the peak amplitude. Note that losses are negligible, so both the original and dispersed impulse contain the same energy.

The figure also illustrates pulse spreading in terms of group delay. If the 300-MHz center frequency of the impulse is used in Equation 3.27, a delay of $0.6\mu s$ ($\times c/2 = 90$ m) is obtained. This is a reasonable approximation for the delay to the centroid of the dispersed pulse. Alternatively, Equation 3.27 specifies the delay of any narrow subband in the UWB signal. A subband centered at 400 MHz is delayed by about 50 m, while a subband at 200 MHz is delayed by about 200 m. Thus, in the figure the delays of the 400- and 200-MHz frequency components correspond to the delays to the near and far edges of the dispersed pulse, respectively. The highest frequency components of the transmitted impulse suffer the least delay and are the first to arrive at the receiver.

The lower frame in Figure 3.3 illustrates the effect of the ionosphere on an actual target echo. The signal is an echo from the Mir space station taken from pass 8084a. The parameters are those given in Tables 1.1 and 1.3, and the total electron content of 20.0 TECU is the approximate value observed for that pulse. In the figure, the dispersed pulse is the signal received by the radar, while the pulse labeled 'ionosphere removed' is the result after estimating and compensating the ionospheric dispersion. Again, the ionosphere has delayed and dispersed the pulse resulting in a reduction in peak pulse amplitude. The amplitude of the Mir echo is the output value of the matched filter in uncalibrated units. The amplitude of the impulse in the upper frame was chosen such that the Mir echo and the impulse would have the same total energy. Since ionospheric losses are negligible over the 200 to 400 MHz band, all four curves in the figure have the same energy.

The drop in peak amplitude in Figure 3.3 also illustrates a practical problem. The presence of the ionosphere causes the signal level to drop by about 16 dB for the impulse and by about 8 dB for Mir. Thus, when the SNR of an undispersed signal is less than about 20 dB for Mir—a nominal value for the system parameters listed in Table 1.1—the SNR of the dispersed signal is less than about 12 dB. At that SNR level, the target will be partially obscured by noise. For lower SNR levels, the presence of the ionosphere can cause the received signal to be lost in the noise. This would preclude TEC estimation techniques that rely on observations of the signal, such as the one described in Section 3.6.

3.5 Coherence Bandwidth

The dispersive effects of the ionosphere increase as the signal bandwidth increases and as the center frequency decreases. The bandwidth above which the ionosphere begins to cause significant pulse spreading, called the *coherence bandwidth*, is determined by the nonlinear component of the phase contributed by the ionosphere. Coherence bandwidth can be calculated from the quadratic component of the nonlinear ionospheric phase contribution, given by φ_i in Equation 3.24, since the quadratic component is dominant. The Taylor expansion of $\varphi_i(\omega)$ is

$$\varphi_i(\omega) = \varphi_i(\omega_c) + \varphi_i'(\omega_c) \cdot (\omega - \omega_c) + \frac{1}{2}\varphi_i''(\omega_c) \cdot (\omega - \omega_c)^2 + \cdots, \tag{3.33}$$

where φ_i' and φ_i'' are the first and second derivatives of $\varphi_i(\omega)$ with respect to ω, and ω_c is the band center frequency. Using Equation 3.24,

$$\varphi_i(\omega) = \frac{2bN_T}{c} \cdot \left(\frac{1}{\omega_c} - \frac{(\omega - \omega_c)}{\omega_c^2} + \frac{(\omega - \omega_c)^2}{\omega_c^3} + \cdots \right). \tag{3.34}$$

The coherence bandwidth is determined from the frequency, ω_e, at which the quadratic term in Equation 3.34 reaches a specified threshold, φ_c. That is,

$$\varphi_c = \frac{2bN_T}{c} \cdot \frac{(\omega_e - \omega_c)^2}{\omega_c^3},$$

$$\omega_e - \omega_c = \sqrt{\frac{c\omega_c^3\varphi_c}{2bN_T}},$$

where ω_e is the frequency at the edge of the coherent band. The coherence bandwidth, B_c, is then twice the distance from the coherent band edge to the band center,

$$B_c = \frac{1}{2\pi} \cdot 2(\omega_e - \omega_c)$$

$$B_c = \sqrt{\frac{4\pi c\varphi_c}{bN_T}} \cdot f_c^{3/2}, \tag{3.35}$$

where B_c is given in Hz. The quadratic phase threshold is usually set at $\varphi_c = \pi/4$, so that

$$B_c = \sqrt{\frac{\pi^2 c}{b}} \cdot \sqrt{\frac{f_c^3}{N_T}} = 1364 \cdot \sqrt{\frac{f_c^3}{N_T}}. \tag{3.36}$$

As an example, when $f_c = 300$ MHz and $N_T = 10$ TECU, the coherence bandwidth is $B_c = 22$ MHz. Thus, the presence of the ionosphere has a negligible effect on signal amplitude, for this center frequency and TEC, provided the signal bandwidth is less than about 22 MHz.

For a different perspective, note that *Goodman* (1992, p. 281) defines the coherence bandwidth as the inverse of the channel coherence time; that is, the coherence bandwidth is the bandwidth for which the group delay variation across the band equals the undispersed pulse width. With that definition,

$$\left|\frac{d\tau}{df}\right| \cdot B_c = \frac{1}{B_c}$$

$$B_c = \frac{1}{\left|\frac{d\tau}{df}\right|^{1/2}}, \tag{3.37}$$

where τ is the group delay given by Equation 3.27. Equation 3.37 leads to the same coherence bandwidth as Equation 3.36.

3.6 Total Electron Content from Time-Difference of Arrival

If the received signal has a high SNR, say 15 dB or so, the signal itself can be used to obtain an initial TEC estimate. This is done by measuring the variations in group delay with frequency and relating those differences to TEC through Equation 3.27. In this research, the procedure employed, called the *time-difference-of-arrival* (TDOA) technique, realizes an initial estimate of TEC that is accurate to within about ± 2 TECU.

Engineers have measured the TEC of the ionosphere and the interplanetary medium with this method and another that uses differences in phase velocity for many years (see, *Eshleman et al.*, 1960; *Koehler*, 1968). They have used TDOA technique also to estimate TEC in order to correct ranging errors in satellite tracking (e.g., *Katz et al.*, 1978). Ionospheric delays in GPS signals are estimated with a similar technique (e.g., *Wilson et al.*, 1995).

3.6.1 The TDOA Technique

In the TDOA technique, the UWB target echo received by the radar is first filtered to form two subband signals—one near the low-frequency end of the original band and one near the high-frequency end. The difference in group delay between the two subbands, or time-difference-of-arrival, can be used to estimate the TEC. As in the example in Figure 3.3, the center frequency of any subband of the signal can be used to calculate the approximate delay of that subband. Call the center of the lower subband f_1, and the center of the upper subband f_2. Then,

$$\Delta\tau_1 = \frac{2b}{c(2\pi)^2} \cdot \frac{N_T}{f_1^2}, \tag{3.38}$$

$$\Delta\tau_2 = \frac{2b}{c(2\pi)^2} \cdot \frac{N_T}{f_2^2}, \tag{3.39}$$

where $\Delta\tau_1$ is the additional signal delay caused by the ionosphere at frequency f_1, and $\Delta\tau_2$ is the additional delay at f_2. Again, small differences in refractive effects are neglected, in that it is assumed that all frequency components follow the same path to the target, thereby giving the same TEC values in Equations 3.38 and 3.39. The time delay to the target is measured in each subband signal, then the difference between the two time delay values is related to the TEC by

$$\Delta\tau_1 - \Delta\tau_2 = \frac{2b}{c(2\pi)^2}\left(\frac{1}{f_1^2} - \frac{1}{f_2^2}\right) \cdot N_T,$$

so that

$$N_T = \frac{2c\pi^2}{b} \cdot \frac{f_1^2 f_2^2}{f_2^2 - f_1^2} \cdot (\Delta\tau_1 - \Delta\tau_2). \tag{3.40}$$

Note that it is theoretically possible to estimate TEC from the delay observed in a single subband if the satellite track is known with sufficient accuracy. The radar measures the *apparent* range to the target, R_A, given by

$$R_A = R_t + \frac{c}{2}\Delta\tau, \tag{3.41}$$

where R_t is the free-space distance, and $c\,\Delta\tau/2$ is the extra distance added by ionospheric delay. If the radar has been accurately calibrated, it is possible to make an accurate absolute measurement of R_A. If an accurate satellite ephemeris is also available, then R_t can be

calculated and a single subband could be used to calculate $\Delta\tau$ and, in turn, TEC. Using the difference between two subbands, as in Equation 3.40, removes R_t from the equation, so ephemeris errors and biases in the range measurement are removed. This is usually necessary in practice.

Signal delay measurements can be quite noisy (for reasons discussed below), in which case they must be smoothed before being used in estimating the TEC and its variations across the pass. One possible smoothing procedure is described here. First, the subband delay differences are measured in each pulse. Those differences are used in Equation 3.40 to estimate TEC on a pulse-by-pulse basis. A polynomial is fit to the single-pulse TEC estimates to obtain smoothed estimates. The order of the polynomial is based on the SNR of the signal, the size of the target, and the expected amount of structure in the TEC variations across the pass. Smoothed TEC estimates from the polynomial fit are used to remove ionospheric dispersion from the radar signal by compensating the ionospheric phase contribution given in Equation 3.24. This initial TEC estimate is expected to be sufficiently accurate to allow the bulk of the ionospheric dispersion to be removed from the radar data. If the initial TEC estimate is within, say, $\pm$ 20% of the actual value, the data will have a higher SNR after initial ionospheric compensation, thus enabling more accurate measurements of target range in the subband signals. The procedure can then be repeated, if required, to refine the TEC estimates.

3.6.2 Accuracy of the TDOA Technique

Several conditions limit the accuracy of the TEC estimates obtained with the TDOA technique. For example, the satellite has a finite size, and some point in the finite-length echo needs to be chosen before the delay differences can be calculated. It can be quite difficult to choose the same point in the two subband signals, since the scattering characteristics of actual targets often produce large variations across the spectrum of the received echo. Simply stated, the target can look quite different when two (widely-spaced) subbands are compared. This problem is exacerbated at the low SNRs encountered in this research. To avoid the difficulty in finding matching points in the subband signals, either the peak location or the centroid location in each subband can be used as an estimate of target location. The centroid location has been preferred in this research, but both peak and centroid locations tend to gives noisy measurements of target location since they are both affected by target scattering characteristics and system noise. The differences between the shapes of

the subband echoes could be reduced by choosing subbands that are more closely spaced in frequency, but this would reduce the 'leverage' of the measurement since the delay difference is also reduced.

The 'frequency selectivity' of the target can be characterized by the correlation coefficient of the envelopes of the two subband signals. If the correlation coefficient is high, say greater than 0.8, it is easier to select the same point on the target in both bands. Thus, the band-to-band correlation coefficient indicates the expected performance of the TDOA technique. In the case of Mir, for example, with 40-MHz subbands centered on 250 MHz and 350 MHz, the correlation coefficient is typically less than 0.5, even after ionospheric correction. With the correlation coefficient that low, it is indeed difficult to identify the same point in the two signals.

Another limitation is that the SNR must be large enough for the target to be easily detected above the background noise. If the SNR is less than about 12 dB, it may be possible to see the target but difficult to localize it to anything better than a significant fraction of its range extent.[7] Reducing the SNR increases the variance in the range estimate, independent of whether the target location is determined from the peak or centroid of the echo. If the SNR of the received signal is inadequate, it may be necessary to attempt to bring the signal out of the noise with an independent TEC estimate obtained from some other source, such as GPS or an ionosphere model.

A trade-off is required for the choice of the width of the subbands. A large bandwidth is desirable since it maximizes the resolution in the subband signal. This bandwidth must be sufficiently small, however, to avoid significant pulse spreading, since that results in loss of SNR. If a rough estimate of TEC is available, the coherence bandwidth of Equation 3.36 is a reasonable choice.

Finally, the accuracy of the TDOA technique is limited by the accuracy of the group-delay-difference measurements. Given the difficulties described above, it was expected that the TDOA error would be some significant fraction of the range extent of the target. Experience with this research places that fraction somewhere between about 1/5 and 2/5. For Mir, with subband center frequencies of 250 and 350 MHz, and for a range measurement error of 1/4 of the target's total range extent of about 40 m, Equation 3.40 predicts a TEC estimation error of about 3×10^{16} e^-/m^2.

[7] From Figure 2.7 in *Skolnik* (1981), a 12-dB SNR provides a 97% probability of detection for samples that fall on the target, along with about 0.1% probability of false alarm for the other approximately 32,000 samples in the data record.

The TDOA technique provides an initial estimate of the TEC, which is used to remove the bulk of the ionospheric effects from the radar signal. The residual errors, however, are still much larger than can be tolerated for coherent imaging, and the TEC estimates need to be further refined by the techniques described in Chapters 4 and Appendix B.

3.7 Faraday Rotation

As noted in Section 3.2, the presence of the geomagnetic field makes the ionosphere a birefringent medium, causing the polarization of the transmitted signal to change as the signal propagates through the ionosphere. As mentioned earlier, waves incident on the ionosphere are 'split' into two characteristic modes: the ordinary and extraordinary waves. The two modes have opposite polarizations—for QL propagation, the characteristic polarizations are circular, and for QT they are linear. The two components propagate with slightly different phase velocities, resulting in a phase path difference along the same geometric path. This causes the total signal polarization to change gradually as the wave propagates through the ionosphere. The difference in phase path can be used to calculate the net polarization of the total signal at the receiver or at any point along the ray path.

The difference in phase path is calculated by including the magnetic field effects from Equation 3.11 in the phase path length, Equation 3.22. The *differential phase path length* is

$$\Delta l_{\mathrm{p,O}} - \Delta l_{\mathrm{p,X}} = \int (n_{\mathrm{O}} - n_{\mathrm{X}}) dl, \tag{3.42}$$

where the integral is over the ray path, and where n_{O} and n_{X} are the refractive indices for the O and X modes, and $\Delta l_{\mathrm{p,O}}$ and $\Delta l_{\mathrm{p,X}}$ are the ionospheric contributions to the phase path for the O and X modes. Equation 3.42 applies to one-way propagation, so the factor of two in Equation 3.22 has been dropped. Note that at VHF the birefringence is weak, so the difference in angle between the ray and the wave-normal is small and, therefore, can be ignored.

For QL propagation, the differential phase path length is calculated by using Equation 3.14 in Equation 3.42. After dropping higher-order terms,

$$\Delta l_{\mathrm{p,O}} - \Delta l_{\mathrm{p,X}} = \int XY \cos\Theta dl,$$

$$= \int \frac{\omega_N{}^2 \omega_H \cos\Theta}{\omega^3} dl,$$

$$= \frac{2be}{m} \cdot \frac{1}{\omega^3} \cdot \int NB \cos\Theta dl. \tag{3.43}$$

The polarization change can be determined from the difference in phase path length, and related to the rotation of the semi-major axis of the polarization ellipse. For QL propagation, for example, linearly polarized (LP) waves are decomposed into LCP and RCP components on entering the ionosphere. The differing phase velocities of the two components cause the plane of polarization—the semi-major axis of the polarization ellipse—of the original wave to rotate. The total rotation of the polarization plane, called the *Faraday rotation*, is equal to half the difference between the total rotations of the **E** field vectors of the two circularly polarized components. The Faraday rotation, Ω, in radians, is given by

$$\Omega = \frac{k}{2} \left(\Delta l_{p,O} - \Delta l_{p,X} \right). \tag{3.44}$$

Using Equation 3.43,

$$\Omega = \frac{be}{cm} \cdot \frac{1}{\omega^2} \cdot \int NB \cos\Theta dl, \tag{3.45}$$

where positive Faraday rotation is in the direction of rotation of the ordinary wave.

For QT propagation, the two characteristic modes are linearly polarized—one parallel to the geomagnetic field, the other perpendicular. Other polarizations, including LP with a polarization angle neither parallel nor perpendicular to the geomagnetic field, are decomposed into the characteristic modes, which again propagate with slightly different phase velocities. In this case, if the original wave is LP, the phase velocity difference causes the polarization to change from linear to elliptical and eventually to circular. The polarization change continues back through elliptical to linear of the opposite sense. The rotation of the semi-major axis of the polarization ellipse is also given by Equation 3.44. Using Equations 3.12 and 3.13, and dropping higher-order terms,

$$\Omega_{QT} = \frac{\pi}{\lambda} \int \frac{XY^2 \sin^2\Theta}{2} dl = \frac{\pi}{2\lambda} \int \frac{\omega_N{}^2}{\omega^2} \cdot \frac{\omega_H{}^2 \sin^2\Theta}{\omega^2} dl,$$

$$= \frac{be^2}{2cm^2} \cdot \frac{1}{\omega^3} \cdot \int NB^2 \sin^2\Theta dl, \tag{3.46}$$

where Ω_{QT} is the rotation angle of the semi-major axis of the polarization ellipse for QT propagation. For a wave that is originally LP, the semi-major axis rotates through $\pi/2$ radians as the polarization changes from linear to circular. An additional $\pi/2$ rotation changes the polarization back to linear, but orthogonal to the original polarization.

Polarization rotation is much smaller for QT propagation than for QL. This is illustrated by comparing Equations 3.45 and 3.46. They differ by a factor that is equal to the integral of $Y/2\cos\Theta$. Since $Y \sim 1/100$ at VHF, $\Omega \gg \Omega_{QT}$.

For pass 8084a, the Faraday rotation is estimated to have a maximum value of about one radian at the beginning of the pass for the 300-MHz center frequency. This gradually drops to near zero late in the pass as propagation passes through QT. In the region of transition from QL to QT, and in the region of QT propagation, the polarization rotation amounts to no more than a fraction of a degree. At VHF, polarization rotation is only significant during QL propagation.

It should be pointed out that Faraday rotation is a narrowband concept. For the UWB signals used here, the $1/f^2$ dependence in Equation 3.45 can give a wide range of rotation angles over the signal band. At the start of pass 8084a, for example, the Faraday rotation is about 2 radians at the lower band edge (200 MHz), and about 0.5 radians at the upper band edge (400 MHz).

Faraday rotation is an issue for linearly polarized transmitter and receiver systems, whether those systems are used for radar, communications, or radio astronomy. Also, fully-polarimetric radar systems must account for Faraday rotation in order to calculate the target scattering matrix. In the experiments performed for this research, however, the Faraday rotation problem is avoided by using circular polarization. The transmitted waveform is RCP, a characteristic mode for QL propagation. During the occasional short periods during which propagation passes through QT, the difference in phase path length for the two LP characteristic modes is negligible, so the RCP polarization of the transmitted waveform is essentially preserved in propagation through the ionosphere at all angles.

3.8 Ionospheric Irregularities

Spatial variations, or irregularities in electron density are often severe enough to have significant deleterious effects on transionospheric signal propagation. These effects, referred

to as *ionospheric scintillation*, include phase fluctuations, fading and enhancement of amplitude, and refractive bending. A detailed discussion of the effects and their sources is given in *Aarons* (1982). More-recent discussions of specific aspects, along with references to historical and technical details, are given in *Basu et al.* (1996) and *Groves et al.* (1997).

Ionospheric irregularities, which are driven by several processes, occur over a wide range of scale lengths, extending from meters to thousands of kilometers. Diurnal variations in production rate, for example, create features with scale lengths of hundreds to thousands of kilometers. Oscillations in the neutral atmosphere can also produce features having scales of hundreds of kilometers. One source is acoustic gravity waves from tropospheric weather fronts. These waves grow in amplitude as they propagate upward due to decreasing air density. As they propagate through the ionosphere, they modulate the ionospheric layers. This type of wave is an example of a *traveling ionospheric disturbance*, or TID (*Nagpal*, 1983). Features having scale lengths of less than 100 km are primarily generated by ionospheric dynamics, that is, motion of the plasma. The drivers include, for example, magnetic storms, upper atmospheric weather, and the solar wind. At the smaller scales, gravity-driven convection can cause 'bubbles' of lower-density plasma to rise through the equatorial ionosphere and spread along field lines. These regions are tens to hundreds of kilometers in extent, but edge structure can have transient features down to meter scales. The smaller irregularities are of special concern, because they are the cause of scintillation at VHF.

From a statistical perspective, the spatial variations have a power spectral density (PSD) that is *power law*. They exhibit *outer-scale* and *inner-scale* cutoff frequencies—just as Kolmogorov theory predicts for turbulent media (*Kolmogorov*, 1941). According to *Kelley* (1989, p. 142), experimental data have indicated that the power law exponent is usually about $-5/2$, and approaches the Kolmogorov value of $-5/3$ only during periods of 'strong plasma turbulence.' The 'energy' in the variations of the electron density then follows a $Ck^{-2.5}$ form, where k is the *spatial* wavenumber of the variation, and C is the turbulent strength scaling factor. Other work has found that the PSD is more accurately modeled with two distinct scale regions having different power-law exponents (*Rino*, 1982; *Basu et al.*, 1983).

Spatial variations in electron density produce spatial variations in the refractive index, making the ionosphere an inhomogeneous propagation medium. For the purposes of analyzing the effects on radio waves, the medium is often modeled as a phase screen (*Rino*, 1979a,

1979b). Large-scale structures cause ray bending along with changes in the phase and group path lengths. Sufficiently intense small-scale structures produce multipath effects, leading to the large fluctuations in signal amplitude and phase referred to as scintillation. Quantitatively, scintillation occurs when the phase variations induced by ionospheric irregularities approach one radian over the Fresnel zone radius of the ray. For radio stars and geostationary satellites, the Fresnel zone radius is given by $R_f = \sqrt{R_1 \lambda}$, where R_1 is the distance from the irregularity to the receiver. This equation applies to plane wave signals, incident on the ionosphere from above, and received on the ground. From the above considerations, scintillation characteristics depends on the size and severity of the irregularities, the distance to the irregularities, and the frequency of the wave.

Two factors combine to make scintillation more common and more severe at lower frequencies. First, the ionospheric phase contribution of Equation 3.24 is inversely proportional to frequency ($\varphi_i \sim 1/f$). Second, the Fresnel zone radius is inversely proportional to the square root of frequency. For sufficiently low frequencies, any of the irregularity sources listed above could cause scintillation. At VHF, however, the Fresnel zone radius is small enough that only small-scale irregularities due to ionospheric instability provide the necessary size and amplitude of variations. At equatorial latitudes, the dynamics are such that this occurs frequently in the hours between sunset and midnight. At mid-latitudes, the irregularities are less severe and scintillation at VHF is less common.

For sources at altitudes less than about 10,000 km, the Fresnel zone radius is given by

$$R_f = \sqrt{\frac{R_1 R_2}{R_1 + R_2} \lambda}, \tag{3.47}$$

where R_1 is the distance from the ground to the irregularity, and R_2 is the distance from the irregularity to the source. This equation also applies to radar targets in and above the ionosphere. The maximum Fresnel zone radius occurs at the point midway between the radar and target. At the midway point, $R_f = \sqrt{R_t \lambda}/2$, where R_t is the distance from the radar to the target. For pass 8084a, Mir is at an altitude of 378 km, giving a maximum Fresnel zone radius, at 300 MHz, of 300 to 400 m, depending on elevation angle. From Equation 3.24, a 1-radian phase variation requires a TEC variation of about 2×10^{14} e$^-$/m^2. For the measured TEC of 10^{17} e$^-$/m^2, that corresponds to a variation of 1 part in 500, or about 0.2%. Given that the thermal velocity of electrons at that altitude is about 100 km/s and the mean free path is several hundred meters, the density variations over 300 m are

usually less than 0.2%. Naturally, the whole story is much more complicated, depending also on, for example, electron gyro-motion and diffusion. Also, note that the Fresnel zone radius is less than 300 m over most of the path, so the electron-density variations needed to produce scintillation would be somewhat higher than the 0.2% calculated above. Except for periods of high instability, then, significant scintillation is not expected in the Mir echo.

For comparison, consider a satellite at an altitude of 700 km, and a radar frequency of 150 MHz. The maximum Fresnel zone radius becomes 600 m, and the TEC variation for one radian of phase is about 1×10^{14} e^-/m^2. Also, the higher altitude gives a larger TEC so the relative variation is more like 1 part in 2000. In this case, scintillation will be much more common. Again, scintillation decreases as the satellite altitude decreases and as the frequency increases.

When spatial variations cause phase variations of less than a radian over a Fresnel radius, the amplitude of the wave is essentially unaffected, but the ray undergoes angle-of-arrival variations due to refraction. As long as the total bending is less than the beamwidth of the radar antenna, the received signal does not exhibit fading. At 300 MHz, this is never a problem since the beamwidth of the 150-ft dish is about 1.5 degrees and the variations in angle-of-arrival are typically no more than a few hundredths of a degree. These 'low-level irregularities,' however, still present a problem for imaging, since they can cause relatively rapid TEC and phase variations across the aperture. If the variations are too rapid, the autofocus TEC polynomial is not able to provide an adequate fit, leaving residual cross-range phase variations in the data—resulting in a defocused image.

3.9 Radar Signal Polarization

The two satellite ISAR systems used in this research, one at Stanford, California, the other at Ascension Island, United Kingdom, use antenna feeds that provide right-hand circular polarization for transmit and left-hand circular polarization for receive. For QL propagation, these circular polarizations are the characteristic modes, so polarization is preserved in propagation to and from the satellite. For QT propagation, however, the circularly-polarized transmitted signal is decomposed into linearly-polarized (LP) components on entering the ionosphere. From Equation 3.46, the differential phase of the two LP components is usually less than 1 degree, so again, the circular polarization of the total signal is preserved.

For the characteristic modes, the ionospheric phase contribution depends on whether the wave is ordinary or extraordinary. At Ascension Island, the geomagnetic dip angle is small, so $\Theta < 90°$ when looking north, and $\Theta > 90°$ when looking south with respect to the geomagnetic equator. Thus, the transmitted signal is generally ordinary when looking south and generally extraordinary when looking north. At Stanford, the dip angle is about 60 degrees, so the transmitted signal is ordinary except when looking north at low elevation angles.

The characteristic mode of the received signal is the same as that of the transmitted signal. As an example, consider the case where the Stanford radar tracks a satellite that is south of the site. The RCP transmitted signal is ordinary. The signal scattered from the satellite contains both RCP and LCP components. The opposite-sense component of the scattered signal, in this case LCP, is usually much stronger than the same-sense component.[8] Consequently, the radar receives the opposite-sense component. The LCP component of the scattered signal travels in the opposite direction to that of the RCP incident signal, so it also is ordinary. This is a general result; if the transmitted and received signals are opposite-sense circularly polarized, they are either both O or both X.

In reality, antennas and feeds do not have perfect polarization isolation, and a small amount of the opposite polarization leaks into both the transmitted and received signals. This produces three small undesired components in the total received signal:

i) RCP transmitted, same-sense scattered, RCP received,

ii) LCP transmitted, same-sense scattered, LCP received, and

iii) LCP transmitted, opposite-sense scattered, RCP received.

The undesired components are all expected to be much smaller than the primary signal—RCP transmitted, opposite-sense scattered, LCP received. The first component, for example, is lower than the primary signal by the sum of the polarization isolation and the ratio of the target's opposite-sense to same-sense RCS. It is extraordinary during propagation back to the radar, and thus experiences a different phase delay than the primary signal. Because of the differences in phase delay, the three components are not coherent with the primary

[8]The scattering matrix depends on the shape and composition of the target. There are ranges of aspect angles for many targets for which the same-sense circularly polarized component of the scattered signal is larger than the opposite-sense component.

signal. Consequently, their presence in the total received signal increases the clutter in the final image.

Note that a small amount of mode conversion is also produced by the ionosphere. At VHF, this effect is much smaller than the antenna polarization isolation, except possibly when transitioning from QL to QT along the signal path. Mode conversion in the ionosphere is a higher-order effect, and is insignificant for the imaging problem considered here (see also *Ratcliffe*, 1959, p. 176).

Chapter 4

The Effects of the Ionosphere on Radar Imaging

The ionosphere can produce significant detrimental effects in the quality of a radar image, especially at frequencies below about 2 GHz. In this chapter, those effects are analyzed by considering the phase contributed by the ionosphere to the individual radar echoes. The effects are characterized by quantifying their impact on range resolution, cross-range resolution, and the system point spread function.

If ionospheric TEC can be estimated with sufficient accuracy, ionospheric effects can be removed from the radar data. A method for using the radar image to refine the TEC estimates to the requisite accuracy is described in this chapter, and its expected performance is calculated.

Two issues determine the lowest frequency for which the equations and techniques presented here are valid. First, the $1/f$ model for the ionospheric phase contribution is only an approximation. Second, refraction causes bending of the ray. The limitations imposed by these items are evaluated, and enhancements of the model are suggested for extending coverage to yet lower frequencies.

4.1 Phase Errors

A number of error sources contaminate the radar data and degrade image quality. Of those, the phase error introduced into the radar signal by the ionosphere is the major concern of this research. However, some of the other error sources that affect ISAR satellite imaging

are introduced first in this section in order to compare and contrast their effects with those of the ionosphere.

Error sources include any aspects of the overall system that differ from the imaging model. In this research, the imaging algorithm is implemented for the radar/target geometry described in Chapter 2. The imaging model makes several assumptions including (1) the radar and target are separated by a fixed distance, (2) the target rotates in a plane between pulses as though it were mounted on a turntable, (3) the signal propagates in free space, and (4) the distance between radar and target is sufficiently large to treat the wavefronts as planar over the cross-range extent of the target. Any aspects of actual observations that do not match this idealized model need to be compensated or they degrade image quality.

More specifically, coherent imaging relies on the ability to reconstruct the phase history of all points on the target over the observation period. Anything that alters that phase history from what is modeled in the imaging code degrades the quality of the final image. Possible causes of such phase alterations include dispersion in the medium and errors in the estimate of target trajectory, as discussed above. Exactly how the unmodeled phase alterations, called the phase errors, affect the image depends on their magnitude and functional form. In terms of magnitude, for example, to avoid loss in image quality, phase errors at all frequencies should be kept to less than about $\pi/4$ radians, or about 1/8 of the wavelength of the illuminating energy. Also, the functional form can have both frequency and time dependence. If the phase errors vary with frequency but are constant in time, they primarily affect the range resolution of the system. If there is a slow-time variation in the phase errors—that is, with features having scales comparable to the target observation period—the cross-range resolution is degraded as well. The *acceptable* level of phase error in any specific situation, however, depends on the specifications given for image resolution and sidelobe levels.

For satellite imaging at VHF, most differences between the imaging model and the actual data are accurately characterized as frequency-dependent phase errors. These phase errors come from a number of sources, including:

i) system dispersion,

ii) errors in estimation of the target track,

iii) errors in estimation of the target rotation, and

iv) ionospheric dispersion.

Most ISAR and SAR systems need to deal with the first three items, while the fourth is new to this research.

Phase errors caused by system dispersion, the first item in the list, primarily degrade range resolution. Radar systems are usually designed to minimize system dispersion, and residual errors can often be removed, or at least reduced, by calibration and compensation during data processing.

Phase errors associated with uncompensated motion, the second and third items in the list, primarily degrade cross-range resolution. The motion of the target with respect to the radar is estimated from the target ephemeris, then refined with range measurements from the radar data (see Section B.2.3). Range variations are removed with the motion compensation technique of Section 2.4, while target rotation is accounted for in the imaging code. Motion estimation errors, both range and rotation, produce phase errors that vary across the aperture. At moderate error levels of less than about two radians, the primary effect is degradation of the cross-range resolution. More severe errors can destroy the image. In the past, autofocus techniques have been used to refine the motion estimates and reduce these phase errors to acceptable levels.

Ionospheric dispersion, the fourth item in the list, degrades both range and cross-range resolution, because the ionospheric phase contribution is both frequency dependent and space-and-time dependent. Range resolution is degraded by the nonlinear frequency dependence of the $1/f$ phase contribution. That phase contribution varies through the pass since the radar looks through different parts of the ionosphere with each pulse. The phase variations across the aperture degrade cross-range resolution in much the same way as motion estimation errors. The impact of the ionospheric phase contribution is somewhat different in each direction, so the range and cross-range effects are discussed separately in the next two sections.

The effects of the ionosphere on a radar signal are characterized by the ionospheric phase contribution given in Equation 3.24, which can be written as

$$\varphi_{\mathrm{i}}(\omega; s) = \frac{2b}{c} \cdot \frac{1}{\omega} \cdot N_{\mathrm{T}}(s), \tag{4.1}$$

where another independent variable, s, or time in the pass, has been added to emphasize the pulse-to-pulse variations in TEC.[1] The time variable, s, is also called 'slow-time' since

[1]Other parameterizations, such as aspect angle, θ, could be used instead of time in the pass, s, in which case the ionospheric phase contribution would be written as $\varphi_{\mathrm{i}}(\omega; \theta)$. Slow-time is used in Equation 4.1,

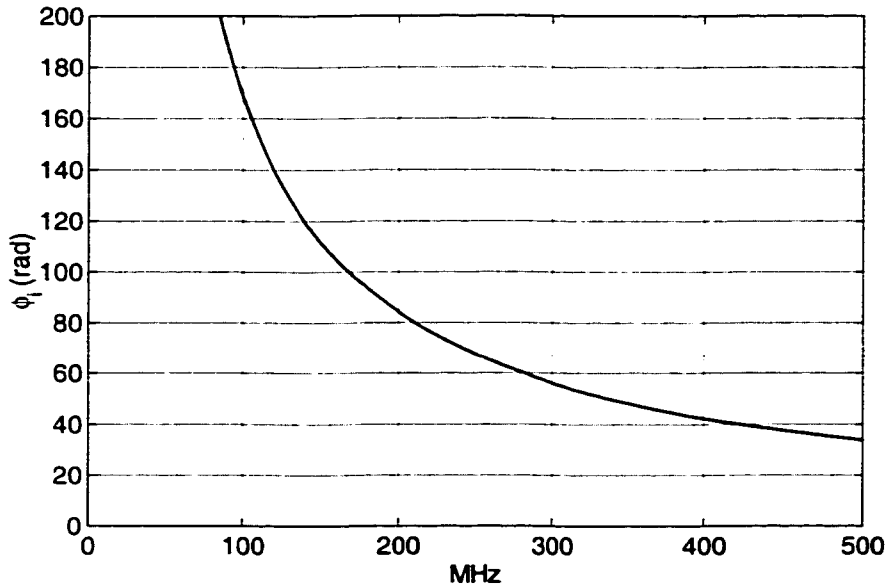

Figure 4.1: Ionospheric phase contribution. Ionospheric dispersion can be characterized by a nonlinear frequency-dependent phase contribution. This plot illustrates the phase contribution for two-way propagation through an ionosphere having a one-way TEC of $10^{16}\,\mathrm{e}^{-}/\mathrm{m}^2$.

it is used to parameterize processes that occur at time scales comparable to the target observation period. In contrast, 'fast-time' processes occur at time scales comparable to $1/B$, the time resolution of the system.

Equation 4.1 is the model used in this work to describe the effects of the ionosphere on VHF radio-wave propagation. It is plotted in Figure 4.1 for a total electron content of 1 TECU. Note that even for this low TEC level, the figure indicates that the ionosphere adds many tens of radians of phase to the signal through the VHF range.

In the following discussions, *ionospheric phase error* refers to the residual phase after estimating TEC and removing the phase specified by Equation 4.1. The degree to which ionospheric phase contributions can be removed, and thus the level of the ionospheric phase error, depends on how accurately TEC can be estimated for use in the $1/f$ phase correction and how well the model fits the real-world situation.

The model for ionospheric effects given by Equation 4.1 is valid as long as the approximations made in its derivation are sufficiently accurate. The accuracy of those approximations

because the radar operates at a constant pulse repetition frequency, producing pulses that are evenly spaced in s.

depends on frequency, bandwidth, and the shape of the electron-density profile along the ray path. Two items limit the applicability of the model: the simplification of the refractive index formula, and ray bending. If these turn out to be significant, the model could be enhanced to cover a wider range of system and ionospheric situations, albeit with an increase in computational complexity.

The simple form of Equation 4.1 was obtained from the Appleton-Hartree formula, Equation 3.11, by discarding higher-order terms. The significance of the discarded terms is evaluated in Section 4.6.

To this point ray bending has been neglected, and it has been assumed that all frequency components of the transmitted signal follow the same ray path to the target. This is an approximation, since the refractive index is frequency-dependent. The implications of a frequency-dependent ray path are analyzed in Section 4.7.

As a rough guideline, the analysis in later sections of this chapter, plus experience to date, suggest that the $1/f$ phase model is valid for UWB signals with frequencies greater than about 150 MHz and with typical ionospheric profiles having TECs of up to about $5 \times 10^{17} e^{-}/m^2$.

4.2 Effect of the Ionosphere on Range Resolution

The radar signal is dispersed during propagation through the ionosphere on its way to the target, and then further dispersed on its way back to the radar. The received signal is compressed with a matched filter—that is, one whose response is 'matched' to the transmitted signal. Ionospheric dispersion, however, causes a mismatch between the phase characteristics of the received signal and those of the filter, thus blurring the output of the matched filter.[2][3] The characteristics of that blurring and the associated signal delay have been well understood for some time, and are described, for example, in *Brookner* (1965).

Pulse compression in a matched filter can be described in terms of impulse synthesis. The individual frequency components of the received signal are given an appropriate phase

[2] As previously mentioned, this research deals with ionospheric conditions for which amplitude scintillation is negligible—that is, the presence of the ionosphere does not affect the amplitude of the spectral components of the signal.

[3] The dispersive effects of the ionosphere could be included in a *generalized* matched filter that would simultaneously compress the transmitted waveform and compensate the ionospheric dispersion. For practical reasons, the two steps are performed separately in this work (see Appendix B for implementation details). The received signal is initially passed through a matched filter to compress the transmitted waveform, then later iteratively compensated for ionospheric dispersion.

correction, and then added to obtain the range-compressed output signal. Errors in the phase correction due to, say, errors in the knowledge of the exact form of the transmitted waveform, result in a failure of the matched filter to achieve the intended optimal compression. The additional phase added by the ionosphere degrades performance in a similar manner.

The final shape of the system impulse response depends on the functional form of the total phase error—the sum of the phase errors from all sources—across the frequency band. For example, a phase error that varies linearly with frequency causes the system output signal to be shifted in time, while one that varies nonlinearly with frequency causes the signal to change shape. (In this discussion, the phase errors are considered in the frequency domain alone—not in the time domain. Thus, the phase errors appear in the system transfer function, thereby degrading the system impulse response.)

Phase errors that have a nonlinear frequency dependence can be expanded in a Taylor series and analyzed in terms of their monomial components. The quadratic component, for example, causes mainlobe broadening, referred to here as *blurring* or *pulse spreading.* Higher-order monomial components are associated with larger sidelobe levels. Other expansions of the phase error function are also useful. Phase errors that vary sinusoidally across the frequency band, for example, introduce paired sidelobes whose levels are determined by the amplitude of the phase-error sinusoid and whose distances from the mainlobe are determined by the 'frequency' of the phase-error sinusoid. In general, phase errors that vary nonlinearly with frequency spread the energy from the ideal impulse response into a wider mainlobe and higher sidelobes. Targets in the image then suffer a loss in range resolution and amplitude, and an increase in sidelobe and artifact levels. *Cook and Bernfeld* (1993) give a detailed discussion of the effects of phase errors on the pulse-compression process, along with illustrations of the resulting pulse shapes.

The quadratic component of the nonlinear phase error usually has the largest effect on the resolution, primarily because it usually contains more energy than the higher-order components. As a result, resolution degradation due to phase errors is often analyzed in terms of the quadratic component of the total error. Blurring starts to become significant when the quadratic component of the phase error reaches about $\pi/4$ radians at the edge of the frequency band of the signal (see *Cook and Bernfeld*, 1993).

With an initial estimate of TEC, the bulk of the ionospheric phase contribution can be removed, after which the phase error is due to the *residual TEC*, the difference between

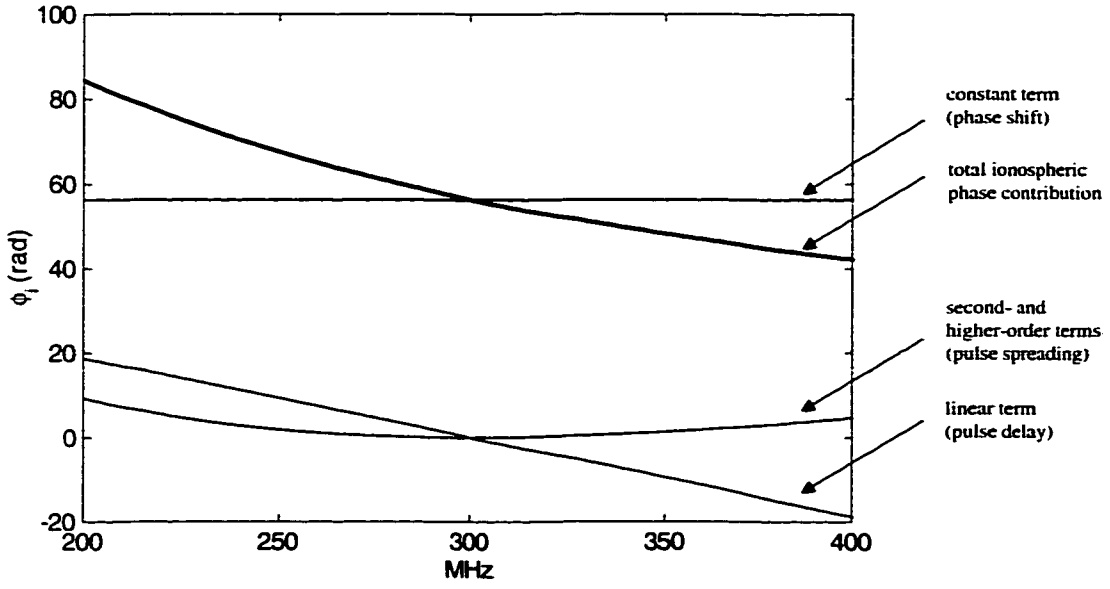

Figure 4.2: Expansion of the ionospheric phase contribution about $f_c = 300$ MHz for $N_T = 10^{16}\,e^-/m^2$. Broadening of the mainlobe in the impulse response starts to become significant when the nonlinear terms reach about $\pi/4$ radians at the band edge. Even at the 1.0 TECU level illustrated in the figure, the nonlinear phase terms reach several radians at the band edge, causing significant spreading of 200-MHz bandwidth pulses.

the true and estimated values. If the quadratic component of the phase produced by the residual TEC is less than $\pi/4$ radians at the edge of the band, the residual ionospheric effects are negligible with regard to pulse spreading.

The range-direction effects of ionospheric phase due to residual TEC can be analyzed by expanding the phase function about the center frequency in the signal band, ω_c. From Equations 3.33 and 4.1,

$$\varphi_i(\omega; s) = \frac{2bN_T(s)}{c} \cdot \left(\frac{1}{\omega_c} - \frac{(\omega - \omega_c)}{\omega_c^2} + \frac{(\omega - \omega_c)^2}{\omega_c^3} + \sum_{n=3}^{\infty} \left((-1)^n \frac{(\omega - \omega_c)^n}{\omega_c^{n+1}} \right) \right). \quad (4.2)$$

This function is plotted in Figure 4.2 across the 200 to 400 MHz frequency band for an ionosphere of 1.0 TECU. The constant term, linear term, and combined second- and higher-order terms of the expansion are also plotted.

The constant term in the expansion merely adds a constant phase to the filter output. It does not spread the pulse in the range direction, but Section 4.3 shows that it is the largest contributor to spreading in the cross-range direction, as it is not constant in slow-time.

The linear term causes the output to be shifted by the group delay at the center frequency,

$$\Delta\tau = -\left.\frac{d\varphi_{\mathrm{i}}}{d\omega}\right|_{\omega_{\mathrm{c}}} = \frac{2bN_{\mathrm{T}}}{c}\cdot\frac{1}{\omega_{\mathrm{c}}^2}. \tag{4.3}$$

This is the often-quoted $1/f^2$ group delay of the ionosphere. As an example of its magnitude, with $f_{\mathrm{c}} = 300$ MHz and $N_{\mathrm{T}} = 10^{17}\mathrm{e}^-/\mathrm{m}^2$, the group delay is about 300 ns.

The quadratic and higher-order terms blur the output. The amount of blurring can be determined from the values of the terms at the edge of the band. At the upper band edge, the expansion of the ionospheric phase contribution can be written as

$$\varphi_{\mathrm{e}} = \frac{2bN_{\mathrm{T}}}{c}\cdot\frac{1}{\omega_{\mathrm{c}}}\cdot\left\{1-\left(\frac{\omega_{\max}-\omega_{\mathrm{c}}}{\omega_{\mathrm{c}}}\right)+\left(\frac{\omega_{\max}-\omega_{\mathrm{c}}}{\omega_{\mathrm{c}}}\right)^2+\cdots\right\}, \tag{4.4}$$

$$\varphi_{\mathrm{e}} = \frac{bN_{\mathrm{T}}}{\pi c}\cdot\frac{1}{f_{\mathrm{c}}}\cdot\left\{1-\left(\frac{B_{\mathrm{F}}}{2}\right)+\left(\frac{B_{\mathrm{F}}}{2}\right)^2+\cdots\right\}, \tag{4.5}$$

where $\omega_{\max}$ is the maximum angular frequency in the band, and B_{F} is the fractional bandwidth defined in Equation 2.16.

The relative importance of the cubic and higher-order terms can then be determined by comparing their phase contributions at the band edge to those of the quadratic term. The ratio of the magnitude of the cubic term to the quadratic term is

$$\left|\frac{\varphi_{\mathrm{e3}}}{\varphi_{\mathrm{e2}}}\right| = \frac{(f_{\max}-f_{\mathrm{c}})}{f_{\mathrm{c}}} = \frac{B_{\mathrm{F}}}{2}, \tag{4.6}$$

where φ_{e2} is the quadratic term, φ_{e3} is the cubic term, and $f_{\max}$ is the maximum frequency. For example, with $f_{\mathrm{c}} = 300$ MHz and $B = 200$ MHz, the cubic component of the phase at the band edge is 1/3 that of the quadratic component. This example indicates that, for UWB signals, the cubic and higher-order terms may account for a significant part of the total phase error. However, once TEC has been estimated sufficiently well to mitigate the quadratic term, all higher-order terms become proportionally smaller and less significant. Also, note that phase errors larger than $\pi/4$ can be tolerated at the band edge for the cubic and higher-order terms before spreading becomes significant. For the quadratic term, the phase error should be less than about $\pi/4$ at the band edge, while for the cubic term that limit is about $\pi/2$. Thus, as suggested above, performance can be analyzed by consideration of the quadratic term alone.

For the quadratic phase term, φ_{e2}, to be less than $\pi/4$ at the band edge,

$$|\varphi_{e2}| = \frac{bN_T}{\pi c} \cdot \frac{1}{f_c} \cdot \left(\frac{B_F}{2}\right)^2 < \pi/4. \tag{4.7}$$

This can be interpreted as a limit on the residual TEC. First, note that the quadratic phase term, and thus pulse spreading, is proportional to the square of the fractional bandwidth and inversely proportional to the center frequency—both factors conspiring to degrade range resolution for VHF UWB signals. For negligible spreading, the maximum residual TEC is then given by

$$\begin{aligned} N_T &< \frac{\pi^2 c}{b} \cdot \frac{f_c}{B_F^2}, \\ N_T &< 1.86 \times 10^6 \cdot \frac{f_c}{B_F^2} = 1.86 \times 10^6 \cdot \frac{f_c^3}{B^2}. \end{aligned} \tag{4.8}$$

This equation specifies the accuracy required in the TEC estimate to achieve full range resolution. It is plotted in Figure 4.3, as a function of bandwidth, for several center frequencies between 100 and 1000 MHz. Equation 4.8 can also be derived from the coherence bandwidth, Equation 3.36, by making the coherence bandwidth, B_c, equal to the system bandwidth, B, and then solving for N_T.

To illustrate the sensitivity of range resolution to residual TEC, consider the system parameters of Table 1.1. For the center frequency, $f_c = 300$ MHz, and the bandwidth, $B = 200$ MHz, the residual TEC must be less than about $1.3 \times 10^{15}\,\mathrm{e^-/m^2}$ to realize full range resolution. Note that the sensitivity to ionospheric effects decreases as the bandwidth decreases and as the frequency increases.

The finest-possible range resolution, as limited by residual TEC, is calculated by using the coherence bandwidth, Equation 3.36, in the range-resolution formula, Equation 2.3, giving

$$\delta x_r \geq \frac{\sqrt{bc}}{2\pi} \cdot \sqrt{\frac{N_T}{f_c^3}} = 1.099 \times 10^5 \cdot \sqrt{\frac{N_T}{f_c^3}}, \tag{4.9}$$

where '$\geq$' indicates that the system bandwidth must also be sufficient to support the specified resolution. From Equation 4.9, the finest-possible range resolution is limited by the residual TEC and the center frequency.

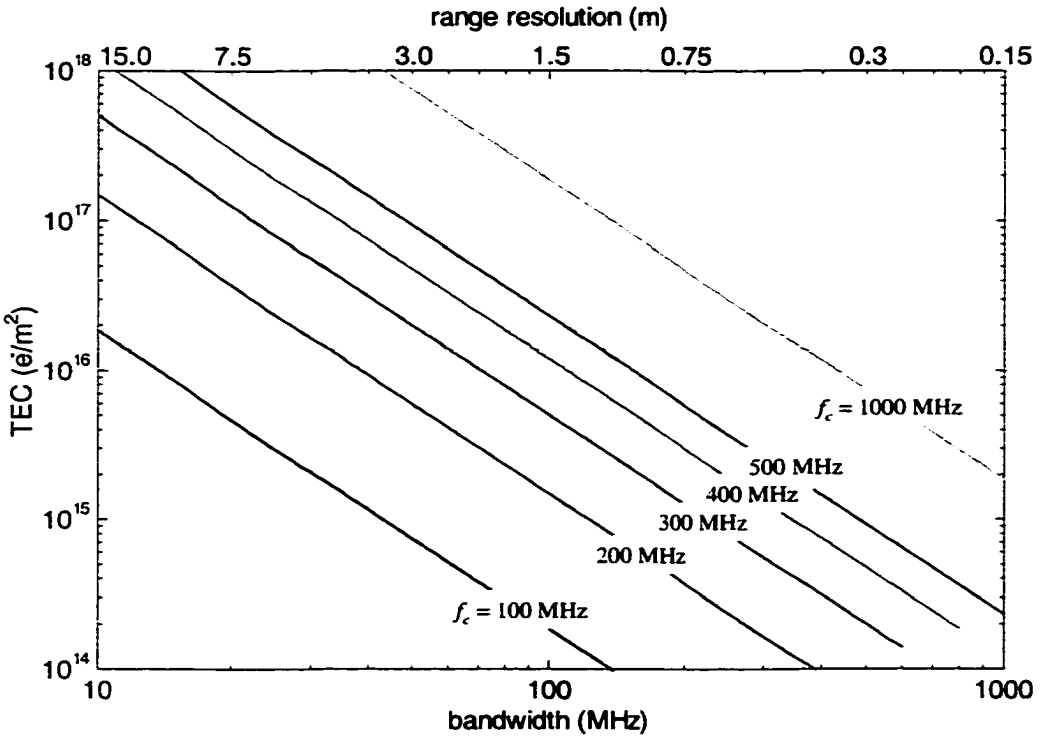

Figure 4.3: Maximum residual TEC for which full range resolution can be achieved. Range resolution is indicated by the upper axis, while the corresponding coherence bandwidth is indicated by the lower axis. Given a bandwidth and center frequency, this plot illustrates the level of residual, or uncompensated, TEC for which the quadratic phase error reaches $\pi/4$ at the edge of the band. Conversely, for a residual TEC, this plot illustrates the maximum coherent bandwidth, and thus the maximum range resolution, as a function of center frequency.

4.3 Effect of the Ionosphere on Cross-Range Resolution

Cross-range compression of the point-target response can also be treated as a matched filter problem with phase-error requirements similar to those of the range-compression problem. As with range compression, the ionospheric phase contribution causes a mismatch between the signal and the cross-range compression filter, thereby causing cross-range blurring in the image.

The cross-range compression filter is derived from the point-target, or impulse, response of the system in the cross-range direction. In the absence of the ionosphere, that response

is given by the system Green's function,

$$F_g(\omega; s) = \frac{\exp(-i2(\omega/c)R(s))}{(R(s))^2}, \tag{4.10}$$

where $R(s)$ is the range to the target as a function of the slow-time variable, s (see, for example, *Curlander and McDonough*, 1991, p. 138). The Green's function is compensated for signal amplitude falloff with range by multiplying by $(R(s))^2$, giving the *complex received signal*.

$$v_a(\omega; s) = \exp(-i2(\omega/c)R(s)). \tag{4.11}$$

Note that multiplying by $(R(s))^2$ provides a constant-amplitude target echo signal over the observation period, but it also increases the noise amplitude with increasing target range. The complex received signal is a function of frequency—that is, the point-target response changes across the band of the UWB radar waveform. For the purposes of estimating nominal cross-range blurring effects, however, it suffices to use the center frequency[4], ω_c, giving

$$v_a(s) = \exp(-i2k_c R(s)), \tag{4.12}$$

where $k_c = 2\pi/\lambda_c = \omega_c/c$ is the wavenumber at the center frequency.[5]

The cross-range compression filter is derived in most introductory SAR textbooks (e.g., *Curlander and McDonough*, 1991). It is a matched filter for $v_a(s)$, so its impulse response is given by

$$h_a(s) = v_a^*(-s) = \exp(i2k_c R(-s)), \tag{4.13}$$

where $v_a^*(-s)$ is the time-reversed complex conjugate of $v_a(s)$. This filter realizes the full cross-range resolution given in Equation 2.4. Note, however, that it is not optimal for target detection in low-SNR environments; for maximizing the probability of target detection, use the matched filter for $F_g(\omega; s)$—that is, $F_g^*(\omega; -s)$.

The ionosphere adds time-varying phase to the complex received signal, thus producing a mismatch between the received signal and the response of the cross-range compression

[4]A full analysis, incorporating the integrated effect across all frequencies, is included in Section 4.4.

[5]The point-target response, as given in Equation 4.12, is often used to derive the cross-range compression filter for both SAR applications (e.g., *Curlander and McDonough*, 1991, p. 138) and ISAR applications (e.g., *Mensa*, 1991, p. 91). In this research, cross-range compression is realized with the polar format algorithm described in Chapter 2. Equation 4.12 is used only to obtain an expression for cross-range blurring effects produced by phase errors.

filter. This mismatch blurs the image in the cross-range direction, in much the same way that phase variations with frequency blur the image in the range direction.

The effects of the ionosphere on cross-range resolution can be determined by analyzing the variations in TEC across the aperture. Note that while range resolution is calculated with a constant TEC and a variable frequency, cross-range resolution is calculated with a variable TEC and a constant frequency. To facilitate the analysis, expand the ionospheric phase contribution of Equation 4.1 in a Taylor series about the aspect angle at the center of the pass, θ_0, giving

$$\varphi_{\mathrm{i}}(\theta) = \frac{b}{\pi c f}\left\{N_{\mathrm{T}}(\theta_0) + N'_{\mathrm{T}}(\theta_0)(\theta-\theta_0) + \frac{1}{2}N''_{\mathrm{T}}(\theta_0)(\theta-\theta_0)^2 + \cdots\right\}, \tag{4.14}$$

where the aspect angle, θ, is related to slow-time, s, through the target rotation rate, $\omega_{\mathrm{t}}(s)$, and where $N_{\mathrm{T}}(\theta_0)$, $N'_{\mathrm{T}}(\theta_0)$, and $N''_{\mathrm{T}}(\theta_0)$ are the TEC and its first and second derivatives evaluated at the center of the pass. Here the effects differ from those in the range direction because the independent variable is now aspect angle rather than frequency. The constant term in the expansion merely adds a constant phase to all echoes and thus to the final image. The linear term shifts the image in the cross-range direction in a manner analogous to how linear phase over frequency shifts the image in the range direction. It also has a weak defocusing effect, similar to that evaluated in Section 2.6.2 for uncompensated radial target motion. The quadratic and higher-order terms cause most of the cross-range blurring. Since cross-range compression is also a matched-filter process, that blurring becomes significant when the quadratic phase term reaches about $\pi/4$ radians at the ends of the aperture.

From Equation 4.14, the requirement on the quadratic component of residual TEC at the edge of the aperture, $N_{\mathrm{T2}} = N''_{\mathrm{T}}(\theta_0)(\theta_{\max}-\theta_0)^2/2$, is then

$$N_{\mathrm{T2}} < \frac{\pi^2 c f_{\mathrm{c}}}{4b} = 0.465 \times 10^6 \cdot f_{\mathrm{c}}. \tag{4.15}$$

This equation provides a simple link between the variations in residual TEC across the aperture and cross-range blurring. With the preceding approximations, the maximum tolerable quadratic component of residual TEC depends only on center frequency and not on range or cross-range resolution, because N_{T2} is the value at the edge of the aperture, independent of the size of the aperture.

To illustrate the sensitivity of cross-range resolution to the quadratic component of residual TEC, consider the system parameters of Table 1.1. For the center frequency f_c = 300 MHz, the quadratic component of the residual TEC at the edge of the aperture, N_{T2}, must be less than about $1.4 \times 10^{14} e^-/m^2$. Such precision is not available from most TEC measurement systems. Considering that the TDOA technique of Section 3.6 produces a TEC estimate that is almost two orders of magnitude less precise, it may be difficult to meet the residual TEC requirement of Equation 4.15. However, Equation 4.15 presents an intriguing opportunity: cross-range focus quality provides a very sensitive indication of TEC *variations* across the pass and thus the potential for very precise measurements of TEC.

The finest-possible cross-range resolution, as limited by the quadratic component of the residual TEC variations, is calculated by using the *coherent aperture*, Θ_c, in place of the actual aperture, Θ, in the cross-range resolution equation (Equation 2.4). The coherent aperture is defined in this research as the aperture for which the quadratic component of $\varphi_i(\theta)$ reaches $\pi/4$. For a given N_{T2}, increasing the actual aperture beyond the coherent aperture does not improve cross-range resolution. From Equation 4.15 and the definition of N_{T2},

$$\frac{N_T''(\theta_0)}{2}\left(\frac{\Theta_c}{2}\right)^2 = \frac{\pi^2 c}{4b} \cdot f_c,$$

so

$$\Theta_c = \sqrt{\frac{\pi^2 c}{b}} \cdot \sqrt{2\frac{f_c}{N_T''(\theta_0)}} = 1364 \cdot \sqrt{2\frac{f_c}{N_T''(\theta_0)}}. \tag{4.16}$$

For apertures less than about 45 degrees, the cross-range resolution from Equation 2.4 is

$$\delta x_c \approx \frac{\lambda}{2\Theta} = \frac{c}{2f_c\Theta}. \tag{4.17}$$

After substituting from Equation 4.16,

$$\delta x_c \geq \frac{c}{2f_c\Theta_c} = \frac{1}{2} \cdot \sqrt{\frac{bc}{2\pi^2}\frac{N_T''(\theta_0)}{f_c^3}},$$

$$\delta x_c \geq \frac{\sqrt{bc}}{2\pi}\sqrt{\frac{1}{2}\frac{N_T''(\theta_0)}{f_c^3}} = 1.099 \times 10^5 \cdot \sqrt{\frac{1}{2}\frac{N_T''(\theta_0)}{f_c^3}}, \tag{4.18}$$

where '$\geq$' indicates that the actual aperture must also be sufficient to support the specified resolution. From Equation 4.18, the finest-possible cross-range resolution is limited by the

quadratic component of residual TEC and the center frequency. Note the similarity between this equation and Equation 4.9, the corresponding equation for the range resolution.

Equations 4.15 and 4.18 are probably of less value in predicting imaging performance than their range-direction counterparts, Equations 4.8 and 4.9, because evaluation of Equations 4.15 and 4.18 requires knowledge of TEC variations across the aperture—something that is much more difficult to predict than the TEC itself.

The limitations on cross-range resolution imposed by the ionosphere can also be described in terms of the *cross-range coherence bandwidth*, $B_{\rm cr}$, defined in this research for apertures less than about 45 degrees as

$$B_{\rm cr} = f_{\rm c} \cdot \Theta_{\rm c}. \tag{4.19}$$

$B_{\rm cr}$ is the approximate span of the frequency-domain support region in the cross-range direction for an angular aperture of $\Theta_{\rm c}$ (see also Figure 2.5). Substituting from Equation 4.16,

$$B_{\rm cr} = \sqrt{\frac{\pi^2 c}{b}} \cdot \sqrt{2\frac{f_{\rm c}^3}{N''_{\rm T}(\theta_0)}} = 1364 \cdot \sqrt{2\frac{f_{\rm c}^3}{N''_{\rm T}(\theta_0)}}. \tag{4.20}$$

Again, note the similarity between this equation and Equation 3.36, the coherence bandwidth in the range direction.

The analysis of this section makes several assumptions that affect the interpretation and accuracy of Equations 4.15 and 4.18. First, it was implied that the second- and higher-order coefficients in the Taylor expansion were monotonically decreasing, with the quadratic term being the largest nonlinear component. This may not be true in all situations, especially during periods of ionospheric instability. All of the nonlinear components of the TEC variations contribute to cross-range blurring—not just the quadratic component. Rather than using a Taylor expansion about the center of the aperture, it would be better to write

$$\varphi_{\rm i}(\theta) = \frac{b}{\pi c f}\left(N_{\rm Tc} + N_{\rm Tl}(\theta) + N_{\rm Tnl}(\theta)\right), \tag{4.21}$$

where $N_{\rm Tc}$ and $N_{\rm Tl}(\theta)$ are the best constant and linear fits to the residual TEC in, say, a minimum rms sense, and $N_{\rm Tnl}(\theta)$ is the nonlinear component. In this context, Equation 4.15 could be used—admittedly, with some extrapolation beyond its scope—to set a residual

TEC requirement in terms of Equation 4.21. For example, to achieve maximum cross-range resolution at a center frequency of 300 MHz, a linear fit to the TEC should have 'fit residuals' that do not exceed about $1.4 \times 10^{14}\,e^{-}/m^2$ over most of the aperture.

Cross-range blurring could also be evaluated directly in terms of Equation 4.21. One idea is to consider the 'energy' in the nonlinear component of $\varphi_i(s)$—that is, the integral of the square of the nonlinear component of the phase error across the aperture. It may be possible to relate that nonlinear phase energy to resolution and sidelobe levels with results that are more appropriate for the expected random structure of $N_T(\theta)$ than the Taylor expansion described above. This idea was not investigated in this research.

Another assumption is that the angular aperture is uniformly sampled in aspect angle, θ, by constant-rate sampling in slow-time, s. This is not the case for satellite ISAR when the radar uses a constant pulse repetition frequency (PRF), since the satellite rotation rate, as viewed from the radar, is not constant.

One particular component of the nonlinear phase variation does not produce blurring. A sinusoidal phase variation having the same period as the target rotation shifts the target in cross-range, without blurring (see Section 2.6). For analysis of specific functions of N_T, that sinusoidal component could be removed before expanding the function. For apertures of less than about 30 degrees, a straight line provides an approximate fit to that sinusoid, so much of the sinusoidal variation is captured in the linear term of the Taylor series expansion.

Considering the assumptions made in its derivation, Equation 4.15 provides a link between TEC and focus quality that is accurate to within about a factor of two. That is, to achieve full cross-range resolution, the maximum quadratic component of the residual TEC should be between -50% and $+100\%$ of that given by Equation 4.15. Experimental data collected during this research, some of which are presented in Chapter 5, have produced TEC estimates with a precision agreeing with that predicted by Equation 4.15.

Equations 4.8 and 4.15 provide specifications for maximum tolerable levels of residual TEC. For the radar parameters of Table 1.1, those equations indicated that a TEC accuracy of about $1.3 \times 10^{15}\,e^{-}/m^2$ is required to achieve the expected range resolution, and a TEC precision of about $1.4 \times 10^{14}\,e^{-}/m^2$ is required to achieve the expected cross-range resolution. For this example, the cross-range resolution is almost an order of magnitude more sensitive to TEC. However, while range resolution is sensitive to absolute TEC, cross-range resolution is sensitive only to its nonlinear variations.

In addition to quantifying the TEC estimation accuracy required to achieve full resolution, Equations 4.8 and 4.15 also provide simple tools for calculating actual resolution as limited by higher levels of residual TEC. Given actual ionospheric conditions, Equation 4.8 can be used to estimate the coherence bandwidth, and thus the range resolution as limited by any uncompensated TEC. Likewise, Equation 4.15 can be used to estimate the maximum 'coherent aperture,' and thus the cross-range resolution. These equations are also applicable to higher-frequency radars, such as those operating at L- or S-band. For those systems, ionospheric effects are usually small enough to be ignored, but situations do arise in which the ionosphere degrades radar performance at frequencies of up to about 2 GHz. In those situations, Equations 4.8 and 4.15 quantify the limits imposed by the ionosphere on *microwave* radar resolution.

4.4 Effect of the Ionosphere on the Point Spread Function

If the ionosphere is considered to be part of the overall radar system, its effects on the radar image can be characterized by the system point spread function (PSF). Using the PSF to analyze those effects becomes increasingly important as the angular aperture is expanded beyond about 30 degrees, because range and cross-range effects become increasingly coupled, thereby requiring modification or reinterpretation of the results of the two previous sections.

The ionospheric phase contribution is a two-dimensional function of frequency and aspect angle (see Equation 4.1 and the footnote following it). That phase contribution can be thought of as a complex weighting function that is applied to the two-dimensional frequency-domain radar data. As such, the ionosphere acts as a two-dimensional filter whose blurring effects on the radar image can be characterized by the filter's two-dimensional impulse response, or PSF. When the response of that *ionospheric filter* is combined with the ideal system response through two-dimensional convolution, one obtains the overall *system PSF* as compromised by the ionosphere.

The system PSF can be calculated from the ionospheric phase contribution and the frequency-domain support region, the intersection of the annulus and sector described in Section 2.2. First, the *system transfer function* is calculated by windowing the ionospheric phase contribution to limit its extent to the frequency-domain support region. The system PSF is then the inverse two-dimensional Fourier transform of the system transfer function.

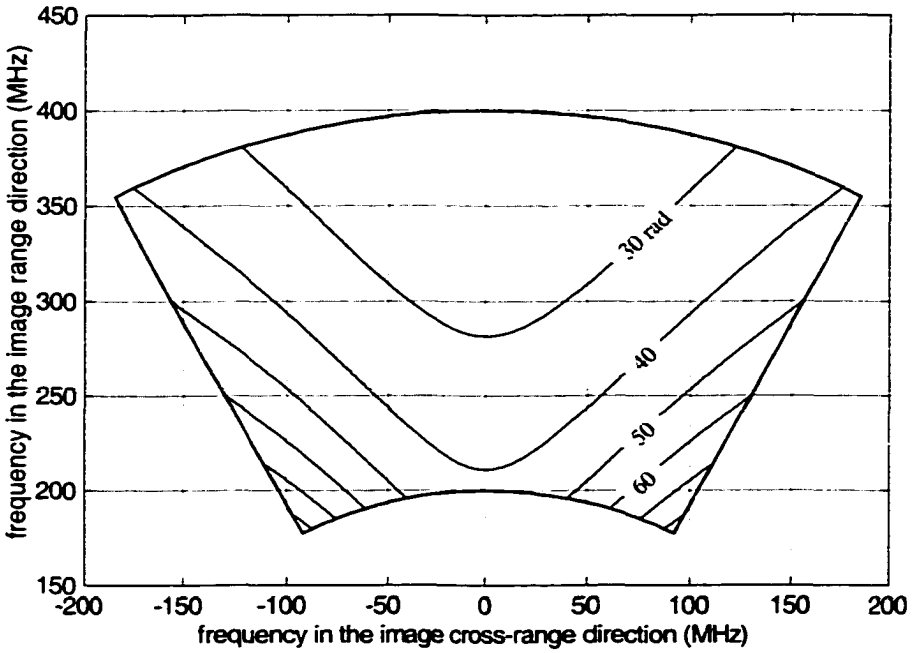

Figure 4.4: An example of the ionospheric phase contribution over a two-dimensional frequency-domain support region. In this example, the ionospheric phase contribution is given by $\varphi_{\rm i}(f;\theta) = b/(c\pi) \cdot N_{\rm T}(\theta)/f$, with $N_{\rm T}(\theta) = 0.5 \cdot (\theta/27.5°)^2 + 0.5$ TECU, and where θ is the aspect angle as illustrated in Figure 2.5. The frequency-domain support region is also the same as that illustrated in Figure 2.5.

The unknown functional form of the TEC, $N_{\rm T}(\theta)$, precludes a general analysis of the two-dimensional impulse response of the 'ionospheric filter,' but some understanding of its characteristics can be realized by examining specific situations. Figure 4.4 is an example of the phase introduced by the ionosphere over a two-dimensional frequency-domain support region. In range, along radial lines, the phase is given by $C_{\rm r}/f$, where $C_{\rm r}$ is a scaling factor that depends on the TEC in the direction of the radial line. In azimuth, along circular arcs, the phase is given by $C_{\rm a}N_{\rm T}(\theta)$, where θ is the aspect angle and $C_{\rm a}$ is a scaling factor that depends on the frequency at the arc radius. The phase values plotted in Figure 4.4 correspond to a residual TEC of less than 1 TECU, a value typical of what might be expected after removing the bulk TEC estimated with the TDOA technique. In the figure, the TEC is quadratic in θ, ranging from 0.5 TECU at the center of the aperture to 1.0 TECU at the ends. Thus, $N_{\rm T2} = 0.5$ TECU.

The PSF for the system transfer function of Figure 4.4 is plotted in Figure 4.5a. For

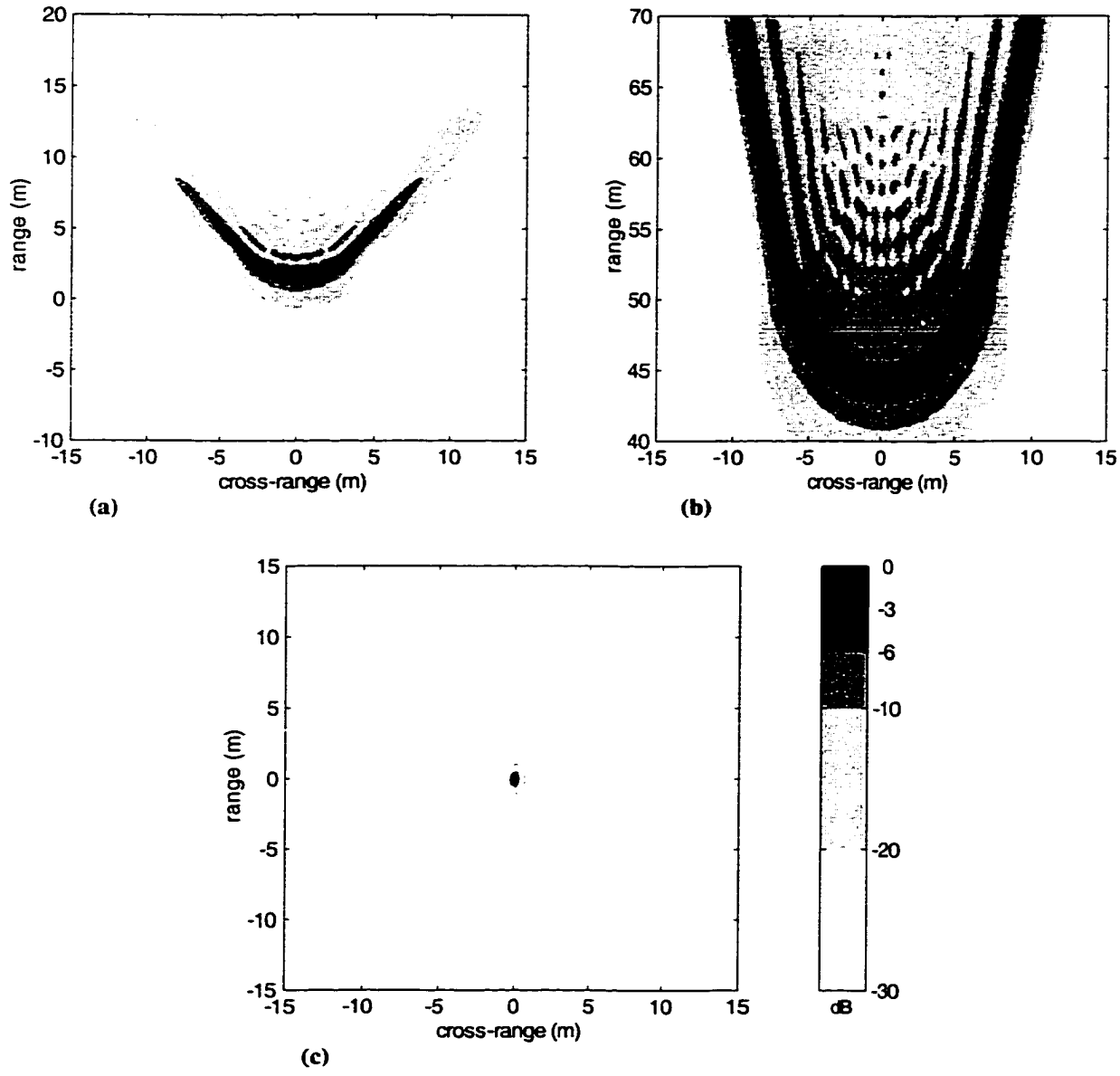

Figure 4.5: An example of the system PSF as degraded by the ionosphere. Frame (a): The PSF for the system transfer function illustrated in Figure 4.4. Frame (b): The PSF for $N_T(\theta) = 2.5 \cdot (\theta/27.5°)^2 + 12.0$ TECU, the approximate TEC level observed during pass 8084a over the center 55 degree aperture. Frame (c): The PSF for $N_T(\theta) = 0$, that is, the ideal system PSF when the ionosphere has been fully compensated. The same gray-scale applies to all three frames. Its units are dB relative to the peak value in each frame. The peak values in (a) and (b) are about 15 dB and 27 dB, respectively, below the peak value of the ideal PSF in (c).

comparison, the PSF for a TEC approximately equal to that observed during pass 8084a is plotted in Figure 4.5b, and the ideal PSF—one with no ionosphere or with the ionosphere fully compensated—is plotted in Figure 4.5c.

The spreading of the point-target response illustrated in Figure 4.5a should be expected, since both the magnitude of the residual TEC and its quadratic variation across the aperture are much larger than the limits set by Equations 4.8 and 4.15. From those equations, with $f_c = 300$ MHz and $B = 200$ MHz, the requirements for full resolution are $N_T < 0.13$ TECU and $N_{T2} < 0.014$ TECU, while the values used in Figure 4.5a are $N_T = 0.5$ to 1.0 TECU and $N_{T2} = 0.5$ TECU. For this example, even after residual TEC has been reduced to less than 1 TECU—a relatively modest level—Figure 4.5a indicates a resolution of, at best, about 10 m in cross-range by 3 m in range, along with large extended sidelobes. Of course, the resolution is markedly poorer, as illustrated in Figure 4.5b, if no attempt is made to compensate the ionosphere.

Coupling between range resolution and cross-range resolution is also illustrated by the PSF in Figure 4.5a. For the range direction, the residual TEC is about a factor of five or so larger than the limit specified in Equation 4.8. The expected spreading can be estimated by using $N_T = 0.5$ TECU and $f_c = 300$ MHz in Figure 4.3, providing a predicted range resolution of about 1.5 m. Referring back to Figure 4.5a, that predicted range resolution (1.5 m) corresponds approximately to the width of the bowl-shaped 3-dB region along lines parallel to the range axis. The actual range resolution, however, is determined from the full range extent of the bowl-shaped region, about 10 m. Range resolution has been compromised beyond the level determined from Figure 4.3 by range/cross-range coupling arising from the large (55-degree) angular aperture.

4.5 Ionosphere Estimation through Imaging

As found in Sections 4.2 and 4.3, realizing full resolution with a wide-aperture UWB radar requires TEC estimates as much as two orders of magnitude more accurate than those achieved using the TDOA technique of Section 3.6. The required improvement in the TEC estimates can be attained, in many situations, by searching for a correction that produces an optimal image.

Blurring of a radar image by both range- and TEC-estimation errors can be characterized by the phase contributions of those errors to the radar signal. As such, the blurring

effects have some similarities, but since the functional forms of the range and TEC phase contributions are different, the blurring effects also have differences. To improve target range estimates to a level where their blurring effects are negligible, ISAR imaging algorithms often use an autofocus procedure. One such procedure is described in Section 2.5. To estimate target range, that autofocus procedure includes a search for the range error function that produces the highest-quality image. The search can be extended by adding a second function, the TEC-estimate error function. The goal of the extended autofocus procedure would be to also improve TEC estimates to the point where their errors have negligible blurring effects. Since range errors and TEC errors have differing effects on the quality of the image, it should be possible to find an autofocus solution that provides good estimates for both range and TEC.

Most aspects of the autofocus procedure do not need to be changed when another free variable, the TEC, is added. Image quality is still quantitatively defined in terms of a cost function. With the extended procedure, the multidimensional space of range and TEC errors is searched for the point that produces an optimal image. The most significant difference between the two procedures is that the error space now has more dimensions, one for each of the coefficients of the TEC-estimation polynomial, than it did in the range-error-only case. More dimensions in the error space leads to an increase in computational cost. In exchange, one obtains the TEC.

The ability to find an optimal autofocus solution depends on (1) the variation of the surface of the cost function due to noise or radar system artifacts, (2) the number and character of local optima in the search space, and (3) the search technique. If the globally optimal image is found, there is still the question of whether it is the same as the 'correct' image. The issues in finding the optimal image and the possibility of differences between the optimal and correct images were also discussed in Section 2.5.

If the autofocused image is the same as the correct image, the resulting TEC estimate is expected to achieve the accuracy given in Equations 4.8 and 4.15. The accuracy of the constant and linear terms of the estimate can be determined from the range resolution, while the accuracy of the second- and higher-order terms can be determined from the cross-range resolution. From Equations 4.8 and 4.15, *better estimates of absolute TEC can be obtained by using larger fractional bandwidths and lower frequencies, while better estimates of TEC variations across the aperture can be obtained also by using lower frequencies.*

The accuracy of the TEC and range estimates produced by the autofocus procedure is limited by the ability to separate their effects on the image. Unfortunately, the phase errors caused by TEC- and range-estimation errors are not fully separable; there are some strong similarities in their effects on the image. To illustrate, consider a TEC estimate that is accurate to within a factor of about four of that given in Equations 4.8 and 4.15. A near-optimal image can be obtained by 'fixing' that TEC estimate and searching over the space of range errors. Likewise, the range estimate can be fixed and a near-optimal image found by searching over TEC errors. This coupling between range and TEC increases the probability that the autofocus algorithm will get stuck in a local optimum. The reason for the coupling, especially for narrowband signals, is that the cross-range blurring caused by phase errors across the aperture could have originated from either range or TEC errors. The effects begin to differ as the bandwidth is increased because TEC phase errors have a $1/f$ frequency dependence, while range errors have an f frequency dependence. The degree of range/TEC coupling depends on fractional bandwidth and center frequency since those parameters determine the variations in phase versus frequency and, thus, the amount of defocusing at the upper and lower band edges. The coupling is likely to degrade the precision of the TEC estimate from that given in Equation 4.15 by a small amount, depending on the SNR of the data. Even though cross-range focus is an accurate indicator of phase error, it is not possible to separate entirely the causes of this error, except for the idealized situation of a point target in a noise-free environment.

Range and TEC errors differ in their effects in the image range direction; TEC errors cause blurring while range errors only cause translation. The level at which TEC errors cause measurable range-direction blurring, and thus the approximate threshold at which range and TEC errors can be distinguished, is given in Equation 4.8.

Another difference between range error and TEC error is their 'functional complexity.' The range error can often be specified by a low-order polynomial and, in fact, some autofocus techniques only solve for the quadratic component of that error. For VHF ISAR, the aperture is often sufficiently wide that a higher-order polynomial is needed, but even in that case it can usually be specified to sufficient accuracy by a few coefficients. The TEC, however, typically has smooth but random variations across the aperture. It may not be well-characterized by a low-order polynomial, especially during periods of ionospheric instability. In most experiments to date, however, the TEC residual after removal of a low-order polynomial trend has been found to be sufficiently small, albeit random, to have

a negligible effect. Knowledge of the power-scaling factor and the exponent in the power spectral density, discussed in Section 3.8, could be used to determine the polynomial order needed for an adequate fit. Such information usually is not available a priori. For lack of an independent measurement of the level of ionospheric structure during any specific satellite pass, the order of the TEC-estimation polynomial has been increased, in this research, until the higher-order terms no longer have a significant effect on image quality.

The accuracy of the final TEC estimate could be checked by comparison with measurements from other sources. Unfortunately, the sources currently available do not have the required accuracy or sample spacing to verify this technique. They can serve, however, to confirm the consistency of the TEC estimate.

Another consistency check can be made by examining the PSF in the final image. If some component of the target has scattering characteristics that approximate those of an ideal point scatterer, the 3-dB width and sidelobe levels could be compared to the theoretical values. The differences would be due to residual phase from errors in range and TEC estimates, and could be used to experimentally evaluate the TEC estimation error. In reality, targets are not made up of ideal point scatterers, and the 3-dB width and sidelobe levels in the image will be at least partially determined by variations in the target's complex scattering amplitude over the range of angles used in forming the image.

4.6 Limitations of the $1/f$ Phase Model

The $1/f$ phase model of Equation 4.1 is an approximation of the effects of the ionosphere on a radio-wave signal. It becomes less accurate as the fractional bandwidth is increased and as the frequency is decreased. At some point, the unmodeled components of the ionospheric effects become large enough to degrade image quality. Up to that point the TEC is suitable for adequately characterizing ionospheric effects, but beyond that point additional parameters are needed to obtain an adequate model. In this section, the performance of the $1/f$ phase model is evaluated, and estimates of the conditions under which it becomes inadequate are derived in terms of fractional bandwidth, center frequency, and ionospheric conditions.

The $1/f$ phase model is adequate for modeling ionospheric effects, provided the approximations used in its derivation are sufficiently accurate. To determine when it becomes inadequate, the $1/f$ phase estimate can be compared to the more precise phase estimate

obtained by using the Appleton-Hartree formula (Equation 3.11). The methodology is to expand the Appleton-Hartree formula in negative powers of f, then evaluate the significance of the phase contributions from the higher-order terms. An expansion in negative powers of f is appropriate since the refractivity varies inversely with f, and thus the functional form is captured with a minimal number of terms. However, to use Equation 3.11 one needs to know the electron density, geomagnetic field, and angle Θ at all points along the ray path. Analytic solutions for the ionospheric phase contributions of Equation 3.23 do not exist when the full Appleton-Hartree formula is used. Even with the simpler QL approximation of Equation 3.14, analytic solutions exist for only a few simple electron-density profiles in a plane-stratified medium with a uniform magnetic field. For realistic profiles in a spherically symmetric geometry, the integration along the ray path must be done numerically.

4.6.1 Derivation of the Higher-Order Phase Terms

From Equations 3.22 and 3.23, the phase contributed by the ionosphere is given by

$$\varphi_{\mathrm{i}} = -\frac{4\pi}{\lambda}\int (n-1)dl, \tag{4.22}$$

where the integral is evaluated along the one-way path of the ray. The refractivity is obtained by expanding the Appleton-Hartree formula, Equations 3.11,

$$\begin{aligned} n^2 &= 1 - \frac{X(1-X)}{(1-X) - \frac{1}{2}Y^2\sin^2\Theta \pm \left\{\frac{1}{4}Y^4\sin^4\Theta + Y^2\cos^2\Theta(1-X)^2\right\}^{1/2}} \\ n^2 &= 1 - \frac{\frac{\omega_N^2}{\omega^2}\left(1-\frac{\omega_N^2}{\omega^2}\right)}{\left(1-\frac{\omega_N^2}{\omega^2}\right) - \frac{1}{2}\frac{\omega_{HT}^2}{\omega^2} \pm \left\{\frac{1}{4}\frac{\omega_{HT}^4}{\omega^4} + \frac{\omega_{HL}^2}{\omega^2}\left(1-\frac{\omega_N^2}{\omega^2}\right)^2\right\}^{1/2}}, \end{aligned} \tag{4.23}$$

where the upper sign applies to the ordinary wave, and where the longitudinal and transverse components of ω_{H} are defined by

$$\omega_{\mathrm{HL}} = \omega_{\mathrm{H}}\cos\Theta \tag{4.24}$$

$$\omega_{\mathrm{HT}} = \omega_{\mathrm{H}}\sin\Theta. \tag{4.25}$$

Equation 4.23 is now expanded about $\omega = \infty$.[6] Including terms up to sixth order in $1/\omega$,

$$\begin{aligned} n &= 1 - \frac{\omega_N^2}{2}\left(\frac{1}{\omega^2}\right) \pm \frac{\omega_N^2}{2}\omega_{HL}\left(\frac{1}{\omega^3}\right) - \frac{\omega_N^2}{2}\left(\frac{\omega_N^2}{4} + \omega_{HL}^2 + \frac{\omega_{HT}^2}{2}\right)\left(\frac{1}{\omega^4}\right) \\ &\pm \frac{\omega_N^2}{2}\left(\frac{\omega_N^2\omega_{HL}}{2} + \omega_{HL}^3 + \omega_{HL}\omega_{HT}^2 + \frac{\omega_{HT}^3 \tan\Theta}{8}\right)\left(\frac{1}{\omega^5}\right) \\ &- \frac{\omega_N^2}{2}\left(\frac{\omega_N^4}{8} + \frac{3\omega_N^2\omega_H^2}{4} + \omega_{HL}^4 + \frac{3\omega_{HL}^2\omega_{HT}^2}{2} + \frac{\omega_{HT}^4}{2}\right)\left(\frac{1}{\omega^6}\right). \end{aligned} \tag{4.26}$$

The fifth- and sixth-order terms are included for future reference. Using Equations 3.4, 3.5, 4.24, and 4.25, and keeping terms up to fourth order in $1/\omega$,

$$n = 1 - b\cdot\frac{N}{\omega^2} \pm \frac{be}{m}\cdot\frac{NB\cos\Theta}{\omega^3} - \frac{b^2}{2}\cdot\frac{N^2}{\omega^4} - \frac{be^2}{m^2}\cdot\left(\cos^2\Theta + \frac{\sin^2\Theta}{2}\right)\frac{NB^2}{\omega^4}. \tag{4.27}$$

This is used in Equation 4.22 and integrated over the ray path to obtain the two-way accumulated phase introduced by the ionosphere,

$$\begin{aligned} \varphi_i &= -\frac{4\pi}{\lambda}\int (n-1)dl \\ &= \frac{2b}{c\omega}\int N dl \mp \frac{2be}{cm\omega^2}\int NB\cos\Theta dl \\ &\quad + \frac{b^2}{c\omega^3}\int N^2 dl + \frac{2be^2}{cm^2\omega^3}\int\left(\cos^2\Theta + \frac{\sin^2\Theta}{2}\right)NB^2 dl, \end{aligned}$$

where a factor of two has been included, so the integrals are evaluated over the one-way path. This can be written as

$$\varphi_i = \varphi_{i1} \mp \varphi_{i2} + \varphi_{i3a} + \varphi_{i3b}, \tag{4.28}$$

where

$$\varphi_{i1} = \frac{2b}{c\omega}\int N dl, \tag{4.29}$$

[6] This expansion was done with the help of Maple® V Release 4, a symbolic math program.

$$\varphi_{i2} = \frac{2be}{cm\omega^2} \int NB \cos\Theta dl, \tag{4.30}$$

$$\varphi_{i3a} = \frac{b^2}{c\omega^3} \int N^2 dl, \tag{4.31}$$

$$\varphi_{i3b} = \frac{2be^2}{cm^2\omega^3} \int \left(\cos^2\Theta + \frac{\sin^2\Theta}{2}\right) NB^2 dl. \tag{4.32}$$

Here φ_{i1} is the $1/f$ phase model of Equation 4.1,[7] φ_{i2} is the second-order correction to that model, and φ_{i3a} and φ_{i3b} are the third-order corrections. The second-order correction varies as the inverse square of frequency and an integral involving the product of the electron density and the geomagnetic field along the ray path. The third-order corrections vary as the inverse cube of frequency and integrals again involving the electron density and geomagnetic field.

Note that for QL propagation, Faraday rotation is produced by the φ_{i2} term, since the φ_{i2} phase contribution is opposite for the O and X waves. The Faraday rotation given in Equation 3.45 is 1/2 the φ_{i2} term given in Equation 4.30. The factor-of-two difference appears because the former equation applies to one-way propagation, while the latter equation applies to two-way propagation. For QT propagation, $\cos\Theta \approx 0$, so $\varphi_{i2} \approx 0$. Polarization changes for QT propagation are produced by the $\sin\Theta$ components of the $1/\omega^5$ and higher-order terms of Equation 4.26.[8]

For the $1/f$ term, the shape of the electron-density profile does not matter—only the number of electrons passed along the way. The shape of the profile, however, does affect the values of the higher-order terms of the ionospheric phase contribution. To determine those values for a specific situation, the electron density, geomagnetic field, and ray angle Θ all must be known over the ray path. This makes computation of the higher-order terms infeasible, or at least very difficult, for an operational system.

[7] Equations 3.24 and 4.1 were obtained by approximating the Appleton-Hartree formula. They remain unchanged, as the first-order model, when the geomagnetic field is included and a full expansion of the Appleton-Hartree formula is used. Thus, TEC captures all first-order ionospheric effects.

[8] Note that the $1/\omega^5$ term in Equation 4.26 has a singularity at $\Theta = 90°$ due to the $\tan\Theta$ factor. However, the original expression, Equation 4.23, is well behaved at $\Theta = 90°$, so it can be used to evaluate the refractive index at that point. Alternatively, the refractive index can be evaluated asymptotically (as $\Theta \to 90°$) from Equation 4.26.

4.6.2 Phase Contributions of the Higher-Order Terms

In this section, the phase contributions of the higher-order terms are compared to those of the total electron content, the first-order term, to evaluate their importance for the radar imaging problem. Specifically, order-of-magnitude estimates are made for the ratios of the phase contributions of the higher-order terms to those of the TEC term. Then, for an actual experiment where TEC and φ_{i1} are measured (using the imaging techniques of Section 4.5), the higher-order phase contributions can be estimated and compared to the threshold at which they begin to degrade image quality.

The ratio of the second-order phase contribution to the first-order phase contribution is

$$\frac{\varphi_{i2}}{\varphi_{i1}} = \frac{e}{m\omega} \cdot \frac{\int NB\cos\Theta dl}{\int N dl}. \tag{4.33}$$

Using a uniform magnetic field with magnitude $B = B_0$, and noting that $\cos\Theta \leq 1$,

$$\frac{\varphi_{i2}}{\varphi_{i1}} \leq \frac{eB_0}{m\omega} = \frac{\omega_{H0}}{\omega}, \tag{4.34}$$

where ω_{H0} is the electron gyro-frequency when $B = B_0$. With $B_0 = 0.5$ gauss, $\omega_{H0} =$ 1.4 MHz, giving

$$\frac{\varphi_{i2}}{\varphi_{i1}} \leq \frac{1.4 \times 10^6}{f}. \tag{4.35}$$

From these equations, with $\Theta = 45°$, the ratio of the second-order term, φ_{i2}, to the TEC term, φ_{i1}, is approximately equal to the reciprocal of the frequency in megahertz. For example, for $f = 300$ MHz, the phase contributed by the second-order term is approximately 1/300 of that contributed by the TEC. The significance of this additional phase is evaluated below.

For the third-order term, φ_{i3a}, which is independent of the geomagnetic field,

$$\frac{\varphi_{i3a}}{\varphi_{i1}} = \frac{b}{2\omega^2} \cdot \frac{\int N^2 dl}{\int N dl}. \tag{4.36}$$

A general inequality can be used to simplify the ratio of the integrals; for any non-negative function N,

$$\int N^2 dl < N_{\max} \int N dl, \tag{4.37}$$

where N_{max} is the maximum value along the ray. Then,

$$\frac{\varphi_{i3a}}{\varphi_{i1}} < \frac{bN_{max}}{2\omega^2}. \tag{4.38}$$

Using $N_{max} = 10^{12}\,e^-/m^3$, for example,

$$\frac{\varphi_{i3a}}{\varphi_{i1}} < \frac{2 \times 10^{13}}{f^2}. \tag{4.39}$$

For $f = 100$ MHz, the ratio $\varphi_{i3a}/\varphi_{i1}$ is about 1/500, while for $f = 300$ MHz, it is about 1/4500. These are conservative numbers; for typical electron-density profiles, the ratio is closer to 1/1000 at 100 MHz, and 1/10,000 at 300 MHz. Thus, at 300 MHz the φ_{i3a} term is smaller than the second-order term, φ_{i2}, by a factor of anywhere from about ten to thirty.

For the other third-order term, φ_{i3b}, which does depend on the geomagnetic field,

$$\frac{\varphi_{i3b}}{\varphi_{i1}} = \frac{e^2}{m^2\omega^2} \cdot \frac{\int NB^2(\cos^2\Theta + \sin^2\Theta/2)dl}{\int N dl}. \tag{4.40}$$

Note that $(\cos^2\Theta + \sin^2\Theta/2)$ varies between 0.5 and 1.0; for this approximation, use a worst-case value of 1.0. Again, using a uniform magnetic field with $B = B_0 = 0.5$ gauss,

$$\frac{\varphi_{i3b}}{\varphi_{i1}} \leq \left(\frac{eB_0}{m\omega}\right)^2 = \left(\frac{\omega_{H0}}{\omega}\right)^2 = \frac{2 \times 10^{12}}{f^2}. \tag{4.41}$$

This is just the square of the second-order ratio, $\varphi_{i2}/\varphi_{i1}$. For $f = 300$ MHz, $\varphi_{i3b}/\varphi_{i1} \sim$ 1/45,000.

The relative significance of the φ_{i2}, φ_{i3a}, and φ_{i3b} terms can now be determined by comparing Equations 4.35, 4.39, and 4.41. To complete the example with $f = 300$ MHz, the φ_{i2}, φ_{i3a}, and φ_{i3b} phase contributions are approximately 1/300, 1/4500, and 1/45.000 respectively, below the phase contribution of the TEC.

4.6.3 An Example of the Higher-Order Terms

As a specific example of the magnitudes of φ_{i2}, φ_{i3a}, and φ_{i3b}, Figure 4.6 is a plot of their values as calculated along a vertical path to satellite altitude for pass 8084a. The electron-density profile employed is the Chapman fit to the IRI-95 prediction as described

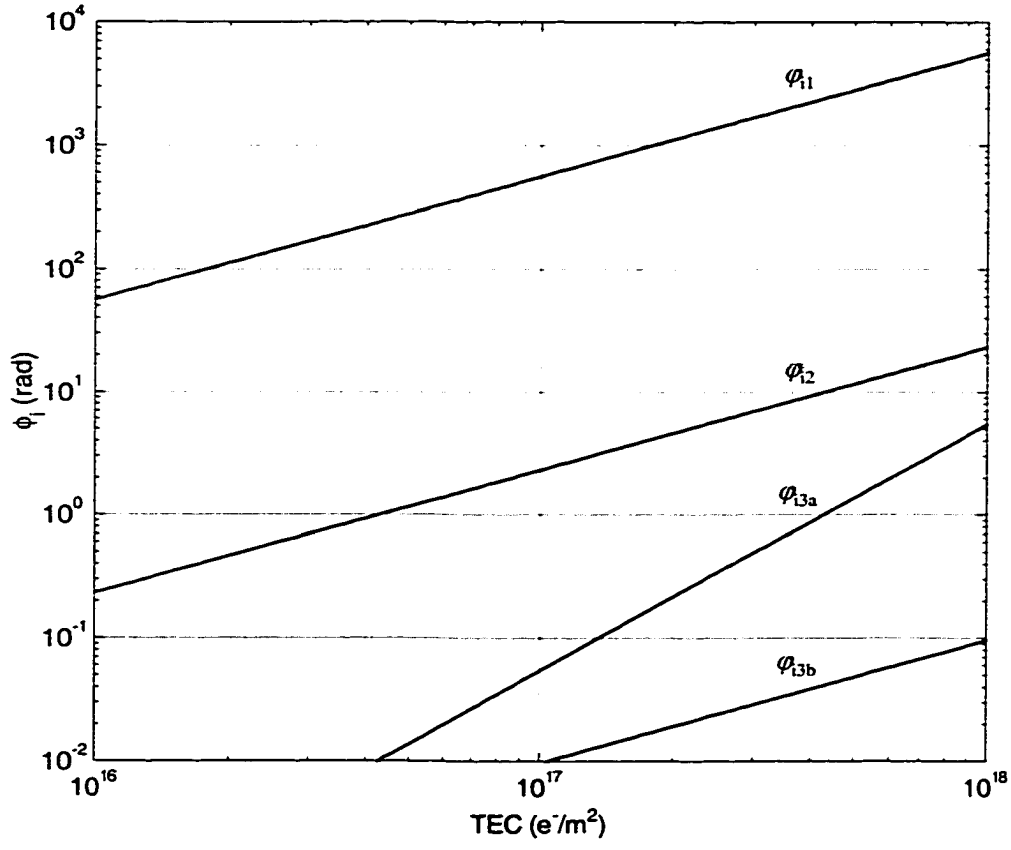

Figure 4.6: An example of φ_{i1}, φ_{i2}, φ_{i3a}, and φ_{i3b} versus TEC for pass 8084a. These are the phase contributions of the $1/f$, $1/f^2$, and $1/f^3$ terms with $f = 300$ MHz. The calculations use a Chapman electron-density profile and an Earth-centered magnetic dipole. Details are provided in the text.

in Section 3.1 and plotted in Figure 3.1. The geomagnetic field is modeled with an Earth-centered magnetic dipole having a flux density of 0.5 gauss along the geomagnetic equator at the Earth's surface. Also, $f = 300$ MHz and $\Theta = 0°$ are used in the calculations. Note that with $\Theta = 0°$, the φ_{i2} and φ_{i3b} curves provide a worst-case estimate of the actual φ_{i2} and φ_{i3b} phase contributions. The curves are parameterized by vertical TEC (vTEC) to the satellite altitude, with the Chapman profile scaled in amplitude to provide the TEC values in the plot. The integrals are evaluated to a target altitude of 378 km, the actual value for pass 8084a.

For a planar geometry (flat Earth, constant satellite altitude, and plane-stratified ionosphere), the abscissa variable in Figure 4.6 can be interpreted as slant TEC since the TEC

and the path integrals in φ_{i2}, φ_{i3a}, and φ_{i3b}, all scale as the secant of the zenith angle. The curves are slightly different in a spherically symmetric geometry, but for this example those differences are negligible. More generally, for the spherically symmetric geometry there is less weighting in the integrals at the higher altitudes since zenith angle decreases with increasing altitude, but the difference is small and insignificant in comparison to the errors in the estimate of the electron-density profile.

Considering the differences between the actual situation and the models used for electron density and geomagnetic field, the curves in Figure 4.6 may differ from actual conditions by as much as a factor of 2:1. To remove the higher-order phase contributions from the radar data it would be necessary to estimate them more accurately by measuring the electron-density profile and using a better model for the geomagnetic field. Nonetheless, Figure 4.6 provides a quick way to determine whether the higher-order terms are significant for this pass or others that have similar satellite altitudes.

To approximate the higher-order terms for pass 8084a, the TEC is first measured, then used as the abscissa value in Figure 4.6. During the autofocus process, the slant TEC was found to vary between about 12 TECU at the point of closest approach (PCA), and about 20 TECU at the ends of the pass (see Chapter 5 for details). From Figure 4.6, at PCA, $\varphi_{i2} \approx 3$ radians, $\varphi_{i3a} \approx 0.1$ radians, and $\varphi_{i3b} \approx 0.01$ radians, while at the ends of the pass, $\varphi_{i2} \approx 5$ radians, $\varphi_{i3a} \approx 0.2$ radians, and $\varphi_{i3b} \approx 0.02$ radians. For this example, φ_{i3a} and φ_{i3b} have a negligible effect on the image, but φ_{i2} is at a level where it may begin to degrade image quality. The severity of that degradation is evaluated in the next section.

The phase contributions from the plot can also be compared to the rule-of-thumb values calculated from Equations 4.35, 4.39, and 4.41. From the calculations used to produce Figure 4.6, with $N_T = 12$ TECU, $\varphi_{i1} \approx 680$ radians, $\varphi_{i2} \approx 2.8$ radians, $\varphi_{i3a} \approx 0.079$ radians, and $\varphi_{i3b} \approx 0.012$ radians. Thus, $\varphi_{i2}/\varphi_{i1} \approx 1/240$, $\varphi_{i3a}/\varphi_{i1} \approx 1/8600$, and $\varphi_{i3b}/\varphi_{i1} \approx 1/57{,}000$, while the order-of-magnitude values calculated in the previous section were $\varphi_{i2}/\varphi_{i1} \approx 1/300$, $\varphi_{i3a}/\varphi_{i1} \approx 1/4500$, and $\varphi_{i3b}/\varphi_{i1} \approx 1/45{,}000$. In this case, the rough estimates of φ_{i2}, φ_{i3a}, and φ_{i3b} from Equations 4.35, 4.39, and 4.41 are within a factor of about two of the actual values.

For a different perspective, φ_{i2} and φ_{i3a} are plotted against frequency in Figure 4.7, again for the parameters of pass 8084a, and for $N_T = 5$, 10, and 20 TECU. For this example, φ_{i3a} is only significant ($> \pi/4$ radians) for frequencies below about 180 MHz, while φ_{i2} is significant for frequencies below about 500 MHz. Note that φ_{i3a} increases more rapidly

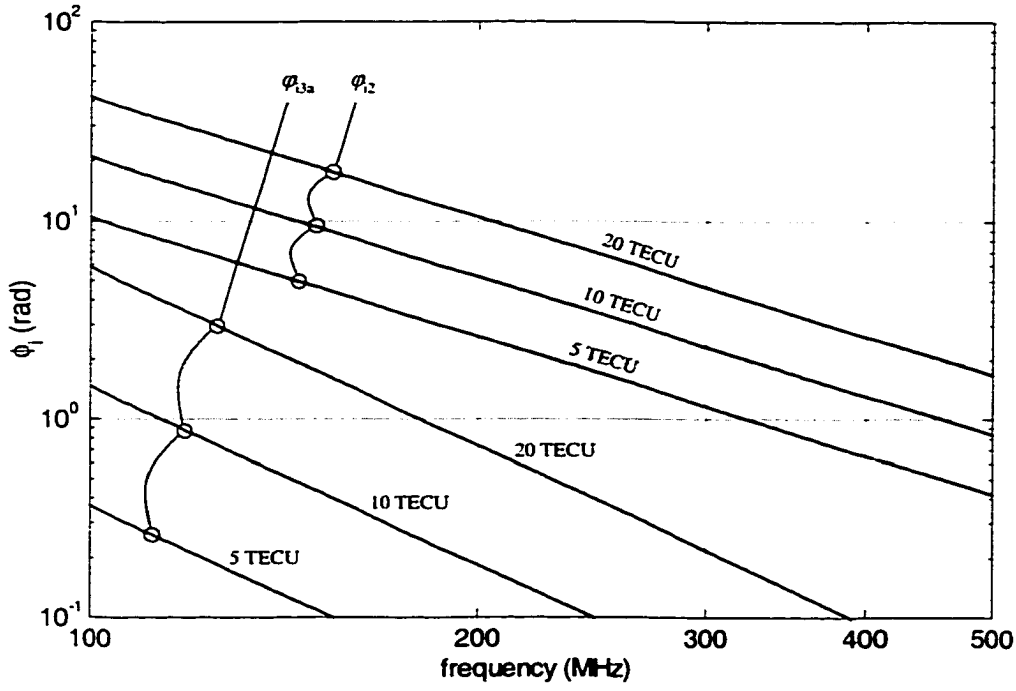

Figure 4.7: An example of φ_{i2} and φ_{i3a} versus frequency for pass 8084a. The electron-density profile and geomagnetic field are the same as those used in Figure 4.6.

than φ_{i2} with TEC and decreasing frequency; for lower frequencies or higher TEC levels, φ_{i3a} may also be needed in the model. At 150 MHz, for this example, φ_{i3a} becomes larger than φ_{i2} when $N_T > \sim 200$ TECU.

To get an idea of the sensitivity of the higher-order terms to the shape of the electron-density profile, the calculations used in constructing Figures 4.6 and 4.7 were repeated for a uniform density profile extending upward from 100 km. The higher-order phase contributions for the uniform profile differ from those in the figures by less than about 25% at all TEC levels. Note that for a uniform profile, φ_{i2} is smaller, while φ_{i3a} is larger. The difference between the actual profile and the IRI model (or its Chapman fit) will be somewhat less than the difference between the IRI model and the uniform profile. Thus, if the TEC is accurately known and the IRI profile is used, it should be possible to predict φ_{i2}, φ_{i3a}, and φ_{i3b} to significantly better than 25%.

4.6.4 Defocusing Effects of the Higher-Order Terms

The higher-order terms—φ_{i2}, φ_{i3a}, and φ_{i3b}—affect range and cross-range resolution in a manner similar to how the first-order term affects range and cross-range resolution—that is, through phase contributions to the radar signal. As a result, the techniques used in Sections 4.2, 4.3, and 4.4 to analyze the effects of residual TEC (the first-order term) can also be used to analyze the effects of the higher-order terms on the radar image. However, the blurring effects of the higher-order terms differ, to some extent, from those of the first-order term due to their different functional forms. Also, the higher-order terms are much smaller than the first-order term, so their effects may be negligible, depending on frequency, bandwidth, aperture, and ionospheric conditions. As long as the higher-order terms have a phase contribution less than about one radian, their effects on the image are negligible. For larger phase contributions, those effects need to be evaluated. This section describes one approach to performing that evaluation.

For the higher-order terms, range blurring again is caused by the nonlinear component of the phase contribution across the signal frequency band, while cross-range blurring is caused by the nonlinear component of the phase contribution across the aperture. For the φ_{i2} term, the phase contribution goes as $1/f^2$, while for the φ_{i3a} and φ_{i3b} terms it goes as $1/f^3$. In both the range and cross-range directions, the magnitude of the nonlinear components of the unmodeled ionospheric phase contributions are inversely related to frequency, so the lower frequency components of the radar signal are more severely defocused.[9]

The φ_{i2} term is the dominant component of the unmodeled ionospheric phase contribution in most situations, so its effects are the focus of this section. If φ_{i2} can be estimated with sufficient accuracy, those effects can be removed from the radar data. If both the φ_{i1} and φ_{i2} terms are compensated in the radar data with sufficient accuracy, the φ_{i3a} and φ_{i3b} terms can become the dominant sources of unmodeled phase. However, given their typical values, as calculated in the previous section, it is unlikely that the φ_{i3a} and φ_{i3b} terms would have a measurable effect in most situations. If they are deemed important for a specific problem, their effects can be evaluated with the same techniques used in the previous sections for φ_{i1}, and in this section for φ_{i2}.

[9]Note that residual range error produces the reverse effect; since range errors have a phase contribution that increases linearly with frequency, the largest phase error, and thus the worst defocusing, occurs in the higher frequency components of the radar signal.

In the range direction, image blurring is evaluated by examining the quadratic component of the φ_{i2} phase term, just as it was evaluated by examining the quadratic component of the TEC phase term in Section 4.2. First, expand φ_{i2} from Equation 4.30 in positive powers of f about the center frequency, f_c,

$$\varphi_{i2}(f) = \frac{beS_2}{2\pi^2 cm} \cdot \frac{1}{{f_c}^2} \left(1 - \frac{2}{f_c}(f - f_c) + \frac{3}{{f_c}^2}(f - f_c)^2 + \cdots\right), \tag{4.42}$$

where

$$S_2 = \int NB\cos\Theta dl. \tag{4.43}$$

At the edge of the frequency band, the quadratic term is then

$$\varphi_{i2e} = \frac{beS_2}{2\pi^2 cm} \cdot \frac{3}{{f_c}^4} \cdot (f_{max} - f_c)^2 = \frac{3beS_2}{8\pi^2 cm} \cdot \left(\frac{B_F}{f_c}\right)^2. \tag{4.44}$$

For a quadratic phase error less than $\pi/4$ radians, the requirement is $\varphi_{i2e} < \pi/4$, or

$$\left(\frac{f_c}{B_F}\right)^2 > \frac{3be}{2\pi^3 cm} \cdot S_2$$

$$\frac{f_c}{B_F} > 213 \cdot \sqrt{S_2}. \tag{4.45}$$

For a given center frequency and bandwidth, this equation specifies the value of S_2 above which φ_{i2} begins to degrade image range resolution.

For pass 8084a, $f_c = 300$ MHz and $B_F = 2/3$, so $f_c/B_F = 4.5 \times 10^8$. The maximum value of S_2 can be estimated from the measured TEC, along with an IRI profile and a geomagnetic field model, as was done when calculating φ_{i2} for Figure 4.6. Using those results for the worst-case $N_T = 20$ TECU (at the endpoints of the aperture), $S_2 \approx 9.0 \times 10^{12}$, so $213 \cdot \sqrt{S_2} = 6.3 \times 10^8$. Thus, the requirement of Equation 4.45 is not satisfied at the end of the aperture, although the quadratic component of φ_{i2} at that point, $1.4 \times (\pi/4)$, is still relatively small. If left uncompensated, the φ_{i2} term would produce a small amount of blurring in the range direction for this example.

In the cross-range direction, focus quality is compromised by the nonlinear component of the φ_{i2} phase variations across the aperture—just as in the case of residual TEC as described in Section 4.3. Again, the residual phase requirement in the cross-range direction may be more restrictive than in the range direction since the full φ_{i2} phase contribution

impacts cross-range resolution, not just its quadratic frequency dependence. The φ_{i2} phase contribution varies across the aperture with slow-time, s, because S_2 changes from pulse to pulse. From Equation 4.30, the φ_{i2} dependence on slow-time can be written as (see also Equation 4.21)

$$\varphi_{i2}(f, s) = \frac{be}{2\pi^2 cmf^2} \left(S_{2c} + S_{2l}(s) + S_{2nl}(s)\right), \tag{4.46}$$

where S_{2c} and $S_{2l}(s)$ are the constant and linear components of $S_2(s)$, and $S_{2nl}(s)$ is the nonlinear component. To analyze the cross-range blurring, the phase contributions at the center frequency, f_c, are evaluated across the aperture as a function of slow-time (see Section 4.3 for details). At the center frequency, f_c,

$$\varphi_{i2}(s) = \frac{be}{2\pi^2 cmf_c^2} \left(S_{2c} + S_{2l}(s) + S_{2nl}(s)\right). \tag{4.47}$$

The nonlinear term in the above equation degrades cross-range resolution. For $\varphi_{i2}(s)$ to have a negligible effect on cross-range resolution, a sufficient condition is that the nonlinear component be less than $\pi/4$ radians, giving

$$\begin{aligned} \frac{be}{2\pi^2 cm{f_c}^2} \cdot S_{2nl}(s) &< \frac{\pi}{4} \\ S_{2nl}(s) &< \frac{\pi^3 cm}{2be} {f_c}^2 = 1.7 \times 10^{-5} \cdot {f_c}^2. \end{aligned} \tag{4.48}$$

This equation places a limit on the nonlinear variations of $S_2(s)$ across the aperture. It may be difficult to evaluate in practice since calculation of $S_2(s)$ requires knowledge of the electron density and the vector **B** along the ray path for each radar pulse.

If the requirements of Equations 4.45 and 4.48 are met—that is, if the center frequency is high enough or the bandwidth is small enough—φ_{i2} has a negligible effect on image quality; otherwise, φ_{i2} should be estimated and compensated in the radar data. Two approaches can be taken. First, the shape of the electron-density profile can be estimated with, say, a Chapman or IRI profile, and the geomagnetic field can be modeled. Then TEC uniquely determines S_2, so both φ_{i1} and φ_{i2} phase corrections can be made to the radar signal. Alternatively, S_2 can be treated as yet another unknown in the autofocus procedure. Its variations across the aperture would then be described with a polynomial, and the autofocus procedure would be used to search for the coefficients that provide the best focus. Since the φ_{i2} phase contribution is much smaller than the TEC phase contribution, a lower-order

polynomial would probably be satisfactory. The appropriate order could be evaluated from the TEC phase contribution and Equation 4.34. Of course, adding free variables to the autofocus search is undesirable, because it increases the amount of computation. Since the exact shape of the electron-density profile is unknown, the best solution may be a hybrid. For example, use a nominal profile to estimate the bulk of the φ_{i2} phase contribution, then use autofocus to search for a small, constant or at least low-order, correction to that estimate.

4.7 Refraction Effects

To this point it has been implicitly assumed that the ray follows a straight-line path between the radar and satellite. That assumption is an approximation, since variations in the refractive index cause the ray to bend as it passes through the troposphere and ionosphere. As a result, the actual path of the ray differs from the straight-line path, causing a change in the phase path length from that previously calculated. The bending of the ray affects the phase of the received signal, and thus the radar image.

This section analyzes the effects of ray bending on the radar imaging problem. For frequencies greater than about 150 MHz, this research found that ray bending has no significant effect, except possibly for the combination of large TEC levels and low elevation angles. The complexities of the analysis preclude a general solution for the additional phase path caused by ray bending. Closed-form solutions can be obtained, however, for a few simple electron-density profiles in a spherically symmetric geometry (e.g., see *Croft and Hoogasian*, 1968). For more realistic situations, numerical integration is required.

For the purposes of this section, the ionosphere is modeled as isotropic ($\mathbf{B} = 0$), stationary, and spherically symmetric. Such a model is suitable for determining the first-order effects of ray bending, and thus the significance of ray bending to satellite imaging at VHF.

4.7.1 Ray Bending in the Troposphere and Ionosphere

Tropospheric ray bending causes the satellite to appear at a slightly greater distance and higher elevation than would be measured with free-space propagation (e.g., *Skolnik*, 1981, pp. 447-450). The apparent increase in range is a result of the combination of a lower propagation velocity in the troposphere than in free space and a small bending of the ray. It is on the order of a 1–2 meters vertically, depending on atmospheric conditions, and

about a factor of 3 larger at 20-degrees elevation. The difference in elevation angle between the straight line to the satellite and the curved ray path at the radar is called the *angular error at the source*. This difference is on the order of a few hundredths of a degree for elevation angles between about 30 and 60 degrees (the typical elevation-angle range during data collection in this research). Further discussion of tropospheric refraction and examples of its effects can be found in *Smith and Weintraub* (1953), *Millman* (1965), *Bean and Dutton* (1966), *Brookner* (1977a), and *Zebker et al.* (1997).

Tropospheric refraction is not dispersive at radio wavelengths. The refractive index is independent of frequency up through the microwave band, so all frequency components have the same velocity and follow the same ray path. Neither the angular error at the radar nor the increase in apparent range present a problem for imaging of satellite at meter wavelengths. The angular error is much smaller than the antenna beamwidth and has no measurable effect on the signal. The increase in apparent range is a small component of the total range error. As such, its effects are removed by autofocus.[10]

Variations in refractive index also produce ray bending in the ionosphere. Since the refractive index is lower in the ionosphere than at the ground, a satellite in the middle of the ionosphere appears at a higher elevation than would be expected from a straight-line path. This is illustrated in Figure 4.8.[11] As in the troposphere, the nonzero refractivity leads to an increase in the group delay or apparent range to the satellite. The frequency dependence of the refractivity in the ionosphere, however, causes the effects of refraction to differ from those of the troposphere. Since the magnitude of the refractivity is proportional to the inverse square of frequency, the curvature of the ray is also inversely related to frequency. As a result, lower frequency components of the signal deviate further from the straight-line path, producing differing dispersion characteristics from those previously calculated for the straight-line path. The change in the dispersion characteristics, if significant, should be modeled and removed from the signal. A procedure for calculating the change in the dispersion characteristics is described in this section.

Although the actual ray has a longer geometric length than the straight-line ray, its phase path length is shorter than that of the straight-line ray in the same medium. This result follows from Fermat's principle, which asserts that the phase path length of the actual

[10] Note that the autofocus algorithm does not discriminate between the sources of range error, it merely finds an optimal estimate for the total.

[11] At altitudes above the peak of the electron-density profile, the refractive index increases with altitude, causing the ray to bend down in the upper ionosphere.

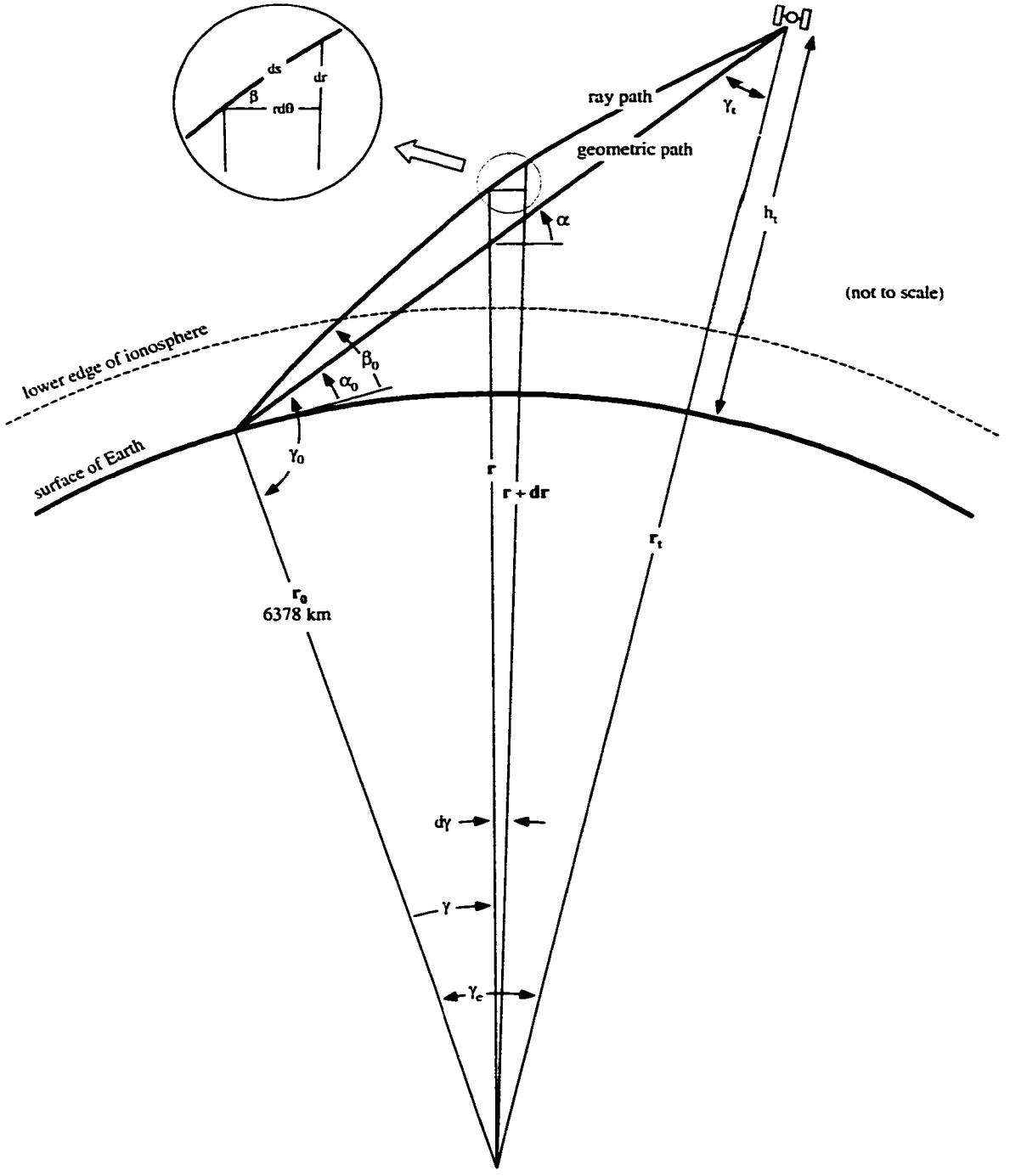

Figure 4.8: Ray path geometry. The troposphere and ionosphere are modeled as spherically symmetric shells around Earth. Variations in refractive index with altitude cause the ray path to bend. Differences between the actual path and the straight-line, or geometric, path may affect some results of previous sections.

ray between any two points is shorter than the phase path length of any other curve joining those points[12] (e.g., *Born and Wolf*, 1980, p. 128). Thus, the actual ionospheric phase contribution is less than previously calculated—albeit, negligibly so in many situations.

4.7.2 Ray Tracing[13]

A closed-form expression for the additional phase path caused by bending of the ray does not exist. This makes it difficult to obtain general conclusions about the significance of the difference between the straight-line and bent-ray phase path lengths. Solutions for specific situations, however, can be obtained through *ray-tracing* techniques. One technique for ray tracing in a spherically symmetric geometry with an arbitrary electron-density profile is described below (see also *Croft and Hoogasian*, 1968; *Budden*, 1988). It is used later in this section to calculate the dispersive effects of ray bending on Mir pass 8084a.

The ray-bending calculations use the geometry and variables illustrated in Figure 4.8. The radius vector, $\mathbf{r}$, is the vector from the center of the Earth to the ray. The radius of the Earth is r_0, and the distance from the center of the Earth to the satellite is r_t. The elevation angle of the ray, $\beta(r)$, is the angle between the normal to the radius vector and the ray. At the ground it is the *launch angle*, $\beta_0 = \beta(r_0)$. Similarly, the straight-line, or LOS elevation angle, $\alpha(r)$, is the angle between the normal to the radius vector and the straight-line connecting the radar and the satellite. At the radar the elevation angle is $\alpha_0 = \alpha(r_0)$.

With the aid of the figure, the straight-line geometry can be solved directly. The satellite altitude, h_t, and the LOS elevation angle, α_0, uniquely determine γ_t, γ_e, and the range to the target along the straight-line path, r_g, through

$$\gamma_t = \sin^{-1}\left(\frac{r_0}{r_0 + h_t}\cos(\alpha_0)\right), \tag{4.49}$$

$$\gamma_e = \frac{\pi}{2} - \gamma_t - \alpha_0, \tag{4.50}$$

$$r_g = \sqrt{r_0^2 + (r_0 + h_t)^2 - 2r_0(r_0 + h_t)\cos\gamma_e}. \tag{4.51}$$

[12]This statement of Fermat's principle has some 'neighborhood' requirements that are met for ionospheric propagation at VHF.

[13]The ray-tracing procedure of Section 4.7.2 is well known to those involved in studies of radio wave propagation (see above citations). It is described here to provide continuity in documenting the specific method used for calculating the refractive effects of the ionosphere.

In a spherically symmetric geometry, the elevation angle of the ray, $\beta(r)$, can be evaluated with the aid of Bouguer's rule,

$$rn(r)\cos\beta(r) = r_0\cos\beta_0, \tag{4.52}$$

where r is the distance from the center of the Earth to the ray, and $n(r)$ is the refractive index at r. This equation comes from Snell's law and the observation that, in a spherically symmetric geometry, $rn(r)\cos\beta(r)$ does not change along the ray path (see *Born and Wolf*, 1980). Now r_0, r, and $n(r)$ are known, and β_0 can be calculated, so Bouguer's rule provides the elevation angle of the ray at all altitudes, and thus at all points along the ray path. It can also be written in forms that will be used below:

$$\cos\beta = \frac{1}{rn} r_0\cos\beta_0 \tag{4.53}$$

$$\sin\beta = \frac{1}{rn}\sqrt{(rn)^2 - (r_0\cos\beta_0)^2} \tag{4.54}$$

$$\tan\beta = \frac{1}{r_0\cos\beta_0}\sqrt{(rn)^2 - (r_0\cos\beta_0)^2}. \tag{4.55}$$

Determining the effects of ray bending involves first 'finding' the ray path, and then integrating the parameters of interest, such as phase and group path lengths, over the curved ray. To find the curved ray, consider the differential ray segment, $d\mathbf{s}$, and the geometry illustrated in Figure 4.8. The angle subtended by the ray, γ_e, is given by:

$$\gamma_e = \int_0^{\gamma_e} d\gamma = \int_{r_0}^{r_t} \frac{dr}{r\tan\beta} = \int_{r_0}^{r_t} \frac{r_0\cos\beta_0}{r\sqrt{(rn)^2 - (r_0\cos\beta_0)^2}} dr. \tag{4.56}$$

Since γ_e is already known from Equation 4.50, Equation 4.56 can be used to find the launch angle, β_0. In Equation 4.56, β_0 is an inseparable part of the integrand of a definite integral, so the equation can only be solved with a numerical root-finding technique. The integral is also evaluated numerically. Once β_0 is known, the ray path is uniquely specified, since Bouguer's rule then gives the elevation angle at all points along the ray path.

The one-way phase path length along the curved ray is calculated through numerical integration of

$$l_{\mathrm{p,c}} = \int_0^{s_t} n\,ds = \int_{r_0}^{r_t} \frac{n}{\sin\beta}\,dr = \int_{r_0}^{r_t} \frac{rn^2}{\sqrt{(rn)^2 - (r_0\cos\beta_0)^2}}\,dr. \tag{4.57}$$

The one-way group path length (see Equation 3.31) along the curved ray is calculated through numerical integration of

$$l_{\mathrm{g,c}} = \int_0^{s_t} \frac{ds}{n} = \int_{r_0}^{r_t} \frac{dr}{n\sin\beta} = \int_{r_0}^{r_t} \frac{r}{\sqrt{(rn)^2 - (r_0\cos\beta_0)^2}}\,dr. \tag{4.58}$$

4.7.3 Evaluating the Significance of Ray Bending

This section evaluates the significance of the effect of ray bending on the signal received by the radar by comparing the phase path length along the straight-line ray, $l_{\mathrm{p,s}}$, to that along the curved ray, $l_{\mathrm{p,c}}$. The difference in the radar signal phase due to ray bending is then calculated from the difference between the actual and straight-line phase path lengths.

For the straight-line ray, the phase path length is given by

$$l_{\mathrm{p,s}} = \int_0^{s_t} n\,ds = \int_{r_0}^{r_t} \frac{n}{\sin\alpha}\,dr = \int_{r_0}^{r_t} \frac{rn}{\sqrt{r^2 - (r_0\cos\alpha_0)^2}}\,dr, \tag{4.59}$$

where the expression for $\sin\alpha$ is obtained by observing that, in the geometry of the figure,

$$r\cos\alpha = r_0\cos\alpha_0. \tag{4.60}$$

The difference between the phase observed in the received signal and that predicted by the straight-line approximation is

$$\varphi_{\mathrm{e,c}}(\alpha_0, h_t, f) = -2k(l_{\mathrm{p,s}} - l_{\mathrm{p,c}}) \tag{4.61}$$

$$\varphi_{\mathrm{e,c}}(\alpha_0, h_t, f) = -2k\int_{r_0}^{r_t} n\left[\frac{1}{\sqrt{1-\left(\frac{r_0\cos\beta_0}{nr}\right)^2}} - \frac{1}{\sqrt{1-\left(\frac{r_0\cos\alpha_0}{r}\right)^2}}\right] dr. \tag{4.62}$$

Thus, the error in the estimate of signal phase caused by ray bending is a function of frequency, satellite altitude, elevation angle, and the electron-density profile.

The effects of the $\varphi_{e,c}$ phase errors on the image can be analyzed in the same manner as phase errors produced by uncompensated TEC, as done in the previous sections. In both cases, the phase errors vary with frequency and elevation angle. Note, however, that the phase errors caused by ray bending have a different functional dependence on frequency and elevation angle than those due to uncompensated TEC. The general effects, as discussed for uncompensated TEC, also apply here: (1) variations across the aperture degrade cross-range resolution if they exceed about $\pi/4$ radians, (2) the linear component of the frequency dependence causes a range shift that is corrected by autofocus, and (3) the nonlinear component of the frequency dependence degrades range resolution if it exceeds about $\pi/4$ radians across the band.

4.7.4 Ray Bending Effects for Mir Pass 8084a

To examine the magnitude of the ray bending effects, this research evaluated β_0 and $\varphi_{e,c}$ for the spherically symmetric component of the ionosphere observed during Mir-pass 8084a; the results are plotted in Figures 4.9 and 4.10. The Chapman fit to the electron-density profile, as described in Section 3.1, is used with $N_m = 6.3 \times 10^{11} e^-/m^3$, $z_m = 266$ km, and $H = 71$ km. The satellite altitude, h_t, is 378 km, and the Earth radius, r_0, is the WGS-84 value, 6378.137 km. The calculations are made for satellite elevation angles of $\alpha_0 = 30$, 45, 60, and 75 degrees, and for frequencies between 200 and 400 MHz.

The angle error at the radar, $\beta_0 - \alpha_0$, is plotted in Figure 4.9. As expected, the angle error is largest at low frequencies and low elevation angles. Also, $\beta_0 - \alpha_0 > 0$, so the satellite appears higher than would be expected from the straight-line approximation. For this example, the worst-case launch-angle error, occuring at 200 MHz and 30 degrees elevation, is less than 3/100 of a degree. This small error has no measurable effect on the received signal.

The additional two-way signal phase, $\varphi_{e,c}$, caused by bending of the ray is plotted in Figure 4.10. As expected from Fermat's principle, the actual phase path is less than that calculated along the straight-line ray, as indicated by the negative values in the figure. For this example, the worst-case signal phase error, again occuring at 200 MHz and 30 degrees elevation, is less than about 0.5 radians. This is sufficiently below the $\pi/4$ threshold to have negligible effect on the image in either range or cross-range. However, if the phase error were larger, its effects would need to be evaluated not from its absolute value, but from its variations with frequency and aspect angle.

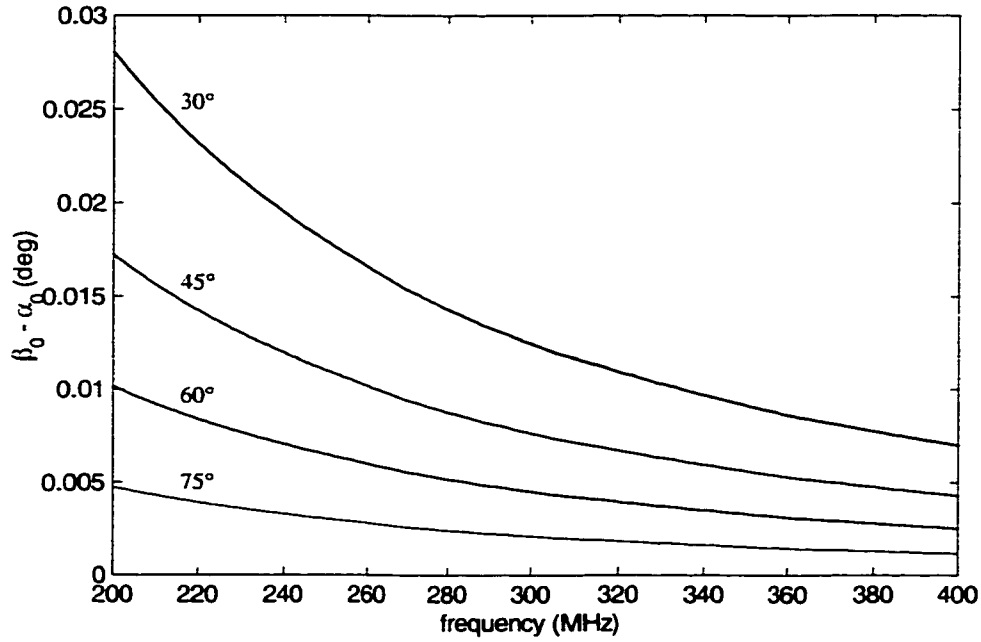

Figure 4.9: An example of launch-angle error at the radar for target elevation angles of 30°, 45°, 60°, and 75°. This is the angle difference between the actual ray and the straight-line approximation at the radar for Mir pass 8084a over the frequency band of the radar waveform. A spherical shell model was used for the ionosphere with the Chapman profile illustrated in Figure 3.1.

Based on this example, it is expected that ray-bending effects can be ignored in moderate ionospheric conditions for frequencies above 200 MHz and elevation angles above about 30 degrees. When using frequencies below 200 MHz, or when large TEC levels are observed, ray bending may affect image quality, especially at low elevation angles. In those cases, the preceding analysis could be repeated using an estimate of the electron-density profile to determine the signal phase error caused by ray bending. That signal phase error could then be compensated, to first-order, to remove the effects of ray bending from the radar data.

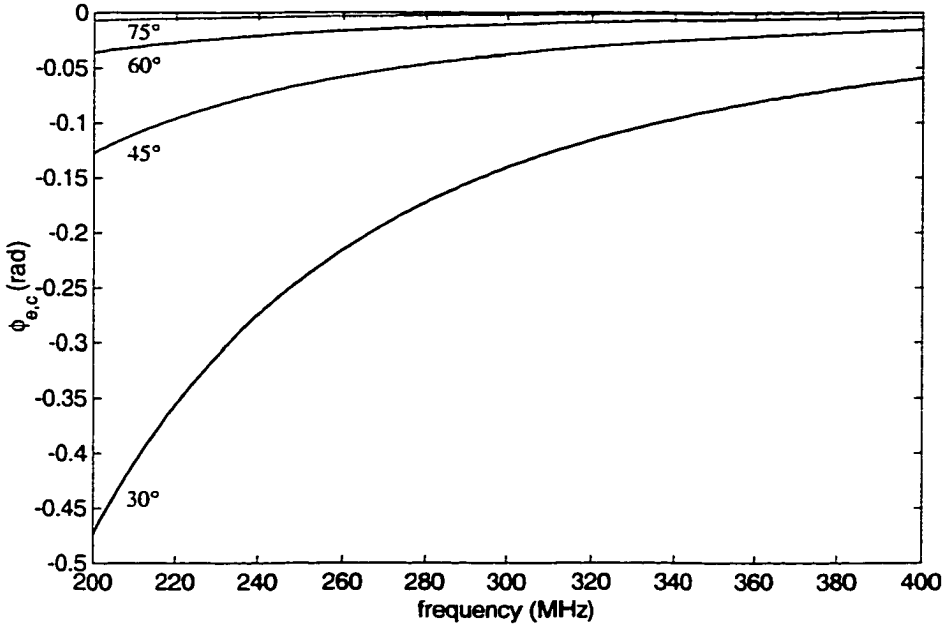

Figure 4.10: An example of the two-way signal phase error caused by ray bending at target elevation angles of 30°, 45°, 60°, and 75°. The system and ionosphere parameters are those of Mir pass 8084a, and the same as those used in Figure 4.9.

Chapter 5

Experimental Results

The theory and techniques of the previous chapters were developed to accurately estimate and remove ionospheric effects from radar data. This chapter presents evidence that those developments are valid and applicable to actual data.

Early in the project, the author generated simple synthetic data sets to be used in testing of the techniques and to aid in their development. Positive results from testing with the simulated data provided some confidence that the theory was correct and that the techniques could be used to estimate and remove ionospheric effects. The true test, however, is whether such techniques work with actual data. Radar data sets collected at Stanford, California, and Ascension Island, United Kingdom, were used to further test and refine the techniques, and to quantify algorithm performance.

Between December 1996 and January 1998, the research team collected approximately 20 usable data sets using the Stanford 'Big Dish' as satellites passed in view of the radar through the benign mid-latitude ionosphere.[1] After initial success at Stanford, members of the team made three trips to Ascension Island to install equipment and collect radar data during satellite passes through the equatorial ionosphere. They installed and partially tested the radar during the first trip in October 1997. They completed radar setup and testing and collected approximately 10 usable data sets during the second trip in March 1998. On the final trip, in June 1998, they collected approximately 10 more usable data set.

[1] Several data sets are deemed unusable due to radar system problems or ephemeris errors greater than about ±5 km.

Table 1.1 lists some of the parameters that characterize the Stanford and Ascension radar systems. Appendix A describes the two radar systems.

This chapter provides a detailed review of one data set, designated 8084a, to illustrate the data-processing procedures developed in this research and to demonstrate the results and performance of those procedures. The geometry and ionospheric conditions extant during collection of this data set are those used for illustrations earlier in this thesis. The implementation of the data-processing procedures is described in Appendix B. Example images from other data sets are included in Appendix C.

5.1 Pass 8084a, the Mir Space Station

The author collected the 8084a data set from Ascension Island on March 25, 1998, during one pass of the Mir space station. Radar images and total electron content estimates are included in this chapter, together with some of the intermediate results obtained during data processing.

Two measurements, from the 8084a data set, verify the performance of the imaging and TEC-estimation procedures. First, the resolution in the radar image is compared to the theoretical system-limited resolution. Second, TEC estimates calculated independently from six subapertures are checked for consistency in their areas of overlap. These verification steps indicate that, at least for this data set, the data-processing procedures are able to achieve full image resolution together with the TEC-estimation accuracy derived in Chapter 4.

Table 5.1 lists some of the parameters that characterize the radar configuration and the radar/satellite data-collection geometry for pass 8084a.

5.2 Flight Track Geometry

The flight track geometry during the 160-second data-collection period is illustrated in the plots in Figure 5.1. During that period, Mir traveled approximately 1180 km along its orbit between the points marked '×' and 'o' in the 'Lat/Lon' plot. The data-collection period is centered on the *point of closest approach* (PCA), which occurs at about record 4100 and is marked with an '∗' in the three plots. At PCA, Mir is northeast of the island at a range of 448 km and an elevation of 56.5 degrees.

Pass name	8084a
Target	Mir
Site	Ascension Island
Date (UT)	March 25, 1998
Start time (UT)	08:22:34.0
PRF	50 Hz
Data-collection period	160.0 s
Number of pulses	8000
Samples per pulse	32768 (complex)
Satellite altitude	378 km
Maximum elevation	56.5°
Satellite stabilization	inertial
Full pass aperture	108.7°
Out-of-plane angle	$< 0.8°$
Sunspot number	79
vTEC to target altitude	$\sim 1 \times 10^{17}\ e^-/m^2$
Radar parameters	as specified in Table 1.1
Waveform parameters	as specified in Table 1.1

Table 5.1: Pass 8084a parameters. The radar data set, named 8084a, was collected at Ascension Island during one pass of the Mir space station. That data set is reviewed in detail in this chapter.

As described in Chapter 2, the ISAR imaging algorithm uses a coordinate frame that is fixed to the target, and oriented such that the LOS vectors remain as close as possible to the image plane. The direction to the radar in that target-fixed frame must be calculated for each radar pulse. The calculation is complicated by the translation and rotation of the radar, or Earth, frame relative to the target frame during the pass. The calculation accounts for the LOS vector directions, the type of satellite stabilization (in this case, inertial), and Earth rotation. Once a coordinate frame has been fixed to the target, it is rotated so that two user-selected LOS vectors lie in the image, or x-y, plane (see Figure 2.3). In this case, the LOS vectors at 1/4 and 3/4 of the way through the pass—that is, at records 2000 and 6000—are selected. Those LOS vectors then define the orientation of the target frame along with the image plane.

The spherical azimuthal and polar angles specifying the direction to the radar in the target frame are plotted in Figure 5.2. In the figure, the azimuthal angle, θ, is the aspect angle, and the polar angle, ϕ, is related to the out-of-plane angle, ξ, by $\xi = 90 - \phi$ (degrees).

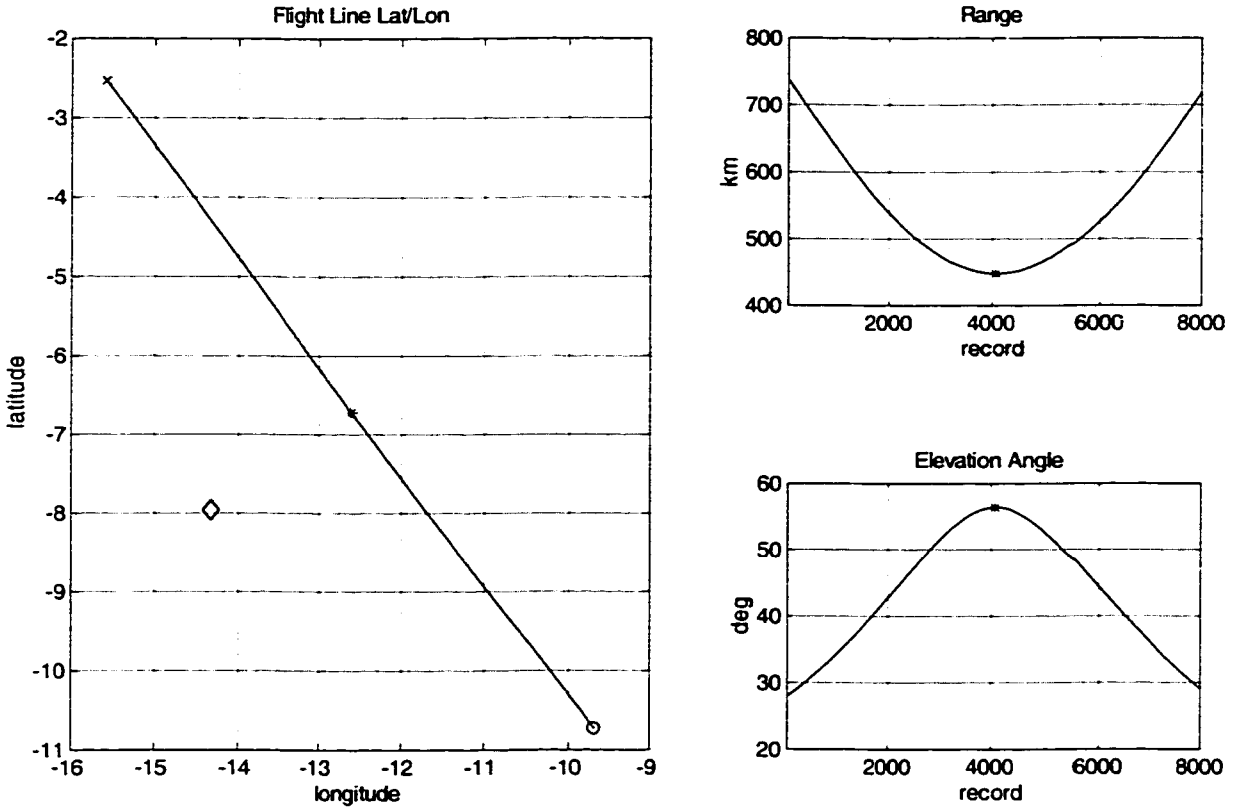

Figure 5.1: Flight track for pass 8084a. The 'Lat/Lon' plot (left) illustrates the latitude and longitude of the satellite during the data-collection period. Data collection begins at the point marked '×' and ends at the point marked 'o.' The '◇' indicates the location of Ascension Island. The range plot (upper right) illustrates the range to the satellite as a function of record number. The elevation angle plot (lower right) illustrates the elevation angle of the satellite at the radar, again as a function of record number. To determine the time in the pass, divide the record number by the PRF, 50 Hz.

The plot of the aspect angle indicates a full-pass aperture of 108.7 degrees, while the plot of the polar angle indicates a maximum out-of-plane angle of less than about 0.8 degrees.

If the full 108.7-degree angular aperture were used in forming an image, the potential cross-range resolution would be about 0.3 m at the 300-MHz center frequency. However, the apparent resolution, as measured by the 3-dB width of target features in the image, is subject to the scattering characteristics of the parts of the target (see Section 2.8). In the experimental data collected to date, this research found that scattering from most parts of the satellite is sufficiently directional, in comparison to the large span of the aspect angle, that ideal system-limited resolution is not observed in the final image. Near-ideal

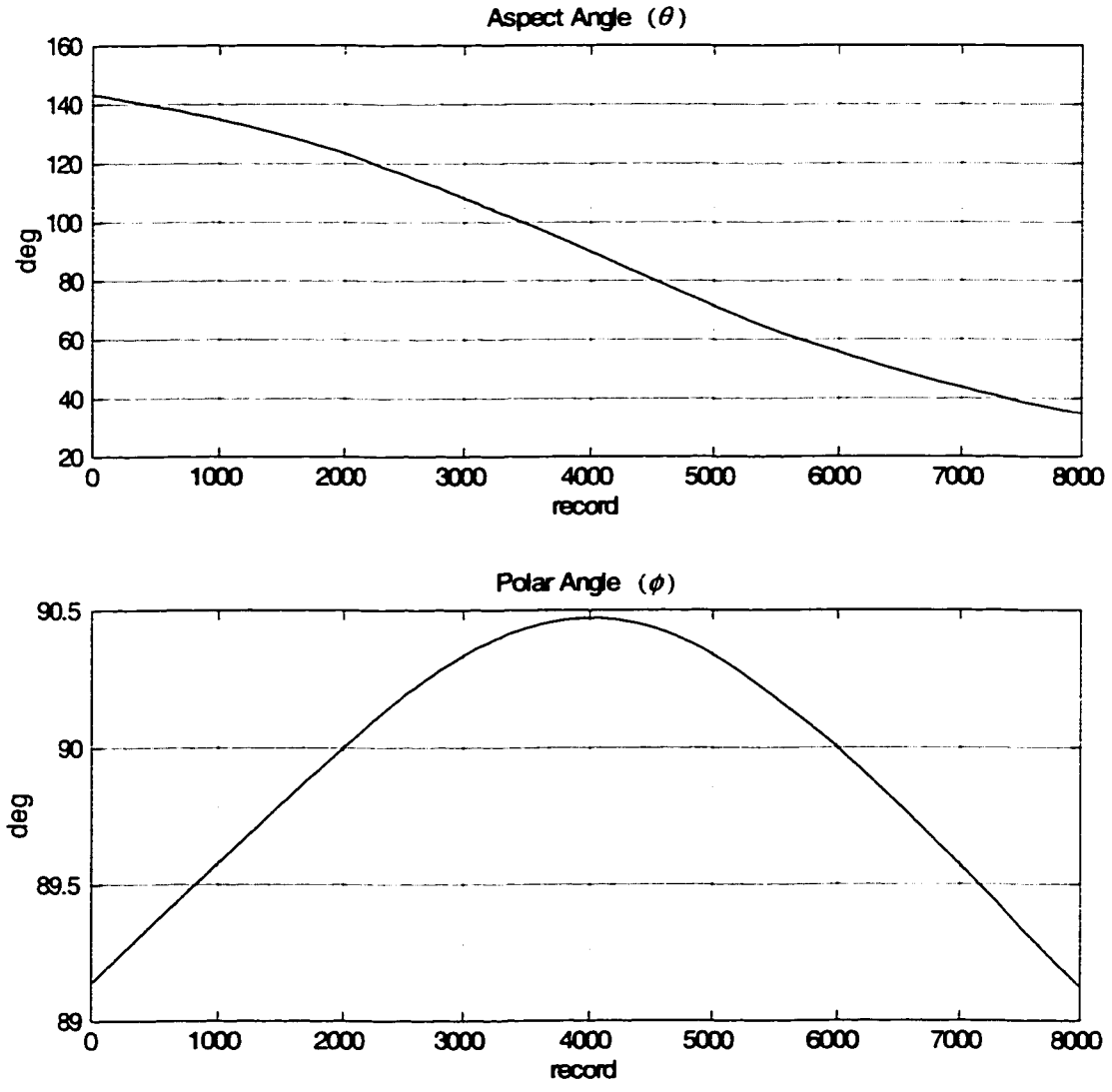

Figure 5.2: Aspect and polar angles for pass 8084a. These are the angles of the LOS vectors in the target-fixed coordinate frame. The aspect angle is the azimuthal angle in the x-y, or image, plane. The polar angle, ϕ, is related to the out-of-plane angle, ξ, through $\xi = 90 - \phi$ (degrees).

resolution has been demonstrated, however, on some parts of the satellite using subapertures over which the complex scattering amplitude of those parts remains reasonably constant.

The out-of-plane angle reaches a maximum of 0.8 degrees at the beginning and end of the pass. The equations referenced in Section 2.2 can be used to evaluate the impact of that angle on the resolution of scatterers outside the image plane, assuming a target size of about 30 m and a wavelength of about 1 m. In this experiment, the out-of-plane angle has a negligible effect on image quality, provided the angle remains less than about 2 degrees. The stability of the satellite attitude, however, also affects the out-of-plane angle; satellite 'wobble' produces an additional sinusoidal variation in the actual out-of-plane angle. From the empirical evidence provided by this data set, it appears that the variations in the out-of-plane angle remain less than 2 degrees over the apertures used for imaging in the following sections.

The radar image is a projection of the complex scattering amplitude of the target onto the image plane. From the perspective of the radar, the image plane is defined approximately by a planar fit to the LOS vectors in the radar frame. For image interpretation purposes, then, the image shows the orientation of Mir at PCA in a plane that is tipped toward the radar from Mir's horizon by the elevation angle, 56.5 degrees.

Figure 5.2 illustrates that the aspect angle changes more slowly at the ends of the pass than at the center. From the ISAR perspective, that variation in the rate of change of the aspect angle can be viewed as a target rotation rate that varies between a maximum of 0.95 degrees/s near PCA and a minimum of 0.39 degrees/s at the end of the pass. These rotation rates, together with the PRF, determine the adequacy of the sampling of the aperture. From Equation 2.5, with a minimum wavelength of 0.75 m, corresponding to the maximum frequency of 400 MHz, and a maximum cross-range distance between any two points on the target of less than 40 m, the maximum change in aspect angle between pulses is $\delta\theta_{\max} = \lambda_{\min}/2W_{\mathrm{cr}} = 0.75/80 = 0.0094$ radians $= 0.54$ degrees. The minimum PRF, given by Equation 2.6, is then $\mathrm{PRF} \geq \omega_{\mathrm{t}}/\delta\theta_{\max} = 0.95/0.54 = 1.8$ Hz at PCA, and 0.72 Hz at the end of the pass. The actual PRF of 50 Hz oversamples the Doppler frequency space by a factor of 28 or more. The pulses could be decimated before imaging but all are used in forming the final image to maximize the SNR. The aperture oversampling factors, in this example, improve the SNR over the minimum PRF case by 14.5 dB at the center of the pass and 18.8 dB at the end of the pass. This difference acts to partially compensate for lower SNR at the ends of the pass caused by the R^{-4} dependence of target echo power.

Specifically, the R^{-4} dependence leads to a single-pulse SNR that is 8.7 dB lower at the ends of the pass than at PCA. The higher oversampling factors at the ends of the pass recover about 3.9 dB of that difference during imaging.

5.3 Preprocessing

Preprocessing includes data-quality analysis, pulse compression, and filtering to remove interference (see Appendix B for implementation details). A few of the intermediate results are illustrated and described in this section.

The average amplitude spectrum of the data set from pass 8084a was calculated as the mean spectral magnitude of all 8000 records. The results are plotted in Figure 5.3. The plot covers the full 250-MHz bandwidth of the digitized data with a spectral bin width of about 7600 Hz. The envelope is shaped largely by 100-MHz low-pass filters at the inputs to the I and Q digitizers. This gives a ±100-MHz signal bandwidth, centered on the 300-MHz frequency of the local oscillator. The variations in the level of the envelope are an indication of the spectral flatness of the receiver system, including antenna, preamplifier, cabling, receiver, and digitizer. The 'notch' at 300 MHz is due to the inability of the base-band system to respond to frequencies below about 100 kHz. The two strong narrowband 'spikes' at 198.6 and 402.0 MHz are tones that are coupled into the signal path for use in analyzing the system's performance. The comb of narrowband signals between 240 and 270 MHz is external interference, thought to be coming from geostationary satellites. Some of the smaller spikes are also external interference, while others are system intermodulation products. The spike at 175 MHz is an artifact of the digitizers used in this experiment.

In the VHF band, external interference can significantly degrade system performance. The interference levels in Figure 5.3 are relatively low with respect to those observed at other locations, since these data were collected at a remote site on Ascension Island. In contrast, the problem is especially severe at Stanford, where the urban environment generates a high level of interference that is coupled into the signal path through the antenna sidelobes. Sources of such interference include VHF TV, airborne communications, land-based mobile communications, and radio repeater stations. At Ascension, the interference levels are orders of magnitude lower than those at Stanford, but to maximize the SNR in the final image, the interference still needs to be excised from the Ascension data. That excision is

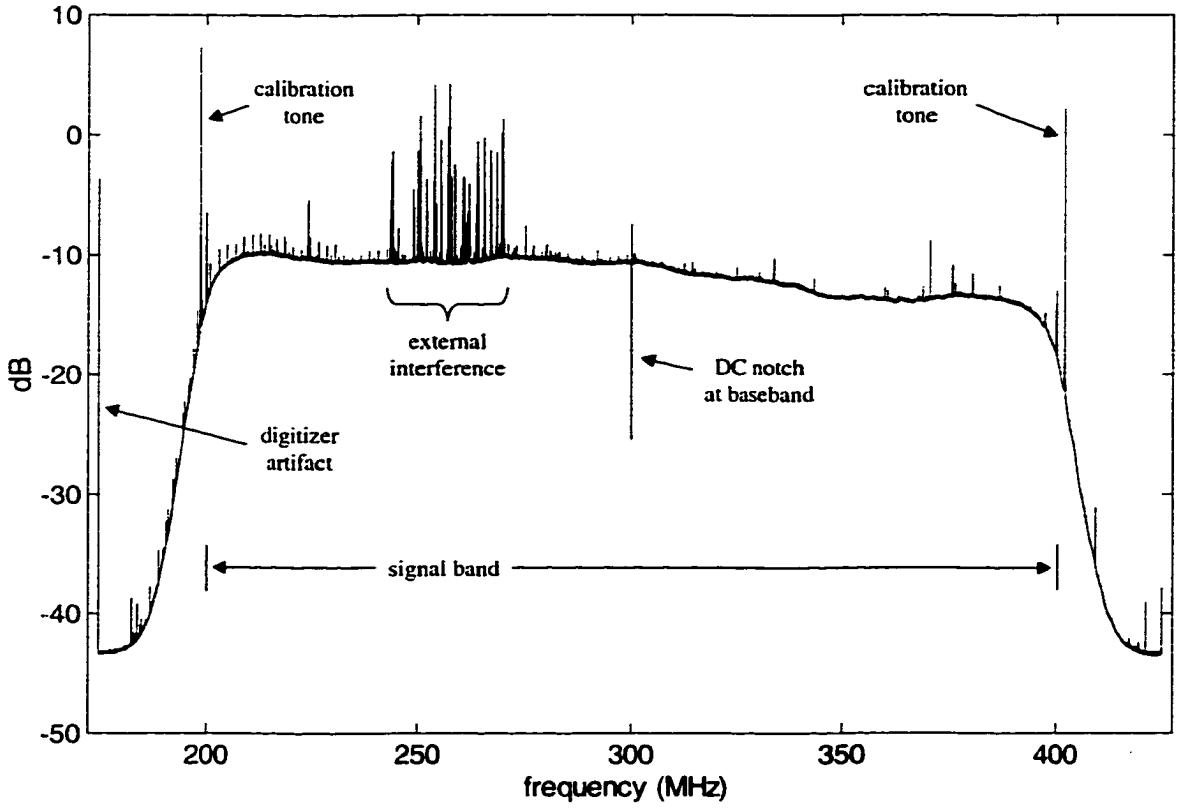

Figure 5.3: Average spectrum for pass 8084a. The satellite echoes and system noise are largely contained in a 200-MHz bandwidth covering frequencies between 200 and 400 MHz. The energy in the envelope is dominated by system noise. The spikes between 200 and 400 MHz are due to external interference. The two spikes at 198.6 and 402 MHz are system-generated tone signals.

performed by 'notching,' or zeroing-out, the spectral bins that are dominated by interference signals.

Most of the energy in the spectral envelope plotted in Figure 5.3 comes from sky noise and front-end amplifier noise. The Mir echo is present in the spectral data, but it is not apparent in the plot since it is at least 20 dB below the noise level.

After the average spectrum is reviewed to evaluate interference levels, the radar data are filtered to provide windowing, range compression, and interference excision, as described in Section B.1.4. Figure 5.4 is a plot of the maximum amplitude, after filtering, in each of the 8000 records. This plot is used to assist in the initial detection of a target in the data records. In contrast, other applications often use a plot of the average power in each record

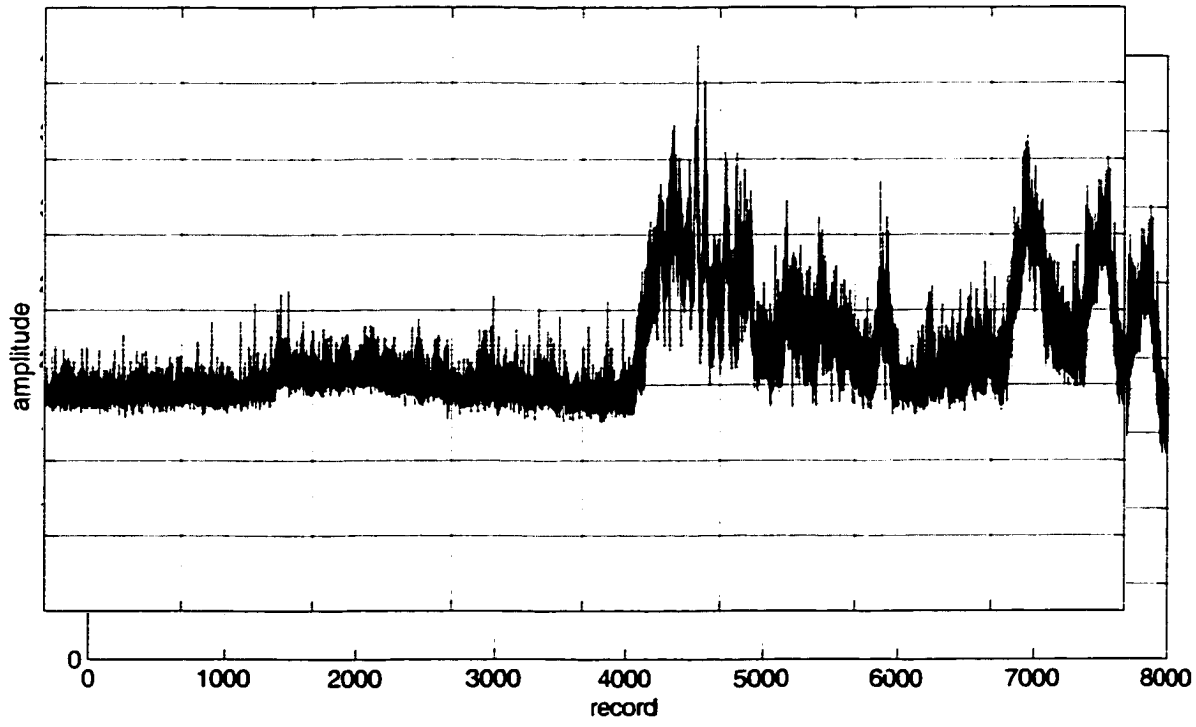

Figure 5.4: Maximum amplitude in each record before TEC compensation for pass 8084a. The median value of the maximum noise amplitude in a single record is about 145. The target echo is not visible in the noise in the early part of the pass, but is well above the noise in the latter half of the pass due to the strong scattering from the solar panels.

to assist in signal detection. Maxima are plotted in this research, because of the short time extent of the target echo relative to the time extent of the data record. Specifically, at this point in the processing procedure, each record contains about 30 samples of target echo and about 30,000 samples of noise, so the total noise energy is usually much larger than the total target energy. Note that later, after the target has been detected and tracked through the data, most of the noise samples are cropped off the ends of the records. No ionospheric corrections have been made to the data prior to producing Figure 5.4. Mir is centered in the antenna beam through all 8000 records in the plot, but the SNR in the early part of the pass is insufficient for Mir to be apparent above the background noise level.

The approximate signal and noise levels can be determined from Figure 5.4. The noise samples have a Rayleigh amplitude distribution with a probability density function given by

$$\mathrm{p}(z) = \frac{z}{\sigma^2} \exp\left(\frac{-z^2}{2\sigma^2}\right), \tag{5.1}$$

where z is the sample amplitude and σ is the standard deviation of the underlying bivariate Gaussian distribution of the I and Q samples (e.g., *Whalen*, 1971, p. 102). The cumulative distribution function is

$$\mathrm{P}(z) = 1 - \exp\left(\frac{-z^2}{2\sigma^2}\right), \tag{5.2}$$

and the second moment, or average power, is

$$\mathrm{E}\{z^2\} = 2\sigma^2. \tag{5.3}$$

The noise power can be estimated from the values plotted in the first 1500 records of Figure 5.4, since the signal amplitudes are significantly lower than the values in the plot. The median value of the maximum noise amplitude in a single record is about 145. That value corresponds to the maximum of approximately 30,000 independent samples of a Rayleigh random variable. Using the cumulative distribution function, Equation 5.2, $\sigma \approx 145/\sqrt{2\ln(30000)} \approx 32$. The mean noise amplitude, the square root of the second moment, is then $\sqrt{2}\sigma = 45$. The statistics of the signal-plus-noise case are difficult to calculate analytically, but relatively easy to simulate. Examination of the Mir data reveals that only about 10 samples are within 3 dB of the peak amplitude in each record. Thus, simulations of expected maximum amplitude in the signal-plus-noise case use a 10-sample signal in a 30,000-sample noise record. From the simulations, the target signal amplitudes in the plot correspond to the signal-to-noise ratios listed in the following table.

amplitude	145	154	175	207	247	298	362
SNR (dB)	$-\infty$	10	12	14	16	18	20

In the first 1500 records, the SNR remains less than about 10 dB, so the plot illustrates the noise level with no indication of a target. The SNR reaches 12 dB at times between records 1500 and 4500. From records 4500 to 8000, Mir is oriented such that the solar panel arrays are glinting, causing the SNR to rise above 16 dB over some periods in the latter half of the pass.

After filtering, the data are used for initial target tracking and TEC estimation, as described in Section B.2. In the absence of ionospheric dispersion, and with the system parameters applicable to this run, the single-record SNR for Mir, after pulse compression, is expected to vary between about 15 and 20 dB. When the data are subject to the dispersive effects of the ionosphere, however, the SNR is reduced by several dB, and the target can be easily lost in the noise, as evidenced in Figure 5.4.

5.4 Initial Estimation of TEC and Range

After pulse compression, the TEC was estimated with the time-difference-of-arrival (TDOA) technique of Section 3.6. First, the data were filtered into two 30-MHz subband data sets, one centered on 250 MHz and the other on 350 MHz. Then, the time difference between the target's locations in the two subbands was measured. The differences for the 8000 records in pass 8084a are plotted in Figure 5.5.

The widths of the subbands were chosen based on an initial TEC prediction from the Fully Analytic Ionospheric Model (FAIM). The FAIM prediction varied between about 10 and 16 TECU through the pass. Anticipating $N_T = 10^{17} e^-/m^2$ and $f_c = 350$ MHz in Equation 3.36 gives a coherence bandwidth of about 28 MHz. A 30-MHz bandwidth was used, as a wider bandwidth reduces errors in the TDOA estimates caused by frequency-selective scattering effects.

For this particular data set, the low SNR, especially in the first half of the pass, causes significant errors in the measurements of the time-difference-of-arrival. The TDOA algorithm uses the location of the sample with the largest amplitude to estimate the apparent range to the center of the target. However, that sample contains both noise power and target echo power, so its location is less likely to fall on the brightest part of the target when the SNR drops below about 12 dB. This is apparent in the first half of the pass where the SNR is usually below 12 dB. For the last half of the pass, the SNR is greater than 15 dB for most records, so the TDOA measurements are much more accurate.

The structured short-period variations in the time differences in the latter half of this pass are not an indication of rapid TEC variations. Rather, they are believed to be caused by differences in the scattering characteristics of the target between 250 and 350 MHz as a function of aspect angle. That is, the frequency selectivity of the target causes the peak locations in the two subbands to occur at different points on the target, producing TDOA measurement errors that are some fraction of the range extent of the target.

The dominant 'bowl' shape of the TEC across the pass is a geometric effect caused by the increasing path length through the ionosphere as the zenith angle increases. This geometric effect is removed from the data with an oblique-to-vertical mapping in which the ionosphere is approximated with a thin spherical shell located at the altitude of the peak electron density. With the oblique-to-vertical mapping, the individual slant TEC (N_T)

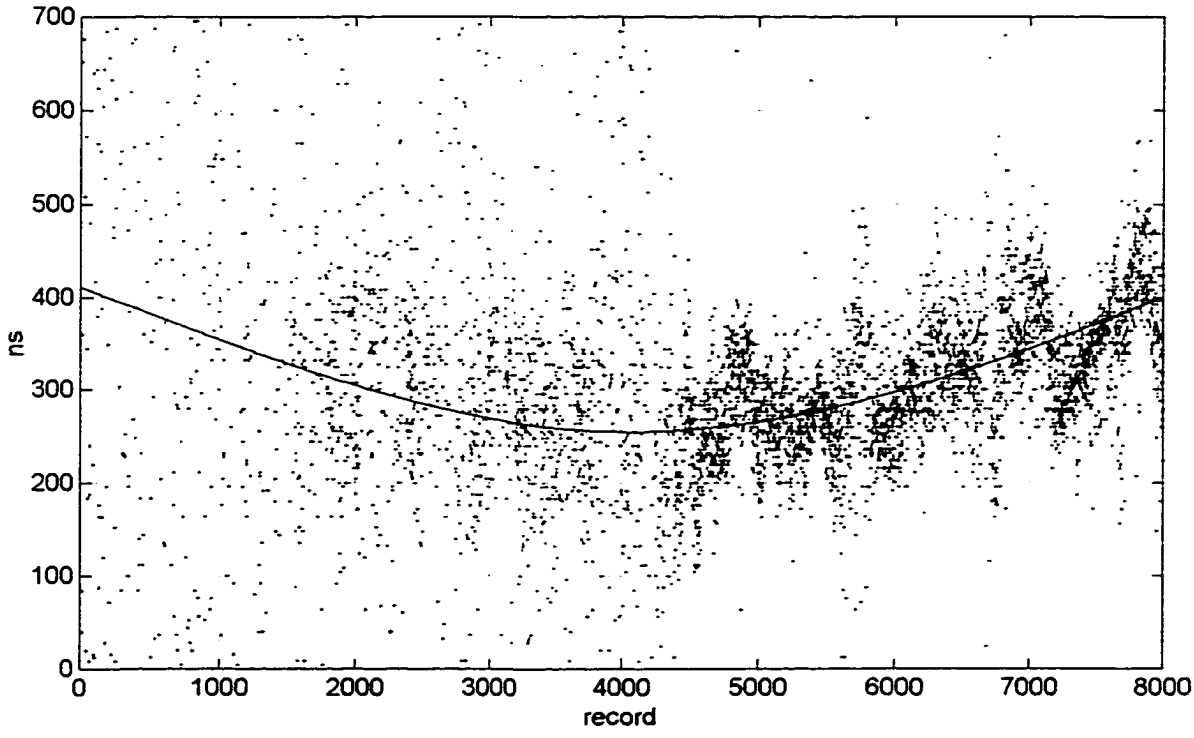

Figure 5.5: Subband group delay differences for pass 8084a. The dots are estimates of the group delay differences between the 250- and 350-MHz measurements for each of the 8000 data records. In the first half of the pass, the SNR is usually below about 12 dB, so the group delay difference estimates are noisy. The solid line is a polynomial fit to the individual estimates.

estimates are converted to equivalent vertical TEC (vTEC) estimates through

$$\text{vTEC} = N_{\text{T}} \sqrt{1 + \left(\frac{r_0}{r_0 + z_{\text{m}}} \cos \alpha_0 \right)^2}, \tag{5.4}$$

where α_0 is the target elevation angle, r_0 is the Earth radius, and z_{m} is the altitude at the peak electron density.

A low-order polynomial is fit to the individual TEC measurements to reduce the effects of noise and target structure on the preliminary TEC estimate. This provides a smooth TEC estimate that can then be used to remove the bulk of the ionospheric effects. In this research, the polynomial is fit to the vTEC estimates, after applying the oblique-to-vertical conversion given above. By fitting to the vTEC estimates, the polynomial does not need to track the geometric component of the slant TEC variations, thereby possibly reducing its

order. After fitting a polynomial to the vTEC estimates, smooth estimates of slant TEC are obtained by reversing the oblique-to-vertical mapping.

For pass 8084a, the scatter of the slant-delay points (see Figure 5.5)—due to the SNR of the data and, to a lesser extent, the scattering characteristics of the target—limits the polynomial fit to the vTEC to a constant. The smoothed vTEC estimates obtained from that fit are plotted in Figure 5.6, along with the corresponding slant TEC estimates. For this example, $z_m = 266$ km, which is the altitude of the peak electron density found in Figure 3.1. Note that a constant vTEC corresponds to a laterally homogeneous ionosphere. Finer-scale variations about this homogeneous model in the actual ionosphere are estimated and compensated during imaging.

After estimating the total electron content with the TDOA technique, the smooth polynomial values are used in Equation 4.1 to compensate the radar data for the bulk of the ionospheric effects. Since this first step in ionospheric compensation can significantly reduce ionospheric dispersion, the resulting data usually have a higher SNR. In pass 8084a, for example, the SNR rises above 10 dB in most records during the first half of the pass, after compensating for the initial TEC estimates plotted in Figure 5.6. In this example, the TDOA technique was applied only once. With some other data sets, this research found that the TEC estimate could be improved with a second iteration.

In the next data-processing step, range errors are estimated and corrected so that the target remains at a constant range in the center of the record through the data set. At the time Mir passed by the radar, the freshest available orbital element set had been generated from tracking data collected 14.6 hours earlier (see Appendix A for further discussion of element sets). Mir's low orbit can change significantly in that period. In this data set, for example, the range error was found to vary from about -800 m at the beginning of the pass to $+800$ m at the end.

Errors in the track prediction raise two concerns during data collection. First, the target is at slightly different azimuth and elevation angles than expected, resulting in signal loss due to antenna-pointing error. For pass 8084a, this effect is negligible, since the antenna-pointing error is much smaller than the beamwidth. Second, the target is at a different range than expected, causing a misregistration between the target echo and the range gate and digitization window. As the range error increases, a point is reached where part of the echo extends beyond the edge of the digitization window, causing that part of the echo to be lost. For pass 8084a, the range error was small enough that this did not occur, and

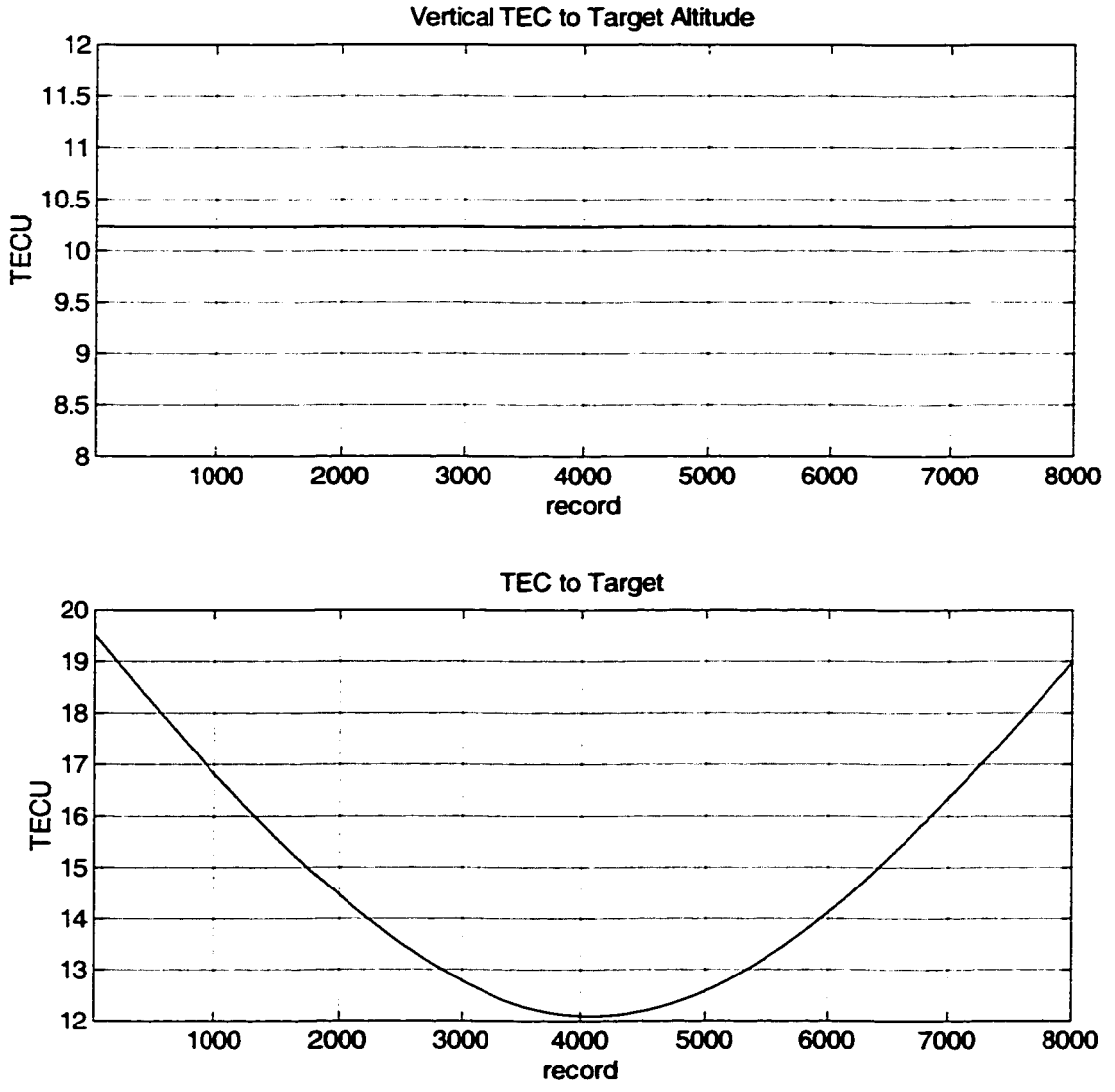

Figure 5.6: Initial TEC estimates for pass 8084a. The upper plot illustrates the estimates of vTEC obtained by fitting a constant value to TDOA measurements that have been converted from the spherical measurement geometry to equivalent vertical measurements. The lower plot is the corresponding slant TEC obtained by converting the constant vTEC values back into the spherical measurement geometry through Equation 5.4.

no data were lost. In this case, the pulse length was about 101 μs, and the digitization window, about 131 μs. The extra 15 μs on each end provided an error margin in the range prediction of about $\pm$2200 m, well above the actual error of $\pm$800 m.

An element set with an epoch 7.9 hours after the pass was downloaded the following day. The ephemeris generated from that element set exhibits range errors that go from about +200 m at the beginning of the pass to about $-$150 m at the end of the pass. This newer ephemeris was used during data processing to provide the best initial target track estimate.

The errors in orbital element sets are often due to errors in the estimate of atmospheric drag, especially for low Earth orbit (LEO) satellites. In such cases, the differences between the predicted and observed satellite tracks can be largely characterized as along track time errors—that is, the satellite follows the predicted track but is either slightly early or slightly late. Range errors can then be reduced by shifting the ephemeris in time to obtain an optimal fit between predicted and observed range. A plot of the differences between the observed ranges and the time-shifted ephemeris ranges for pass 8084a is included in Figure 5.7. In this case, a 30.3-ms delay of the ephemeris data reduces the range error from about $\pm$200 m to about $\pm$15 m. Note that delays in the radar hardware have not been calibrated to the level necessary to obtain an accurate measurement of *absolute* range, so the measured range may have a constant offset. As a result, the constant component of the range difference was removed before plotting so that the residual range error passes through zero at PCA in the plot.

The residual range error, estimated with a quadratic fit to the individual measurements, is also plotted in Figure 5.7. This residual error may be due to (1) higher-order ephemeris errors or (2) residual TEC errors. In either case, the range error at this point is small enough to be readily estimated to the requisite accuracy during the autofocus procedure.

The translational motion of the target is removed from the radar data by shifting each data record by the appropriate amount, as determined from the time-shifted ephemeris and the quadratic fit to the residual range error. In the process, the data record length is reduced by keeping only the 512 samples centered on the target for imaging. The result for pass 8084a is illustrated in Figure 5.8, which is an amplitude image of the fully preprocessed data set (the figure displays samples 181–340). The abscissa indicates pulse number and the ordinate indicates sample number, with near-range at the bottom of the figure. Vertical slices through the image indicate amplitude in individual pulses, while horizontal slices

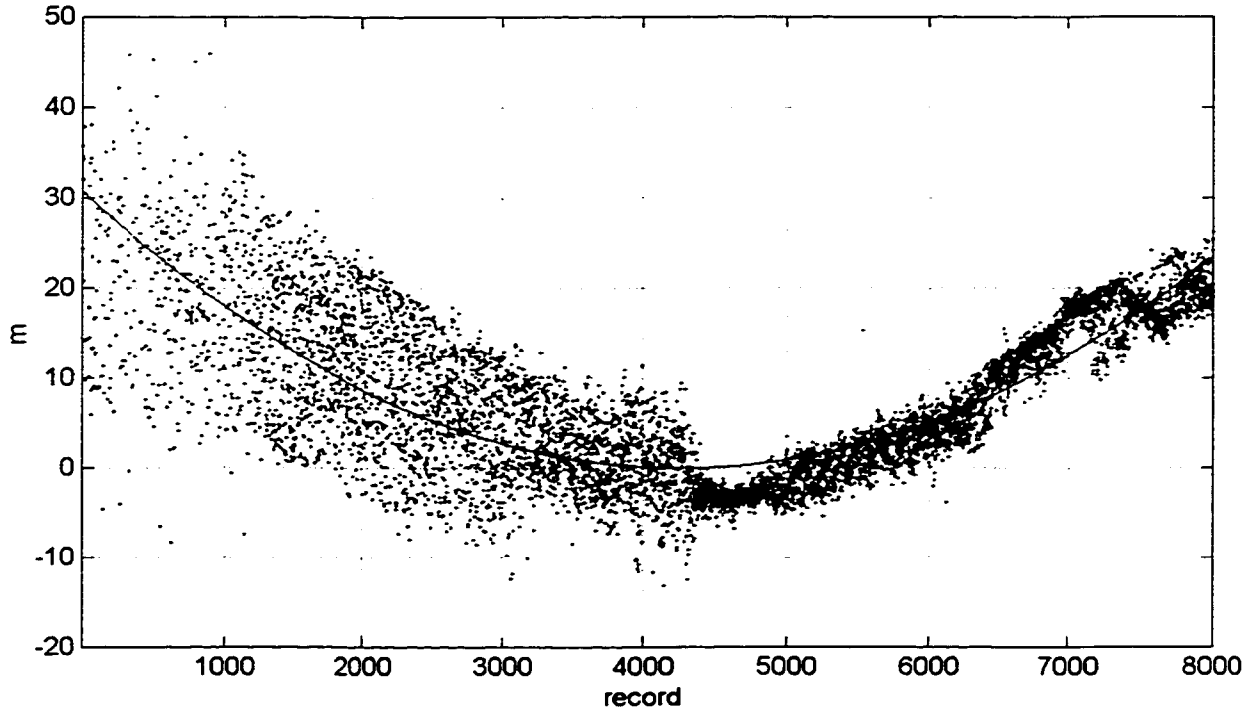

Figure 5.7: Residual range error after time-shifting the ephemeris. The dots indicate the distance from the centroid of the target to the center of the record after compensating for the target range estimates obtained from the time-shifted ephemeris. The solid curve is a quadratic fit to the residual range errors.

indicate amplitude at a constant range. In the image, an R^2 gain has been applied to the samples in each record to correct for the range falloff of echo amplitude. This is evident in Figure 5.8, where the darker background at the ends of the pass indicate a higher noise level than at the center.

Echoes from several parts of Mir are apparent in the preprocessed data. Those parts can be identified by relating their positions in the preprocessed data to the positions of the dominant scatterers in the ISAR images included in the next section.

5.5 Imaging

The final stage of data processing, following preprocessing and initial estimation and compensation of range and TEC, involves forming images of the target from the radar data. As previously discussed, the range and TEC estimates are not sufficiently accurate at this

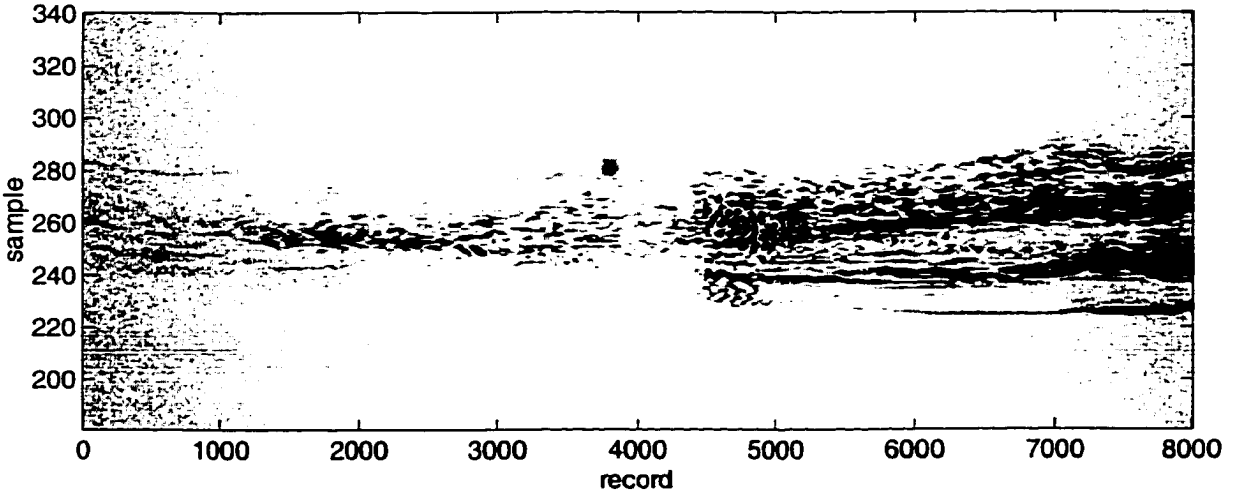

Figure 5.8: Preprocessed data set for pass 8084a. This 'image' illustrates the amplitude of the Mir echo in the radar data records after preprocessing and compensating for the initial estimates of range and TEC. The time-sample spacing of 4 ns corresponds to a range-sample spacing of 0.6 m. The ~60-sample range-extent of the echo corresponds to the ~40-m range-extent of the target. Note the stronger echo signal during the last half of the pass when the solar panels are glinting. Also note the lower noise level as indicated by a lighter background at the center of the pass when Mir is closest to the radar.

point in the processing procedure to achieve system-limited resolution in the radar image, so autofocus techniques are used to refine the range and TEC estimates to the point where the theoretical band-limited resolution is achieved. Autofocusing of the radar image produces full-resolution images and improved range and TEC estimates that are expected to have the level of accuracy calculated in Chapter 4.

A fully autofocused image for pass 8084a, using a 55-degree subaperture centered on PCA, is included in Figure 5.9. This image is an example of what the Mir space station 'looks like' at meter wavelengths. The aperture used in forming this image is about half of the 108.7-degree aperture available from the full data set. In the figure, the image range direction is vertical and the image cross-range direction is horizontal. The system-limited range resolution, as calculated from the 200-MHz bandwidth, is about 0.75 m. The system-limited cross-range resolution, as calculated from the 55-degree aperture, is about 0.54 m.

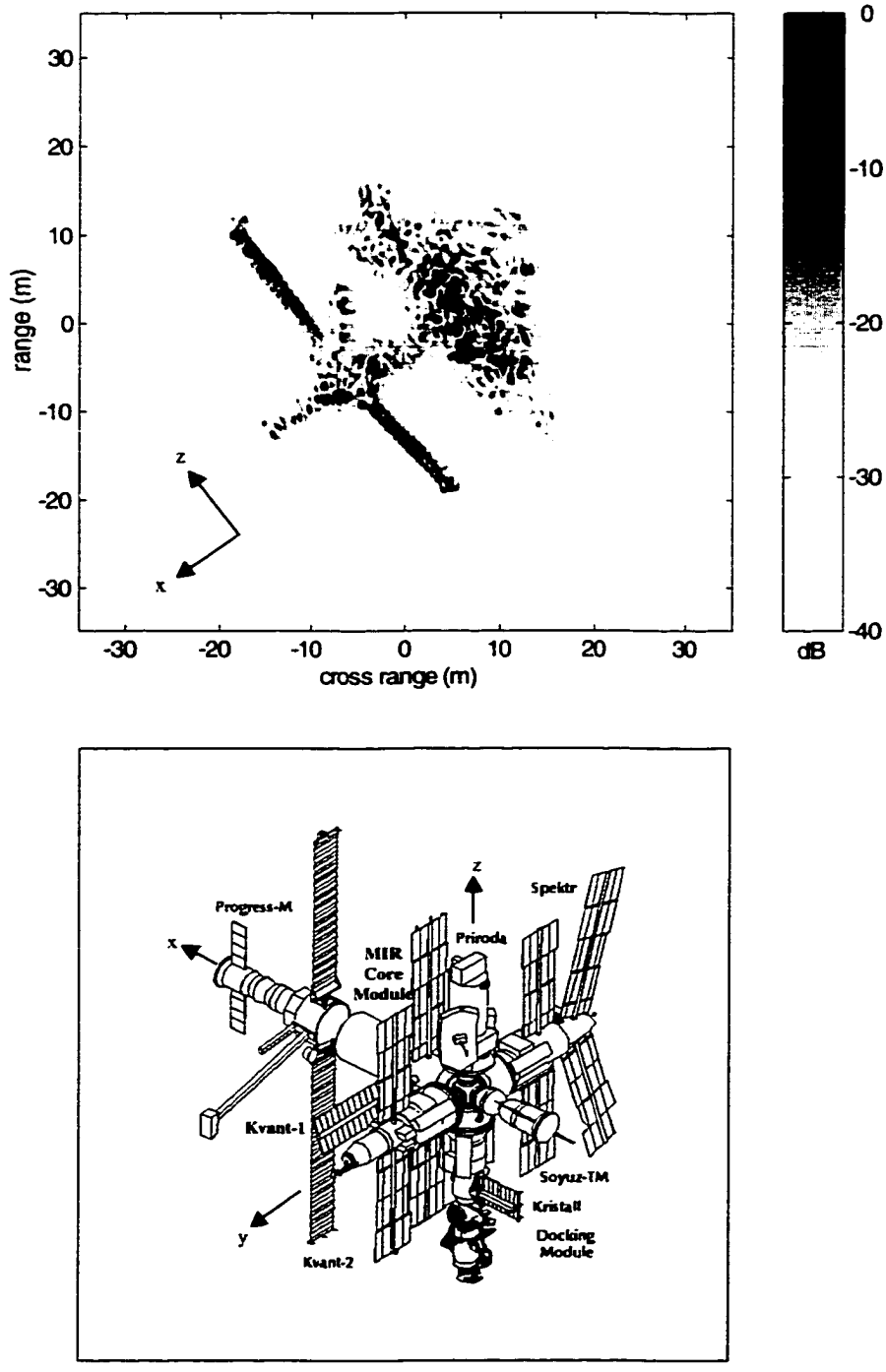

Figure 5.9: Image and drawing of Mir. A VHF radar image of the Mir space station along with a drawing that identifies its various modules. The gray-scale indicates power in dB relative to the largest value in the image. Note that the image and drawing are displayed from different perspectives.

A NASA drawing of the Mir space station is also included in Figure 5.9 to assist in identifying the various modules of Mir in the radar image.[2] The image plane in the radar image roughly corresponds to the x-z plane in the drawing. In the image, the two long solar panels that extend from the upper left to the lower right are the long 'corrugated' solar panels on Kvant-1. The axis through the Mir core module, the x-axis in the drawing, extends from the lower left to the upper right in the radar image. The module in the lower left of the image is a docked Progress supply ship.

The cluttered appearance in the upper right half of the image in Figure 5.9 is the result of the combined scattering of the four cylindrical modules, Kvant-2, Kristall, Spektr, and Priroda, along with the six solar panels attached to them and the three solar panels attached to the Mir core module. For this pass, the orientation of Mir is such that those modules and solar panels all project into a single area in the image, giving the area a cluttered or mottled appearance. Other scattering mechanisms, such as multipath and shadowing (see Section 2.8), are believed to contribute to the cluttered appearance of the area.

The scattering characteristics of Mir can change, sometimes quite dramatically, as the aspect angle changes through the data-collection period. To illustrate those changes in the scattering characteristics, an image formed with data from the last half of the pass is included in Figure 5.10. The aperture for that image is also 55 degrees, so the system-limited resolution is again 0.75 m in range by 0.54 m in cross-range. Figures 5.9 and 5.10 illustrate the sensitivity of the target scattering characteristics to aspect angle. The angular aperture used in forming the image in Figure 5.10 was shifted by 22.5 degrees from that used in Figure 5.9, resulting in 50% overlap in the apertures. Half of the radar data are common to both images, yet different features are evident. For example, note the 'bumps' along the Kvant-1 solar panels, which correspond to corrugations in the solar panel structures. Those corrugations are not apparent in the image in Figure 5.9, but become obvious over the aspect angles used in Figure 5.10.

The impact of ionospheric effects on VHF radar images can be illustrated by comparing images formed with and without ionospheric compensation. An example is included in Figure 5.11. The left frame is a Mir image for which no ionospheric corrections were made during preprocessing or imaging. This image and Figure 5.9 were formed from the same radar data records. The ionosphere has caused the image to be shifted in range and blurred

[2]The drawing was obtained from URL http://www.hq.nasa.gov/osf/mir/mirguide.html, Office of Space Flight, NASA Headquarters, Washington, DC, October, 1999. (All web pages referenced in this chapter were in existence on November 1, 1999.)

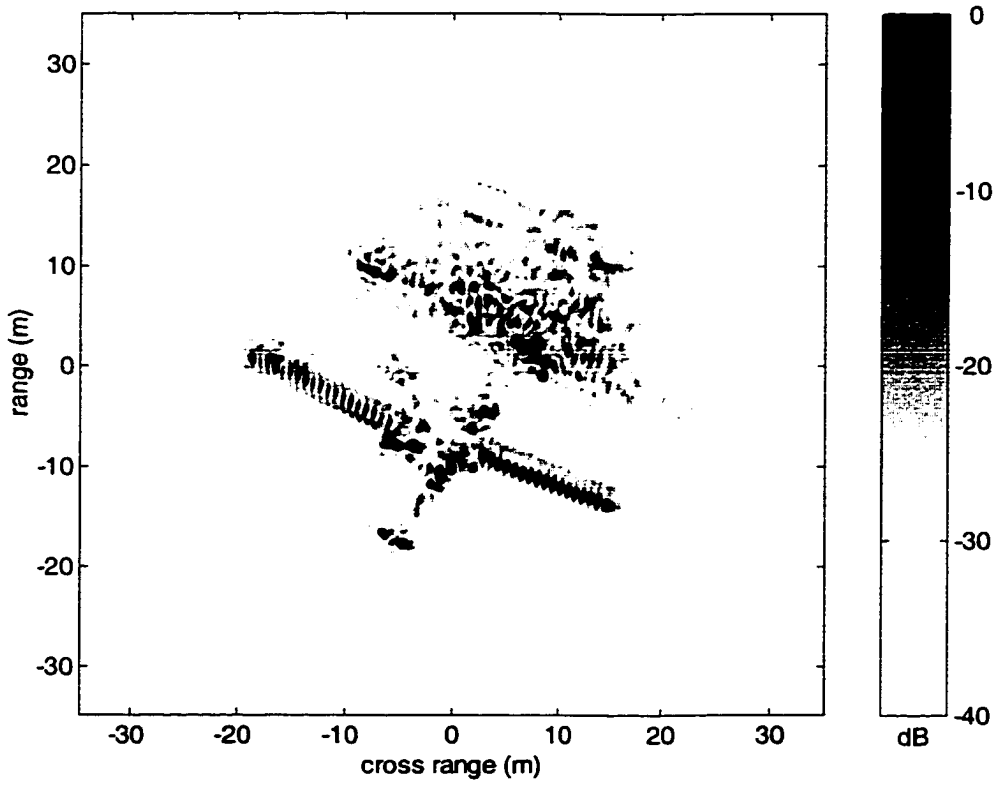

Figure 5.10: Mir, 55-degree subaperture image #2. This image uses the last half of the full 8084a data set. The differences between this image and the one in Figure 5.9 are caused by variations in the target's scattering characteristics with aspect angle. The gray-scale indicates power in dB relative to the largest value in the image.

in both range and cross-range. The center frame is the image formed after compensating the radar data for the TEC estimates obtained with the TDOA technique, which were plotted in Figure 5.6. The image is significantly better; most of the range shift has been removed by compensating for the bulk ionosphere, and the energy in the image is now largely localized to an area of about the size of the target. However, range and cross-range focus are still poor. The right frame is the fully autofocused image, created with the final estimates of TEC and target range.

The aspect-angle dependence of the scattering characteristics can be further illustrated by dividing the full aperture into smaller subapertures. In Figure 5.12, or example, the full 108.7-degree aperture of pass 8084a was divided into six 31-degree subapertures, with 50% overlap between adjacent subapertures. The subapertures were autofocused separately to provide six images along with six overlapping estimates of TEC. To provide the same

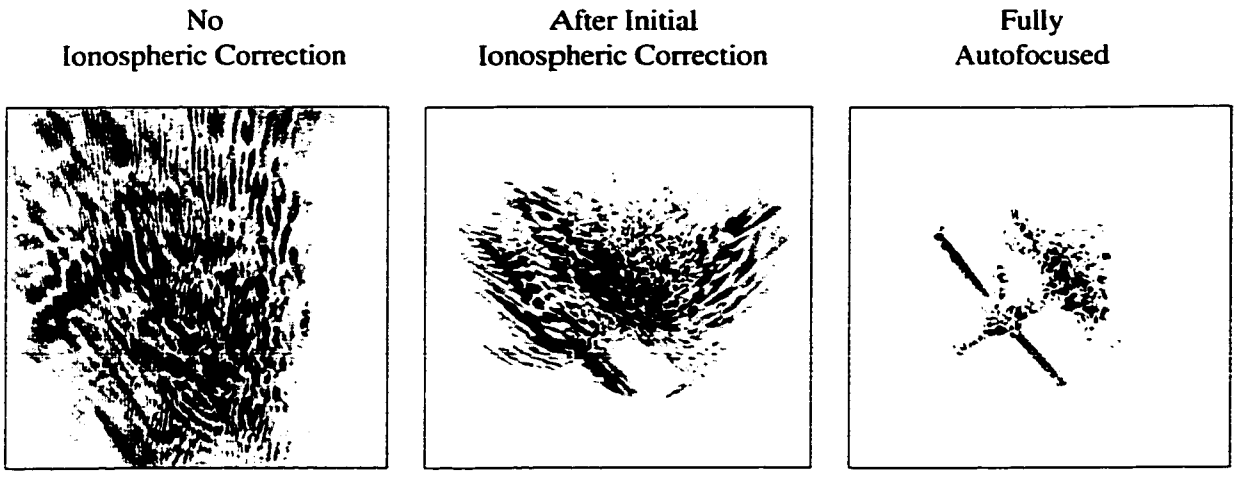

Figure 5.11: An example of ionospheric blurring effects. The left image was created with no ionospheric compensation. The center image was created after compensating for the initial TEC estimates plotted in Figure 5.6. The right image was created after compensating for the final TEC estimates obtained during autofocus; it was displayed earlier in Figure 5.9. Figure 4.5 illustrates the point-spread functions that correspond approximately to the TEC levels in these three images. To account for group delay and to keep the figure window centered on the target, the left and center images have been shifted in range by 60 m and 5 m respectively. Note that the corrected flight track, obtained from the fully autofocused image, was used when forming the three images; the differences between the three images are believed to be due only to differences in the levels of residual ionospheric TEC.

orientation, each image has been rotated by the central aspect angle of the subaperture. The arrow in each image indicates the direction to the radar at the central aspect angle.

As the aspect angle changes from image to image in Figure 5.12, different target features are emphasized. Features normal to the LOS at the center of the aperture are bright, while those parallel to the LOS can disappear altogether. For example, in the upper-left image the Mir core module is approximately normal to the LOS vector over much of the aperture, making its echo bright in the radar image. In the lower-right image the Mir core module is approximately parallel to the LOS vector over much of the aperture, making its echo much weaker in that radar image.

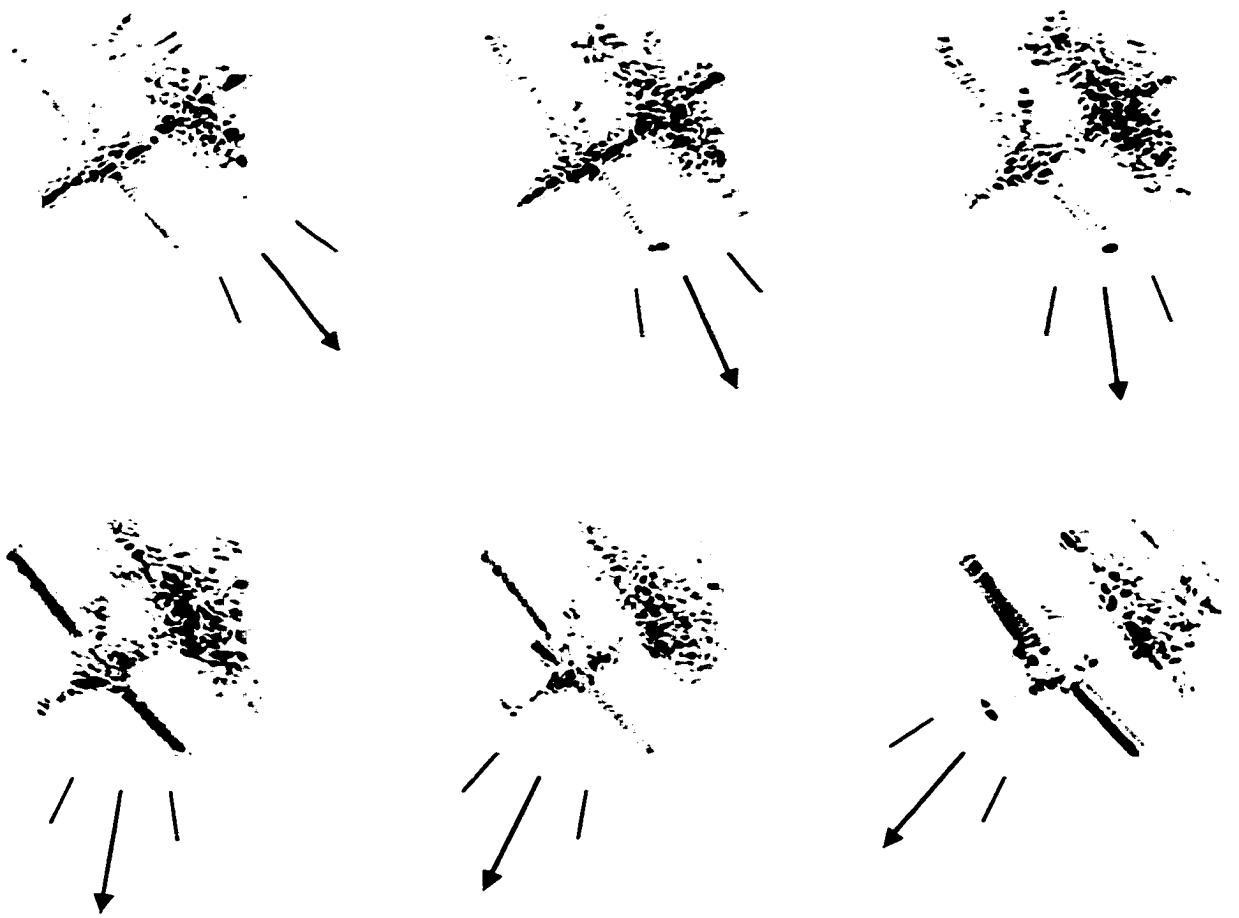

Figure 5.12: 31° subaperture images. Each image covers a 31° subaperture section of the full data set. Adjacent subapertures overlap by 50%. The arrows indicate the direction to the radar at the center of the subapertures, while the radial lines on each side of the arrows indicate the angular aperture.

5.6 Performance Validation

The accuracy of the TEC estimates and the quality of the final images must be evaluated in order to validate the theory and techniques developed in this research. Also, those evaluations should be done for a variety of ionospheric conditions and for targets that exhibit a variety of scattering characteristics to ensure that the accuracy is not adversely affected by the experimental configuration. At this time, the data-processing procedures developed in this research have been applied to only about six satellite passes, so full validation will require further testing (see Suggestions for Future Research, Section 6.3). However, the

results to date are consistent with the expected performance as calculated in the previous chapters. The results for pass 8084a are described in this section.

5.6.1 Verification of Image Resolution

It is important to measure the resolution in the final image in order to validate the end-to-end performance of the VHF radar imaging and autofocus algorithms. As discussed in Chapter 4, system-limited resolution can be achieved across the full image only after TEC has been adequately estimated and its effects compensated. Conversely, if system-limited resolution can be demonstrated, the validity of the data-processing algorithms and the accuracy of the TEC estimates are confirmed.

One way to evaluate image resolution and image quality is to measure the point-target response in the image. This response can be compared to the system point-spread function, which gives the ideal response to a point target in the absence of ionospheric effects and system errors. If a suitable point target were available in the scene, the resolution could be checked by measuring the mainlobe width in the image and comparing it to the expected mainlobe width. Likewise, sidelobe levels in the image could be compared against those in the theoretical impulse response. In terrain-mapping applications, corner reflectors or spheres are often placed in the scene and used as proxies for an ideal point target. Such objects are not present on the candidate satellites listed in Table 1.2, so the only feasible option in this research is to examine target components that behave like point targets. Given the scattering issues discussed in Section 2.8, it is not expected that any parts of the satellite would behave exactly like point targets over the wide bandwidths and large angular apertures that are needed for high-resolution VHF imaging. However, the scattering difference is a question of degree. The scattered signal from some objects may be sufficiently constant in amplitude and phase to achieve system-limited resolution over smaller bandwidths and/or smaller apertures. Such objects can be identified, if they exist, by careful examination of the image.

Quite fortunately, pass 8084a does present a part of Mir, the solar panel array on the right side of Kvant-1 in the image in Figure 5.10, that behaves enough like a row of point targets to enable a check of cross-range resolution over the last half of the pass. The array is actually a foldable row of 36 smaller panels, each about a half meter wide by two meters long. At full extension, the array length is about 15 m. From the image it appears that pairs of the smaller panels are acting as dihedral reflectors, providing a large RCS and a

row of scattering centers. The signal scattered from the dihedral reflectors is sufficiently constant in amplitude and phase over most of the 55-degree aperture to allow system-limited cross-range resolution to be achieved.

The solar panel array is displayed in detail in Figure 5.13. A photograph of the array, clipped from a larger photograph taken from Space Shuttle Atlantis Mission STS-86, is included in the upper frame.[3] The corresponding section from the radar image, rotated and magnified, is included in the middle frame and displayed at the same scale. The distances between the bright spots in the image match the distances between panel pairs in the photograph. The tilt of the array about its long axis, however, is not necessarily the same in the two frames.[4]

Amplitude in the image along a slice through the center of the array is plotted in the lower frame. The location of the slice is illustrated by the black line in the image. A larger plot of a section of the slice is included in the right frame to demonstrate the 3-dB mainlobe width. The center peak in the right frame, corresponding to a dihedral pair of panels near the center of the array, has a 3-dB width of 0.51 m.

The system-limited cross-range resolution, calculated from Equation 2.4 using a 300-MHz center frequency and 55-degree aperture, is 0.54 m. With the 'boxcar,' or unity, windowing of the spectral data used for this image, the ideal 3-dB mainlobe width is 0.89 times the system-limited resolution, giving an ideal 3-dB mainlobe width of $0.89 \times 0.54 = 0.48$ m. The demonstrated cross-range resolution, 0.51 m, agrees well with this predicted value, 0.48 m.

The actual range resolution is determined from the 3-dB width of scattering centers in the image range direction. The dihedral scattering centers illustrated in Figure 5.13 have a 3-dB range extent of about 0.9 m, somewhat larger than the predicted range resolution—probably because the panels have some physical range extent. Fortunately, the bright spot in the lower left corner of the image in Figure 5.13 does appear to originate from a 'point-like' object. The corresponding part of Mir that gives rise to this scattering center is unknown;

[3]See URL http://spaceflight.nasa.gov/history/shuttle-mir/photos/sts86/postflight/hires/86710007.jpg, NASA, Human Space Flight, Johnson Space Center, Houston, TX, for a copy of the full photograph. See URL http://www.ksc.nasa.gov/shuttle/missions/sts-86/countdown.html, NASA, Kennedy Space Center, Cape Canaveral, FL, for information about mission STS-86.

[4]With 36 panels, the solar array is expected to have 18 dihedral pairs, but the image appears to have only 17 bright spots. There are a couple possible explanations for the difference. One possibility, the two end panels may be pointing outward, and thus not acting as a dihedral reflector. Another possibility, the inner pair of panels may be shadowed by other components. There is evidence of possible shadowing in the lower amplitude and stretching of the leftmost bright spot in the image.

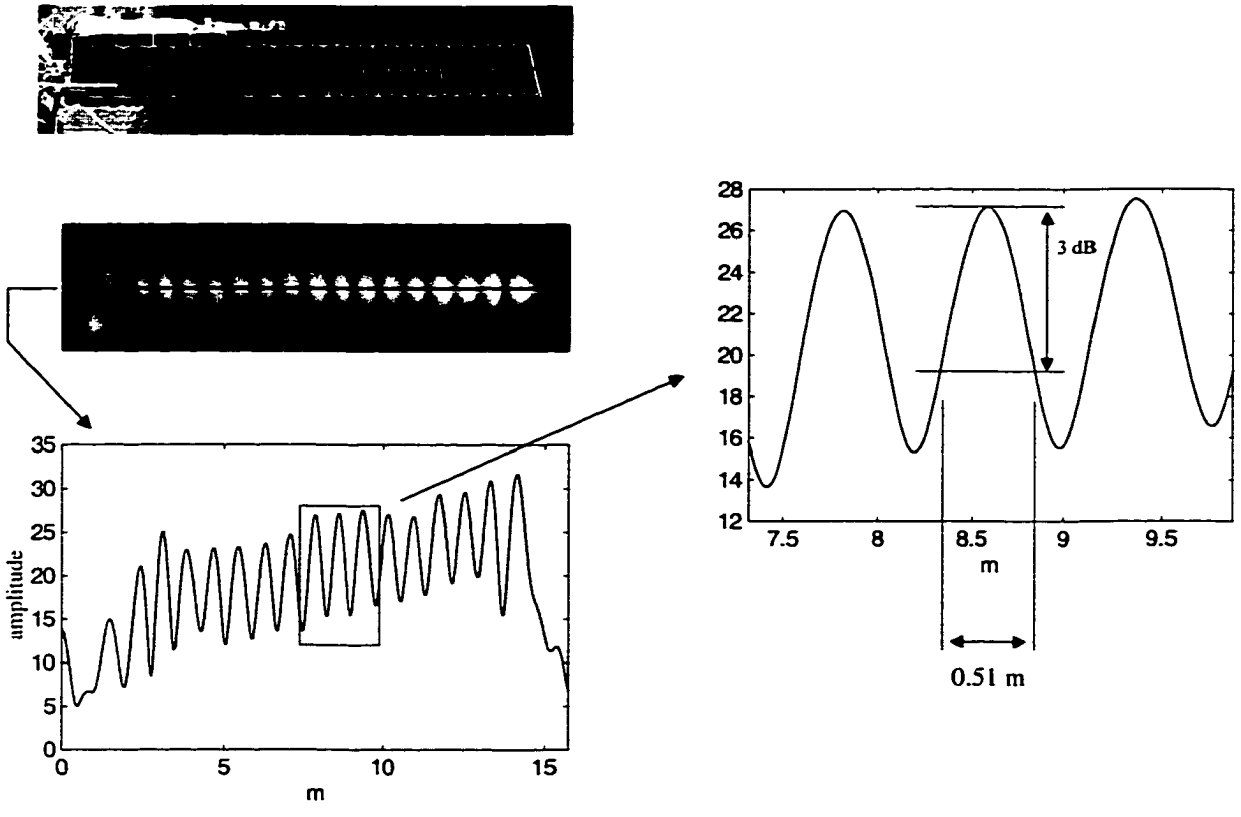

Figure 5.13: Verification of cross-range resolution for Mir pass 8084a. The upper frame is a photograph of one of the solar panels on Kvant-1, clipped from a large photograph of Mir taken from the space shuttle, Mission STS-86, on October 3, 1997. The middle frame is the corresponding image of the solar panel, clipped from the larger image displayed in Figure 5.10. Note that the photograph was taken many months before the radar data. The lower frame is a plot of the amplitude along a slice through center of the solar panel's image. The right frame is an expanded view of part of the amplitude slice, along with a measurement of the 3-dB mainlobe width.

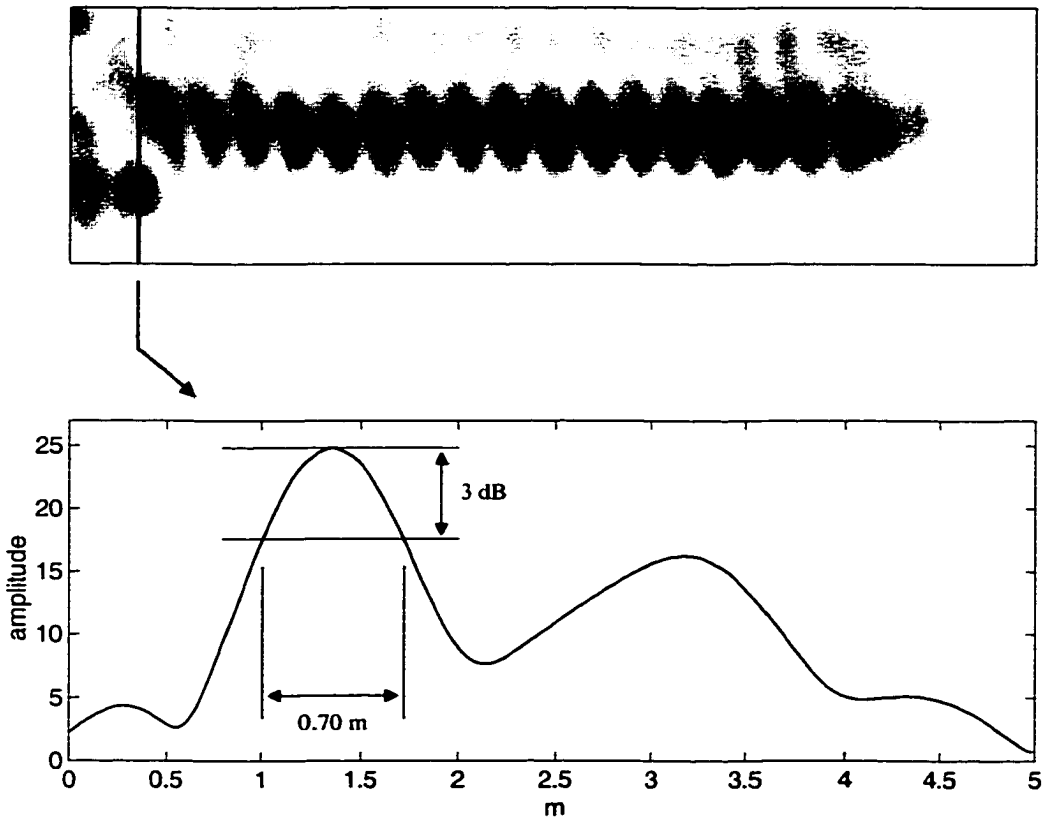

Figure 5.14: Verification of range resolution for Mir pass 8084a. The upper frame is the image of the right solar panel from Figure 5.10 (this figure displays a larger area than Figure 5.13). The lower frame is a plot of the amplitude along the vertical slice through the image indicated by the line in the upper frame. The line cuts through a scattering center that is suitable for measuring range resolution, although the identity of the corresponding physical part of Mir is not known.

it may be part of one of the short booms that extend out from Kvant-1. The image of the point-like object and solar array is displayed again in the top frame of Figure 5.14 with a vertical line indicating a slice through the point-like object in the range direction. The amplitude along that slice is plotted in the lower frame. The peak along the slice has a 3-dB width of 0.70 m.

The system-limited range resolution, calculated from Equation 2.3 using a 200 MHz bandwidth, is 0.75 m. Since a boxcar window was applied to the spectral data in the range direction as well, the ideal 3-dB mainlobe width is $0.89 \times 0.75 = 0.67$ m. Thus, the demonstrated range resolution, 0.70 m, agrees well with the predicted value, 0.67 m.

System-limited resolution has been demonstrated in this example, confirming that autofocus has converged to the correct image and that ionospheric effects have been fully mitigated.

5.6.2 Verification of TEC Estimation Accuracy

It is also important to verify the accuracy of the TEC estimates in order to further validate the end-to-end performance of the VHF radar imaging and autofocus algorithms. Ideally, the TEC estimates produced by the autofocus procedure should be compared to independent high-precision measurements. At present, however, no suitable independent measurements are available; instead, the TEC estimates are verified by indirect means only.[5] Three approaches to indirect verification are considered, then used to check the TEC estimates obtained from pass 8084a radar data.

i) The TEC estimates can be compared to measurements from other sources such as GPS or ionosondes after accounting for differences in altitude.

ii) The TEC estimates can be compared to predictions produced by ionospheric models such as IRI-95 or FAIM.

iii) The radar data can be divided into subapertures, then autofocused to produce TEC estimates over subsections of the pass. Those subaperture TEC estimates can be compared in their areas of overlap to check consistency; the difference between the subaperture estimates is expected to be less than twice the expected maximum error in each estimate.

The first method of indirect verification—comparison of the autofocus measurements of TEC with measurements from other sources—has two significant limitations. (1) The TEC measurements correspond to different endpoints and different paths through the ionosphere. (2) In many cases, the independent measurements are expected to be far less accurate than

[5]One way of obtaining TEC measurements of sufficient precision for direct comparison with the autofocus estimates is through analysis of the dual-frequency beacon signals transmitted by some satellites. Candidates include the remaining Navy Transit satellites and the Russian Musson satellites. If those satellites could be imaged, the autofocus estimates of TEC could be compared directly to the dual-frequency beacon measurements of TEC. The advantage of such a comparison is that the beacon and radar signals would follow the same path through the ionosphere, both encountering the same TEC. Unfortunately, the Transit and Musson satellites are too small and too high to be detected with the current system's limited transmitter power, so other methods of validation are required.

the autofocus measurements. In the case of GPS, for example, the TEC is measured to the altitude of the GPS satellite, about 20,000 km, whereas for the radar data, the TEC is measured to the altitude of the target, about 378 km for pass 8084a. Furthermore, the accuracy of the GPS TEC measurement—about 2 TECU—is at least an order of magnitude poorer than the accuracy expected through the imaging procedure.

TEC estimates, obtained from GPS measurements, are available from NASA global ionospheric maps[6] in near-real time for all locations on Earth. These maps have an accuracy of about ±2 TECU over land areas. At the time of pass 8084a, the NASA global ionospheric maps provided a TEC estimate of about 20 TECU at Ascension Island. For typical electron-density profiles, the TEC to the Mir altitude of 378 km is about half that to the GPS altitude of 20,000 km (within about −20% to +40%). Thus, based on the GPS measurements, the vertical TEC estimate of about 10 TECU to the Mir altitude (plotted in Figure 5.6) is within the bounds of what would be expected.

The second indirect verification of TEC measurement accuracy was done by comparing the autofocus measurements with predictions from FAIM. The upper frame in Figure 5.15 illustrates the results with plots of the TEC estimates from the six subaperture images of Figure 5.12 and the TEC predictions from FAIM. The subaperture estimates overlay quite well but are 20 to 25% larger than the FAIM predictions. This level of agreement between measured and modeled TEC is considered to be quite good, as the differences are well within the expected accuracy of the model (see *Brown et al.*, 1991).

The third method is much more precise than the first two. Instead of comparing the TEC estimates to those from other sources, this method verifies the consistency of the TEC estimates across the aperture by first calculating the differences between the subaperture estimates in their areas of overlap, then comparing those differences to the maximum expected error in the individual subaperture estimates. If the analyses of the preceding chapters are valid, and the TEC variations are not too rapid, the subaperture TEC estimates are expected to agree to within the accuracies calculated in Equations 4.8 and 4.15. This level of agreement would suggest that imaging is able to separate scattering and ionospheric effects, and that the assumptions made in deriving Equations 4.8 and 4.15 are appropriate.

The agreement between the subaperture estimates is illustrated in finer detail with the 'detrended' values plotted in the middle frame of Figure 5.15. First, to obtain these values,

[6]Global ionospheric maps are available at URL http://sideshow.jpl.nasa.gov/gpsiono, NASA, Jet Propulsion Laboratory, Pasadena, CA.

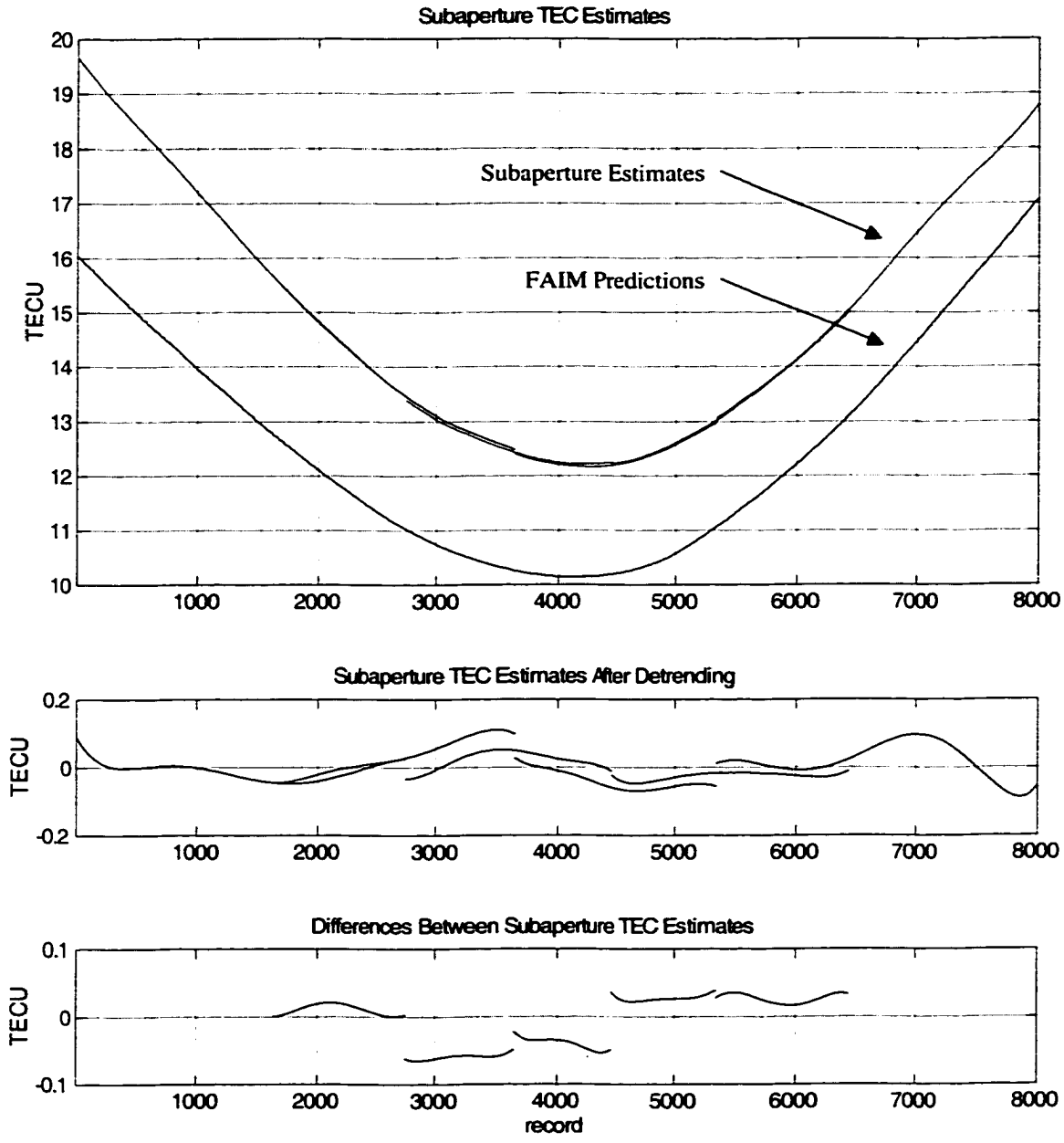

Figure 5.15: TEC estimates from the six 31° subapertures. The upper plot contains the TEC estimates from the six 31° subapertures, along with the FAIM TEC predictions. The middle plot contains the TEC estimates after subtracting the sum of the laterally homogeneous component (plotted in Figure 5.6) and a fourth-order polynomial that was fit to the data for detrending. This plot illustrates the agreement between the subaperture TEC estimates, both for overlapping and non-overlapping apertures. The lower plot contains the differences between the TEC estimates in the overlapping areas of the subapertures. These differences are consistent with the TEC accuracy calculations of Chapter 4.

the laterally homogeneous component of the TEC (plotted in Figure 5.6) is subtracted from the subaperture TEC estimates of the top frame, giving the residual TEC estimates. Then, the residual TEC estimates are detrended by subtracting a fourth-order polynomial that has been fit to them. The result, plotted in the middle frame, illustrates the finer-scale TEC variations (which are quite small in this example) and the agreement between the subaperture TEC estimates. Note that the differences between the subaperture TEC estimates are largely constant offsets, as expected from the tighter bounds of Equation 4.15 than Equation 4.8. Also, note the discontinuities between subaperture estimates that do not use any common data, located near records 2700, 3600, 4500, and 5300. In all cases, the differences between the TEC estimates are less than 0.1 TECU.

The differences between adjacent subaperture TEC estimates in the areas of overlap are plotted in the lower frame of Figure 5.15. Using the parameters from pass 8084a in Equation 4.8, the expected worst-case absolute-error in the TEC estimates is about ± 0.13 TECU. If the individual TEC estimates are within these bounds, the differences between the subaperture estimates in the areas of overlap are expected to be no more than twice as large in the worst case. The subaperture differences in the figure are in fact about a factor of two lower than the expected worst-case error in the individual subaperture TEC estimates, providing some confidence that autofocus has converged to a TEC estimate that meets the specified accuracy of ± 0.13 TECU. However, note that the TEC estimation error is a random variable, and this experiment represents only one outcome. For a statistically significant sampling of that variable, many more experiments, or additional satellite passes, would be needed.

It is also noted in this example that 50% of the data are common to adjacent subapertures, so the TEC estimates may be 'pulled' to a common (incorrect) solution by, for example, systematic errors or unmodeled target scattering characteristics such as shadowing. Again, full validation would require analysis of such effects, but for this data set the full system-limited resolution was achieved (see Section 5.6.1), indicating that the subaperture TEC estimates are indeed within the requisite accuracy.

Equation 4.15 places a tighter bound on the quadratic and higher-order errors in the TEC estimates than Equation 4.8 places on the absolute errors.[7] Using the center frequency from pass 8084a in Equation 4.15, those nonlinear errors are expected to be less than about

[7]The nonlinear errors were discussed in Section 4.3. They are the differences between the actual error and a linear fit to the actual error.

±0.014 TECU. In the worst case, the difference between two estimates are expected to be no more than twice as large, or within ±0.028 TECU. In Figure 5.15, the TEC difference having the largest nonlinear excursion is the one between the first two subapertures—that is, the left-most curved line segment in the lower plot, between records 1700 and 2800. The nonlinear component of that curved line segment remains within ±0.013 TECU of its corresponding best linear fit. The value of ±0.013 TECU is considerably less than twice the nonlinear precision estimate, ±0.028 TECU, obtained from Equation 4.15. This level of consistency between the subaperture estimates suggests that the nonlinear component of the TEC estimation error meets the expected precision given by Equation 4.15.

To recap, in the areas of overlap between adjacent subapertures, the absolute values of the two TEC estimates differ by less than the accuracy predicted in Equation 4.8—as they should. Also, the nonlinear variations of the two TEC estimates differ by less than the precision predicted in Equation 4.15. This agreement provides further evidence that the prescribed TEC estimation accuracy is indeed achieved, at least for this example.

Chapter 6

Conclusion

This research investigates the feasibility of mitigating ionospheric effects in radar data. It includes analysis of the effects of the ionosphere on a radar image, development of ionospheric estimation and compensation techniques, and testing of those techniques on actual radar data. It shows that ionospheric effects can be compensated to a level where they have a negligible effect on radar image resolution, at least for stable ionospheric conditions and frequencies above about 200 MHz.

6.1 Summary

This research is primarily concerned with radar imaging using frequencies between the central VHF and lower UHF ranges—that is, between about 150 and 500 MHz. Using VHF for radar imaging raises a number of issues that are not significant at frequencies above about 1 GHz. For example, to form high-resolution radar images at VHF, ultra-wideband signals and large angular apertures are needed. Also, since parts of the target are about the same scale as both the wavelength and the resolution cell size, resonant scattering effects from those parts will be present in the image.

The polar-format algorithm is used here for producing the radar images. It is a suitable choice for large angular apertures, provided the distance to the target is much larger than the cross-range extent of the image area.

It was demonstrated that the ionosphere can severely degrade VHF radar image resolution. However, for moderate ionospheric conditions and frequencies above about 200 MHz,

the ionospheric effects on a radar echo can be described as filtering with a $1/f$ phase response. That phase response scales linearly with the TEC. Thus, if the TEC can be estimated to sufficient accuracy, on a pulse-by-pulse basis, the effect of the ionosphere on the radar echo can be mitigated.

Estimation of total electron content is done in two stages. First, group delay differences between subbands in the radar signal are used to obtain an initial TEC estimate. That estimate has an accuracy of about 1–2 TECU, which is sufficient to remove much of the ionospheric effect. In order to approach expected, or theoretical, image resolution, the TEC estimation error must be reduced by another one or two orders of magnitude, depending on fractional bandwidth and angular aperture. This improvement is achieved by using the radar image to refine further the initial estimate. Basically, the residual TEC estimation error is modeled with a polynomial, and an autofocus algorithm is used to search for the polynomial that produces an optimal image. The precision of the final TEC estimate, given by Equations 4.8 and 4.15, depends on the center frequency, the fractional bandwidth, and the angular aperture.

The effects of residual, or uncompensated, TEC on the radar image are analyzed in Chapter 4. Those effects are evaluated in terms of range and cross-range resolution. However, for UWB signals or large angular apertures, a full characterization requires evaluation of the ionospheric effects on the system point spread function.

The theory and techniques developed in this research were tested on actual radar data. Those data, covering frequencies between 150 and 400 MHz, were collected at Stanford, California, and Ascension Island, United Kingdom. A detailed case study using data collected at Ascension Island (see Chapter 5) illustrates the techniques and provides examples of VHF radar images of satellites. Additional satellite images are included in Appendix C.

To validate directly the performance of the techniques presented in this research, it would be necessary to have independent high-precision estimates of TEC and target range that could be compared with the estimates obtained through imaging. Indirect validation was the only feasible option in this research, since independent high-precision estimates were not available for the LEO satellites that could be seen with the Stanford or Ascension Island radar systems.

Sections 5.6.1 and 5.6.2 describe two methods of indirect validation for the case study presented in Chapter 5. First, full resolution in the radar image can only be achieved if the residual TEC is below the levels given in Equations 4.8 and 4.15. The full cross-range

resolution, given by Equation 2.4, was demonstrated in an image by measuring the 3-dB width of corrugations on a Mir solar panel. Thus, the TEC estimates for that example must be within the prescribed precision.

The second indirect method of validation involves checking the consistency of the TEC estimates across subapertures. The full aperture was divided into overlapping subapertures, which were independently autofocused. If the TEC estimates from the subapertures are accurate to the levels given in Equations 4.8 and 4.15, the differences between adjacent subaperture estimates, in their areas of overlap, are expected to be less than twice the maximum error in the individual estimates. This was also verified in the example in Chapter 5.

Given the above evidence, ionospheric effects can be mitigated, and full-resolution radar images can be produced at frequencies above about 200 MHz in moderate ionospheric conditions. Also, total electron content can be estimated to the high levels of precision given by Equations 4.8 and 4.15, through autofocusing of the radar image. However, to achieve the precision given by those equations, several things are necessary: (1) The theory used in deriving the equations must represent a sufficiently accurate model of the real world; (2) Autofocus must converge to the *correct* image; (3) TEC variations must be smooth enough to be adequately fit by the estimation polynomial; (4) The SNR must be large enough for noise to have a negligible effect on the TEC estimates.

6.2 Limitations

This thesis describes techniques for extending current satellite-imaging capabilities to lower frequencies. However, in some situations these extensions are inadequate for characterizing the actual ionosphere to sufficient precision to achieve full image resolution. Those situations can be divided into two categories: higher-order ionospheric effects and ionospheric irregularities.

6.2.1 Higher-Order Ionospheric Effects

The limitations in imaging performance due to higher-order ionospheric effects are discussed in Sections 4.6 and 4.7. At frequencies above about 150 MHz, the two most significant higher-order effects are errors in the $1/f$ phase model and refraction. At frequencies below

about 100 MHz, other ionospheric effects such as mode coupling and losses can become significant, but for the most part, those effects are negligible above 150 MHz.

The two primary higher-order effects—errors in the $1/f$ phase model and refraction—become more significant with lower frequency, lower target elevation angle, and higher TEC. They also depend somewhat on the electron-density profile along the radar-target ray path. From calculations in Sections 4.6 and 4.7, the higher-order ionospheric effects are negligible, in most cases, for frequencies greater than 200 MHz, elevation angles greater than 30 degrees, and vertical TECs to target altitudes less than about 50 TECU. Outside those bounds, the higher-order effects begin to degrade image quality if they are not compensated.

The effects on the radar echo caused by errors in the $1/f$ phase model and ionospheric refraction are largely dispersive. It may be possible to estimate and compensate them, as described in Sections 4.6 and 4.7, in much the same way that TEC effects are estimated and compensated. If successful, compensation of these higher-order phase contributions would extend the ability to image satellites beyond the frequency, elevation angle, and vertical TEC bounds listed above.

Calculations show that higher-order effects are negligible in the radar data processed to date. Consequently, this research has not attempted to estimate or compensate the higher-order ionospheric phase contributions in those data.

6.2.2 Ionospheric Irregularities

Ionospheric irregularities, discussed in Section 3.8, are likely to present the most significant limitation to radar imaging at frequencies above 150 MHz. At low to moderate levels, ionospheric irregularities cause variations in the TEC that need to be estimated adequately to realize full image resolution. Severe irregularities, however, produce scintillation, making radar imaging infeasible.

The degree to which the techniques developed in this research are able to handle ionospheric irregularities depends on the spatial scales of the irregularities, the 'depth' or variation in electron density in the irregularities, and the number of degrees of freedom of the function used during imaging to represent TEC variations. The ability to mitigate ionospheric effects depends on how well the TEC estimation function is able to fit the actual TEC variations. If the residual errors—the differences between the estimation function and the actual TEC—are below the values given in Equations 4.8 and 4.15, ionospheric dispersion can be compensated to the point where it has a negligible effect on the image. With

regards to the impact of ionospheric irregularities on VHF radar imaging, three situations can occur:

i) The variations in TEC across the aperture can be fit adequately with the TEC estimation polynomial. This case can be handled with the techniques described in this research.

ii) The variations in TEC across the aperture are too rapid to be adequately fit with a polynomial of order less than about 20. It may be possible in the future to handle this case, or some subset thereof, with extensions to this research.

iii) Ionospheric irregularities are sufficiently severe to produce scintillation (the rapid signal fading and phase fluctuations caused by multiple scattering from the irregularities). In this case, UWB radar imaging is infeasible.

For smooth TEC variations (item i), the techniques described in this research can be used to form VHF radar images. As irregularities become more severe, the TEC exhibits more rapid variations across the aperture, thereby requiring a higher-order TEC estimation polynomial. Based on experience to date, the order of the TEC estimation polynomial can only be increased to about 20 before the amount of computation needed to autofocus the image becomes excessive.

When TEC variations become too rapid (item ii), residual errors in the TEC estimation function begin to degrade image quality. In the limit, it is possible that the TEC variations from pulse to pulse could have a random component greater than the acceptable levels given in Equations 4.8 and 4.15. In that case, an independent TEC estimate would be needed for each pulse. It may be possible to use the radar data to obtain sufficiently accurate individual-pulse TEC estimates, but that would require development of new techniques with capabilities beyond those described in this research.

When ionospheric irregularities become sufficiently severe (item iii), they produce scintillation which, in the extreme case, can destroy the coherence and information content of the radar echo, making imaging infeasible. With less-severe scintillation, phase and amplitude noise are added to the echo, thereby degrading the final image and compromising the accuracy of the TEC estimates (see also *Knepp and Dana*, 1985, and *Knepp and Mokole*, 1992, for a discussion of scintillation effects on radar images at microwave frequencies).

Ionospheric irregularities can be described from a statistical perspective with a power-law power spectral density. Given a power-law exponent and turbulent strength scaling

factor, corresponding to, say, a particular time and location on Earth, one could determine whether a polynomial could provide an adequate fit to the TEC, and what polynomial order would be needed. Using measured statistics for the power-law exponent and strength scaling factors, one could then determine the probability that the ionospheric-estimation and -mitigation techniques described here would be adequate at a specific time and location on Earth.

6.3 Suggestions for Future Research

This research has demonstrated the feasibility of radar imaging through the ionosphere at very high frequencies, but a large amount of work remains before these results can be transitioned to an operational system. Some of the areas that would benefit from further research are listed below.

i) The techniques for ionospheric estimation and mitigation can be extended and tested with lower frequencies and higher fractional bandwidths.

ii) As discussed in Section 6.2.2, the limitations caused by ionospheric irregularities should be evaluated, both in terms of how often and how severely they would degrade image quality. For example, one could ask: What is the probability that full image resolution can be achieved as a function of latitude, time of day, season, sunspot number, etc.?

iii) The effects of higher-order ionospheric phase contributions and ionospheric irregularities should be evaluated experimentally by collecting data over a wide range of ionospheric conditions.

iv) The autofocus algorithm plays a primary role in this research. One concern has been that the optimal image found by the autofocus algorithm may differ from the correct image. It is important to know whether this can occur, and if it does, to what degree. A first step may be to relate the performance of various autofocus algorithms to the scattering effects of the target and the errors in the initial range and TEC estimates. Also, further research would benefit from more computationally efficient algorithms that use, for example, search algorithms that converge more quickly than the simplex algorithm.

v) Fully polarimetric data could be collected to allow calculation of the full target scattering matrix. Fully polarimetric data can also be used to calculate Faraday rotation as well as the received ordinary and extraordinary waves. Faraday rotation, in turn, can be used to calculate directly the $1/f^2$ component of the higher-order ionospheric phase contribution. The $1/f^2$ phase contribution could then be compensated (see Section 4.6). Since the $1/f^2$ term is usually the largest component of the higher-order ionospheric phase contribution, its compensation would significantly reduce the higher-order ionospheric phase effects on the radar image.

Appendix A

Radar System Description

The radar data used for examples in this thesis were collected at SRI International's radar sites at Stanford, California, and Ascension Island, United Kingdom. Those data were collected with the 'Big Dish,' the 150-ft (45.7 m) parabolic dish antenna at Stanford that has been in operation since the early 1960s, and with a new 88-ft (27 m) dish antenna at Ascension Island. With the exception of the Big Dish, the radar systems were designed and built for this project. They use commercial off-the-shelf hardware for most subsystems, except for the high-power amplifiers and the dish antennas and their steering control systems. Both systems are easily configured to provide a wide choice of frequency, bandwidth, and waveform type. Nominal parameters for the two systems are listed in Table 1.1.

Radar data are collected while a satellite passes in view of the radar site, as illustrated in Figure A.1. The data-collection period, usually restricted to the time when the satellite is at an elevation angle above about 30 degrees, is referred to, in this work, as a satellite *pass*. Each data set, corresponding to a single satellite pass, is given a unique identification number. For example, a data set collected during one pass of the Mir space station at Ascension Island is designated '8084a.' That particular data set is reviewed in detail in this thesis.

In order to follow a satellite while it is in view of the radar, accurate satellite ephemeris is needed. The ephemeris is calculated from a *two-line element set* that is downloaded from the Orbital Information Group (OIG), Goddard Space Flight Center (GSFC), just prior to the time of the pass. The azimuth and elevation angles of the satellite from the dish, along with satellite range, are then calculated from the ephemeris. The angles are used

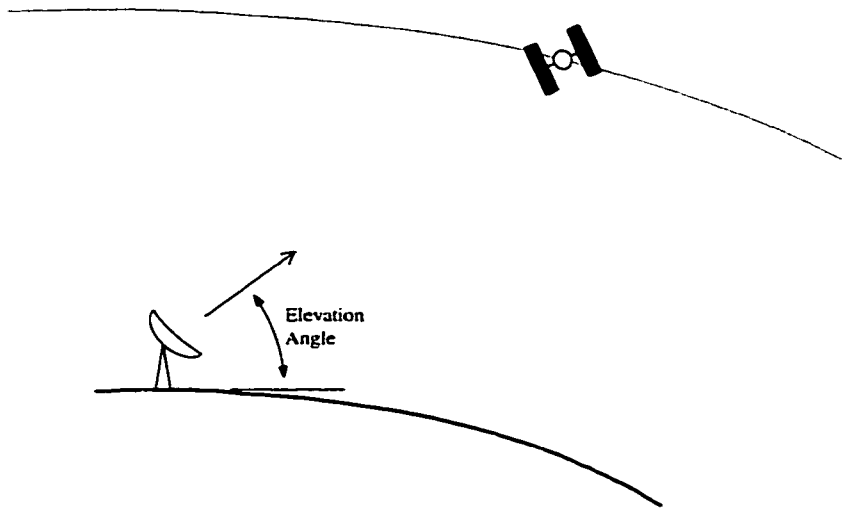

Figure A.1: Radar imaging of satellites. The dish antenna follows the satellite while it is in view. Pulses are transmitted by the radar, and the satellite echoes are received and digitized during the time the satellite elevation angle is above about 30 degrees.

for steering the dish antenna, while the satellite range is used to calculate the appropriate gating period for the received signal, together with the signal digitization period.

The dish antenna is illuminated by a wideband quad-ridged feed horn that is configured to transmit right-circular-polarization and receive left-circular-polarization. The dish is fully illuminated—the pattern of the feed horn is 3 dB lower at the edge of the dish than at the center—at about 200 MHz and under-illuminated at higher frequencies to provide a nearly-constant beamwidth (and gain) across the 200 to 400 MHz frequency band. Circular polarization is used to avoid Faraday fading—the fading of linearly-polarized VHF signals caused by rotation of the polarization ellipse during propagation through the ionosphere.

The radar includes a wideband class-AB transmitter that can operate over a 100 to 500 MHz frequency range, at a 5% duty cycle, with a maximum pulse length of about 100 μs. It is driven by a 1-GHz arbitrary waveform generator, enabling the use of a variety of waveforms and guaranteeing a stable transmitted pulse shape.

A wideband homodyne receiver is used to mix the received signal directly to baseband. The baseband signal is digitized with dual 8-bit digitizer, one each for the I and Q channels. The digitizers have a maximum sample rate of 500 MHz, but are usually operated

at 250 MHz in this system since the bandwidth of the transmitted waveform is usually less than 250 MHz. All system timing is derived from a single 10-MHz rubidium master oscillator to preserve pulse-to-pulse coherence over the full satellite pass.

With the nominal 100-μs pulse and 200-MHz bandwidth, pulse compression gains of about 20,000 are realized with matched-filter processing of the received signal. Given the relatively modest 9-kW transmitter power along with the large distances from the radar to the satellites, the full 100-μs pulse length at maximum transmitter power is needed to achieve positive SNR for several of the satellites of interest.

The pulse repetition frequency (PRF) of the radar can be varied from pass to pass. It is generally chosen so that there is only one pulse in flight at a time. This mode of operation ensures that pulse transmission does not overlap reception of the previous pulse.

The receiver is enabled, and the data are digitized, from about 15 μs before the expected leading edge of the target echo until about 15 μs after the trailing edge. This $\pm$15-μs margin allows for errors of up to about $\pm$2 km in the satellite range estimates. For each transmitted pulse, therefore, the total digitization period is about 130 μs, producing 32768 complex samples at the 250-MHz digitization rate. In this work, a *record* is the set of 32768 complex samples of the received signal corresponding to a single transmitted pulse.

During a typical satellite pass, 8192 records are collected; 8000 are target echoes, and 192 are *surface sensor records.* The surface sensor records contain samples of the transmitted waveform obtained from a sensor located on the surface of the dish. Half of the surface sensor records are recorded immediately prior to the satellite pass, and half are recorded immediately after the satellite pass. These samples of the transmitted waveform are used to monitor transmitted signal stability and to build a matched filter for pulse compression.

Appendix B

Data Processing Procedures

The theory developed in the preceding chapters has been used in this research to implement algorithms for TEC estimation and high-resolution VHF ISAR imaging. Those algorithms have been tested on actual radar data with the goal of validating the theory and evaluating the performance of the algorithms.

This appendix describes the data-processing procedure, the combination of algorithms used to process the raw radar data to obtain TEC estimates and a high-resolution image. The data-processing procedure is divided into three stages:

1) Preprocessing

   i) data formatting, data-quality analysis

   ii) filtering, interference identification and excision

   iii) pulse compression

2) Initial estimation of TEC and range using individual records

   i) TEC estimation using the TDOA technique

   ii) range estimation through target tracking

   iii) compensation of the radar data for initial range and TEC estimates

3) Imaging

   i) image formation using the polar-format algorithm

   ii) autofocusing to refine TEC and range estimates

The goal of the first stage is to produce a data set that is equivalent to what would have been collected with a perfect bandlimited impulse radar, by correcting and compensating the actual radar data. The steps in the first stage include data-quality analysis, data 'cleanup,' and compensation for the actual radar system transfer function.[1]

The goal of the second stage is to produce a radar data set that is equivalent to what would have been collected with the target on a turntable in an anechoic chamber—the classical experimental ISAR configuration. Stage two includes compensating the data produced in stage one for the initial estimates of range and TEC. Initial estimates of range are made by tracking the target through the individual records. Initial estimates of TEC are made with the TDOA technique.

In the final stage, the radar image is produced using the ISAR techniques described in Chapter 2. The initial range and TEC estimates are not sufficiently accurate to achieve theoretical resolution in the radar image, so an autofocus algorithm is used to refine those estimates to the accuracy needed to achieve theoretical resolution.

If the estimation and compensation steps in the three stages could be performed perfectly, resolution in the final ISAR image would be limited by only the fundamental parameters of center frequency, bandwidth, and angular aperture. As discussed in Chapters 2 and 4, several differences between the imaging model and the actual data compromise the accuracy of the compensation. The primary differences are caused by (1) limitations in the ability to estimate and correct for the ionosphere, (2) residual errors in the estimate of the position and orientation of the target, and (3) external noise and interference.

B.1 Preprocessing

The initial steps of cleaning, calibrating, and range-compressing the data are collectively referred to as preprocessing. Again, the goal of preprocessing is to produce a data set that is equivalent to what would have been collected with a perfect bandlimited impulse radar—that is, a radar that transmits a spectrally-flat bandlimited impulse and has a unity transfer function. The top half of the flowchart in Figure B.1 illustrates the preprocessing procedure, with the individual blocks described in the following subsections.

[1] To measure the system transfer function, the transmitted waveform is received and recorded through a horn antenna, called the *surface sensor*, which has been placed on the surface of the dish at its center. The signal from the surface sensor is recorded at the beginning and end of each satellite pass, then used to form the matched filter for pulse compression.

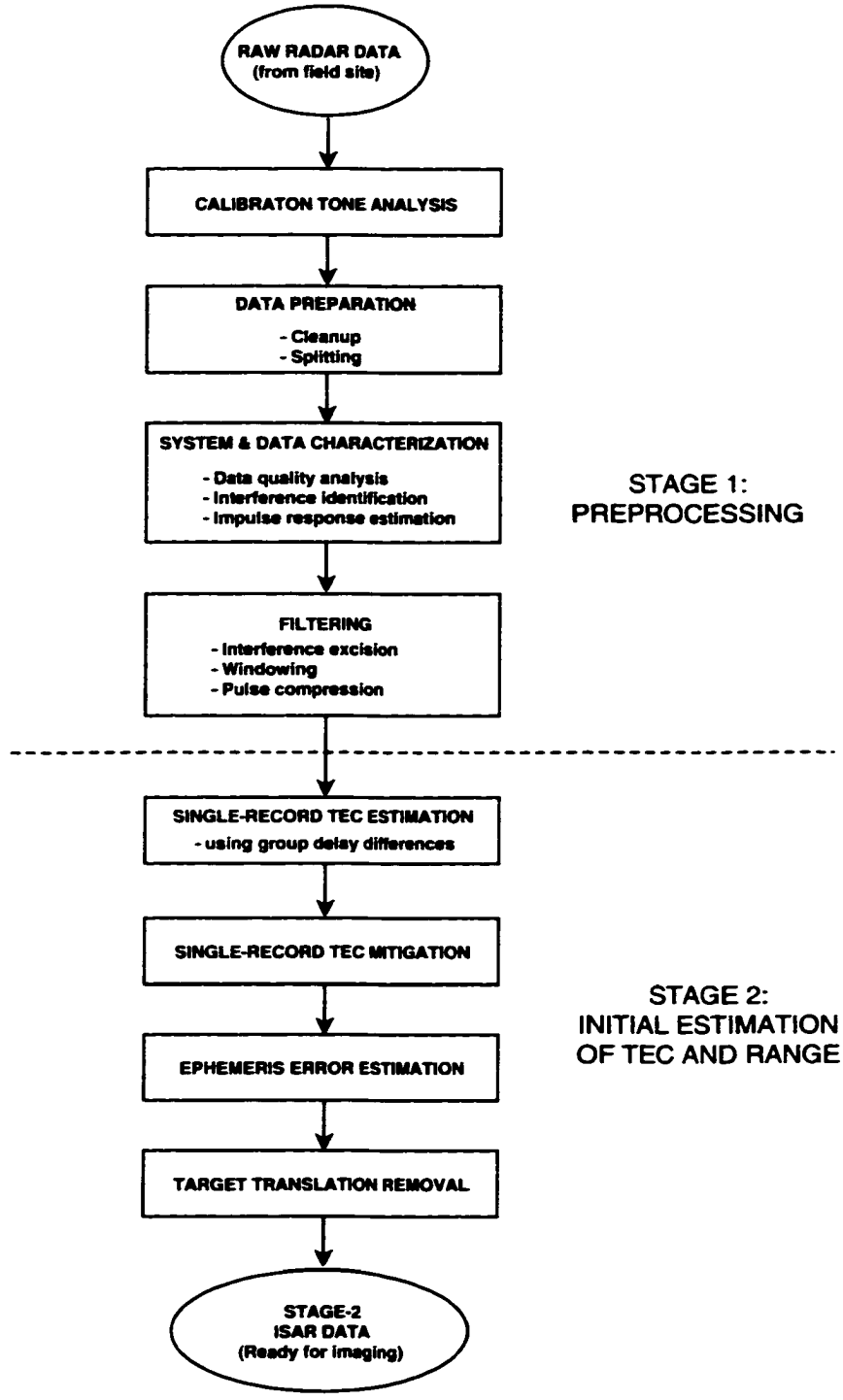

Figure B.1: Flowchart for stages 1 and 2 of data processing.

B.1.1 Calibration Tone Analysis

To monitor some aspects of radar system performance, low-level continuous wave (CW) tones, called *calibration tones*, are leaked into the data stream at the surface of the dish antenna and at the input of the receiver. The tones are derived from the system's 10-MHz reference and placed near the band edge so that they can be removed from the data with minimal impact on the radar signal. During preprocessing, the amplitudes and phases of the tones are measured in each data record. These measurements indicate system performance in terms of system phase coherence, system gain drift, I/Q amplitude and phase imbalance, missing samples, analog nonlinearities, analog saturation, and digitizer holdoff delay. In some cases, the measurements can be used to correct problems in the data, but their main purpose is to help identify system problems. Two tones are used to help localize the source if problems do appear.

B.1.2 Data Preparation

Radar data, surface-sensor data, and record headers are separated into three files. The headers are parsed to identify missing or anomalous records; 'filler records' are inserted where appropriate. The alignment of the I and Q channels is checked in the calibration tone processing results, and the channels are shifted, as needed, and balanced in amplitude and phase. The two radar control files, including the digitizer holdoff delay file and the target ephemeris file, are then processed to match their information to the appropriate data records.

B.1.3 System and Data Characterization

A variety of statistics are calculated from the radar and surface-sensor data sets to assist in monitoring system health and data quality. As part of the statistics, an average amplitude spectrum is calculated to determine overall system amplitude response and to identify the frequencies of external RF interference sources. Histograms are calculated for the I and Q channels to identify any missing bins or stuck bits and to estimate the variations in bin widths, which produce digitizer differential nonlinearities. Saturation levels are calculated to identify file sections that may have excessive saturation and to provide feedback for future settings of receiver gain. Also, means and variances are calculated in the I and Q channels to estimate and monitor channel offset and gain differences.

The system impulse response is estimated from the surface-sensor records and network analyzer measurements of the differences between the receive and surface-sensor signal paths. First, several surface-sensor records are aligned and averaged to reduce the noise level in the estimate. That estimate is then compensated for differences between the actual radar signal path and the surface-sensor signal path.[2]

The large fractional bandwidth of the transmitted waveform makes it difficult to design and build a radar with a linear phase and flat amplitude response over the full band. Fortunately, a nonlinear variation in the system phase response, or system dispersion, is not a fundamental problem since it can be compensated, to the accuracy to which it can be measured, during filtering of the radar data. However, an inverse filter is used for pulse compression, so deviations from a flat amplitude response reduce the SNR of the preprocessed data below what it would be in a system having the same noise figure with a flat spectral response. The inverse filter reduces system SNR because it applies the most gain to the weakest frequency components of the signal—those with the lowest SNR. The reduction in SNR in the inverse filter has not been a significant problem since the Stanford radar provides an amplitude response that is flat to within about 2 dB over a 200-MHz bandwidth.

B.1.4 Filtering

Interference excision can be a critical part of data processing when operating at VHF. In data collected at the SRI 150-foot dish at Stanford, California, the received signal is dominated by external RF interference from other VHF sources in the Bay Area. The average power of the interference is often more than 30 dB above the system noise level. If not removed, the interference signal can raise the background 'clutter' level in the radar image to the point where the clutter fully obscures the image. Also, interference can significantly degrade the system noise figure since the gain of the front-end amplifiers must be reduced to avoid saturation. The interference signals can be partially excised from the radar data since most are narrowband while the radar waveform is wideband. By removing the interference from the received data, its contribution to clutter in the image is also removed.

[2]The surface-sensor signal path includes the surface-sensor horn, while the radar signal path includes the receive horn, CP hybrid, TR switch, front-end filters, and front-end amplifier. The differences between the two paths have been measured with a network analyzer so that those differences can be compensated.

In this work, interference is removed by notching, or zeroing out, any bins in the Fourier transform of the signal that have unacceptably high interference levels. A constant false alarm rate (CFAR) algorithm (see *Skolnik*, 1981, p. 392) is used to identify those bins that contain most of the energy from the dominant interference sources. In the implementation of the CFAR algorithm, a frequency-dependent noise floor is first defined with a smooth envelope that has been fit to the average spectral amplitude of the data. Then, spectral bins having power levels greater than a user-defined threshold above the noise floor are identified as interference sources and zeroed out.

The notching procedure places zeros in the spectral data; consequently, it increases the sidelobe levels in the range-compressed pulse. This leads to a tradeoff between image clutter produced by interference and image artifacts produced by zeros in the spectrum. The optimal level of interference excision depends on signal, noise, and interference levels and on the bandwidth-time product of the transmitted waveform. To date, the interference threshold has been chosen heuristically—through comparison of the clutter and artifacts in the final images when different thresholds are used. For the data sets collected at Stanford, an interference threshold of 10 dB has provided a suitable balance between the effects of residual interference and the effects of zeros in the spectrum.

A spectral amplitude-weighting vector is applied to the radar data, in the frequency domain, to (1) notch out the interference and calibration tones, (2) remove out-of-band noise, (3) compensate for variations in the spectral amplitude of the transmitted waveform, and (4) taper the amplitude spectrum to provide range-direction sidelobe control.

Pulse compression is performed with a pseudo-inverse filter by applying phase compensation to the spectral data. This phase compensation is the negative (conjugate) of the phase of the transmitted waveform combined with the phase of the radar system transfer function. Note that, when the spectrum is flat, the pseudo-inverse filter used here is identical to the matched filter.

B.2 Initial Estimation of TEC and Range

Stage two of the data-processing procedure includes estimation of ionospheric TEC and target range using the individual records of the radar data set, followed by compensation of the radar data for those initial estimates. To ensure the convergence of the autofocus

algorithm in stage three, the range and TEC estimates made in this stage must be accurate enough to obtain at least partial coherence between adjacent records.

The lower half of the flowchart in Figure B.1 illustrates the initial estimation and compensation steps; the individual steps are described in the following subsections.

B.2.1 Single-Record TEC Estimation

The ionospheric TEC is estimated initially with the group delay difference technique described in Section 3.6. First, the range-compressed data generated in stage one are filtered to obtain two subband data sets: one near the low-frequency edge of the band and the other near the high-frequency edge of the band. The filter bandwidths usually are chosen to be less than the expected coherence bandwidth to avoid significant pulse spreading in the subband data records (see Section 3.5). For example, for TEC levels of less than about $2 \times 10^{17} e^-/m^2$ and frequencies greater than about 200 MHz, a bandwidth of 10 to 20 MHz is suitable. The target is then tracked through the low-frequency and high-frequency data sets, with the target location chosen from either the peak or centroid of the target echo in each subband record. The difference between the locations of the target in the low- and high-frequency subband data, called the time-difference-of-arrival (TDOA), provides an estimate of the difference between the group delays at the center frequencies of the two bands. The TDOA values are used in the equations given in Section 3.6 to estimate the TEC.

The TDOA technique produces a relatively accurate TEC estimate when the target acts as a point scatterer and the radar echo has a high SNR. In the case of extended frequency-selective targets, such as Mir, along with SNR levels typical of the Stanford radar, the group delay difference estimates are noisy. The noise level is reduced by fitting a low-order polynomial to the single-record TDOA estimates and then calculating the TEC from the smoothed TDOA values. For Mir and the nominal parameters of the Stanford radar, the TDOA technique provides an initial estimate of TEC having an accuracy of about $10^{16} e^-/m^2$.

B.2.2 Single-Record TEC Mitigation

Once the TEC has been estimated, the ionospheric effects can be removed from the radar data by applying an inverse filter. As discussed in Section 3.4, that inverse filter is a

phase-only filter that has a $1/f$ frequency response. To remove the ionospheric effects from the radar data, the smoothed TEC estimates are used in Equation 4.1 to determine the necessary phase corrections, which are then applied to the radar data in the frequency domain.

B.2.3 Ephemeris Error Estimation

The path of the satellite is calculated for antenna pointing and range gating from public-domain two-line element sets.[3] Those element sets are produced from observations of the satellite made several hours before the satellite passes over the Stanford or Ascension radar sites. Changes in the satellite orbit during those several hours, along with errors in the original two-line element sets, can cause significant errors in the satellite range estimates. For example, for objects that suffer from significant atmospheric drag, such as Mir, the ephemeris data typically have range errors of 1 or 2 km with occasional passes having errors of up to 5 km. For higher-elevation satellites, where atmospheric drag is less severe, the range errors have usually been between a few hundred meters and a kilometer.

Range errors need to be minimized, to the extent possible, prior to ISAR imaging. To create an ISAR image, the range to the target must be known to within a fraction of a wavelength over the extent of the aperture—that is, to within about 10 cm for the frequencies used in this research. This level of accuracy can be achieved by using autofocusing techniques—provided the range errors have been reduced, before beginning the autofocusing process, to a level where at least partial coherence exists between adjacent data records. Minimizing range errors prior to imaging also reduces the autofocus search space and thus the amount of computation needed to autofocus the image. Furthermore, by minimizing the search space, the autofocus algorithm is less likely to converge to an incorrect or suboptimal solution.

The actual range to the target is estimated by finding the peak return in each record of the data set, removing outliers, and then fitting a polynomial to the locations of the remaining peaks. The accuracy of the range estimates obtained by tracking the peak return is limited by the range extent and complexity of the target, since the location of the peak of the echo does not always come from the same part of the target. In the case of Mir,

[3]Two-line element sets are available from the Orbital Information Group (OIG) at the NASA Goddard Space Flight Center (GSFC). They are sufficiently accurate to calculate antenna pointing and range gating for the radar systems used in this research.

for example, the location of the largest amplitude in the echo has been observed to jump from one part of the satellite to another as the parts of the satellite glint, interfere with each other, or move behind other parts. These range jumps, in the case of Mir, are often a significant fraction of the range extent of the target, with values of 5 to 10 m commonly observed. These discontinuities in the sequence of range measurements can be reduced to some extent by tracking the centroid of the target rather than the peak.

The accuracy of the range estimate is also degraded through the group delay of any residual ionospheric TEC, left over after estimation with the TDOA technique.

The largest component of error in the ephemeris data can be characterized by a time shift. That is, the satellite follows the same track in inertial space but is a little earlier or later than predicted. That time shift is estimated by comparing the measured range observed in the radar data with the predicted range listed in the ephemeris. Earth rotation during the pass is included in the time-shifted range calculations. The time shift that gives the best fit between the predicted and measured range is recorded for use in the target-translation-removal processing block.

Residual range-estimation errors result from noise, uncompensated ionospheric effects, target range extent, and higher-order errors in the ephemeris (a time shift removes only the largest ephemeris error component). The cumulative residual range error is estimated by fitting a low-order polynomial to the difference between the predicted range, after time-shifting the ephemeris, and the measured range. This residual range error has been found to be some fraction of the range extent of the target. For example, the residual range error, for Mir, has usually been about 10 to 20 m.

B.2.4 Target Translation Removal

The ISAR imaging code uses a system model in which the target remains at a fixed range with the only target motion being rotation with respect to the radar. Variations in target range must be compensated in the radar data so that the radar data match the imaging model. This is done by time-shifting the data records by $2/c$ times the range estimates from target tracking.

Since the data are digitized at baseband after mixing with the local oscillator, the phase of the local oscillator must be accounted for when time-shifting the data. As described in Section 2.4, that is done by multiplying each record by $\exp(i2\pi f_c \Delta t)$, where f_c is the local oscillator frequency and Δt is the time shift.

B.3 Imaging

Following initial estimation and compensation of range and TEC, images are produced from the radar data with the ISAR techniques described in Chapter 2. Since the initial range and TEC estimates are not sufficiently accurate to achieve full resolution, the imaging algorithm includes a search for range and TEC corrections that do produce full resolution. That algorithm, called autofocus, uses the information in the radar data themselves to correct the range and TEC estimates.

The autofocus search is over a multi-dimensional space that characterizes the errors to an appropriate level of accuracy. In this research, the range and TEC errors are described with orthogonal Legendre polynomials. Each coefficient of those polynomials corresponds to one dimension of the search space.

The quality of the image must be defined and quantified with a cost function to give the autofocus algorithm a metric for comparison of different images and to enable it to search for the optimal image (see Section 2.5). When the autofocus search is complete, the final image is expected to have the range and cross-range resolutions specified in the equations of Section 2.3. Also, range and TEC estimates are expected to be accurate to the levels derived in Chapter 4.

The imaging procedure described here (and illustrated in the flowchart in Figure B.2) is an implementation of the autofocus algorithm. It uses the contrast of the image amplitude as the cost function and the simplex method as the optimization technique. The procedure, which is relatively easy to implement, provides a flexible and robust method for searching the multi-dimensional range and TEC error space if the initial range and TEC estimates are sufficiently accurate. On the down side, however, it is relatively slow to converge and, as a result, computationally expensive.

The following subsections describe the steps involved in implementing the imaging procedure. Those steps correspond to the blocks in the flowchart in Figure B.2.

B.3.1 Range and TEC Error Estimation

Initial estimates of the range and TEC errors are needed as a starting point for the autofocus algorithm. Since those errors are minimized during stage two of data processing, an initial estimate of zero error is usually sufficient when forming the first images for a satellite pass.

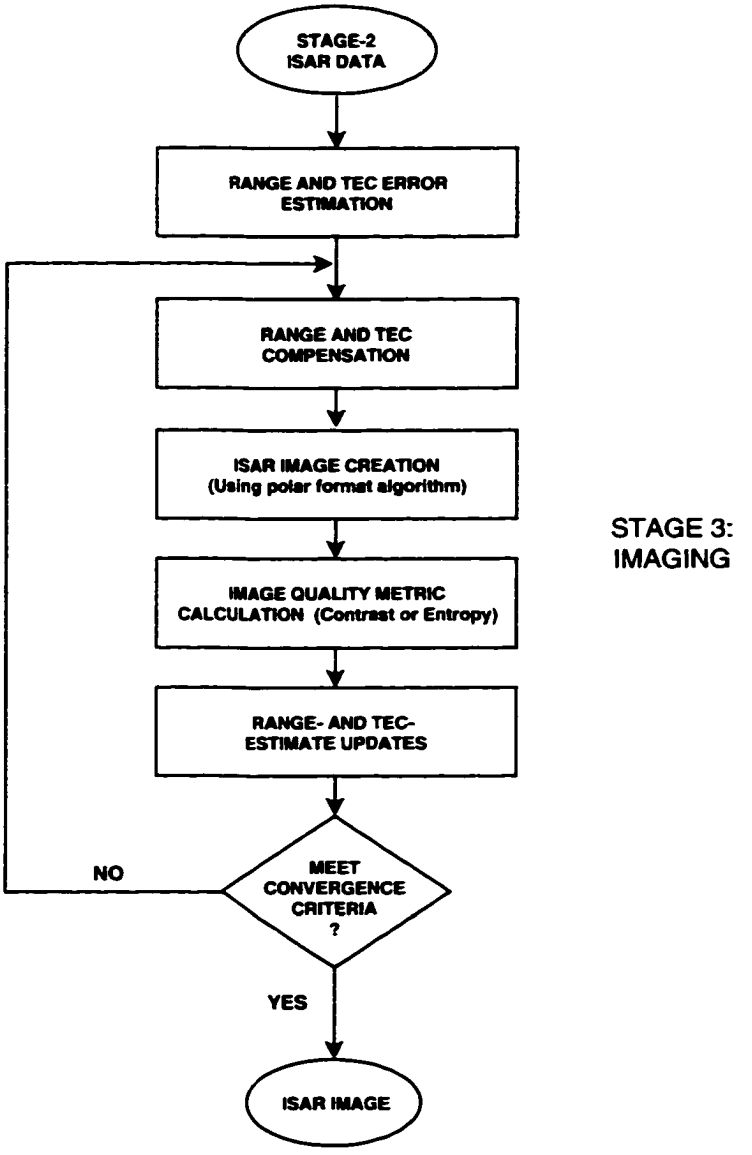

Figure B.2: Flowchart for stage 3 of data processing; the imaging procedure.

Autofocus search time can be significantly reduced by improving the initial range and TEC estimates through imaging of subaperture data—that is, imaging of data from only part of the satellite pass. Reducing the aperture size also reduces the imaging computations, since fewer records are used and fewer pixels are needed in the lower-resolution subaperture image. Range- and TEC-error solutions from a subaperture image can then be used as initial estimates for a wider aperture. Also, the subaperture error solutions can be extrapolated and used to calculate initial estimates for adjacent subapertures. This subaperture processing procedure can be repeated until images are produced over the full aperture, thereby providing range and TEC estimates across the full satellite pass.

B.3.2 Range and TEC Compensation

In each iteration of the autofocus loop, the range and TEC estimates are updated and the radar data are compensated for the new estimates. Since both range compensation and TEC compensation are linear, they can be applied in an incremental manner by compensating for only the differences from the previous iteration. The TEC estimate corrections are made in the frequency domain by applying the TEC phase compensation of Equation 4.1. The range estimate corrections are also made in the frequency domain to allow subsample range-shifting by applying a linear phase shift. The range and TEC corrections are combined into a single frequency-domain phase compensation given by

$$\phi(f) = 2\pi \left(\Delta t \cdot f + \frac{b}{2\pi^2 c} \cdot \Delta N_{\mathrm{T}} \cdot \frac{1}{f} \right), \tag{B.1}$$

where $\phi(f)$ is the frequency-domain phase compensation, Δt is the time shift, and ΔN_{T} is the TEC correction.

B.3.3 ISAR Image Creation

Once range and TEC corrections have been made, standard ISAR techniques are used to produce images from the data. The polar-format algorithm, described in Chapter 2, is the procedure usually used for imaging in this research. The steps in that algorithm are:

i) Calculate the one-dimensional Fourier transform of the radar data records,

ii) Resample the polar frequency-domain data onto a two-dimensional rectangular grid, and

iii) Calculate the inverse two-dimensional Fourier transform of the resampled data.

The result is an image of the spatial distribution of the complex scattering amplitude of the target.

Images can also be produced with the coherent tomographic or back-projection algorithm described in Section 2.2. That algorithm is mathematically equivalent to the polar-format algorithm, but calculations are performed in the time domain rather than the frequency domain, and it uses iterative rather than block operations. The back-projection algorithm can be summarized as:

For each sample in each radar data record:

i) Calculate the distance from the spatial location of the sample to the image origin,

ii) Determine the line of pixels in the image that have that same distance to the image origin, and

iii) Add the value of the sample into each of the pixels on the line; that is, back-project the sample into the line of pixels in the image.

Again, the result is an image of the spatial distribution of the complex scattering amplitude of the target.

Both polar-format and tomographic algorithms have been used for ISAR image creation in this research, with results that are identical to within the accuracy of the approximations used in their implementations.

B.3.4 Image Quality Metric Calculation

In order to use the image to correct for errors in the range and TEC estimates, a quantitative measure of image quality, called the image cost function, is needed. The contrast of the image has been used as the cost function during most of this research.

Image contrast, discussed in Section 2.5, is defined in this work as the ratio of the standard deviation of the image to the mean of the image. When using contrast as a quality metric, the optimal image is defined as the one having the largest contrast. That image may or may not be the same as the correct image—that is, the one that has zero range and TEC errors.

The underlying assumption in using contrast as an image-quality metric is that image resolution and image quality are strongly correlated with image contrast. Strong correlation exists, for example, when the target echo comes from discrete, or localized, scattering centers. If the target exhibits primarily distributed scattering or volumetric scattering, image quality and resolution are not necessarily correlated with image contrast; in that case, image contrast becomes a poor measure of image quality. This could be expected since the correct image of a distributed or volumetric target has lower variance, and thus lower contrast.

As another perspective on how image contrast works as an image-quality metric, note that for each point in the image, the imaging process coherently adds the appropriate samples from each radar data record. When range errors are eliminated, phase errors in those samples are also eliminated, so the samples add to a maximum, thus producing maximum image contrast.

The cost function can also be defined in terms of a *generalized contrast*, where the image amplitude is raised to an exponent before calculating the ratio of the standard deviation to the mean. An exponent of one then gives the contrast of the image amplitude, while an exponent of two gives the contrast of the image power. In principle, image amplitude could be raised to any exponent before the contrast is calculated. As the exponent in the generalized contrast is increased, higher-order statistics of the image become increasingly important and have a stronger effect on the autofocus solution. Thus, larger exponents place more emphasis on the bright areas of the target, thereby making the autofocusing algorithm more aggressive in trying to 'push' the signal energy into the brightest areas of the image. From the experience gained with the data collected in this research, exponents of two or greater work well if the bright parts of the target are point scatterers. For extended targets such as large cylinders and solar panels, better image quality has been obtained when using exponents between 1.2 and 1.5. These smaller exponents increase the relative contribution of dimmer parts of the target to the contrast, but they also cause the autofocus solution to be more sensitive to noise.

Contrast of image amplitude, with an exponent between about 1.2 and 1.5, has provided the best results for the Mir data sets.

B.3.5 Range- and TEC-Estimate Updates

The range and TEC estimates are modified and gradually improved by the autofocus search algorithm, which uses the simplex method in this research. Given a start point, the algorithm chooses $n + 1$ points to define the boundaries of an initial search volume, called a simplex, in the n-dimensional search space. The simplex is expanded, moved, and contracted according to the simplex search algorithm until it is within a user-specified tolerance of the range and TEC values that maximize the cost function. A detailed description of the simplex method can be found in *Press et al.* (1992).

B.3.6 Convergence Criteria

The autofocus search is complete when some convergence criteria have been met. Those criteria can include the accuracy of the range- and TEC-error estimates or the threshold at which increases in image contrast have a negligible effect on image quality. A combination of these two conditions has been used in this work.

Appendix C

Images From Other Data Sets

This appendix provides examples of some of the other satellite images produced during the course of this research.

C.1 Pass 8028a

Pass name	8028a
Target	Mir and Endeavour (STS-89), docked
Site	Stanford
Date (UT)	January 28, 1998
Start time (UT)	03:57:14.0
PRF	40 Hz
Data collection period	200 s
Satellite altitude	387 km
Maximum elevation	44.2°
Satellite stabilization	inertial
Full pass aperture	111.2°
Out-of-plane angle	$< 1.1°$
Sunspot number	89
vTEC to target altitude	$\sim 2 \times 10^{16}\ e^-/m^2$

Table C.1: Pass 8028a parameters.

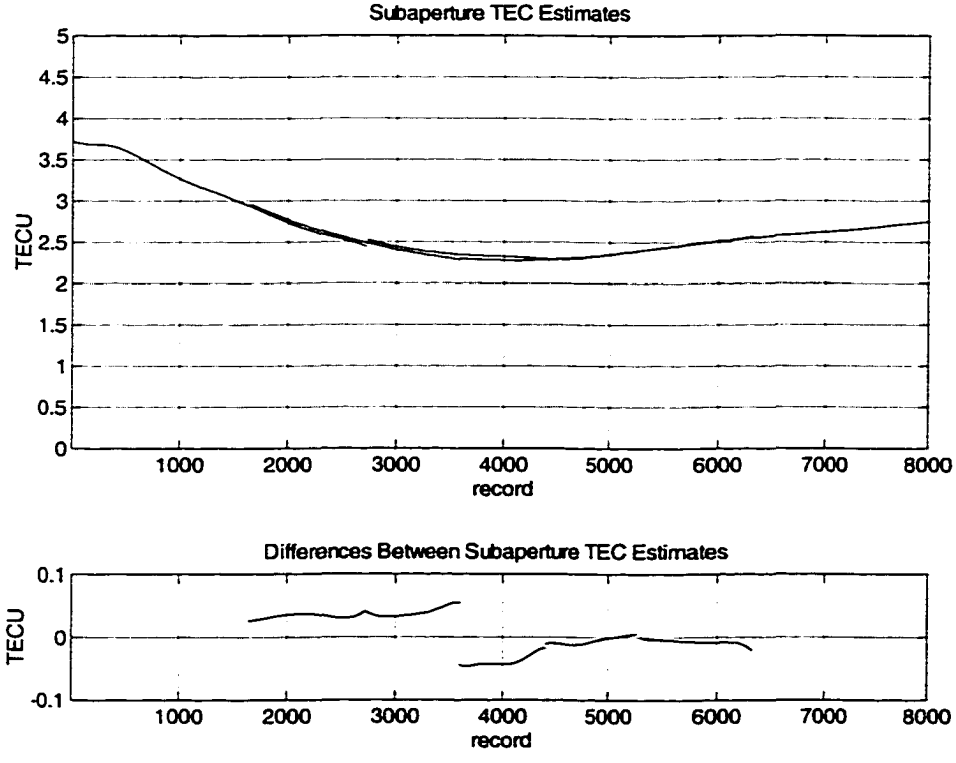

Figure C.1: TEC estimates from pass 8028a.

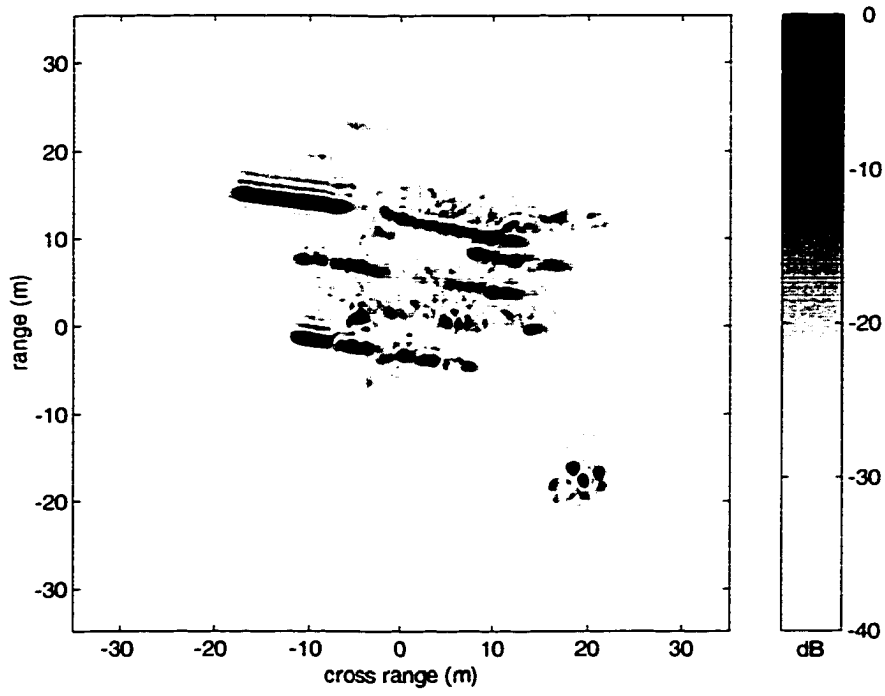

Figure C.2: Mir/Endeavour image. This image was generated from records 4559–8000 of pass 8028a.

Pass name	8028a
Frequency band	230–390 MHz
Data records	4559–8000
Angular aperture	45.0°
Range resolution	0.94 m
Cross-range resolution	0.63 m

Table C.2: Parameters for the Mir/Endeavour image of Figure C.2.

C.2 Pass 8159a

Pass name	8159a
Target	Mir and Discovery (STS-91), docked
Site	Ascension Island
Date (UT)	June 8, 1998
Start time (UT)	02:39:52.0
PRF	50 Hz
Data collection period	160 s
Satellite altitude	378 km
Maximum elevation	50.7°
Satellite stabilization	inertial
Full pass aperture	104.6°
Out-of-plane angle	$< 0.8°$
Sunspot number	104
vTEC to target altitude	$\sim 9 \times 10^{15}$ e$^-$/m^2

Table C.3: Pass 8159a parameters.

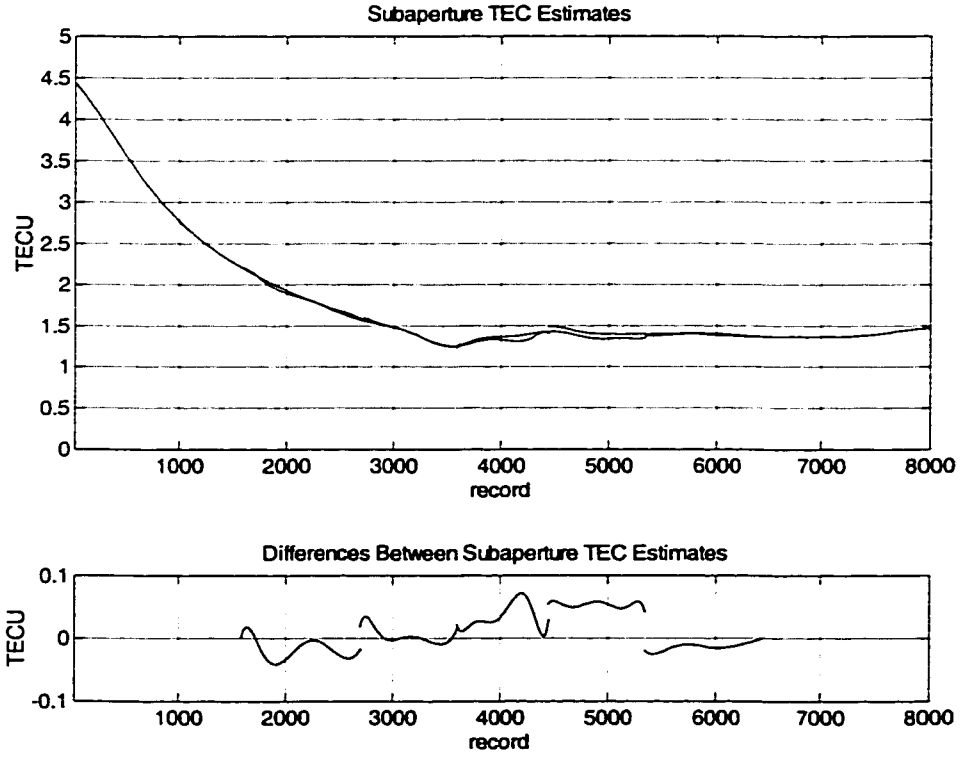

Figure C.3: TEC estimates from pass 8159a.

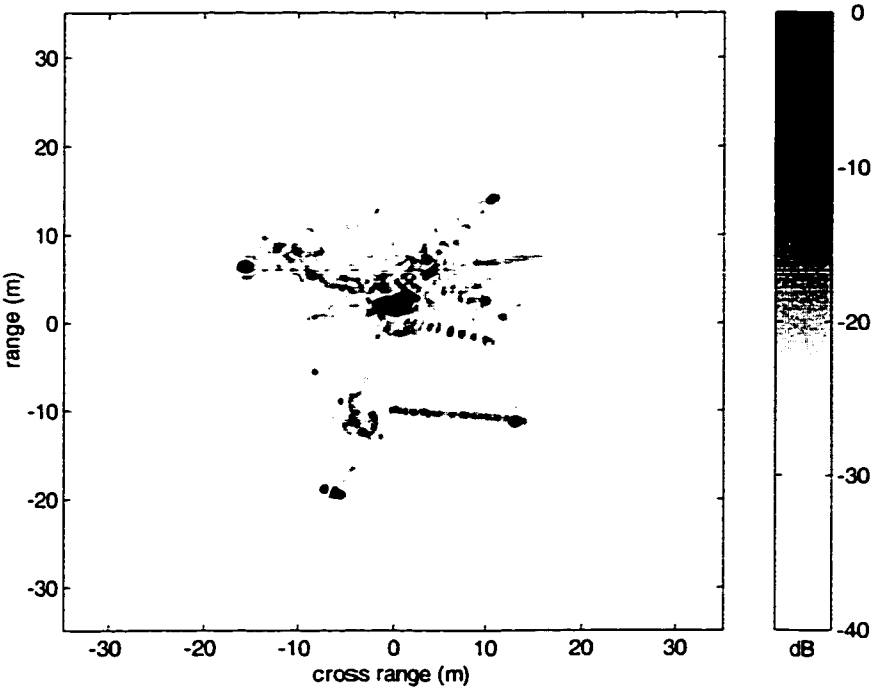

Figure C.4: Mir/Discovery image. This image was generated from records 4433–8001 of pass 8159a.

Pass name	8159a
Frequency band	200–400 MHz
Data records	4433–8001
Angular aperture	45°
Range resolution	0.75 m
Cross-range resolution	0.65 m

Table C.4: Parameters for the Mir/Discovery image of Figure C.4.

C.3 Pass 8159b

Pass name	8159b
Target	Cosmos 2347
Site	Ascension Island
Date (UT)	June 8, 1998
Start time (UT)	05:29:40.0
PRF	50 Hz
Data collection period	160 s
Satellite altitude	411 km
Maximum elevation	60.1°
Satellite stabilization	nadir
Full pass aperture	97.6°
Out-of-plane angle	$< 0.6°$
Sunspot number	104
vTEC to target altitude	$\sim 5 \times 10^{15}$ e$^-$/m^2

Table C.5: Pass 8159b parameters.

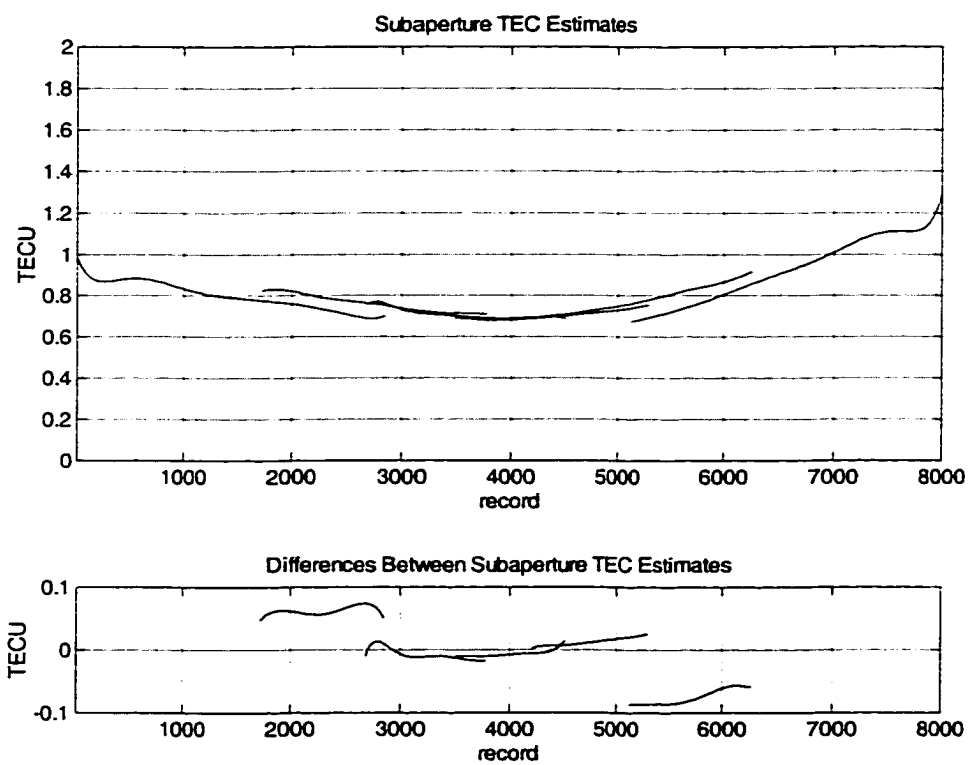

Figure C.5: TEC estimates from pass 8159b.

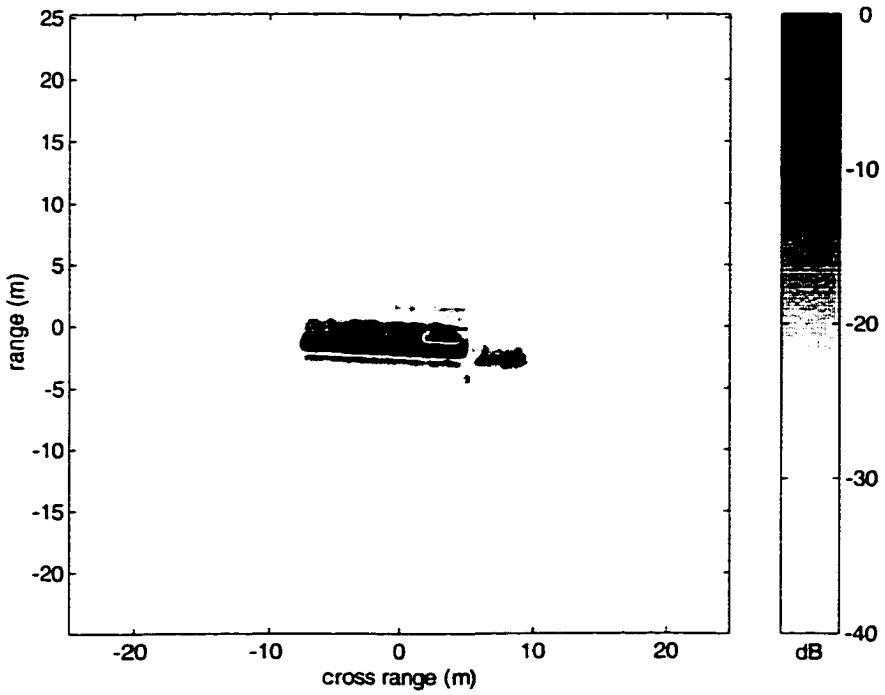

Figure C.6: Cosmos 2347 image. This image was generated from records 2049–5952 of pass 8159b. For information about Cosmos 2347, see Federation of American Scientists. URL http://www.fas.org/spp/guide/russia/military/sigint/eorsat.htm, Washington, DC.

Pass name	8159b
Frequency band	200–400 MHz
Data records	2049–5952
Angular aperture	60.0°
Range resolution	0.75 m
Cross-range resolution	0.50 m

Table C.6: Parameters for the Cosmos 2347 image of Figure C.6.

Bibliography

Aarons, J., Global morphology of ionospheric scintillations, *Proc. IEEE*, *70*, 360–378, 1982.

Anderson, D. N., J. M. Forbes, and M. Codrescu, A fully analytic, low- and middle-latitude ionospheric model, *J. Geophys. Res.*, *94*, 1520–1524, 1989.

Anderson, D. N., M. Mendillo, and B. Herniter, A semi-empirical low-latitude ionospheric model, *Radio Sci.*, *22*, 292–306, 1987.

Appleton, E. V., URSI Proc., in *Washington Assembly*, URSI, 1927.

Appleton, E. V., Wireless studies of the ionosphere, *J. Instn. Elect. Engrs.*, *71*, 642, 1932.

Arikan, O. and D. C. Munson, Jr., A new backprojection algorithm for spotlight-mode SAR and ISAR, in *Innovative Science and Technology for Government and Civilian Applications*, pp. 1453–1456, SPIE, 1989.

Ausherman, D. A., A. Kozma, J. L. Walker, H. M. Jones, and E. C. Poggio, Developments in radar imaging, *IEEE Trans. Aerospace and Electronic Systems*, *AES-20*, 363–400, 1984.

Axellson, S. R. J., Frequency and azimuthal variations of radar cross section and their influence upon low-frequency SAR imaging, *IEEE Trans. Geoscience and Remote Sensing*, *33*, 1258–1265, 1995.

Barton, D. K., Satellite tracking, in Berkowitz, R. S. (ed.), *Modern Radar, Analysis, Evaluation, and System Design*, pp. 625–649, John Wiley & Sons, 1965.

Basu, S. *et al.*, High resolution topside in situ data of electron densities and VHF/GHz scintillations in the equatorial region, *J. Geophys. Res.*, *88*, 403–415, 1983.

Basu, S. *et al.*, Scintillations, plasma drifts, and neutral winds in the equatorial ionosphere after sunset, *J. Geophys. Res.*, *101*, 26795, 1996.

Baum, C. E., Concepts in transient/broadband electromagnetic target identification, in Carin, L. and L. B. Felsen (eds.), *Ultra-Wideband, Short-Pulse Electromagnetics 2*, pp. 515–525. Plenum Press, 1995.

Baum, C. E., E. J. Rothwell, K. Chen, and D. P. Nyquist, The singularity expansion method and its application to target identification, *Proc. IEEE*, *79*, 1481–1492, 1991.

Bean, B. R. and E. J. Dutton, *Radio Meteorology*, National Bureau of Standards, Monograph 92, U.S. Govt. Printing Office, 1966.

Berizzi, F. and G. Corsini, Focusing of two dimensional ISAR images by contrast maximization, in *Proc. 22nd European Microwave Conference*, no. 22 in series 2, pp. 951–956, 1996.

Bilitza, D., K. Rawer, L. Bossy, and T. Gulyaeva, International reference ionosphere—past, present, and future, *Adv. Space Research*, *13*, 3–23, 1993.

Blacknell, D., A. P. Blake, C. J. Oliver, and R. G. White, A comparison of SAR multilook registration and contrast optimisation autofocus algorithms applied to real SAR data, in *International Conference - Radar '92*, vol. 365, pp. 363–366, IEE, 1992.

Blacknell, D. and S. Quegan, SAR motion compensation using autofocus, *Int. J. Remote Sensing*, *12*, 253–275, 1991.

Blejer, D., C. Frost, and S. Scarborough, UHF ground penetrating measurements of buried and partially buried trihedrals, in *Proc. SPIE*, vol. 2217, pp. 50–62, SPIE, 1994.

Booker, H. G., Fifty years of the ionosphere. the early years—electromagnetic theory, *J. Atmospheric and Terrestrial Physics*, *36*, 2113–2136, 1974.

Born, M. and E. Wolf, *Principles of Optics*, Pergamon Press, 6th edn., 1980.

Bracewell, R. N., Strip integration in radio astronomy, *Aust. J. Phys.*, *9*, 198–217, 1956.

Bracewell, R. N., *Two-Dimensional Imaging*, Prentice–Hall, 1995.

Bracewell, R. N. and A. C. Riddle, Inversion of fan-beam scans in radio astronomy, *Astrophys. J.*, *150*, 427–434, 1967.

Breit, G. and M. A. Tuve, A test of the existence of the conducting layer, *Phys. Rev.*, *28*, 554, 1926.

Bromaghim, D. R. and J. P. Perry, A wideband linear FM ramp generator for the long-range imaging radar, *IEEE Trans. Microwave Theory and Techniques*, *MTT-26*, 322–325, 1978.

Brookner, E., Effect of ionosphere on radar waveforms, *J. Franklin Inst.*, *280*, 1–22, 1965.

Brookner, E., Effects of the atmosphere on laser radars, in Brookner, E. (ed.), *Radar Technology*, chap. 15, pp. 213–226, Artech House, 1977a.

Brookner, E., Pulse-distortion and Faraday-rotation ionospheric limitations, in Brookner, E. (ed.), *Radar Technology*, chap. 14, pp. 201–212, Artech House, 1977b.

Brown, L. D., R. E. Daniell, Jr., M. W. Fox, J. A. Klobuchar, and P. H. Doherty, Evaluation of six ionospheric models as predictors of total electron content, *Radio Sci.*, *26*, 1007–1015, 1991.

Brown, W. D. and G. D. Cable, The spatial variance of ionospherically-induced phase errors in SAR imagery, in Goodman, J. M. (ed.), *1993 Ionospheric Effects Symposium*, pp. 88–98, U.S. Govt. Printing Office, 1993.

Brown, W. M., Walker model for radar sensing of rigid target fields, *IEEE Trans. Aerospace and Electronic Systems*, *AES-16*, 104–107, 1980.

Brown, W. M. and R. J. Fredericks, Range-Doppler imaging with motion through resolution cells, *IEEE Trans. Aerospace and Electronic Systems*, *AES-5*, 98–102, 1969.

Brunzell, H., Extraction of discriminant features from impulse radar data for classification of buried objects, in *IGARSS '97*, pp. 1285–1287, IEEE, 1997.

Budden, K. G., *The Propagation of Radio Waves, The theory of radio waves of low power in the ionosphere and magnetosphere*, Cambridge University Press, 1988.

Bush, R. W., Transionospheric propagation effects on coherent integration by ground-based radars, in Goodman, J. M. (ed.), *Effect of the Ionosphere on Space and Terrestrial Systems*, pp. 522–529, U.S. Govt. Printing Office, 1978.

Cantalloube, H. M. J. *et al.*, Autofocusing of (inverse) synthetic aperture radar for motion compensation, in *Proc. IEEE 1996 National Aerospace and Electronics Conference*, vol. 1, pp. 309–316, IEEE, 1996.

Carrara, W., S. Tummala, and R. Goodman, Motion compensation algorithm for widebeam stripmap SAR, in *Algorithms for Synthetic Aperture Radar Imagery II*, vol. 2487, pp. 13–23, SPIE, 1995a.

Carrara, W. G., R. S. Goodman, and R. M. Majewski, *Spotlight Synthetic Aperture Radar, Signal Processing Algorithms*, Artech House, 1995b.

Chapman, S., The atmospheric height distribution of band absorbed solar radiation, *Proc. Phys. Soc.*, *51*, 93–109, 1939.

Chen, C. and H. C. Andrews, Multifrequency imaging of radar turntable data, *IEEE Trans. Aerospace and Electronic Systems*, *AES-16*, 23–52, 1980a.

Chen, C. and H. C. Andrews, Target-motion-induced radar imaging, *IEEE Trans. Aerospace and Electronic Systems*, *AES-16*, 2–14, 1980b.

Chen, Y. *et al.*, Inverse synthetic aperture radar imaging techniques for sea-surface targets, in *IGARSS '87. Remote Sensing: Understanding the Earth as a System*, pp. 723–728, 1987.

Clemmow, P. C. and J. P. Dougherty, *Electrodynamics of Particles and Plasmas*, Addison–Wesley, 1969.

Cook, C. E. and M. Bernfeld, *Radar Signals, An Introduction to Theory and Application*, Artech House, 1993.

Coster, A. J., Radar, laser, and telescope parameters of various Lincoln Laboratory affiliated facilities, Tech. Rep. 91M-0703, MIT Lincoln Lab., 1991.

Coster, A. J., E. M. Gaposchkin, L. E. Thornton, G. R. Krumpholz, and T. A. Cott, Ionospheric effects in satellite tracking, in Goodman, J. M. (ed.), *1993 Ionospheric Effects Symposium*, pp. 80–87, U.S. Govt. Printing Office, 1993.

Croft, T. A. and H. Hoogasian, Exact ray calculations in a quasi-parabolic ionosphere with no magnetic field, *Radio Sci.*, *3 (New Series)*, 69–74, 1968.

Curlander, J. C. and R. N. McDonough, *Synthetic Aperture Radar, Systems and Signal Processing*, John Wiley & Sons, 1991.

Cutrona, L. J., W. E. Vivian, E. N. Leith, and G. O. Hall, A high resolution radar combat-surveillance system, *IRE Trans. Military Electronics, MIL-5*, 127–131, 1961.

Daniell, Jr., R. E., L. D. Brown, D. N. Anderson, M. W. Fox, P. H. Doherty, D. T. Decker, J. J. Sojka, and R. W. Schunk, Parameterized ionospheric model: A global ionospheric parameterization based on first principles models, *Radio Sci., 30*, 1499–1510, 1995.

Decker, D. T., D. N. Anderson, and A. J. Preble, Improving IRI-90 low-altitude electron density specification, *Radio Sci., 32*, 2003–2019, 1997.

Desai, M. D. and W. K. Jenkins, Convolution backprojection image reconstuction for spot-light mode synthetic aperture radar, *IEEE Trans. Image Processing, 1*, 505–517, 1992.

Eshleman, V. R., P. B. Gallagher, and R. C. Barthle, Radar methods of measuring the cislunar electron density, *J. Geophys. Res., 65*, 3079–3086, 1960.

Farrell, J. L., J. H. Mims, and A. Sorrell, Effects of navigation errors in maneuvering SAR, *IEEE Trans. Aerospace and Electronic Systems, AES-9*, 758–776, 1973.

Fitzgerald, T. J., Ionospheric effects on synthetic aperture radar at VHF, in *IEEE National Radar Conference, 1997*, vol. 1, pp. 237–239, IEEE, 1997.

Fleischman, J. G., S. Ayasli, E. M. Adams, and D. R. Gosselin, Part I: Foliage attenuation and backscatter analysis of SAR imagery, *IEEE Trans. Aerospace and Electronic Systems, 32*, 135–144, 1996.

Flores, B. C., S. Tariq, and J. S. Son, Image focus quality indicators for efficient inverse synthetic aperture radar phase correction, in *Algorithms for Synthetic Aperture Radar Imagery III*, vol. 2757, pp. 2–13, SPIE, 1996.

Goodman, J. M., *HF Communications, Science and Technology*, Van Nostrand Reinhold, 1992.

Green, A. L., Early history of the ionosphere, *J. Atmospheric and Terrestrial Physics, 36*, 2159–2165, 1974.

Grosch, T. O., Ground penetration radar technology review, Tech. Rep. GPR-1, MIT Lincoln Lab., 1994.

Groves, K. M. *et al.*, Equatorial scintillation and systems support, *Radio Sci.*, *32*, 2047–2064, 1997.

Gustavsson, A., P. O. Frölind, H. Hellsten, T. Jonsson, B. Larsson, and G. Stenström, The airborne VHF SAR system CARABAS, in *IGARSS '93*, pp. 558–562, IEEE, 1993.

Hagfors, T., B. Nanni, and K. Stone, Aperture synthesis in radar astronomy and some applications to lunar and planetary studies, *Radio Sci.*, *3 (New Series)*, 491–509, 1968.

Happ, L. *et al.*, Low-frequency ultra-wideband synthetic aperture radar 1995 BoomSAR tests, in *IEEE National Radar Conference, 1996*, vol. 1, pp. 54–59, IEEE, 1996.

Hargreaves, J. K., *The Solar-Terrestrial Environment*, Cambridge University Press, 1992.

Hartree, D. R., The propagation of electro-magnetic waves in a refracting medium in a magnetic field, *Proc. Camb. Phil. Soc.*, *27*, 143, 1931.

Held, D. N. *et al.*, The NASA/JPL multifrequency multipolarization airborne SAR system, in *IGARSS '88*, pp. 345–349, IEEE, 1988.

Hildebrand, B. P., Statistics of focused and defocused radar maps, *IEEE Trans. Aerospace and Electronic Systems*, *AES-10*, 615–621, 1974.

Hoffman, L. A., K. H. Hurlbut, D. E. Kind, and H. J. Wintroub, A 94-GHz radar for space object identification, *IEEE Trans. Microwave Theory and Techniques*, *17*, 1145–1149, 1969.

Ishimaru, A., Y. Kuga, J. Liu, Y. Kim, and T. Freeman, Ionospheric effects on synthetic aperture radar at 100 MHz to 2 GHz, *Radio Sci.*, *34*, 257–268, 1999.

Jakowatz, Jr., C. V., P. H. Eichel, and D. C. Ghiglia, Autofocus of SAR imagery degraded by ionospheric-induced phase errors, in *Millimeter Wave and Synthetic Aperture Radar*, pp. 46–52, SPIE, 1989.

Kak, A. C. and M. Slaney, *Principles of Computerized Tomographic Imaging*, IEEE, 1988.

Katz, A. H., M. D. Grossi, R. S. Allen, and D. E. Donatelli, Adaptive correction of the effect of the ionosphere on range determination by terrestrial radars, in Goodman, J. M. (ed.), *Effect of the Ionosphere on Space and Terrestrial Systems*, pp. 512–521, U.S. Govt. Printing Office, 1978.

Kelley, M. C., *The Earth's Ionosphere, Plasma Physics and Electrodynamics*, Academic Press Inc., 1989.

Kim, Y. and J. van Zyl, Ionospheric effects on polarimetric and interferometric space-borne SAR, in *IGARSS '98*, IEEE, 1998.

Kirk, Jr., J. C., Motion compensation for synthetic aperture radar, *IEEE Trans. Aerospace and Electronic Systems*, *AES-11*, 338–348, 1975.

Klobuchar, J. A., S. Basu, and P. H. Doherty, Potential limitations in making absolute ionospheric measurements using dual frequency radio waves from GPS satellites, in Goodman, J. M. (ed.), *1993 Ionospheric Effects Symposium*, pp. 187–194, U.S. Govt. Printing Office, 1993.

Knepp, D. L. and R. A. Dana, The impact of strong scintillation on space-based radar design: Clutter rejection, *Radio Sci.*, *20*, 366–374, 1985.

Knepp, D. L. and E. L. Mokole, Space-based radar coherent processing during scintillation: VHF through L-band, *Radio Sci.*, *27*, 47–61, 1992.

Knowles, S. H., Ionospheric limitations to coherent processing of transionospheric radars, in Goodman, J. M. (ed.), *The Effect of the Ionosphere on Communication, Navigation, and Surveillance Systems*, pp. 85–91, U.S. Govt. Printing Office, 1987.

Koehler, R. L., Radio propagation measurements of pulsed plasma streams from the Sun using Pioneer spacecraft, *J. Geophys. Res.*, *73*, 4883–4894, 1968.

Kolmogorov, A. N., The local structure of turbulence in incompressible viscous fluids for very high Reynolds numbers, in Friedlander, S. K. and L. Topper (eds.), *Turbulence, Classic Papers on Statistical Theory*, Wiley–Interscience, 1961.

Kovaly, J. J., Radar techniques for planetary mapping with orbiting vehicle, *Annals N.Y. Academy of Sciences*, *187*, 154–176, 1972.

Lanyi, G. and T. Roth, A comparison of mapped and measured total ionospheric electron content using global positioning system and beacon satellite observations, *Radio Sci.*, *23*, 483–492, 1988.

Lassen, H., *Elekt. Nachr. Tech.*, *4*, 324, 1927.

Lawrence, R. S., C. G. Little, and H. J. A. Chivers, A survey of ionospheric effects upon earth-space radio propagation, in *Proc. IEEE*, pp. 4–27, 1964.

Leadabrand, R. L., R. B. Dyce, A. Fredriksen, R. I. Presnell, and J. C. Schlobohm, Radio frequency scattering from the surface of the moon, *Proc. IRE*, *48*, 932–933, 1960.

Lerch, Jr., C. S., Satellite surveillance radar, in Skolnik, M. I. (ed.), *Radar Handbook*, chap. 32, McGraw–Hill, 1st edn., 1970.

LeToan, T., A. Beaudoin, J. Riona, and D.Guyon, Relating forest biomass to SAR data, *IEEE Trans. Geoscience and Remote Sensing*, *30*, 1992.

Macovski, A., *Medical Imaging Systems*, Prentice–Hall, 1983.

McCord, H. L., The equivalence among three approaches to deriving synthetic array patterns and analyzing processing techniques, *IRE Trans. Military Electronics*, *MIL-6*, 116–119, 1962.

McCorkle, J. W., Early results from the Army Research Laboratory ultra-wide-bandwidth foliage penetrating SAR, in *Proc. SPIE*, vol. 1942, pp. 88–95, SPIE, 1993.

Mensa, D. L., *High Resolution Radar Cross-Section Imaging*, Artech House, 2nd edn., 1991.

Mersereau, R. M. and A. V. Oppenheim, Digital reconstruction of multidimensional signals from their projections, *Proc. IEEE*, *62*, 1319–1338, 1974.

Millman, G. H., Atmospheric effects on radio wave propagation, in Berkowitz, R. S. (ed.), *Modern Radar, Analysis, Evaluation, and System Design*, pp. 317–377, John Wiley & Sons, 1965.

Mims, J. H. and J. L. Farrell, Synthetic aperture imaging with maneuvers, *IEEE Trans. Aerospace and Electronic Systems*, *AES-8*, 410–418, 1972.

Munson, Jr., D. C. and W. K. Jenkins, A common framework for spotlight mode synthetic aperture radar and computer-aided tomography, in Chan, S. P. (ed.), *15th Asilomar Conf. on Circuits, Systems and Computers*, pp. 217–221, 1981.

Munson, Jr., D. C., J. D. O'Brien, and W. K. Jenkins, A tomographic formulation of spotlight-mode synthetic aperture radar, *Proc. IEEE*, *71*, 917–925, 1983.

Nagpal, O. P., Travelling ionospheric disturbances, in Tyagi, T. R. (ed.), *Proc. Int. Symp. on Beacon Satellite Studies of the Earth's Environment*, pp. 35–44, 1983.

Ostro, S. J., Planetary radar astronomy, *Rev. Modern Physics*, *65*, 1235–1279, 1993.

Pettengill, G. H., Measurements of lunar reflectivity using the Millstone radar. *Proc. IRE*, *48*, 933–934, 1960.

Pettengill, G. H., D. B. Campbell, and H. Masursky, The surface of Venus, *Scientific American*, *243*, 54–65, 1980.

Press, W. H., S. A. Teukolsky, W. T. Vetterling, and B. P. Flannery, *Numerical Recipes in C, The Art of Scientific Computing*, Cambridge University Press, 2nd edn., 1992.

Quegan, S. and J. Lamont, Ionospheric and tropospheric effects on synthetic aperture radar performance, *Int. J. Remote Sensing*, *7*, 525–539, 1986.

Radon, J., (On the determination of functions from their integrals along certain manifolds), *Ber. Saechs. Akad. Wiss. Leipzig, Math. Physics Kl.*, *69*, 262–277, 1917.

Ramo, S., J. R. Whinnery, and T. Van Duzer, *Fields and Waves in Communication Electronics*, John Wiley & Sons, 1994.

Ratcliffe, J. A., *The Magneto-Ionic Theory and its Applications to the Ionosphere*, Cambridge University Press, 1959.

Rawer, K., Low and equatorial latitudes in the international reference ionosphere (IRI), *Adv. Space Research*, *18*, 1996.

Rawer, K., D. Bilitza, and S. Ramakrishnan, Goals and status of the international reference ionosphere, *Rev. Geophys.*, *16*, 177–181, 1978.

Rees, M. H., *Physics and Chemistry of the Upper Atmosphere*, Cambridge University Press, 1989.

Rignot, E. J., R. Zimmermann, and J. J. van Zyl, Spaceborne applications of P band imaging radars for measuring forest biomass, *IEEE Trans. Geoscience and Remote Sensing*, *33*, 1162–1169, 1995.

Rino, C. L., A power law phase screen model for ionospheric scintillation, 1. Weak scatter, *Radio Sci.*, *14*, 1135–1145, 1979a.

Rino, C. L., A power law phase screen model for ionospheric scintillation, 2. Strong scatter, *Radio Sci.*, *14*, 1147–1155, 1979b.

Rino, C. L., On the application of phase screen models to the interpretation of ionospheric scintillation data, *Radio Sci.*, *17*, 855–867, 1982.

Rino, C. L. and J. Owen, The effects of ionospheric propagation disturbances on satellite-borne synthetic aperture radars, Tech. Rep. DNA-TR-84-406, SRI International, 1984.

Sardón, E. and N. Zarraoa, Estimation of total electron content using GPS data: How stable are the differential satellite and receiver instrumental biases?, *Radio Sci.*, *32*, 1899–1910, 1997.

Sargis, P. D., F. D. Lee, E. S. Fulkerson, B. J. McKinley, and W. D. Aimonetti, Ground-penetrating radar for buried mine detection, in *Proc. SPIE*, vol. 2217, pp. 38–49, SPIE, 1994.

Scudder, H. J., Introduction to computer aided tomography, *Proc. IEEE*, *66*, 628–637, 1978.

Sheen, D. R., C. M. Strawitch, and T. B. Lewis, UHF wideband SAR design and preliminary results, in *IGARSS '94*, pp. 289–291, IEEE, 1994.

Sheen, D. R., S. C. Wei, T. B. Lewis, and S. R. deGraff, Ultrawide-bandwidth polarimetric SAR imagery of foliage obscured objects, in *Proc. SPIE*, vol. 1631, pp. 106–113, SPIE, 1992.

Sherwin, C. W., J. P. Ruina, and R. D. Rawcliffe, Some early developments in synthetic aperture radar systems, *IRE Trans. Military Electronics*, *6*, 111–115, 1962.

Skolnik, M. I., *Introduction to Radar Systems*, McGraw–Hill, 2nd edn., 1981.

Smith, E. K. and S. Weintraub, The constants in the equation for atmospheric refractive index at radio frequencies, *Proc. IRE*, *41*, 1035–1037, 1953.

Taylor, J. D., Ultra-wideband radar overview, in Taylor, J. D. (ed.), *Introduction to Ultra-Wideband Radar Systems*, CRC Press, 1995.

Thomas, G. *et al.*, Selective motion compensation in ISAR imagery using time-frequency filtering, in *Algorithms for Synthetic Aperture Radar Imagery III*, vol. 2757, pp. 14–24, SPIE, 1996.

Thompson, T. W. and R. B. Dyce, Mapping of lunar radar reflectivity at 70 centimeters, *J. Geophys. Res.*, *71*, 4843–4853, 1966.

Toups, M. F., S. Ayasli, and J. G. Fleischman, Part II: Analysis of foliage-induced synthetic pattern distortions, *IEEE Trans. Aerospace and Electronic Systems*, *32*, 145–155, 1996.

Vickers, R. S., V. H. Gonzalez, and R. W. Ficklin, Results from a VHF impulse synthetic-aperture radar, in *Proc. SPIE*, vol. 1631, pp. 219–225, SPIE, 1992.

Villard, Jr., O. G., The ionospheric sounder and its place in the history of radio science, *Radio Sci.*, *11*, 847–860, 1976.

Wahl, D. E., P. H. Eichel, D. C. Ghiglia, and C. V. Jakowatz, Jr., Phase gradient autofocus—a robust tool for high resolution SAR phase correction, *IEEE Trans. Aerospace and Electronic Systems*, *30*, 827–834, 1994.

Walker, J. L., Range-doppler imaging of rotating objects, *IEEE Trans. Aerospace and Electronic Systems*, *AES-16*, 23–52, 1980.

Wehner, D. R., *High-Resolution Radar*, Artech House, 2nd edn., 1995.

Whalen, A. D., *Detection of Signals in Noise*, Academic Press Inc., 1971.

Wilson, B. D., A. J. Mannucci, and C. D. Edwards, Subdaily northern hemisphere ionospheric maps using an extensive network of GPS receivers, *Radio Sci.*, *30*, 639–648, 1995.

Zebker, H. A., P. A. Rosen, and S. Hensley, Atmospheric effects in interferometric synthetic aperture radar surface deformation and topographic maps, *J. Geophys. Res.*, *102*, 7547–7563, 1997.